REPUBLIQUE ALGERIENNE DEMOCRATIQUE ET POPULAIRE

MINISTERE DE L'ENSEIGNEMENT SUPERIEUR
ET DE LA RECHERCHE SCIENTIFIQUE

UNIVERSITE ABOU BEKR BELKAID DE TLEMCEN
FACULTE DES SCIENCES
DEPARTEMENT DE PHYSIQUE

UNITE DE RECHERCHE MATERIAUX
ET ENERGIES RENOUVELABLES (URMER)

THESE

Présentée pour obtenir le diplôme de
DOCTEUR EN PHYSIQUE
Spécialité : énergies renouvelables

Par

M. Khalil BENMOUIZA

Sur le Thème

Quantification of solar radiation in Algeria, application to the sizing of photovoltaic systems

Quantification du gisement solaire algérien, application au dimensionnement des systèmes photovoltaïques

Soutenu publiquement le **26 Mai 2015**, devant le jury composé de :

Président :	**Boumediéne BENYOUCEF**	Professeur à l'Université de Tlemcen
Directeur de thèse :	**Ali CHEKNANE**	Professeur à l'Université de Laghouat
Examinateurs:	**Nour- El-Islam BACHARI**	Professeur à L'U.S.T.H.B.
	Amar HADJ-ARAB	Directeur de Recherche C.D.E.R. Bouzaréah
	Ali CHERMITTI	Professeur à l'Université de Tlemcen

Aknowldgment

First and foremost, I am very grateful to the almighty ALLAH S.W.T for giving me the key and opportunity to accomplish my PhD thesis.

I wish to express my deepest appreciation to my supervisor, Pr. CHEKNANE Ali, for encouragement, guidance, suggestions, critics and friendship throughout finishing this project. I am proud and grateful for having had the possibility to work and learn from him.

I would like to thank BENYOUCEF Boumediène , professor in university of Tlemcen for his acceptance to be the president of the eminent jury. Also, I would like to thank, BACHARI Nour El-Islam professor in the university of science and technology – Houari Boumediene in Algeria , Pr. HADJ-ARAB Amar Research director in CDER of Bouzaréah and CHERMITTI Ali professor in the university of Tlemcen for their acceptance to examine this thesis.

I wish to thank all my professors, staff and technicians in the research unit of materials and renewables energies (URMER) in the university of Tlemcen and the semiconductors and functional materials laboratory in the university of Laghouat and also i like to thank Pr. SANTIAGO Silevster from the university of Barcelona for their cooperation, indirect or directly contribution in finishing my thesis.

BENMOUIZA Khalil

To my life, my mother

To my guide, my father

To my sisters and brothers

To all my family and friends

Thank you for believing in me

Contents

List of Figures

List of Tables

General introduction

The growing demand of energy in our modern industrial life requires the search for alternative energy sources outside the limited and polluted current sources, such as fossil fuels. Renewable energy, in its various forms, such as wind and solar energies, is an interactive, available and environment friendly solution. The Sun is the main source of most energy in the Earth. This includes photovoltaic and solar thermal energy, wind energy, geothermal energy, hydropower, and even the energy generated by oil (Sen, 2008).

Solar energy can be used in different range of applications such as generating electricity by photovoltaic effect, architecture and building design (e.g. air conditioning and cooling systems) and other fields, such as health sector (disease control and skin cancer research) (Badescu, 2008). This energy has the advantage of being extremely sustainable and inexhaustible (solar energy received at the Earth for one year is a thousand times higher than the energy produced by oil). However, its amount is not constant in time and place because of its random nature (Wu and Chan, 2011; Huang et al., 2013), due to the gases, clouds and dust within the atmosphere, which absorbs and/or scatter radiation at different wavelengths. In addition, obtaining reliable radiation data at ground level require systematic measurements. However, in most countries the spatial density of radiometric stations is inadequate. Hence, quantification of solar radiation data at each point in the Earth became more and more important due to the increasing number of solar energy applications.

Quantifying the solar radiation is the data set describing the evolution of the solar radiation at a given place and during a given period. Its study is the starting point of any investigation in the field of solar energy. It could be used to simulate the design and the optimization of photovoltaic systems. For that, a large number of solar radiation computation models were developed, ranging from very complicated computer codes to empirical relations (Zhang 2003; Kaplanis and Kaplani2007 ; Boland 2008; Wu and Chan 2011; Pandey and Soupir 2012; Badescu et al. 2013). These models are tested and compared with measured ground data and the accuracy is then improved by researches throughout the years. Moreover, the kinds of measured solar radiation data depend strongly on the application of monthly or daily averaged data which are required for climatology studies and feasibility for solar energy systems. Hourly data are needed to simulate the performance of solar systems or during collector testing. Small scales solar radiations are used for process simulation or designing and optimizing device sizing.

The aim of this thesis is to summarize the main approaches, methods and techniques applied to the reconstruction of solar ground components while analyzing the benefits and limitations of each. Then, we try to develop new models to estimate (Tadj et al., 2014) and forecast solar radiation data (Benmouiza and Cheknane., 2013 ; Benmouiza and Cheknane, 2015) to use it in solar energy applications such as sizing of stand-alone PV systems. Thus, the models are applied and tested in Algeria. The choice of Algeria sites is due to the inter-

esting potentially of solar energy (Mefti and Bouroubi, 1999) . Indeed, it has a considerable territory of solar radiation (more than 2500 sunshine hours per year). Although conditions (geographical, climatic and weather) are very favorable, solar power has not been widely used and this market remains almost untouched. Hence, it is important for a country as Algeria, to estimate the potential of this type of energy in order to identify possible and effective ways to use it in an energy policy perspective .

In Algeria, different main sources of solar radiation information can be found such as radiation measurements made in meteorological and radiometric stations and some estimation models. The first is the most direct, and therefore more accurate, but it is not always available; because in Algeria, for example, weather stations are few and often very remote from each other. In addition, only the sunshine duration can be measured sunshine and rarely we can measure global solar radiation. Hence, it is necessary to study the repartition of the radiometric stations in Algeria as well as analysis of sunshine duration in order to classify and study the amount of solar radiation in the country. The other methods are used to estimate the radiation from a set of input parameters such as sunshine duration, time of sunrise and sunset, temperature, relative humidity, atmospheric pressure and also the geographical coordinates of the place (latitude, longitude and altitude). The later models can be classified into four categories: spectral models, semi-empirical models, meteorological models and physical models. However, long-term solar radiation estimation and measuring is not possible because of some financial and technical limitations. Hence, developing forecasting models is needed in order to get more information about future values of solar radiation amount at any place in Algeria. These data can be used in different applications such as estimation of the PV output systems and stand-alone PV systems sizing .

Thesis outline

For developing all the previously mentioned points, this thesis is structured along logical lines of progressive thought. After an introduction, the methodology of our work revolves around five chapters which link theory to practice as follows;

Chapter 1 is designed to be an introduction to solar radiation fundamental concepts. It presents some basic definitions and useful general information about solar radiation in particular coordinate systems, astronomical variables and the constitution of the atmospheric layers as well as solar radiation at the top of the atmosphere.

Chapter 2 deals with the study and classification of the sunshine hours in Algeria. Before that, we will present the instrumentation used to measure solar radiation components as well as solar radiation databases over the world. At the end of this chapter, a solar map is reconstructed based on Ordinary Kriging interpolation method to classify the energy zones in Algeria.

Chapter 3 we will focus on a range of models encountered in the literature to estimate the components of solar radiation. A comparison between semi empirical, meteorological and physical models is presented. A new approach based on satellite image processing is also pro-

posed to estimate hourly solar radiation at any place in Algeria.

Chapter 4 proposes two novel hybrid models to forecast solar radiation data in small scales. It presents a new hybrid autoregressive moving average (ARMA) and nonlinear autoregressive neural network (NAR) models, and a hybrid k-means and NAR models.

Chapter 5 surveys the algorithms for sizing stand-alone PV systems in small scales based on the study of loss of load probability (LLP).

The thesis will be ended by a general conclusion with some perspectives for future works.

References

Badescu V, Gueymard C, ChevalS,Oprea C, Baciu M, Dumitrescu A, Iacobescu F ,Milos I, Rada C .Accuracy analysis for fifty-four clear-sky solar radiation models using routine hourly global irradiance measurements in Romania.Renew Energy 2013, 55: 85-103.

Badescu V. Modeling Solar Radiation at the Earth.Surface, Ed., Springer, 2008.

Benmouiza K, Cheknane A.Forecasting hourly global solar radiation using hybrid k-means and nonlinear autoregressive neural network models.ENERG CONVERS MANAGE 2013, 75: 561-569.

Benmouiza K, Cheknane A.Small-scale solar radiation forecasting using ARMA and nonlinear autoregressive neural network models. THEOR APPL CLIMATOL 2015, 1-14.

Boland JW .Time series and statistical modelling of solar radiation, Recent Advances in Solar Radiation Modelling.ViorelBadescu (Ed.), Springer-Verlag 2008, pp. 283-312.

Huang J , Korolkiewicz M , Agrawal M , Boland J. Forecasting solar radiation on an hourly time scale using a coupled autoregressive and dynamical system (CARDS) model, Sol. Energy 2013, 87:136-149.

Kaplanis S, Kaplani E . A model to predict expected mean and stochastic hourly glob.Renew. Energy 2007, 32: 1414-1425.

Tadj M, Benmouiza K, Cheknane A.An innovative method based on satellite image analysis to check fault in a PV system lead–acid battery. Simulation Modelling Practice and Theory 2014, 47 : 236-247.

Mefti A, Bouroubi M Y. Estimation et Cartographie de la Composante Globale du Rayonnement Solaire. Rev. Energ. Ren. 1999 , 2 : 219-224.

Pandey P K , Soupir M L . A new method to estimate average hourly global solar radiation on the horizontal surface. Atmos Res 2012, 115:83-90.

Şen Z. Solar Energy Fundamentals and Modeling Techniques.Atmosphere, Environment, Climate Change and Renewable Energy.Springer. 2008.

Tadj M, Benmouiza K, Cheknane A, Silvestere S.Improving the performance of PV systems by faults detection using GISTEL approach. ENERG CONVERS MANAGE2014, 80: 298-304.

Wu J , Chan K C . Prediction of hourly solar radiation using a novel hybrid model of ARMA and TDNN. Sol. Energy 2011, 85: 808-817.

Zhang G.Time series forecasting using a hybrid ARIMA and neural network model.Neurocomputing 2003, 50: 159–175.

Chapter 1

Solar radiation fundamental concepts

1.1 Introduction

The Sun is the main source of energy available on Earth. This includes, thermal, wind, hydroelectric and solar energy. Solar radiation emission from Sun into Earth appears in the form of electromagnetic waves. Solar radiation is absorbed, reflected, or diffused by solid particles in the Earth's atmosphere that depends on the weather, climate and other factors. The incoming radiation at any given point takes different shapes depending on the geometry of the Earth, its distance from the Sun, geographical location of any point on the Earth, astronomical coordinates, and the composition of the atmosphere. This chapter provides the basic astronomical variables and their definitions used in the calculation of solar radiation (energy) assessment. These basic concepts, definitions, and derived astronomical equations furnish the foundations of solar energy evaluation at any given location.

1.2 Nature of Sunlight

Sun has played a dominant role for different natural activities in the universe for the formation of fossil and renewable energy sources. It will continue to do so until the end of the Earth's remaining life, which is predicted to be about 5×10^9 years. The diameter of the Sun is $R = 1.39 \times 10^6$ km. And, its mass is equal to 2×10^{30} Kg that composed predominantly of the two lightest elements, Hydrogen, H, which makes up about 70% of the mass, and Helium, He, about 27%; and the remaining 3% of solar matter is made up of all the other 90 or so elements (McAlester, 1983). The origin of solar radiation received on the Earth is the conversion of H into He through solar fusion. He is steadily being produced from lighter H as four nuclei unite to form one nucleus of helium with a release of electromagnetic energy as presented in Fig.1.1 and Fig.1.2.

The emitted energy of the Sun is 3.8×10^{26}W and it arises from the thermonuclear fusion of H into heat temperatures around 1.5×10^6 K at the core of the Sun. The energy released by the thermonuclear reaction is transported by energetic photons, but because the strong absorption of the peripheral gases, most of these photons do not penetrate the surface. The Sun radiates electromagnetic energy in terms of photons which are light particles. Almost 30% of this incident energy of the Earth is reflected back, but the rest is absorbed and is, eventually, retransmitted to deep space in terms of long-wave infrared radiation. The total power that is

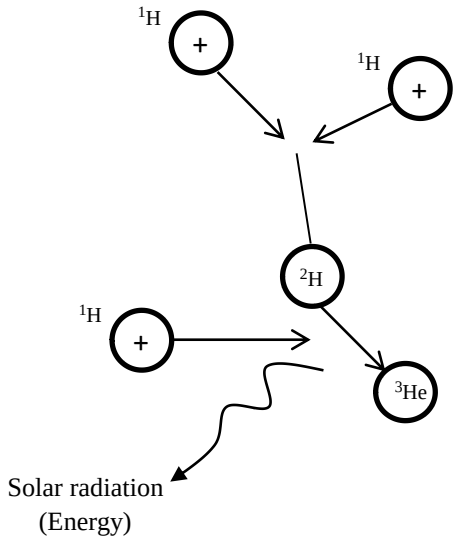

Figure 1.1: H burning in Sun (McAlester 1983).

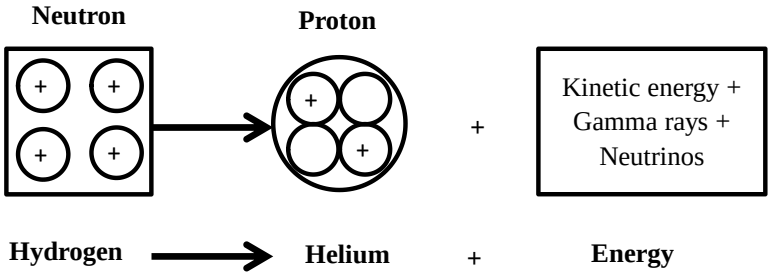

Figure 1.2: Proton conversion into He nuclei plus energy (Şen, 2008).

incident on the Earth's surface from the Sun every year is 1.73×10^{14} kW and this is equivalent to 1.5×10^{18} kWh annually, which is equivalent to 1.9×10^{14} Tons. Compared to the annual world consumption of almost 10^{10} Tons, this is a very huge and inappreciable amount. This energy is considered uniformly spread all over the world's surface and, hence, the amount that falls on one square meter at noon time is about 1 kW in the tropical regions. The amount of solar power available per unit area is known as radiance or radiant-flux density. This solar power density varies with latitude, elevation, season of the year and the time of a particular day. Most of the developing countries lie within the tropical belt of the world where there are high solar power densities, and so they want to exploit this source in the most beneficial ways. On the other hand, about 80% of the world's populations live between latitudes 35°N and 35° S. These regions receive the Sun's radiation for almost 3000 – 4000 h/year. In solar power density terms, this is equivalent to around 2000 kWh/year. Additionally, in these low latitude regions, seasonal sunlight hour changes are not significant. This means that these areas receive the Sun's radiation almost uniformly throughout the year (Şen, 2008).

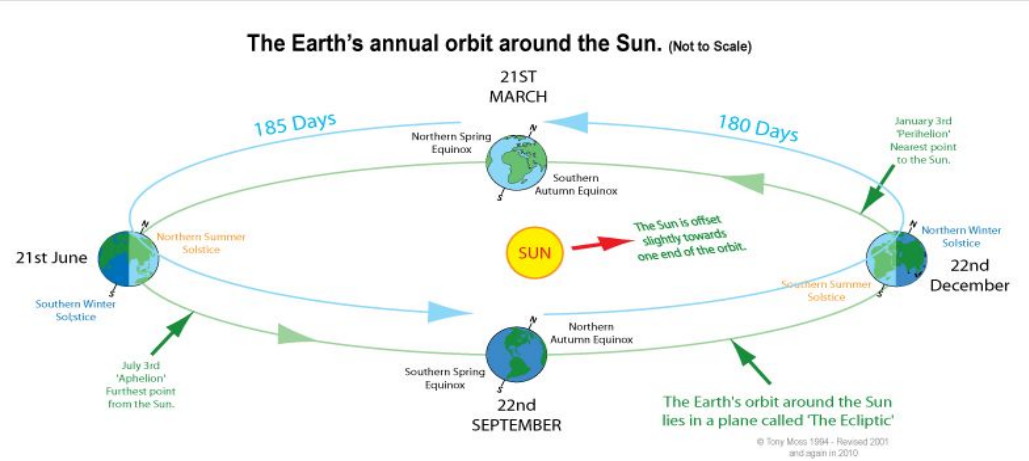

Figure 1.3: The declination angles

1.3 Earth Motion

Earth's orbital movement around the Sun affects the climate, solar radiation, and temporal variations. The total amount of solar radiation reaching the Earth's surface can vary due to changes in the Sun's output, such as those associated with Earth's axis tilt, wobble, and orbital trace. The Earth rotates around the polar axis in 24 hour that generates the day and night. The path of the Earth around the Sun is an ellipse with very low eccentricity (that is to say close to a circle) during 365 days in the year. The angle between the Earth–Sun line and the equatorial plane is called the declination angle, δ, which changes with the date and it is independent of the location. The declination is maximum 23°45' on the summer/winter solstice and 0° on the equinoxes (Stacey 1992) as showed in Fig.1.3. The Sun-Earth distance varies between 147,106 kilometers (3rd January) and 153,106 km (3rd July); its average value is 150,106 km.

Also, the speed of the Earth in its orbit around the Sun is not a uniform movement. It is larger in winter than in summer. Because of that, the duration of spring and summer is longer than the duration of the autumn and winter (duration of summer is 93.6 days, the spring 92.8 days, autumn is 89.8 days and winter, 89.0 days). This variation of the lengths of the seasons is an immediate result of Kepler's second law (law of areas). The combination of movements of the Earth on its axis and around the Sun allows us to determine the position of the Sun, according to the site (latitude and longitude) and time (day of the year and time) on the one hand and day length on the other hand.

1.4 Geographic parameters

Earth is separated by the equator into two hemispheres, the northern hemisphere located on the side of the North Pole and the southern hemisphere, which is situated adjacent to the South Pole. On the other hand, it is divided from west to east by the meridian passing through Greenwich (near London in England).

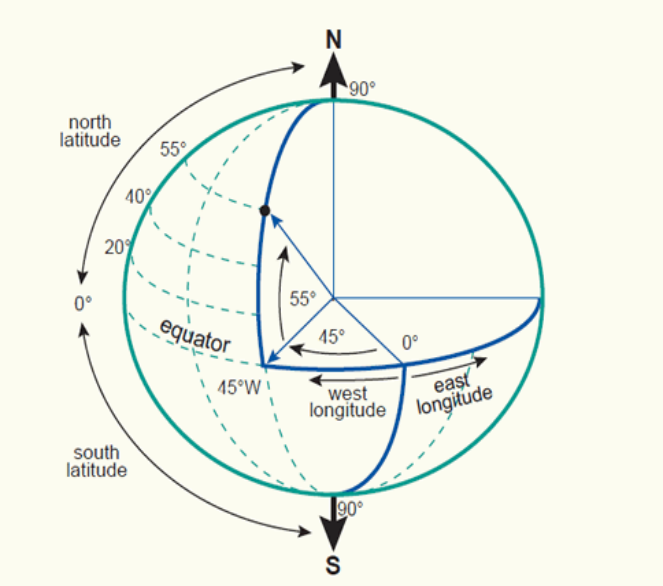

Figure 1.4: Geographic coordinates.

1.4.1 Latitude

In geography, latitude (φ) is a geographic coordinate that specifies the north-south position of a point on the Earth's surface. Latitude is an angle which ranges from 0° at the equator to 90° (North or South) at the poles. , it is counted positively (0 to 90 °) to the north and negatively (0 to -90 °) to the south.

1.4.2 Longitude

Longitude is a geographic coordinate that specifies the east-west position of a point on the Earth's surface. It is an angular measurement, usually expressed in degrees and denoted by (ϕ). The angle extent of 360 ° with respect to a meridian reference, with a range of +180 ° to -180 ° or 180 ° east to 180° west.

1.4.3 Altitude

Altitude or height is a distance measurement, usually in the vertical or up direction, between a reference datum and a point or object. Altitude is commonly used to mean the difference between a point and a mean level, usually the sea level (or level 0) of a location.

1.5 Astronomical parameters

1.5.1 Sun position

Solar radiation and energy calculations require some geometric and time quantities concerning the Sun position relative to the Earth and any point on the Earth. The Sun's position is

marked at every moment of the day and year by two different coordinate systems (equatorial and horizontal).

1.5.1.1 Equatorial coordinates

The Sun movement is marked with respect to the equatorial plane of the Earth using two angles; the declination δ and hour angle ω.

a) Solar declination

The solar declination is the angle of the direction of the Sun with its projection on the equatorial plane. It varies between 23 ° 45 'at the summer solstice (June 21) and -23 ° 45' at the winter solstice (December 21) (Stacey 1992). This variation produces the seasons. The solar declination is expressed by the following equation (Iqbal, 1983)

$$\begin{aligned}\delta = (&0.006918\text{-}0.399912\cos\Gamma + 0.07257\sin\Gamma\text{-}0.006758\cos 2\Gamma \\ &+ 0.000907\sin\Gamma\text{-}0.002697\cos 3\Gamma + 0.00148\sin 3\Gamma)(180/\pi)\end{aligned} \tag{1.1}$$

Γ is the day angle expressed in radians given by

$$\Gamma = 2\pi(N_d - 1)/365 \tag{1.2}$$

Expressing all angles in degrees, then Eq. (1.1) will be expressed as follows.

$$\delta = 23,45^{\circ}.\sin\left[\frac{360}{365}(N_d + 284)\right] \tag{1.3}$$

N_d is the day number of the year, ranging from 1 to 365. (For 1^{st}January $N_d = 1$, and 31^{st} December $N_d = 365$).

b) Hour angle

The hour angle, ω, is the angular distance required for the Earth to rotate once a day, which is equal to 15° multiplied by the number of hours (15×24 = 360°) from local solar noon. It can be defined in degree by

$$\omega = 15(12 - TST) \tag{1.4}$$

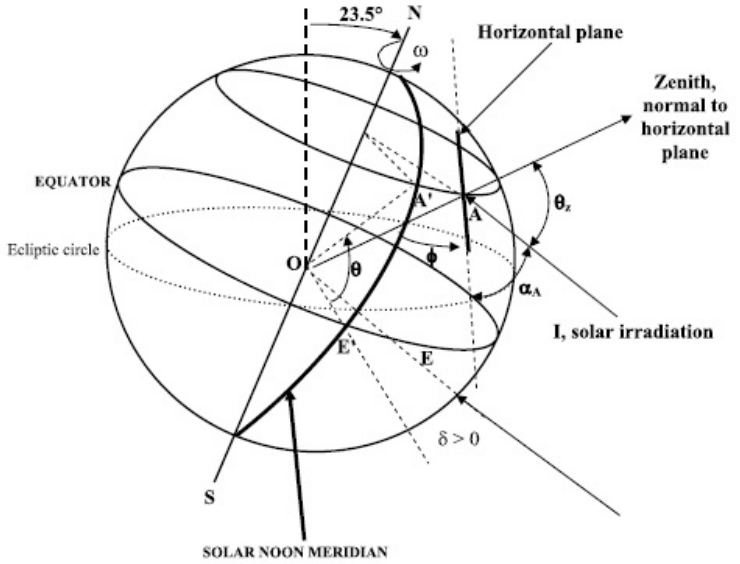

Figure 1.5: Useful angles. (Şen, 2008).

TST is the true solar time. The hour angle is measured from solar noon, it is positive if it is before noon and negative if it is afternoon (ω is 0 ° at noon, -90 ° at 6 PM and 90° in 6 AM).

1.5.1.2 Horizontal coordinates

The horizontal coordinate system is formed by the plane of the astronomical horizon and vertical location. In this reference, the coordinates are the Sun height, h, and the azimuth, θ_z (Iqbal ,1983 ; Duffie and Beckman, 2006).

a) Sun height

The height of the Sun is the angle formed by the direction of the Sun and its projection on the horizontal plane. It is particularly equal to 0 ° at sunrise and sunset in true solar time. Its value is maximum at noon. It expresses by

$$\sin(h) = \cos(\delta)\cos(\phi)\cos(\omega) + \sin(\phi)\sin(\delta) \tag{1.5}$$

b) Azimuth of the Sun

The azimuth of the Sun is the angle between the projection of the Sun direction in the horizontal plane and the South direction

$$\sin(\theta_z) = \frac{\cos(\delta)\sin(\omega)}{\cos(h)} \tag{1.6}$$

It equals to zero at true solar time noon and it is maximum at sunrise and sunset.

1.5.2 Time zones

Geometrical division of time across the world is 24 longitudinal divisions. Time zones are determined by dividing the Earth into 24 lines with 15 degrees of longitude in width. The prime meridian is the Greenwich, which defines the Universal Time. Each country uses the nearest longitude time as principal time.

1.5.3 Solar time

For applications of solar energy, it is necessary to introduce the solar time, which is calculated taking into account the difference between the mean solar time and local time.

1.5.3.1 Mean solar time

The rotation of the Earth around itself introduces the concept of using MST. It is the average time between two successive passages of the meridian of the place, a full rotation of the Earth around itself takes 24 hours.

1.5.3.2 Universal Time

Universal Time (UT) is a time standard based on the rotation of the Earth. It is a modern continuation of Greenwich Mean Time (GMT). GMT is sometimes used loosely as a synonym for UTC. The difference between mean solar time and universal time is called the longitude correction. The relation between universal time and mean solar time is defined by

$$MST = UT \pm (\varphi/15) \tag{1.7}$$

(+) for eastern longitude, and (-) for western longitude.

1.5.3.3 Legal Time

Standard time (or local) is the official time of the state. It differs from the global Greenwich time by a shift in hours.

$$LT = UT + \Delta H \tag{1.8}$$

$\triangle H$ is the time difference between states ($\triangle H$ =1 for Algeria)

1.5.3.4 True solar time

Solar time is a reckoning of the passage of time based on the Sun's position in the sky. The fundamental unit of solar time is the day. True solar time and mean solar time differs. This difference is called the equation of time varies depending on the day (Iqbal ,1986).

$$TST = MST + ET \tag{1.9}$$

ET is the equation of time.

1.5.3.5 Equation of time

This is an equation which takes into account the rotation speed variation of the Earth; it is given in minutes by Spencer (1972)

$$ET = 9.87\sin(2\beta_0) - 7.53\cos(\beta_0) \tag{1.10}$$

β_0 is a function defined in degree by

$$\beta_0 = \frac{360}{365}(N_d - 81) \tag{1.11}$$

1.5.3.6 Transition from the standard time to the true solar time

In general, to convert the standard local time LT true solar time TST, the following expression is used.

$$TST = LT - \Delta H + (\frac{ET + 4\phi}{60}) \tag{1.12}$$

1.5.4 Surface Orientation

Any surface is defined by two angles (α_z, γ):

α_z: the surface azimuth, is the angle between the projection of the normal to the horizontal surface and south direction.

γ: surface height, is the angle between the normal of the surface and its projection on the horizontal plane.

1.5.5 Angle of incidence

The angle of incidence i for a plane of an inclination $\beta^{'}$ is the angle formed by the directional vector of the solar beam and the outgoing normal to the plane. For a south-oriented plane

$$\cos(i) = \cos(\delta)\cos(\omega)\cos(\phi - \beta^{'}) + \sin(\delta)\sin(\phi - \beta^{'}) \tag{1.13}$$

For a north-oriented plane

$$\cos(i) = \cos(\delta)\cos(\omega)\cos(\phi - \beta^{'}) + \sin(\delta)\sin(\phi + \beta^{'}) \tag{1.14}$$

For a horizontal plane ($\beta - 0 = 0$), $cos(i) = sin(h)$.

1.6 Emission from the Sun

1.6.1 Nature of solar radiation

The solar radiation is an electromagnetic wave (Fig. 1.6) emitted by the Sun . We are talking about electromagnetic radiation (EMR) when the radiation behaves like a force field that affects the electrical and magnetic properties of matter. Light is the visible part of EMR, that we can capture it with our eyes (Şen, 2008).

The radiation from the Sun is spread over a wide frequency range at the speed of light, on average, 499 seconds, or 8 minutes and 19 seconds to reach our atmosphere. Solar radiation contains electromagnetic wavelengths as short as 0.2mm (ultraviolet) with maximum energy centred at around 0.4mm (visible blue light).

Fig.1.7 clearly shows that most of solar radiation occurs in the short-wave visible and ultraviolet portions of the electromagnetic spectrum. There is some long-wave component of infrared. However, large bands of these are absorbed by gasses and particles within the upper atmosphere (Badescu ,2008) .

1.6.2 Sunlight spectrum

The Sun sends us an electromagnetic radiation, which is in the field of light. This infrared radiation is composed of visible light and ultraviolet:

- Visible wavelengths between 0.4 μm and 0.8 μm, it comprises 48% of the radiation;
- Ultraviolet (UV) radiation at wavelengths shorter than 0.4 μm, it represents 6% of the radiation;
- Infrared (IR) radiation at wavelengths greater than 0.8 μm it covers 46% of the radiation.

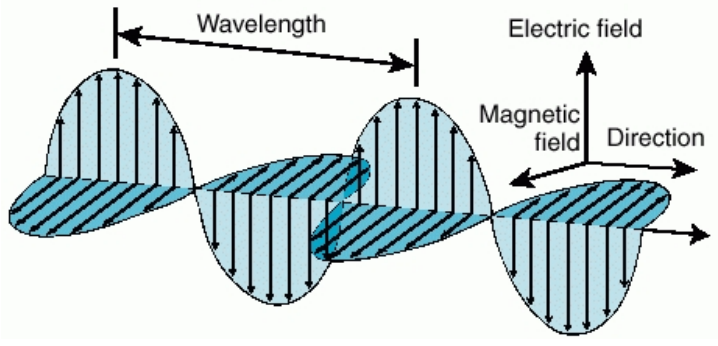

Figure 1.6: Electromagnetic waves.

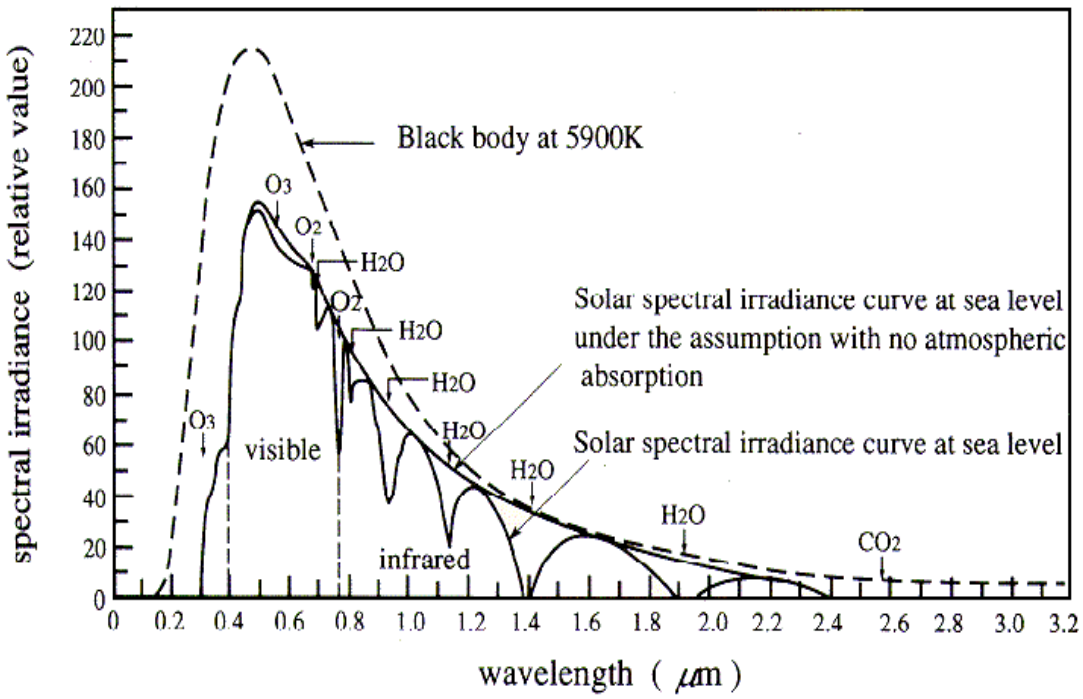

Figure 1.7: Solar spectrum.

1.7 Structure and composition of the Atmosphere

Before arriving at ground level, solar radiation undergoes physical changes in passing through the atmosphere; it interacts with the gaseous and solid constituents of the atmosphere.

1.7.1 Definition of the Earth atmosphere

The atmosphere is the gaseous layer that surrounds our planet. Although it is very thin in comparison to the Earth's radius, its role is filtering the incoming solar radiation that is essential for the presence of life on Earth. It consists of 78.09% Nitrogen, 20.95% Oxygen, 0.93% Argon, and a variety of other gases. The role of the atmosphere is essential to life on Earth because:

- It allows to have an average temperature;
- It limits the temperature differences between day and night, and contributes to global warming by trapping a portion of solar radiation by greenhouse;
- It absorbs most of the harmful ultraviolet radiation of the Sun in the ozone layer.

1.7.2 Structure of the Atmosphere

The atmosphere is divided into layers according to major changes in temperature. Gravity pushes the layers of air down on the Earth's surface. This push is called air pressure. 99% of

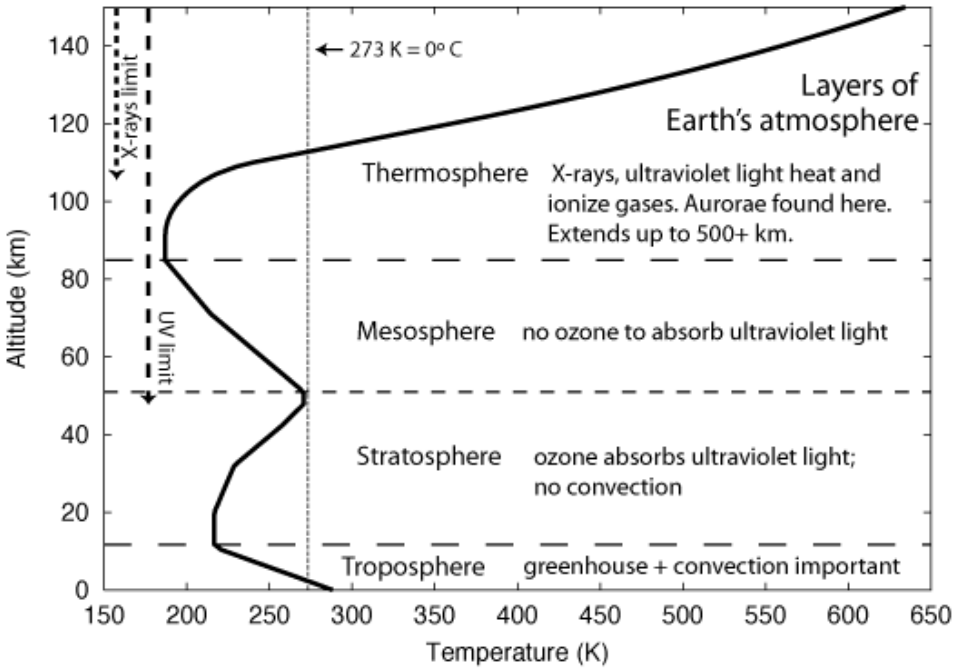

Figure 1.8: Vertical temperature profile in the atmospheric layers.

the total mass of the atmosphere is below 32 kilometres. The World Meteorological Organization (WMO) defines four zones that characterize thermal phenomenon (that is to say, the temperature variations in the atmosphere) as shown in Fig.1.8.

a) Troposphere- 0 to 12 km - Contains 75% of the gases in the atmosphere. This is where you live and where weather occurs. As height increases, temperature decreases.

b) Stratosphere - 12 to 50 km - in the lower part of the stratosphere. The temperature remains constant (-60 degrees Celsius). This layer contains the ozone layer.

c) Mesosphere - 50 to 80 km - in the lower part of the mesosphere. The temperature drops in this layer to about -100 degrees Celsius. This is the coldest region of the atmosphere. This layer protects the Earth from meteoroids.

d) Thermosphere - 80 km and up - The air is very thin. Thermosphere means "heat sphere". The temperature is very high in this layer because ultraviolet radiation is turned into heat. Temperatures often reach 2000 degrees Celsius or more.

1.7.3 Composition of the atmosphere

To characterize the composition of the atmosphere, three regions are defined as follows: Homosphere (which includes the Troposphere, Stratosphere and Mesosphere) in which the composition of dry air is uniform and invariable. Heterosphere wherein the composition of the

air is subject to a systematic variation and vertical photosphere formed exclusively of free electrons and protons. Only Homosphere involved in the phenomenon of propagation of the solar radiation because it contains the main elements that alter the spectral composition of light, as dry air, atmospheric water and aerosols. Moreover, scientists have preferred to add a fourth element defined by cloud cover. In fact, although it composed mainly of water under various conditions, clouds affect solar radiation significantly. We also see that they play an important role in the spectral and directional characterization of solar radiation.

1.7.3.1 The dry atmospheric air

Dry air consists mainly of four parts, namely: Nitrogen (N_2, 78.08% of the volume), Oxygen (O_2, 20.94%), Argon (Ar, 0.93%) and Carbon dioxide (CO_2, 0.033%), called permanent gases. However, these components have variable concentrations, which depending on the latitude, wind, urban site and the season. Among the components of the dry air, the ozone. It is a particular element to be considered in the phenomenon of absorption of solar radiation, despite its low concentration (10-6% by volume of dry air). Indeed, most of the ultraviolet radiation is absorbed by this element, thereby protecting the land of these high-energy radiations. The amount of ozone depends on latitude and season (Şen, 2008). It is significant in an area between 15 and 30 km altitude. In the upper atmosphere, ozone is created by ultraviolet radiation from the Sun.

1.7.3.2 Atmospheric water

The water in the atmosphere is mainly localized in the lower 10 km of the atmosphere. It comes from the evaporation of water from the surface of the Earth, the oceans and seas. Its concentration varies so widely. Water is found as gas molecules (water vapor), a liquid and solid form in the clouds. As for ozone, its influence on solar radiation is important and should determine its atmospheric content. For this, we are interested in the total optical thickness of water vapor at the site concerned that is to say on the total weight of water vapor. The height of perceptible water depends on the ability of the air to contain water vapor, and therefore its relative humidity and temperature. Height of perceptible water varies from 0.1 to 1 cm in the poles and in the desert where the air is dry, 2 to 5 cm in temperate climates and greater than 5 cm in tropical climates (Şen,2008).

1.7.3.3 Aerosols

Aerosols are all particles suspended in the air from various industrial and natural activities: pollen, sand and crystal sea salts carried by wind, volcanic eruptions, meteorite dust, agricultural and forest fires (rain, snow and hail are not considered aerosols). Aerosols have volumes, concentrations, distributions, shapes and compositions of very different materials (Şen, 2008). Their dimensions vary from a few nanometers to hundreds of micrometers (giant particles); they are substantially higher than comparable dry air molecules and the wavelengths of the light radiation. Aerosols are characterized by two coefficients (α and β)

- α , characterizes the average size of airborne particles. More, the higher α describes the smallest aerosols.
- β, The value of the Angstrom turbidity factor (Ångström, 1961), which describes the aerosol content.

Generally, the concentration of aerosols is:

- Greater in polluted site in rural site;
- Superior over the continent than the oceans;
- More important, during drying periods.

1.7.3.4 Clouds

In meteorology, a cloud is a visible mass of liquid droplets or frozen crystals made of water or various chemicals suspended in the atmosphere above the surface of a planetary body. Cloud cover is often considered separately as a filter on a blue sky. Clouds contain suspended particles in the air. This explains why after some thunderstorms the sky looks clear. Cloudiness is the meteorological parameter for estimating the importance took from clouds in the diffusion phenomenon and it is used as the first parameter to calculate the sunshine fraction.

1.7.4 Effect of the atmosphere on solar radiation

1.7.4.1 General Description

When electromagnetic radiation encounters a material medium, two phenomena occur: decrease its energy and a change in its direction. At the output of each molecule encountered, besides the fraction absorbed, two radiations are identified: a transmitted radiation and scattered radiation. After passing through a set of particles (atmosphere cloud), the entire radiation transmitted becomes the direct radiation. The other scattered part is called diffuse radiation. The distributed radiation toward hemisphere part is called the reflected radiation.

1.7.4.2 Concept of the air mass

Air mass defines the direct optical path length through the Earth's atmosphere; it represents how much atmosphere solar radiation has to pass through before reaching earth surface. Air mass coefficient can be used to help characterize the solar spectrum after solar radiation has travelled through the atmosphere. Air mass coefficient is commonly used to characterize the performance of solar cells under standardized conditions, and is often referred to using the syntax "AM" followed by a number. Air Mass (AM) equals 1.0 when the Sun is directly overhead at sea level. "AM 1.5" is almost universal when characterizing terrestrial power-generating panels. Many formulas exist for determining the amount of the air mass, especially Kasten and Young (1989) where the general expression is given by Eq.(1.15)

$$m_a = \left(\frac{P(\lambda)}{P_0}\right) m_r(\mathrm{h}) = \frac{1-0.1\lambda}{\sin(h)+0.50572.(h+6.07995)^{-1.6864}} \tag{1.15}$$

Another formula is proposed by IQBAL to calculate the air mass

$$m_a = \exp\left(-0.0001184.\lambda\right) \frac{1}{\cos(\theta_z) + 0.15.(93.885 - \theta_z)^{-1.258}} \tag{1.16}$$

Where,

- m_a is the corrected air mass;
- m_r is the relative air mass at sea level;
- P is the average atmospheric pressure;
- P_o is the average atmospheric pressure at sea level (P_o=1013 mbar);
- θ_z zenith angle, θ_z= $90° - h$.

1.8 Properties of the electromagnetic waves

1.8.1 Attenuation of solar radiation

During its passage through the atmosphere, solar radiation is attenuated by the phenomena of absorption and scattering and reflection as shown in Fig. 1.9. This attenuation is due to the different atmospheric constituents: gas molecules, water vapor and aerosols. The attenuation of solar radiation is based on the number, size and nature of the molecules and particles encountered. It also varies with the length of the path of solar radiation through the atmosphere (air mass) (Şen,2008).

1.8.1.1 Absorption

As solar radiation passes through the atmosphere, gasses, dust and aerosols absorb the incident photons. Specific gasses, notably ozone (O_3), carbon dioxide ($C0_2$), and water vapor (H_2O), have very high absorption of photons that have energies close to the bond energies of these atmospheric gases. This absorption yields deep troughs in the spectral radiation curve (Spencer ,1972).

a) Absorption by ozone

Ozone (O_3) is characterized by a strong absorption band at wavelengths between 210 and 290 nm in the ultraviolet range and a low absorption between 450 and 770 nm in the visible domain.

b) Absorption steam

Water vapor (H_2O) is an important factor in the attenuation of solar radiation. It absorbs waves located in the area of infrared.

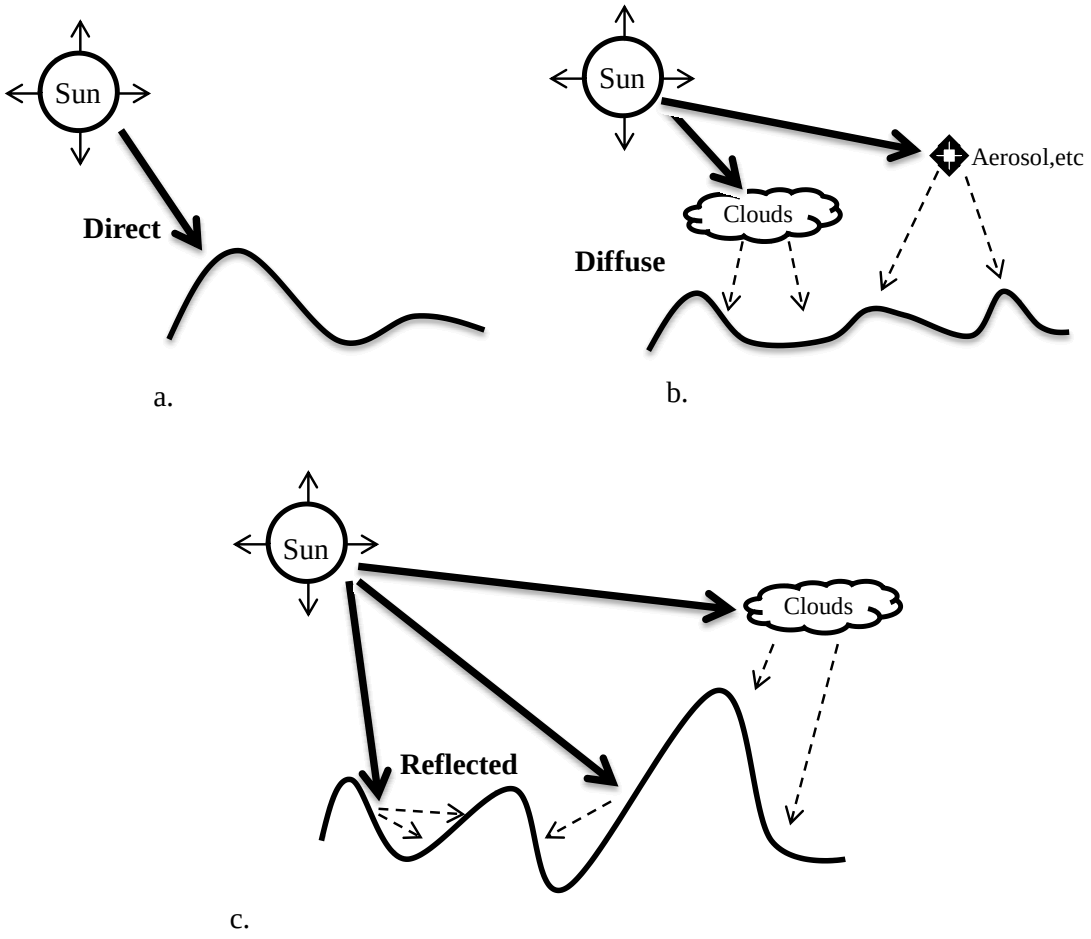

Figure 1.9: Solar radiation path, a) direct, b) diffuse, c) reflected

c) Absorption by gases

The absorption of solar radiation by the gas is very low. In most literatures it is considered negligible.

1.8.1.2 Scattering (diffusion)

Atmospheric scattering can be either due to the molecules of atmospheric gases or due to smoke, haze, and fumes (Richards, 1993). One of the mechanisms for light scattering in the atmosphere is known as Rayleigh scattering, which is caused by molecules in the atmosphere. Rayleigh scattering is particularly effective for short wavelength light (that is, blue light) since it has a λ^{-4} dependence. Beside Rayleigh scattering, aerosols and dust particles contribute to the scattering of incident light known as Mie scattering (Şen,2008).

a) Rayleigh scattering

Rayleigh scattering occurs when the particle size is less than the wavelength of the radiation. These particles can be from the dust, nitrogen or oxygen molecules. Rayleigh scattering scatters more significantly short wavelength. This form of diffusion is predominant in the upper layers of the atmosphere. The extinction coefficient characterizing this type of diffusion is given by Eq.(1.17)

$$k_r(\lambda) = 0.008735\lambda^{-4} \tag{1.17}$$

b) Mie scattering

We talk on Mie scattering when the particles are almost as large as the wavelength of the radiation. This type of diffusion is often produced by aerosols such as dust, pollen, smoke and water. This kind of diffusion affects the larger wavelengths and occurs mainly in the lower layers of the atmosphere where larger particles are more abundant. This process dominates when the sky is cloudy. The extinction coefficient of this type of diffusion is,

$$k_a(\lambda) = \beta\lambda^{-\alpha} \tag{1.18}$$

The calculation of α and β is done experimentally for just the wavelengths λ=380 nm and λ=500 nm. Hence, in most of the cases, is equal to 1.3 for temperate regions. It is close to 0 for smaller particles that increase with the particle size and achieved 4 for larger particles. The β Coefficient is given in Table 1.1 according to different states of the atmosphere (Ångström, 1961),

1.8.1.3 Reflection

When a change of the propagation environment, a part of the electromagnetic wave reflected again towards the original environment. Each body which receives an amount of EMR may reflect a part. Reflected radiation is mainly reflected from the terrain and is, therefore, more important in mountainous areas. When it comes to solar energy reflected by a portion of land area, it calls the albedo.

Table 1.1: β Coefficient according to different stats of the atmosphere.

Atmosphere	β
Very dark blue sky (Pure)	0.02
Clear blue sky	0.05
Blue slightly sky	0.1
Milky blue and almost white sky (polluted sky)	0.2
Highly polluted sky	0.4

Table 1.2: Albedo values. (Şen,2008)

Surface	Albedo (%)
New snow	85
Old snow	75
Clayey desert	29- 31
Green grass	8- 27
Pine forest	6- 19
Calm sea surface	2- 4
Granite	12- 18
Water (depending on angle of incidence)	2- 78
High-level cloud	21
Middle-level cloud (between 3 and 6 KM)	48
Low-level cloud sheets	69
Cumulus clouds	70

a) Definition of albedo

The albedo reflection coefficient is the reflective quality of a surface. It is expressed as a percentage of reflected radiation to incoming radiation and zero percent is total absorptions while 100% is total reflection. To determine the Albedo, a scale of 0-1 is used, with 0 corresponding to the black, for a body without any reflection, and 1 corresponding to a perfect mirror, for a body that is scattered in all directions and without absorption. Table 1.2 shows some Albedo values.

N.B. The different mathematical equations proposed in literature of reflection, absorption and diffusion are discussed in Chapter 3.

1.9 The extraterrestrial solar radiation

Extraterrestrial solar radiation (outside the atmosphere) is the solar radiation that strikes the surface of the atmosphere.

1.9.1 Solar constant

To study the effect of solar radiation on the Earth system, it is necessary to determine the amount of energy reaching the Earth's atmosphere. Once the surface radiance of the Sun is determined, the amount of energy reaching the top of the Earth's atmosphere E_{ext} can be calculated using the following equation (Mil1er, 2010; Koupelis, 2010)

$$E_{ext} = \sigma' T_{su}^4 \left(\frac{R_{su}}{D_{s,e}} \right)^2 \tag{1.19}$$

Where,

- T_{su} is the temperature of the top of the Sun = 5800 K;
- R_{su} is the radius of the Sun;
- $D_{s,e}$ is the average Sun-Earth distance = 1.5×10^8 Km ;
- σ' is the Constant of Stephane Boltzmann = $5.67 \times 10^{-8} W.m^{-2}.K^{-4}$.

The average amount of energy received on a surface perpendicular to incoming radiation at the top of the atmosphere is the solar constant I_0. The generally accepted solar constant of 1368 W/m^2 (Monteith, 1962) is a satellite measured yearly average.

1.9.1.1 Correction of solar constant

Due to the elliptical path of the Earth rotation on the Sun, the distance Sun-Earth is variable that causes a variation in the solar constant values. The correction of the solar constant is given by,

$$I_{sc} = I_0 E_0 \tag{1.20}$$

E_0 is the solar constant correction factor (Duffie and Beckman,1991) expressed by

$$E_0 = \left(\frac{D_{s,e}}{D_{se}}\right)^2 = 1 + 0.033 \cos\left[2\pi(N_d)/365\right] \tag{1.21}$$

D_{se} is the actual Sun- Earth distance.

1.9.2 Global horizontal extraterrestrial solar radiation

The global horizontal solar radiation outside the atmosphere for a site of height h from the Sun is defined as the projection of normal solar radiation amount on this horizontal plane as expressed by the following equation,

$$G_{0,h} = I_{sc} \sin(h) \tag{1.22}$$

a) Global daily extraterrestrial solar radiation

The daily global radiation on a horizontal surface is obtained by integrating equation (1.22) from sunrise to sunset:

$$G_{0,day} = \int_{t_{sr}}^{t_{ss}} I_{sc}(N_d).\sin(h(TST))dt \tag{1.23}$$

t_{sr} and t_{ss} correspond to the sunrise and sunrise times.

b) Global hourly extraterrestrial solar radiation

The global hourly extraterrestrial radiation on a horizontal surface is obtained using the following equation,

$$G_{0,hour} = \int_{t1}^{t2} I_{sc}(N_d).\sin(h(TST))dt \tag{1.24}$$

t_1 and t_2 represent two hour times .

1.10 Solar radiation components at the ground level

As a result of its passage through the atmosphere, the extra-terrestrial radiations are separated into different components, beam (direct), diffuse and reflected solar radiation.

a) Direct beam irradiance (G_b)

Beam irradiance is the energy flux density (units: W/m^2) of the solar radiation incoming from the solid angle subtended by the Sun's disk on a unitary surface perpendicular to the rays.

b) Diffuse irradiance (G_d)

It represents the energy flux density of the solar radiation incoming from the entire sky come on a horizontal surface, excluding the direct beam coming from the Sun's disk.

c) Global irradiance (G)

It is the sum of the direct horizontal and diffuse components, given by,

$$G = G_b + G_d \tag{1.25}$$

The term "global" is associated to the fact that the solar radiation is received from the entire 2π solid angles of the sky vault.

d) Total irradiance (G_t)

It is the sum of beam flux density, diffuse flux density, and the reflected flux density G_r.

$$G_t = G_b + G_d + G_r \tag{1.26}$$

1.10.1 Clearness index

The daily clearness index k_t is the ratio H/H_{ext}, where H and H_{ext} are the monthly average of the daily solar radiation and the daily extra-terrestrial solar radiation on a horizontal surface, respectively.

$$k_t = {}^{H}/_{H_{ext}} \tag{1.27}$$

1.11 Sunshine hours

Sunshine duration during a given period (e.g. within one day) is defined as the sum of the time for which the direct solar irradiance exceeds 120 W/m^2. In other terms, sunshine duration is the period during which the solar disk is clearly visible. In a Sun-Earth system without atmosphere, the daily sunshine is equal to the day length S_0 which depends only on the latitude and declination.

$$S_0 = \frac{2}{15}.a\cos(-\tan(\phi)\tan(\delta)) \tag{1.28}$$

1.11.1 Sunshine fraction

The sunshine fraction noted σ , is the ratio between the measured sunshine duration S and the astronomical day length S_0. It is expressed as follows,

$$\sigma = {}^{S}/_{S_0} \tag{1.29}$$

Sunshine fraction is strictly caused by climatic conditions and the sky cases (clear, cloudy... etc.). It differs from one region to another, depending on the season that reflects the diversity of climate and seasonal regime in the country.

1.12 Conclusion

This chapter introduces the basic concepts necessary for the study of solar radiation. We have discussed various astronomical and geographical as well as the characteristics of the solar radiation parameters at the top of the atmosphere. These basic concepts, definitions, and derived astronomical equations furnish the foundations of the solar energy evaluation at any given location. The next chapter presents the measured solar radiation as well as the sunshine data at ground level that allows us to better situate our problem namely, modeling of the received solar radiation over Algeria.

Nomenclature

$\triangle H$	Time difference.
$D_{s,e}$	Average Sun-Earth distance.
D_{se}	Actual Sun-Earth distance.
$E0$	Solar constant correction factor.
ET	Equation of time.
G	Global radiance at ground level.
$G_{0,day}$	Global daily extraterrestrial solar radiation.
$G_{0,e}xt$	Global horizontal extraterrestrial solar radiation.
$G_{0,hour}$	Global daily extraterrestrial solar radiation.
G_b	Direct beam radiance at ground level.
G_d	Diffuse radiance at ground level.
G_r	Reflected radiance at ground level.
G_t	Total radiance at ground level.
h	Sun height.
H	Monthly average of the daily solar radiation on a horizontal surface.
H_{ext}	Daily extra-terrestrial solar radiation on a horizontal surface.
i	Angle of incidence.
I_0	Solar constant.
I_{sc}	Corrected solar constant.
k_t	Clearness index.
LT	Local Time.
m_a	Corrected air mass.
m_r	Relative air mass at sea level.
MST	Mean solar time.
N_d	Day number of the year.
P	Average atmosphere pressure.
P_o	Average atmosphere pressure at sea level (P_o=1013 mbar).

R_{su}	Radius of the Sun.
S	Measured sunshine duration.
S_0	Day length.
TST	True solar time.
T_{su}	Temperature of the top of the Sun.
UT	Universal Time.
α	Average size of airborne particles.
α_z	Azimuth of a surface.
β	Angstrom turbidity factor.
Γ	Day angle.
γ	Surface height (altitude).
δ	Declination.
$\theta_{z'}$	Azimuth angle.
θ_z	Zenith angle.
σ	The sunshine fraction.
σ'	Constant of Stephane Boltzmann.
φ	Latitude.
ϕ	Longitude.
ω	Hour angle.

References

Ångström A. Techniques of determining the turbidity of the atmosphere. Tellus 1961 ; 13:214–223

Badescu V. *Modeling Solar Radiation at the Earth Surface*, Ed., Springer, 2008.

Duffie J A , Beckman W A. *Solar engineering of thermal processes.* J. Wiley, New York. 1980.

Duffie J A, Beckman W A. *Solar engineering of thermal processes.* Wiley, New York, 1991.

Iqbal M. An Introduction to Solar Radiation. Academic Press, Department of Mechanical Engineering, University of British Columbia, Canada, 1983.

Iqbal M. An introduction to solar radiation. Academic, Toronto, 1986

Kasten F, Young A T. Revised optical air mass tables and approximation formula. Applied Optics 1989; 28:4735–4738.

Koupelis T. In Quest of the Solar System, revised (Jones & Bartlett Learning), 2010.

McAlester A L. *The Earth: an introduction to the geological and geophysical sciences.* 1983, Prentice-Hall, Englewood Cliffs.

Miller F, Vandome A, McBrewster J. *Inverse-Square Law*, VDM Publishing House Ltd., 2010.

Monteith J L. Attenuation of solar radiation: a climatological study. Q J Meteorol Soc 1962; 88:508–521

Richards J A. *Remote sensing digital image analysis: an introduction.* Springer, Berlin, 1993

Şen Z. *Solar Energy Fundamentals and Modeling Techniques. Atmosphere, Environment, Climate Change and Renewable Energy.* Springer. 2008

Spencer J W. Fourier series representation of the position of the sun. Search 1972; 2:172.

Stacey F D. *Physics of the Earth. Brookfield.* Brisbane, 1992.

Chapter 2

Study of solar radiation over Algeria

2.1 Introduction

Algeria is a vast and sunny territory, appropriate to the development of solar energy applications. However, such applications need the evaluation of the distribution of solar radiation. These distributions can indirectly obtain in space and in time from hourly and daily sunshine duration measurement collected in various locations in Algeria. In this chapter, and to study the solar resource available in Algeria, a series of sunshine hours measured in 56 meteorological stations in Algeria during ten years period (1992 / 2002) at different scales of time (month, day) will be analyzed. Before that, we present the instrumentation used in the measurement and describe the data available in trying to extract some useful information. Finally, we attempt to classify the country in areas with the same energetic properties. Then, we study a single site and generalize the results to all the area which it belongs.

2.2 Ground Measurements of Solar Radiation

Generally, the method used for measuring solar radiation is to transform the radiant energy into heat. The overall solar radiation is often measured by solar radiometers. The measured data are collected in some places in the world called surface solar radiation network. In addition, measured data can be reached in some available online databases.

2.2.1 Solar Radiometers

Radiometry is the science of electromagnetic radiation measurement. The generic device is named radiometer. Each of the quantities defined in chapter 1 is measured with a specific device; for instance, the pyrheliometer that measures the direct beam irradiance and the pyranometer that measures the horizontal beam and diffuse irradiances. Details on both instruments will be presented in the following parts.

a) Pyrheliometer

Pyrheliometer is an instrument that measures the direct solar radiation. It should be always oriented toward the Sun. Hence, a two-axis sun tracking mechanism was used for this

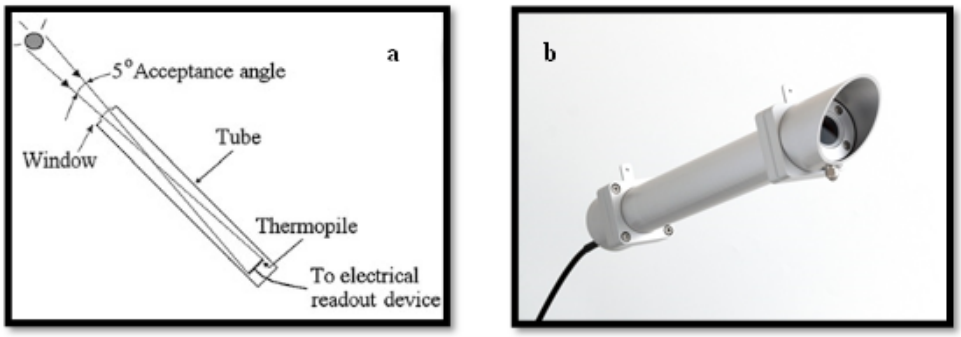

Figure 2.1: a) Schematic of a pyrheliometer. b) Photo of Hukseflux DR01 first class pyrheliometer (Hukseflux 2012).

purpose. Fig.2.1 shows a pyrheliometer that consists of a detector (multi-junction thermopile) placed at the bottom of a collimating tube provided with a quartz window to protect the instrument. The detector is coated with optical black paint (to act as full absorber of solar energy in the wavelengths range 0.280-3 μm). The radiation received from the Sun is limited to a circumsolar region (with an acceptance angle of 5°), the other diffuse radiation from the sky is excluded. At the end of the tube, an electrical readout device is used to give the instantaneous values of direct solar radiation in W/m^2 (Paulescu et al., 2013).

b) Pyranometer

A pyranometer measured the global hemispherical solar radiation (direct + diffuse) with a 360° field of view. The pyranometer is represented in Fig 2.2. It consists of a white disk that limits the acceptance angle to 180° and two domes made of glass to protect the sensor from the weather threat (rain, wind and dust). A cartridge of silica gel inside the dome absorbs water vapour. The diffuse solar radiation can be measured by eliminating the direct beam radiation; a small shading disk can be mounted on an automated solar tracker that ensures that the pyranometer is continuously shaded. However, because the variation of the Sun elevation angle from day to another, the shadow ring must be oriented to ensuring the shadow

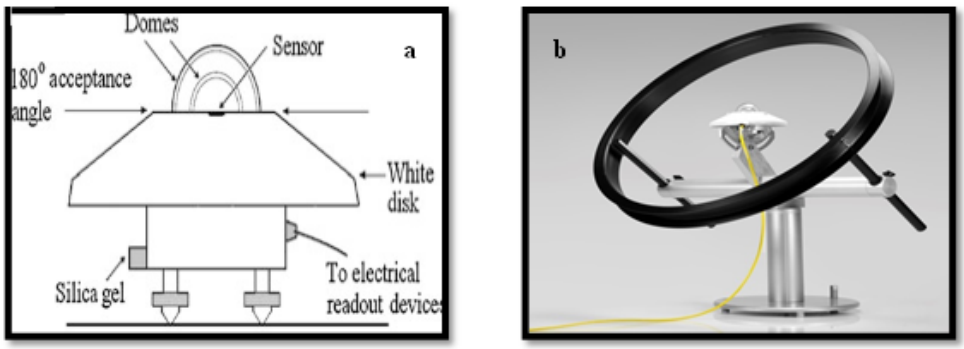

Figure 2.2: a) Schematic of a pyranometer. b) pyranometer equipped with shadow ring.

during the day. In addition, the shadow ring may intercept a part of the diffuse radiation. The percentage of diffuse radiation intercepted by the shadow ring varies during the year with its position and atmospheric conditions for that its value must be corrected (Paulescu et al., 2013).

c) Sunshine duration measurement

Sunshine duration is the sum of the time intervals for which the direct solar radiation exceeds the threshold of $120\,W/m^2$ (WMO 2008). Two methods are used in practice for measuring sunshine duration, the burning card method and pyranometric method. Burning card method is based on the Campbell-stokes (CS) sunshine recorder developed by John Francis Campbell in 1853 and later modified in 1879 by Sir George Gabriel Stokes. It consists of a glass sphere filled with water mounted in a spherical bowl that holds the recording card as shown in Fig 2.3. The glass sphere focuses the beam radiation onto the card, burning a trace whenever the Sun is shining. The position and length of the trace indicate the starting and the duration of the sunshine interval. The Campbell-stokes recorder is still manufactured and used today. However, it presents an error depends on the burning card temperature, humidity and clouds (Kerr and Tabony, 2004).

The pyranometric method consists of determining the sunshine duration during a time interval Δt by multiplying the mean sunshine number (mean of ξ) during Δt. Sunshine number is a Boolean variable stating whether the Sun is covered or not by clouds. It is calculated from the subtraction of the global and diffuse solar radiation. Then, direct radiation obtained is compared with the WMO threshold as illustrated in Eq. (2.1) where θz is the Sun zenith angle. The disadvantage of this method that is depends strongly on the accurate measuring of the global and diffuse radiation.

$$x = \begin{cases} 1 & if \quad (G - G_d)/\cos(\theta_z) > 120\ W/m^2 \\ 0 & otherwise \end{cases} \tag{2.1}$$

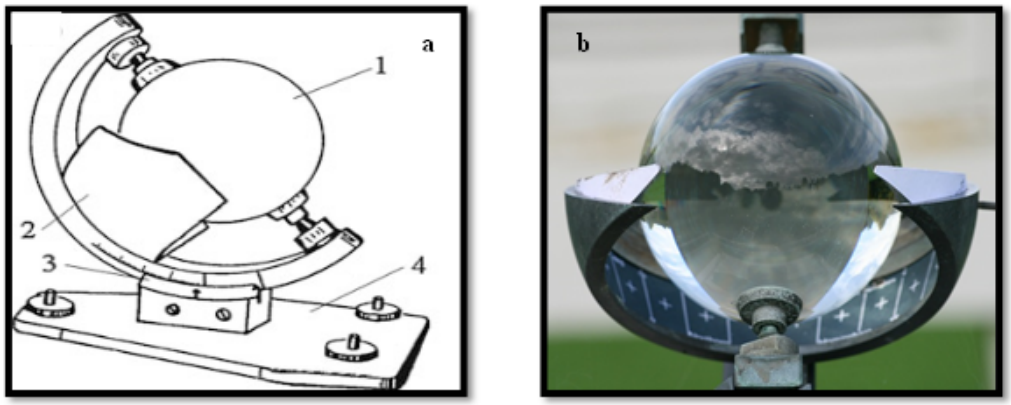

Figure 2.3: a) Schematic of Campbell-Stokes sunshine recorder (1. glass sphere, 2.burning card, 3. Spherical bowl, 4. Sphere and Card holder). b) Photo of a typical Campbell- Stokes sunshine recorder.

Modern instruments such as electronic sunshine recorders (using photodiodes) are used to determine the patent of sunshine. These devices have much time resolution and more precise results that improve the reliability, and the accuracy of the measurements comparing with the CS instruments.

2.2.2 Surface solar radiation networks

The knowledge of the solar energy available at any location depends not only on the total measured values, but also on its temporal repartition, spectral distribution and its nature (global, direct or diffuse). In most areas of the world, measuring solar radiation stations are installed. However, their investment and maintenance cost is considered high. Hence, the national networks consist of a small number of stations even in industrialized countries. In addition, measurements are varying from station to another. The global solar radiation and sunshine duration are available in mean daily or monthly basis. The diffuse, direct and cloud cover data on hourly bases are rarely recorded. Nowadays, some databases are created in the world that based on the interpolation and extrapolation of the available data for estimating solar radiation at each point in the world. However, the error of estimating radiation increases with the distance from the closest station. Moreover, the databases store various format and units using various time idioms. Thus, sometimes even data access and correct interpretation is a difficult task. In following, some surface networks as the World Radiation Data Center (WRDC) and Baseline Surface Radiation Network (BSRN), Photovoltaic Geographical Information System (PVGIS) and METEONORM (METEONORM) are summarized.

a) World Radiation Data Center (WRDC 2012)

World Radiation Data Center (WRDC 2012) is located at the Main Geophysical Observatory in St. Petersburg, Russia and serves as a central depository for solar radiation data collected at over 1000 measurement sites throughout the world. Using the data measured from the WMO (world meteorological organization), the WRDC archive contains mainly measurements of global solar radiation, diffuse solar radiation and sunshine duration in the format of daily sums and monthly mean. Data collected from 1964 to 1993 are accessible online on the site of the US Department of Energy's, National Renewable Energy Laboratory and data collected from 1994 to present are accessible on the site of the Main Geophysical Observatory, St. Petersburg, Russia.

b) Baseline Surface Radiation Network (BSRN 2012).

BSRN is a project of the Radiation Panel from the Global Energy and Water Cycle Experiment (GEWEX 2012) as part of the World Climate Research Program (WCRP 2012). It contains about 40 stations located on the world between latitude 80° N and 90° S. BSRN is used for detecting important changes in the Earth's radiation, which related to the climate changes. It measures solar and atmospheric radiation with instruments of the highest available accuracy and high time resolution (1–3 min).

c) Photovoltaic Geographical Information System (PVGIS 2012)

PVGIS is a server, operated by the Joint Research Centre of the European Commission that offers a map of solar radiation, temperature and other data for Europe and Northern Africa. In Europe, the database is based on interpolation of ground station measurements (1 km grid, period 1981–1990). For Mediterranean Basin and Africa, the maps are developed by processing the HelioClim-1 database (2 km grid resolution, period 1985–2004).

d) Meteonorm (METEONORM 2012)

Meteonorm is a database for solar energy application contains a large database of ground station measurements collected from various sources (more than 8,300 are listed for the version 7). It offers two periods of measurements: (1) from 1961 to 1990 and 1996 to2005 for temperature, humidity, precipitation, and wind speed, and (2) 1961–1990 and 1981–2000 for radiation parameters. The METEONORM outputs are climatology averages and derived products for any point on Earth, estimated by interpolation at very high resolution (0.1–1 km).

2.2.3 Online available databases

Online solar radiation databases are the data derived from satellite data provided by web based systems. The data are saved on servers in some websites, among them:

a) Satel-Light(European Database of Daylight and Solar Radiation)

Satel-Light (2012) was one of the first websites to provide solar radiation data. It's based on the Heliosat model (images produced by the Meteosat satellite every half hour) and covers Europe and a small region of the North Africa. It provides monthly means of hourly and daily values from the period 1996 to 2000.

b) **SoDa**

The project Solar Data (SoDa 2012) is a web service that offers long-term monthly, daily and hourly solar radiation data and other information such as temperature measurements at any place in the world. The SoDa database is processed by MINES ParisTech—ARMINES. (HelioClim 2012).

c) NASA Surface Meteorology and Solar Energy (SMSE 2012)

It is a large archive that covers the entire globe using over 200 satellite-derived meteorological and solar radiation parameters. Data can be retrieved from the SMSE server (SMSE 2012), where they can be used in various solar applications, e.g., sizing and pointing solar modules, solar cooking, tilted solar modules and cloud information.

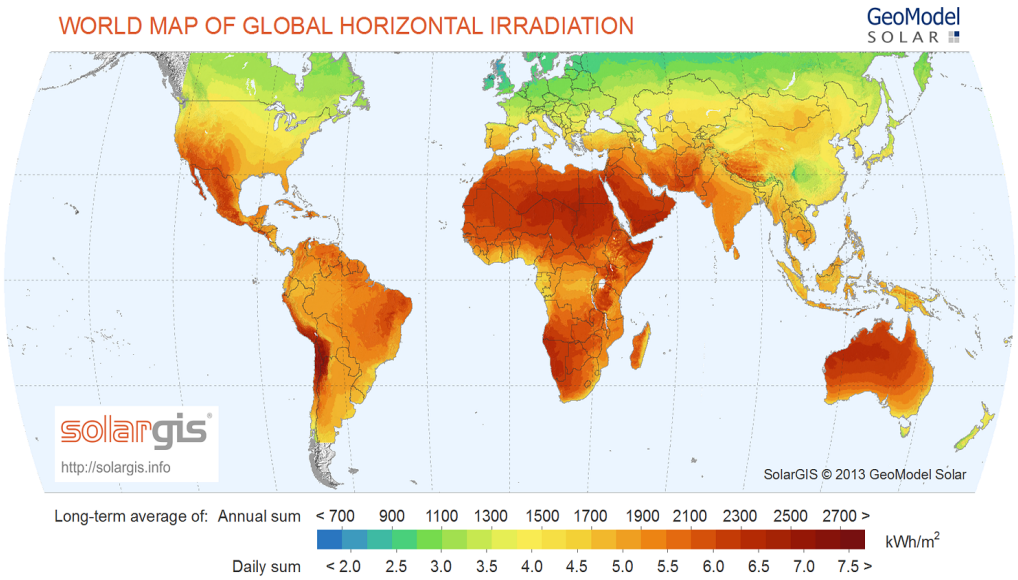

Figure 2.4: The annual solar radiation data in m^2 for the world in 2013 (solarGis, 2013).of a typical Campbell- Stokes sunshine recorder.

2.3 Solar radiation over the world

The amount of solar energy at ground level is about 720.10^{15} kW.h. Depending on the location, solar energy changes between 1000 to 2300 kW.h/year in m^2. That means solar power between 120 W/m^2 to 1000 W/m^2 which depends on the location, atmosphere and weather conditions as expressed in Fig. 2.4, which represents the annual solar radiation data in m^2 over the world. However, only 26.10^{15} kW.h of the total solar energy received at ground level (about 0.5 %) is used to meet our daily needs. A big part of this energy is used to produce electricity by photovoltaic panels (33.6 TWh) or used in thermal power stations (1.6 TWh).

2.4 Solar radiation in Algeria

2.4.1 Presentation

Algeria is a country situated in the North of Africa on the Mediterranean coast with a total area of 2,381,741 square kilometres. Algeria is the tenth-largest country in the world, and the largest in Africa and the Mediterranean. The country is bordered in the northeast by Tunisia, in the east by Libya, in the west by Morocco, in the southwest by Western Sahara, Mauritania, and Mali, in the southeast by Niger, and in the north by the Mediterranean Sea as shown in Fig.2.5. Algeria is divided topographically into three main regions that generally run east-west. The first is the Tell, which is the Mediterranean coastal region. The second is the High Plateaus, which are more inland and are fairly consistent, until the third region, the Sahara, which covers almost 80% of Algeria's land.

Figure 2.5: Map of Algeria.

2.4.2 Meteorological network of Algeria

Algeria has a considered sunny area with mean annual sunshine varies between 2600 h / year in the North and 3500 h / year in the South . However, the number of meteorological stations (56 stations) is low comparing with the total surface of Algeria (more than 2 million km^2). The geographic situation of these stations is shown in Table 2.1.

In addition, Fig 2.6 shows the situation of stations on the Algeria map. It is clearly shown that the most of stations are situated in the north and High Plateaus. However, their number is negligible in the south (Sahara region) where there are high solar radiation values. Hence, we considered that the density of this network is poor and it does not give much information about the amount of solar radiation in Algeria.

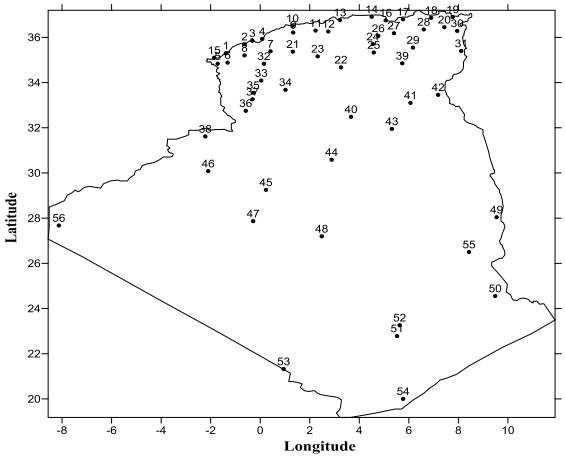

Figure 2.6: Meteorological stations over Algeria.

Table 2.1: Meteorological network of ONM (Mefti,2007)

Nº	Station	Longitude (º)	Latitude (º)	Nº	Station	Longitude (º)	Latitude (º)
1	Beni Saf	1.33 W	35.25	**29**	Batna	6.35 E	35.71
2	Oran	0.60 W	35.63	**30**	Souk-Ahras	7.97 E	36.28
3	Arzew	0.26 W	35.81	**31**	Tebessa	8.11 E	35.41
4	Mostaganem	0.12 E	35.88	**32**	Saida	0.15 E	34.86
5	Maghnia	1.78 W	34.81	**33**	Elkheiter	0.04 E	34.09
6	Tlemcen	1.45 W	35.01	**34**	El Bayed	1.00 E	33.73
7	Mascara	0.30 E	35.6	**35**	Mecheria	0.26 W	33.55
8	S.Belabbes	0.65 W	35.18	**36**	Ainessefra	0.60 W	32.75
9	Chleff	1.33 E	36.21	**37**	Naama	0.30 W	33.26
10	Tenes	1.33 E	36.5	**38**	Bechar	2.25 W	31.63
11	Miliana	2.23 E	36.3	**39**	Biskra	5.73 E	34.8
12	Médéa	2.75 E	36.45	**40**	Ghardaia	3.80 E	32.4
13	Alger	3.25 E	36.71	**41**	Touggourt	6.13 E	33.11
14	Tizi Ouzou	4.50 E	36.91	**42**	El Oued	6.78 E	33.5
15	Ghazaouet	1.86 W	35.1	**43**	Ouargla	5.40 E	31.91
16	Bejaïa	5.05 E	36.75	**44**	El Golea	2.86 E	30.56
17	Jijel	5.57 E	36.8	**45**	Timimoun	0.28 E	29.25
18	Skikda	6.90 E	36.88	**46**	Béni Abbas	2.16 W	30.13
19	Annaba	7.81 E	36.83	**47**	Adrar	0.18 W	27.81
20	Guelma	7.46 E	36.46	**48**	Ain Salah	2.47 E	27.2
21	Tiaret	1.46 E	35.35	**49**	Ain Amenas	9.63 E	28.05
22	Djelfa	3.25 E	34.68	**50**	Janet	9.47 E	24.26
23	KsarChelala	2.32 E	35.16	**51**	Tamanrasset	5.45 E	22.8
24	M'sila	4.50 E	35.66	**52**	Assekrem	5.63 E	23.26
25	Boussaâda	4.20 E	35.33	**53**	B.BajiMokhtar	0.57 E	21.2
26	Bordj	4.66 E	36.06	**54**	Ain Guezzam	5.77 E	19.56
27	Setif	5.25 E	36.18	**55**	Illizi	8.43 E	26.5
28	Constantine	6.61 E	36.28	**56**	Tindouf	8.16 W	27.7

2.4.3 Solar radiation data in Algeria

The data are collected by the ONM (national office of meteorology) that covers 56 stations as follow:

1. Daily and monthly sunshine data for the 56 stations from 1960 to 2002.
2. Hourly direct, diffuse and global solar radiation data for Oran , Ghardaia and Bouzareah with other measurements such as relative humidity and temperature.

However, these databases have many missing data as shown in Fig.2.7 due to the absence of measurements. Hence, we have selected only data from 1992 to 2002 to avoid the missing data.

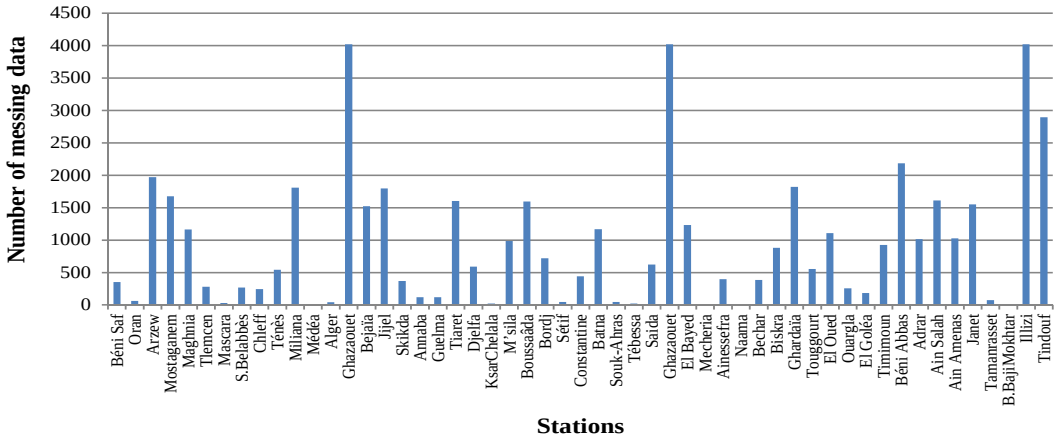

Figure 2.7: Missing data in the Meteorological network of Algeria.

2.4.4 Analysis of the sunshine fraction

To know the amount of solar radiation over Algeria, the analysis of the sunshine fraction is known as an important part that gives information about the amount of the monthly and daily solar radiation basing on Angstrom (1924) equation expressed as follows;

$$\overline{G} = \overline{G_0}\left(a + b\frac{\overline{S}}{\overline{S_0}}\right) \tag{2.2}$$

$\overline{S}$ is the measured mean monthly sunshine, it is calculated using the following equation ;

$$\overline{S} = \frac{1}{N}\sum_{Year=1}^{N_y} S(month, day, location) \tag{2.3}$$

Where, N_y is equal to 10 that represents the number of the years (from 1992 to 2002). The results of the mean monthly measured sunshine hours are presented in Table 2.2.

In what follows, we simulate the sunshine fraction for the 56 stations in order to know the different climatic regions in Algeria based on the analysis of the sunshine fraction values.

Fig.2.8 shows an example of how to calculate the sunshine fraction for Algiers. First, we plot the measured mean monthly sunshine extracted from Table (2.2). Then, we plot the day length S_0. Finally the sunshine fraction is plotted based on Eq. (1.29) (Chapter 1).

Table 2.2: Mean monthly measured sunshine hours.

Stations	Jan	Feb	Mar	Apr	May	Jun	Jul	Aug	Sep	Oct	Nov	Dec
Beni Saf	6.47	7.63	7.99	9.4	9.36	9.91	10.23	9.52	8.6	7.39	6.62	6.09
Oran	6.22	7.46	8	9.4	9.7	10.67	10.86	10.06	8.87	7.38	6.47	5.88
Arzew	6	7.21	7.74	8.93	8.8	8.4	9.46	9.22	8.33	7.19	6.17	5.67
Mostaganem	6.08	7.6	8.38	9.4	9.67	10.71	10.83	9.84	8.81	7.31	6.24	5.89
Maghnia	6.82	7.76	7.89	9.47	9.87	10.75	11.16	10.21	9.09	7.67	7.01	6.28
Tlemcen	6.53	7.45	7.7	9.29	9.61	10.6	10.98	9.98	8.87	7.51	6.7	6.12
Mascara	6.1	7.2	7.57	8.94	9.55	10.67	10.97	9.97	8.81	7.41	6.28	5.85
S-Bel abbes	6.36	7.81	8.02	9.44	9.94	11.32	11.6	10.34	9.14	7.7	6.75	6.22
Chlef	5.75	6.91	7.75	9.13	9.93	11.1	11.53	10.33	9.18	7.58	6	5.2
Médéa	5.14	6.7	7.5	8.44	9.45	10.8	11.45	10.45	8.84	7.26	5.44	4.61
Alger	5.66	7	7.65	8.5	9.06	10.34	10.95	9.93	8.6	7.2	5.81	5.17
Bejaïa	5.18	6.3	7.11	8.02	8.86	9.9	10.83	9.93	7.78	6.73	5.46	4.92
Jijel	4.42	4.36	5.47	6.15	7.36	8.75	9.05	8.49	5.91	4.97	3.8	4.19
Skikda	5.05	6.37	7.34	8.2	9.27	10.29	11.24	10.06	8.13	6.97	5.3	4.51
Annaba	5.47	6.23	7.27	8.16	9.38	10.38	11.5	10.52	8.18	7.11	5.33	4.83
Guelma	5.34	6.22	7.11	7.96	9.21	10.07	11.44	10.19	8.2	7.14	5.51	4.96
Tiaret	5.69	7.2	7.7	8.74	9.57	10.72	11.08	9.84	8.99	7.74	5.98	5.46
Djelfa	5.86	7.58	8.08	9.14	9.88	10.61	10.97	9.68	8.86	8.11	6.56	6.21
M'sila	6.35	8.18	8.56	9.32	10.07	10.82	11.24	10.14	8.92	8.36	6.71	5.91
Boussaada	6.14	7.53	8.23	9.09	9.59	10.11	10.73	9.67	8.44	7.94	6.61	6.23
B.B.Arreridj	5.97	7.41	7.96	9.01	9.72	10.88	11.27	10.06	8.7	7.76	6.37	5.92
Sétif	6.19	7.7	8.1	9.05	9.81	10.97	11.42	10.24	8.88	7.8	5.85	5.29
Constantine	5.24	6.53	7.3	8.25	9.38	10.58	11.32	9.72	8.3	7.26	5.6	5.19
Batna	5.55	7.06	7.75	8.73	9.53	10.4	11.37	10.21	8.7	7.85	6.23	5.66
Souk Ahras	4.94	5.87	6.89	7.82	8.95	9.92	11.05	10	7.93	6.92	5.18	4.82
Tebessa	5.51	6.68	7.56	8.4	9.42	10.18	11.31	10.01	8.3	7.49	6.12	5.5
Saida	6.22	7.6	7.79	9.05	9.64	10.85	11.08	9.74	9.01	7.85	6.54	6.07
El-Bayad	5.92	7.3	7.96	9.19	9.89	10.62	10.73	9.52	9.3	8.11	6.1	5.94
Mecheria	6.71	8.02	7.94	9.24	9.51	10.05	9.64	8.53	8.8	7.93	7.3	6.73
Naama	6.7	8.01	7.9	9.43	9.75	10.15	9.86	8.86	9.05	8.21	7.35	6.79
Bechar	8.1	9.01	9.18	10.65	11.04	11.37	11.06	9.89	9.61	8.94	8.69	8.06
Biskra	7.27	8.68	9	10	10.58	11.42	11.64	10.71	9.07	8.65	7.44	7.4
Ghardaia	7.84	8.96	8.88	10.13	10.44	11.25	11.3	10.18	9.01	8.59	7.91	7.81
Touggourt	7.82	9	9	9.9	10.26	11.37	11.48	10.71	8.99	8.65	7.86	7.81
El Oued	7.65	8.79	9.13	9.84	10.17	11.12	11.41	10.82	8.96	8.5	7.68	7.6
Ouargla	7.73	8.62	8.95	9.67	9.6	10.79	11.06	10.34	8.24	8.39	7.44	6.56
Timimoun	8.57	9.01	9.03	9.63	10.4	10.95	10.79	10.07	8.44	8.91	8.52	8.51
Béni Abbes	8.44	9.08	9.49	10.71	11.06	11.35	10.93	10.07	9.32	9	8.85	8.63
Adrar	8.97	9.3	9.4	9.92	10.35	10.65	10.15	9.08	8.4	9.08	8.77	8.66
In Salah	8.95	9.24	9.1	9.43	9.73	10.64	11.04	10.27	8.39	9.13	8.84	8.71
In Amenas	8.53	9.18	9.02	9.02	9.23	10.27	11.75	11.17	9.41	9.23	8.65	7.69
Djanet	9.27	9.93	9.47	9.53	9.73	10.71	11.83	11.16	10.13	9.74	9.47	8.9
Tamanrasset	9.3	10.13	9.48	10.01	9.53	8.84	10.07	8.9	8.09	9.04	9.52	8.9
BB Mokhtar	8.61	9.33	8.64	8.58	8.18	6.13	4.89	4.83	5.41	8.39	8.56	8.13
Tindouf	8.54	9.54	9.61	10.75	11.45	10.59	10.17	9.43	9.91	9.53	8.45	7.92

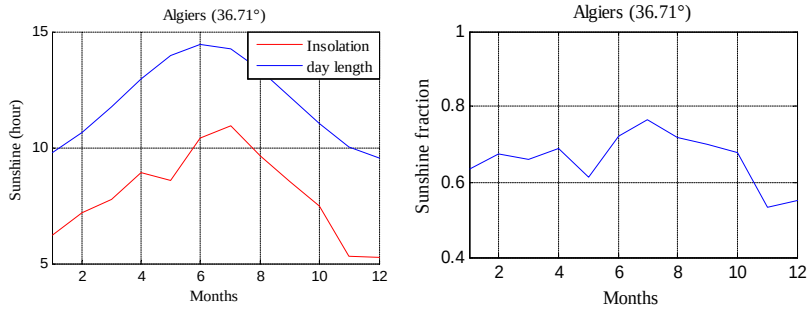

Figure 2.8: Sunshine fraction for Algiers.

We applied the same methodology to obtain the sunshine fraction for other locations. The results for some stations are shown in the following figures.

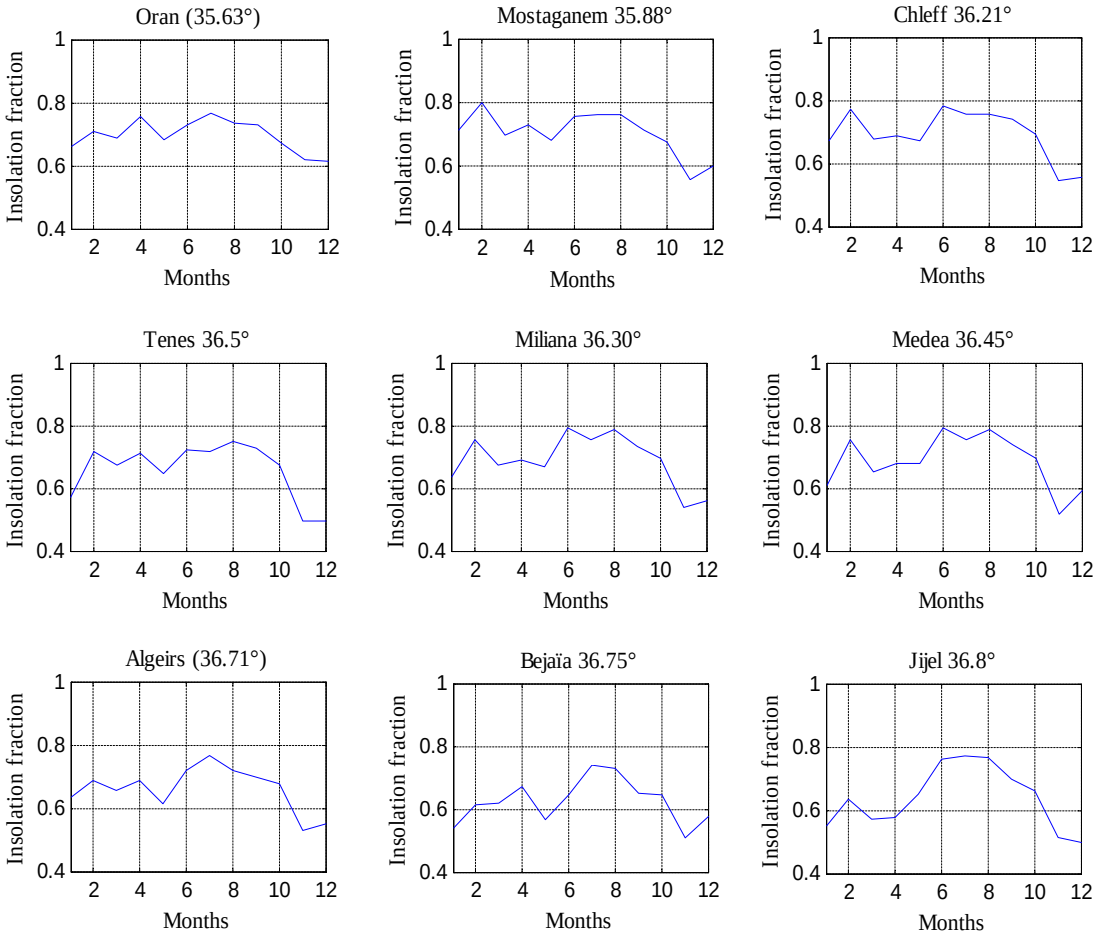

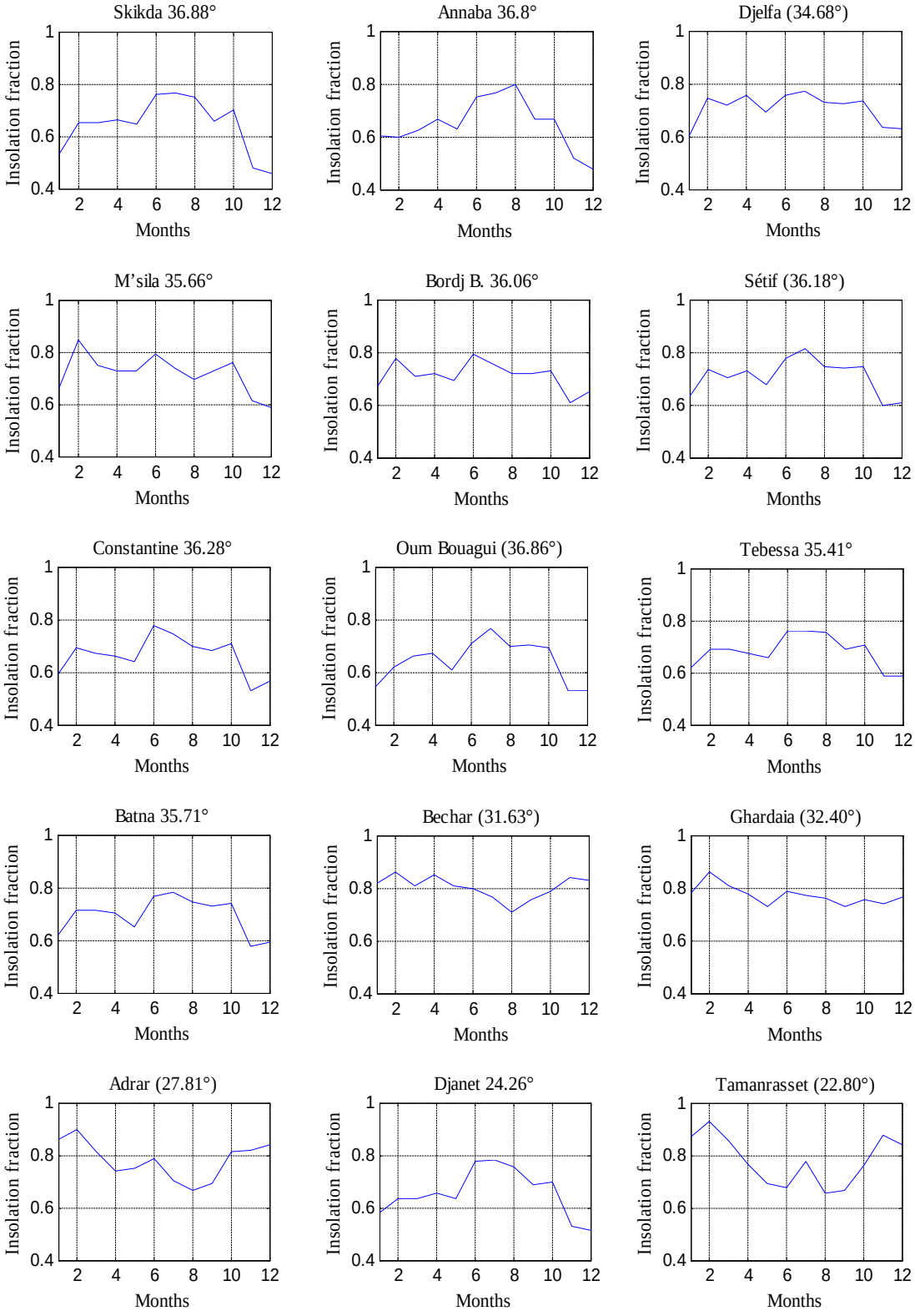

Figure 2.9: Sunshine fraction for some metrological stations in Algeria.

The Curves described above allow us to have a preliminary idea of the distribution of solar radiation in Algeria. According to these curves, we can distinguish three sunshine fraction types in Algeria:

- The first type is found for stations number 1 to 35 situated in the north of the country, including coastal sites and highlands from the east to the west of Algeria. These sites are characterized by two main seasons (winter and summer) with a significant annual change on coastal stations and even less on the highlands. The sunshine fraction varies between 0.5 and 0.8. It is maximum in summer and minimum in winter.

- The second type is found at stations in the north and central Sahara (station number 35 to 49). The sunshine fraction can exceed 0.9 that it is higher than the northern values and the curves are less fluctuated. In addition, the seasonal effect has little influence on these sites.

- The third type is found for stations located in the south of the Sahara (number 50 to 54) where insolation is changing almost inversely with the length of the astronomical day. The sunshine fraction takes low values in summer (0.5 to 0.6) and higher in winter (0.8). These sites are very specific to their geographical location and climatic characteristics.

2.4.4.1 Annual average sunshine across Algeria

The simulation results of the average annual sunshine and the sunshine fraction are shown in Fig. 2.10 and Fig.2.11.

From these figures, the average annual sunshine fraction is between 0.55 and 0.75 in the north of Algeria (latitude between 37 º and 34 º). For the sites in the northern and central Sahara (latitude between 34 º and 26 º), it reaches values of 0.75 to 0.87. And, it falls to 0.7 to 0.6 in regions located at less than 24 ° latitudes (Hoggar and Tassili).

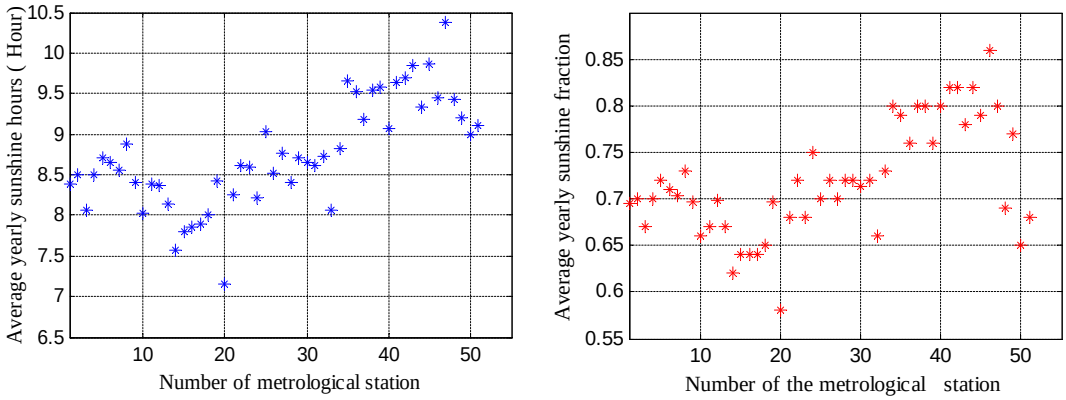

Figure 2.10: Annual average sunshine hours and sunshine fraction for all ONM stations.

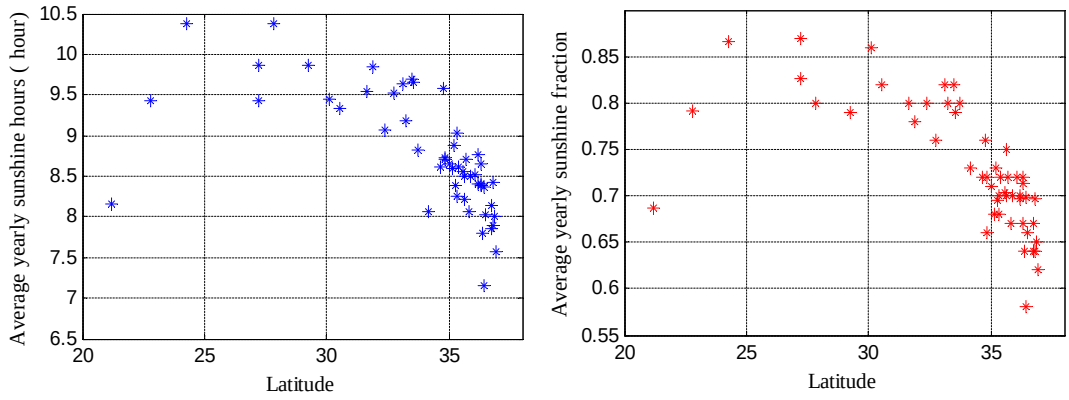

Figure 2.11: Annual average sunshine hours and sunshine fraction for all ONM latitudes.

2.4.5 Sunshine maps in Algeria

Our objective is to determine the amount of solar radiation data in each point in Algeria. However, in real world, it is impossible to get exhaustive values of data at every desired point because of practical constraints. Thus, interpolation is important and fundamental to graphing, analyzing and understanding of 2D data. Interpolation is a method of constructing new data point within the range of a discrete set of known data points. Several methods are proposed in the literature such as linear and nonlinear interpolation as well as other complicated methods like principal analysis components and Kriging methods. In what follows, we try to divide the land of Algeria into zones with similar energetic properties in order to distinguish the similar zones in Algeria based on Kriging interpolation. At the end, a mapping of Algeria for each month of the year is reached.

2.4.5.1 Sunshine maps in Algeria using Kriging method

The simulation results are shown in the following figures that represent the average monthly sunshine maps for Algeria for 12 months of the year. The database used in the simulation is the insolation hours from 1992 to 2002 for all the 56 stations. The maps are plotted using Surfer software. Surfer is a full-function 3D visualization, contouring and surface modeling package, it is used extensively for terrain modeling, bathymetric modeling, landscape visualization, surface analysis, contour mapping, watershed and 3D surface mapping, gridding and volumetrics. It uses different interpolation methods to plot the countour maps among them, the inversed distance to power method , the modified Shepard's method , the minimum curvature method, the nearest neighbor method , the polynominal regression method, Kriging method...etc. In this work, we are based on the Ordinary Kriging method that is used to interpolate the values of a random field with an unobserved location from observations of its value at nearby locations. The description of Kriging theory and its applications are given in detail by Delhomme (1978).

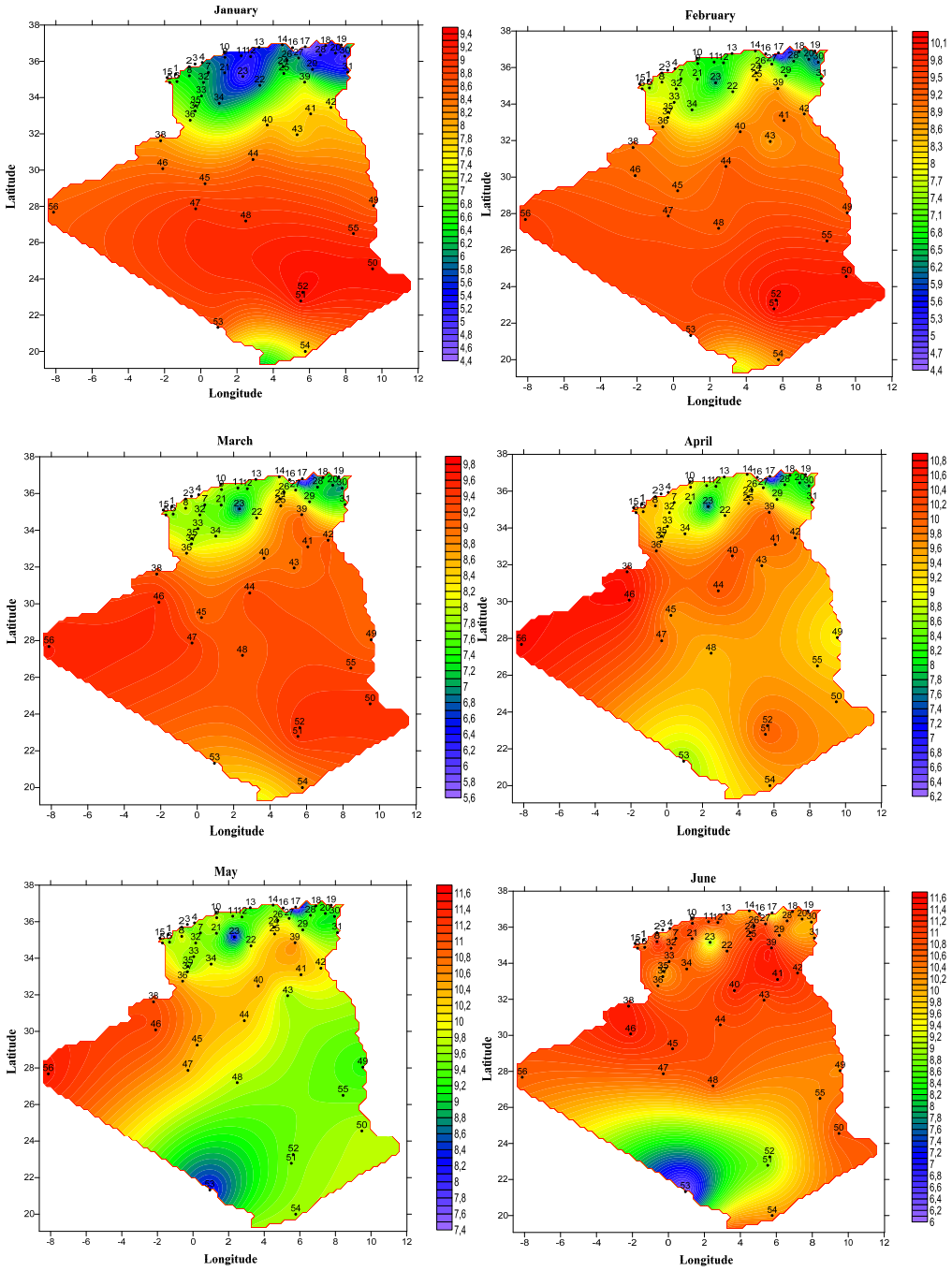
January
February
March
April
May
June
Latitude
Longitude

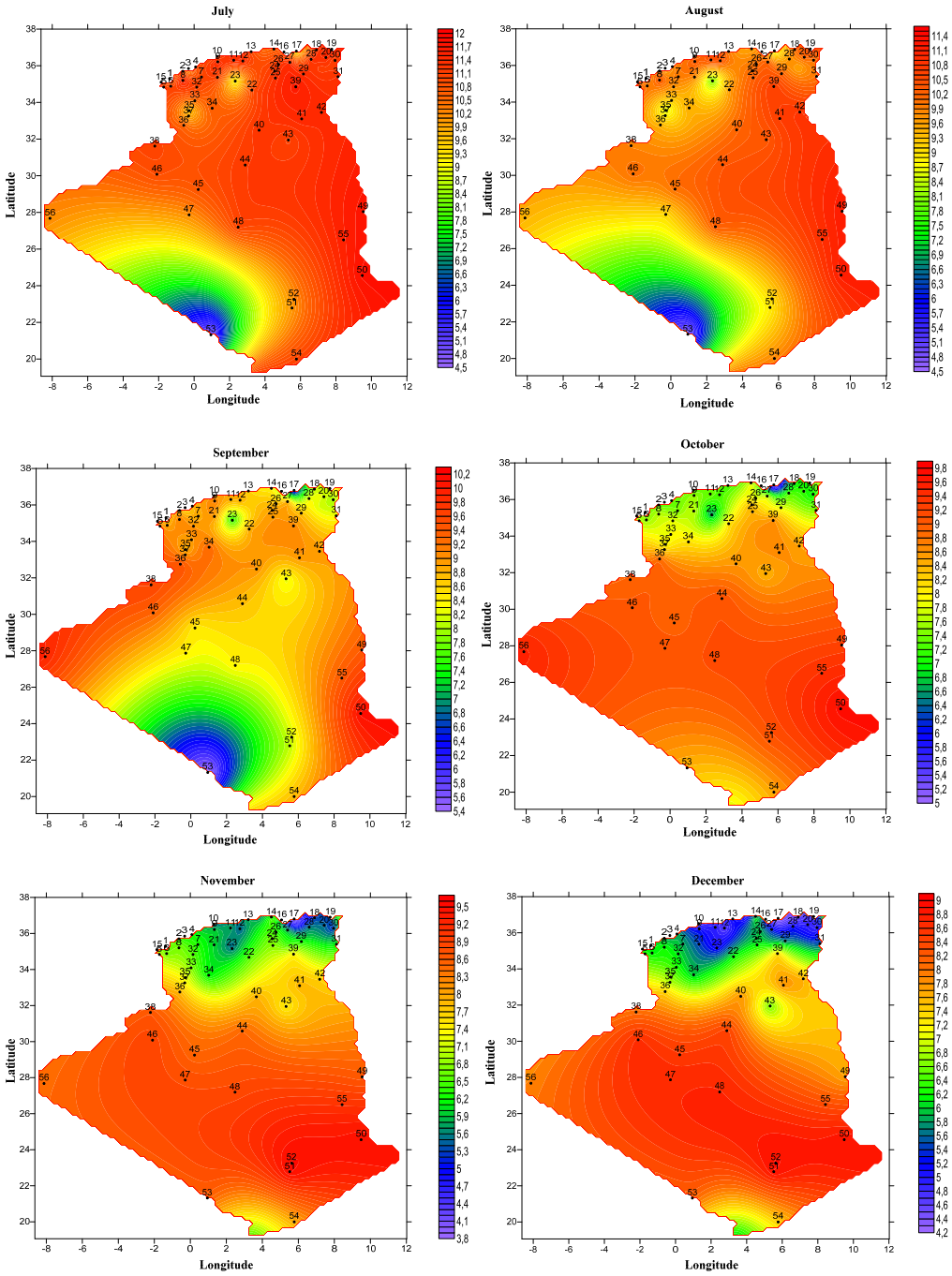

Figure 2.12: Monthly average sunshine maps of Algeria for twelve months of the year.

From these figures, we can distinguish six energetic zones in Algeria:

- *Zone 1*: extends over the coastal regions and eastern high plateaus (stations N°:

16,17,18,19,20,27,28,29,30,31). It is characterized by a low sunshine fraction whose its distribution is not different during the year.

- *Zone 2*: contains the central coastal regions (stations N° : 9,10,11,12,13,14,24,26), it is characterized by a small sunshine fraction, but a little high than zone 1, the distribution is very different during the year. The summer months receive more solar energy than the winter months.
- *Zone 3* : it contains the coastal regions, western high plateaus and internal central regions (stations N°: 1,2,3,4,5,6,7,8,15,21,22,23,25,32). It's characterized by high sunshine fraction (comparing with zone 1 and 2) with a different distribution during the year.
- *Zone 4* : it contains the north of the Sahara (stations N° : 33,34,35,36,37,38,39,40,41,42). It's characterized by high sunshine fraction with a small different distribution between summer and winter months.
- *Zone 5*: it represents the center of the Sahara (stations N°: 43,44,45,46,47,48,49,50,55,56). It has the highest sunshine fraction comparing with other zones. It has a constant distribution during the year.
- *Zone 6*: it represents the south of the Sahara (Hoggar and Tassili, Station N°: 51,52,53,54). The effect of the seasons is reversed. The winter months have a high sunshine fraction comparing with the summer months.

However, according to Table 2.3 that shows the variance and the standard deviation for the spacial distribution of the 56 meteorological stations, we can note that Algeria has considerable territory, which can not be reflect the reality of solar zones in Algeria.

From Table 2.3, we can see that the stations situated in the north of Algeria (N° : 1-37, 39) have the lowest variance and standard deviation compared to the zone of the north and center of sahara (stations N° : 38, 40-48 , 56) and south of Sahara (stations N° : 49-54).

The contour map for each region is reconstructed as shown in Fig. 2.13. We can see from these figures that the average sunshine map is well constructed in the north of Algeria that contains many meteorological stations with small distance between them compared to the Sahara region that needs more installation of this meteorological stations.

Table 2.3: Variance and the standard deviation for the spacial distribution of the 56 meteorological stations

		Distribution		
Station N°:		Longitude	Latitude	Average data
1-37, 39		9.80	2.4	0.39
38, 40-48, 56	Variance	19.90	5.74	0.16
49-54		42.69	24.9	2.8
1-37, 39		3.13	1.54	0.54
38, 40-48 ,56	Standard deviation	4.46	2.3	0.4
49-54		6.53	4.9	1.3

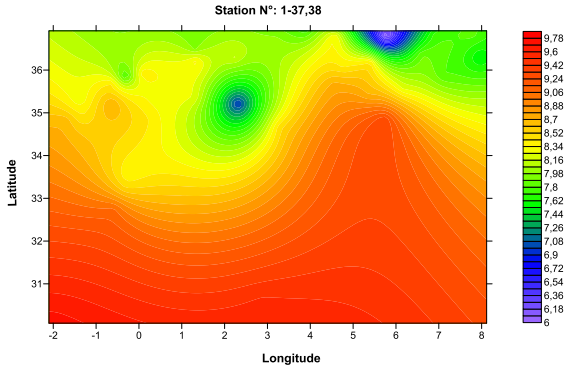

(a) Station N°: 1-37,38

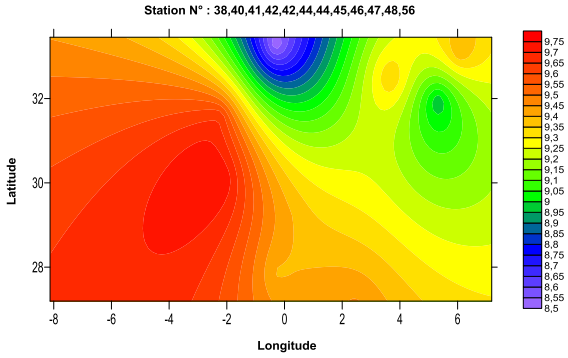

(b) Stations N° : 38, 40-48 , 56

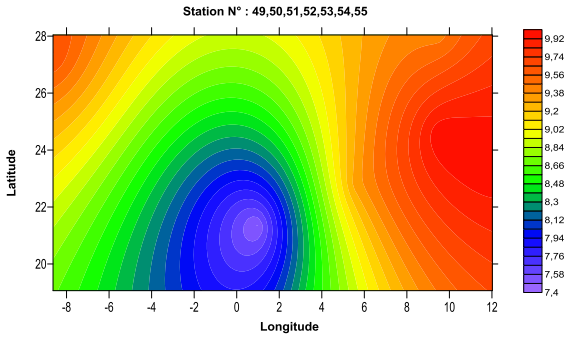

(c) stations N° : 49-54

Figure 2.13: Average sunshine zoning map for each region

2.5 Conclusion

In this chapter, data measured in different regions and at different time scales were presented. These data will develop models to describe fully and accurately the solar field in Algeria. The analysis of seasonal variations of sunshine duration and sunshine fraction for the 56 locations of Algeria showed that this country can be divided into six typical regions; these regions differ from one to another by their climatic features. The results of this analysis can be used to estimate or predict the monthly mean values of sunshine duration for Algeria. More generally,

they could be used to evaluate the solar energy resources available in space and in time for this country.

Nomenclature

a, b	Angstrom coefficients.
Cov	Covariance function.
G	Global radiation.
G_0	Global radiation at the top of atmosphere.
G_d	Diffuse radiation
L	Correlation length.
N	Number of locations.
N_y	Number of the years.
r_j	The residue.
$\overline{S}$	Measured mean monthly sunshine.
S_0	Day length.
$\hat{v_j}$	Actual value.
$\tilde{v_j}$	The estimate.
Var	Variance function .
$\hat{x_j}$	The unknown location.
w_i	Weights.
θ_z	Sun zenith angle.
ξ	Sunshine number.
σ"	Standard deviation.

References

Ångström A. Solar and terrestrial radiation. Q J Roy Meteorol Soc 1924; 50:121-126.

BSRN, 2012. Baseline surface radiation network. http://www.bsrn.awi.de.
Delhomme J P.Kriging in the hydrosciences, Adv. Water Resource 1978, 1:251-266.

Hukseflux, 2012. Radiation measurement sensors. Available online http://www.huksefluxusa.com/radiation-measurement.phpAccessed January 2012.

Kerr A, Tabony R (2004) Comparison of sunshine recorded by Campbell–Stokes and automatic sensors. Weather 59:90–95.

Marius Paulescu, Eugenia Paulescu, Paul Gravila, Viorel Badescu Weather Modeling and Forecasting of PV Systems Operation Green Energy and Technology 2013 . ISBN: 978-1-4471-4648-3.

Mefti A, Bouroubi M Y. Estimation et Cartographie de la Composante Globale du Rayonnement Solaire. Rev. Energ. Ren. 1999 ; 2 : 219-224.

Mefti A. Contribution à la détermination du gisement solaire par traitement de données solaires au sol et d'images Météosat, PhD thesis, USTHB, Algeria, 2007.

METEONORM, 2012. METEONORM software. http://www.meteonorm.com

PVGIS, 2012. Photovoltaic geographical information system. http://re.jrc.ec.europa.eu/pvgis.

Satel-Light, 2012. European database of daylight and solar radiation. http://www.satel-light.com SMSE, 2012.

NASA surface meteorology and solar energy. http://eosweb.larc.nasa.gov/sse/.

SODA, 2012. Solar radiation da ta. http://www.soda-is.com/eng/index.html.

SolarGis, 2013 : http://solargis.info/doc/free-solar-radiation-maps-GHI.

WCRP , 2012. World climate research programme. http://wcrp.wmo.int/wcrp-index.html.

Chapter 3

Estimation of solar radiation at ground level

3.1 Introduction

Studying of solar radiation is essential to estimate its amount at ground level. In practice, there are two sources of solar data; the first consists of the measured ground data available in meteorological networks and radiometric solar stations. And, the other consists of extracting solar data from digital satellite images. However, only a few stations measured irregularly the amount solar radiation data. Hence, in this chapter, we present a description and classification of some solar radiation estimation models based on ground measurements. Moreover, a satellite image processing model is also discussed. The validity of these models will be judged by comparing the obtained results by actually measured values of the available ground stations.

3.2 Classification of the radiometric models

Radiometric models are based on the exploitation of some ground measured parameters to calculate the various components of solar radiation, particularly in areas where there are no radiometric stations. Generally, these models are based on the main meteorological parameters, such as ambient temperature, relative humidity, sunshine duration and some astronomical parameters such as declination of the Sun, the astronomical day length, solar constant, variation of the distance between Earth and Sun and extraterrestrial radiation calculated on a horizontal plane at the top of the atmosphere. Generally, we can classify the radiometric models in four families: spectral models, semi-empirical models meteorological models and physical models.

Spectral models are essentially the calculation of the spectral components of solar radiation on the ground. They are based on the determination of transmission coefficients. They depend on the knowing of the characteristics of certain atmospheric elements such as aerosols and clouds.

Semi-empirical models have a local character and used to calculate the direct, diffuse and global components. They use meteorological and geographical parameters as inputs. The limit

of these models is the fact that they are applicable only in situations of clear sky.

Meteorological models calculate global radiation whatever the sky condition using directly the solar data collected at ground stations. They have the advantage of generating solar radiation data for different inclined surfaces.

Physical models consist of exploiting and processing satellite imagery. These models have proven their efficiency to reconstruct hourly and daily cycles of solar radiation. They depend on the data extracted from satellite images (clearness index, sky cases, cloud cover and thickness... etc.) and global solar radiation received at the ground under clear sky.

3.3 Semi empirical models

3.3.1 Lacis and Hansen

Lacis and Hansen (1974) proposed a model to estimate the global horizontal solar radiation as expressed in the following equation.

$$G = I_{sc} \cos\theta_z \left[\Big(0.647 - \rho_s^{'} - \alpha_0\Big)/(1 - 0.0685\rho) + 0.353 - \alpha_w \right] \tag{3.1}$$

Where

$$\alpha_0 = \frac{0.02118U_0}{1 + 0.042U_0 + 3.23 \times 10^{-4}U_0^2} + \frac{1.082U_0}{(1 + 138.6U_0)^{0.805}} + \frac{0.0658U_0}{1 + (103.6U_0)^3} \tag{3.2}$$

$$\alpha_\omega = \frac{2.9U_\omega}{(1 + 141.5U_\omega)^{0.635} + 5.925U_\omega} \tag{3.3}$$

U_0 is the thickness of condensable water corrected by the optical path of the radiation through the atmosphere layer.

$$U_\omega = wm_a \tag{3.4}$$

Where m_a is the corrected air masses expressed by

$$m_a = m_r \left(\frac{P}{1013}\right)^{0.75} \left(\frac{273}{T}\right)^{0.5} \tag{3.5}$$

$$m_r = \Big[\cos(\theta_z) + 0.15(93.885 - \theta_z)^{-1.258}\Big]^{-1} \tag{3.6}$$

T represents the ambient temperature (°K) And P is the real pressure at ground level (mbar).

3.3.2 Bird and Hulstrom model

This model is based on empirical representations of radiate transfer equations and attempts to take into account the cumulative effects of aerosols, water vapour, ozone and other gases, and Rayleigh (molecular) scattering upon sunlight reaching the Earth's surface (Bird and Hulstrom, 1981).

3.3.2.1 Direct solar radiation

The direct solar radiation on a horizontal surface is calculated by

$$I = 0.975 I_{sc} \tau_r \tau_g \tau_o \tau_w \tau_a \cos(\theta_z) \tag{3.7}$$

a) Absorption by ozone

$$\tau_0 = 1 - \alpha_0 \tag{3.8}$$

α_0 is the ozone absorption factor given by,

$$\alpha_0 = 0.1611 U_0 (1 + 139.48 U_0)^{-0.3035} - 0.002715 U_0 (1 + 0.044 U_0 + 0.0003 U_0^2)^{-1} \tag{3.9}$$

$$U_0 = l m_r \tag{3.10}$$

b) Absorption by water vapour

$$\tau_w = 1 - \alpha_w \tag{3.11}$$

Where α_w is the abortion water vapour factor given by,

$$\alpha_w = 2.4959 . U_w \Big[(1 + 79.034 U_w)^{0.6828} + 6.385 U_w \Big]^{-1} \tag{3.12}$$

c) Absorption by gases

The transmission coefficient after the gas (CO_2 and O_2) absorption is expressed by,

$$\tau_g = \exp(-0.0127 m_a^{0.26}) \tag{3.13}$$

d) Rayleigh diffusion

$$\tau_r = \exp\left[-0.0903 m_a^{0.84}\left(1 + m_a - m_a^{1.01}\right)\right] \tag{3.14}$$

e) Aerosols diffusion

$$\tau_a = \exp\left[-k_a^{0.873} m_a^{0.9108}\left(1 + k_a - k_a^{0.7088}\right)\right] \tag{3.15}$$

Where

$$k_a = 0.2758 k_{a\lambda/\lambda=0.38\mu m} + 0.35 k_{a\lambda/\lambda=0.5\mu m} \tag{3.16}$$

$k_{a\lambda} = \beta\lambda^{-\alpha}$ Represents the Mie scattering; expressed in Chapter 1.

3.3.2.2 Diffuse solar radiation

The diffuse radiation is equal to,

$$D = D_r + D_a + D_m \tag{3.17}$$

Where

- D_r is the diffuse radiation from the Rayleigh diffusion;
- D_a is the diffuse radiation from the aerosols diffusion,
- $D_m$is the diffuse radiation from the phenomena of multi reflection between the ground and the atmosphere.

a) Diffuse radiation from the Rayleigh diffusion

$$D_r = 0.79 I_{sc}\cos(\theta_z)\tau_o\tau_g\tau_w\tau_{aa}0.5(1-\tau_r)/(1 + m_a + m_a^{1.02}) \tag{3.18}$$

And

$$\tau_{aa} = 1 - (1 - w_0)(1 + m_a + m_a^{1.06})(1 - \tau_a) \tag{3.19}$$

$\omega_0 = 0.90$ represents the unitary reflection coefficient, which depends on the type of the aerosols in the atmosphere.

b) Diffuse radiation from the aerosols diffusion

$$D_a = 0.79 I_{sc}\cos(\theta_z)\tau_o\tau_g\tau_w\tau_{aa}F_c(1-\tau_{as})/(1 + m_a + m_a^{1.02}) \tag{3.20}$$

τ_{as} is the dispersion coefficient in the atmosphere (we used in this model)

$$\tau_{as} = \tau_a/\tau_{aa} \tag{3.21}$$

c) Diffuse radiation from the phenomena of multi reflection between the ground and the atmosphere

This type is the multiple reflections (most of the times) of the solar radiation between ground and sky.

$$D_m = (I + D_a + D_r)\rho\rho_a^{'}/(1 - \rho\rho_a^{'}) \tag{3.22}$$

I is the direct horizontal solar radiation, ρ is the ground albedo and ρ_a' is the clear sky albedo given by,

$$\rho_a^{'} = 0.0685 + (1 - F_c)(1 - \tau_{as}) \tag{3.23}$$

3.3.2.3 Global solar radiation

The global horizontal solar radiation is given by the following equation,

$$G = I + D = (I + D_r + D_a)\left(\frac{1}{1 - \rho\rho_a^{'}}\right) \tag{3.24}$$

3.3.3 Davies et Hay model (Davies and HAY ,1978)

3.3.3.1 Direct solar radiation

The direct solar radiation on a horizontal surface is calculated by,

$$I = I_{sc}(\tau_0\tau_r - \alpha_w)\tau_a \cos(\theta_z) \tag{3.25}$$

a) Absorption by water vapour

$$\alpha_\omega = \frac{2.9U_\omega}{(1 + 141.5U_\omega)^{0.635} + 5.925U_\omega} \tag{3.26}$$

b) Absorption by ozone

$$\tau_0 = 1 - \alpha_0 \tag{3.27}$$

α_0 is the ozone absorption coefficient proposed by (Lacis and Hansen,1974)

$$\alpha_0 = \frac{0.02118U_0}{1 + 0.042U_0 + 3.23 \times 10^{-4}U_0^2} + \frac{1.082U_0}{(1 + 138.6U_0)^{0.805}} + \frac{0.0658U_0}{1 + (103.6U_0)^3} \tag{3.28}$$

c) Rayleigh diffusion

$$\tau_r = 0.972 - 0.08262m_a + 0.00933m_a^2 - 0.00095m_a^2 + 0.000437m_a^4 \tag{3.29}$$

d) Aerosols diffusion

The transmission coefficients after the diffusion by aerosols is given by,

$$\tau_a = (0.12445\alpha - 0.0162) + (1.003 - 0.125\alpha)\exp\left[-\beta m_a(1.089\alpha + 0.5123)\right] \tag{3.30}$$

3.3.3.2 Diffuse solar radiation

As the last model, the diffuse radiation is given by,

$$D = D_r + D_a + D_m \tag{3.31}$$

a) Diffuse radiation from the Rayleigh diffusion

$$D_r = I_{sc}\tau_o\tau_a(1 - \tau_r)0.5\cos\theta_z \tag{3.32}$$

b) Diffuse radiation from aerosols diffusion

$$D_a = I_{sc}(\tau_o\tau_a - \alpha_\omega)(F_c\omega_o(1 - \tau_a))\cos\theta_z \tag{3.33}$$

w_0 is the albedo dispersion of the atmosphere (generally equal to 0.6 for urban and industrial areas and 0.9 for agriculture and farming areas). F_c is the atmosphere dispersion coefficient given Table 3.1

c) The diffuse radiation from the phenomena of multi reflection between the ground and the atmosphere

$$D_m = (I + D_a + D_r)\rho\rho_a^{'}/(1 - \rho\rho_a^{'}) \tag{3.34}$$

$\rho_a^{'}$is the clear sky albedo for a specified location given by,

$$\rho_a^{'} = 0.0685 + 0.17\omega_0(1 - \tau_a^{'}) \tag{3.35}$$

Table 3.1: Atmosphere dispersion coefficient values.

$\theta_z(^\circ)$	0	10	20	30	40	50	60	70	80	85
F_c	0.92	0.92	0.9	0.9	0.9	0.85	0.78	0.68	0.6	0.5

3.3.3.3 Global solar radiation

The global horizontal solar radiation is given by the following equation,

$$G = I + D = (I + D_r + D_a)\left(\frac{1}{1 - \rho\rho_a'}\right) \tag{3.36}$$

3.4 Inclined surface

3.4.1 Liu and Jordan model

Liu and Jordan (1960) proposed a model to estimate the amount of solar radiation at ground level basing on the day number, the latitude and the high of the Sun.

3.4.1.1 Direct solar radiation

The expression of the direct solar radiation on titled surface is,

$$I_i = IR_b \tag{3.37}$$

- I is the direct solar radiation on a horizontal plane,
- R_b is the inclination factor given by,

$$R_b = \frac{\cos\theta_i}{\cos\theta_z} \tag{3.38}$$

If the surface is oriented south then

$$R_b = \frac{\cos(\phi - \beta')\cos\delta\cos\omega + \sin(\phi - \beta')\sin\delta}{\cos\phi\cos\delta\cos\omega + \sin\phi\sin\delta} \tag{3.39}$$

In a horizontal surface we have β' = 0 and then the expression of the direct solar radiation on horizontal surface became

$$I_i = I = A\sin(h)\exp\left(\frac{-1}{C\sin(h) + 2}\right) \tag{3.40}$$

3.4.1.2 Diffuse solar radiation

The diffuse solar radiation on titled surface is,

$$D_i = D\left(\frac{1 + \cos\beta'}{2}\right) \tag{3.41}$$

For a horizontal surface we have $D_i = D$

$$D_i = D = B(\sin(h))^{0.4} \tag{3.42}$$

Table 3.2: Coefficient A, B and C for the Lui and Jordan (1960) model.

Type of sky	A	B	C
Clear sky	1300	87	6
medium polluted sky	1230	125	4
Polluted sky	1200	187	2.5

A, B and C are constants depend on the type of sky, as given in Table 3.2

3.4.1.3 Reflected solar radiation

The reflected solar radiation on inclined surface is given by this equation

$$R_i = (I + D)\left(\frac{1 - \cos\beta'}{2}\right)\rho \tag{3.43}$$

3.4.1.4 Global solar radiation on inclined surface

The global solar radiation on inclined surface is equal to the sum of the direct, diffuse and reflected radiation as expressed in the following equation,

$$G = IR_b + D\left(\frac{1 + \cos\beta'}{2}\right) + G\left(\frac{1 - \cos\beta'}{2}\right)\rho \tag{3.44}$$

3.4.2 Temps et Coulson

In this model, based on the Lui and Jordan (1960) model, Temps and Coulson (1977) developed a new model taking into consideration the non-isotropic characters of the reflected radiation from the ground, including maximum intensities near the Sun and the horizons, minimum intensities in the direction normal to that of the Sun. The diffuse radiation on inclined surface is calculated by the following equation (Temps and Coulson, 1977),

$$D_i(\beta, \lambda) = D\left(\frac{1 + \cos\beta'}{2}\right)\left[1 + \sin^3\left(\frac{\beta}{2}\right)\right] + \left[1 + \cos^2(\theta_i)\sin^3(90 - h)\right] \tag{3.45}$$

3.5 Meteorological models

3.5.1 Angstrom model

Angstrom (1924) proposed a linear expression to estimate of the daily , monthly and annual global solar radiation from the sunshine records as expressed in the following equation,

$$\frac{G}{G_0} = a + b\left(\frac{S}{S_0}\right) \tag{3.46}$$

Where, G and G_{ext} are the daily global radiation received on a horizontal surface at ground level and sunshine duration respectively, a and b are model parameters. The estimation of Angstrom coefficients by the application of regression technique yields constant values as

$$b = \frac{\sum_{i=1}^{n} \left[\overline{\left(\frac{G}{G_0}\right)}_i - \overline{\left(\frac{S}{S_0}\right)}_i\right] \left[\overline{\left(\frac{G}{G_0}\right)}_{i-1} - \overline{\left(\frac{S}{S_0}\right)}_{i-1}\right]}{\sqrt{\sum_{i=1}^{n} \left[\overline{\left(\frac{G}{G_0}\right)}_i - \overline{\left(\frac{S}{S_0}\right)}_i\right]^2 \left[\overline{\left(\frac{G}{G_0}\right)}_{i-1} - \overline{\left(\frac{S}{S_0}\right)}_{i-1}\right]^2}} \tag{3.47}$$

$$a = \overline{\left(\frac{G}{G_0}\right)} - b\overline{\left(\frac{S}{S_0}\right)} \tag{3.48}$$

In our study, the coefficients a and b are taken from the work of Mefti and Bouroubi (1999) as expressed in Table 3.3.

Moreover, Katiyar and Pandey (2013) showed the developed angstrom models, which use higher order correlations to estimate the global solar radiation.

3.5.2 Garg model

Garg (1983) developed a model to estimate the average monthly solar radiation using a correlation between relative humidity HR , ambient temperature T and sunshine fraction as expressed in the following equation,

$$\overline{G} = \overline{G_0}\left(0.14 - 0.4\left(\frac{S}{S_0}\right) - 0.0055H_a\right) \tag{3.49}$$

Where

$$H_a = HR(4.7923 + 0.3647T + 0.005T^2 + 0.0003T^3) \tag{3.50}$$

Table 3.3: a and b angstrom model parameters for Algeria (Mefti and Bouroubi,1999)

Location	a	b	Validation
Algeries	0.49	0.45	Lat $>$ 35.5°
Saida	0.41	0.55	33°$<$Lat $<$ 35.5°
Bechar	0.5	0.23	31°$<$Lat $<$ 33°
Béni Abbes	0.33	0.65	23°$<$Lat $<$ 31°
Tamanresset	0.25	0.7	Lat $<$23°

3.5.3 Hussain model

Basing on Garg (1983) model, Hussain (1984) proposed a model for estimating the global solar radiation on horizontal surface using average monthly humidity and sunshine fraction as follows,

$$\overline{G} = \overline{G_0}\left(0.394 - 0.364\left(\frac{S}{S_0}\right) - 0.0035H_a\right) \tag{3.51}$$

3.6 Average monthly diffuse solar radiation

The diffuse solar radiation is calculated using the following equation ,

$$D = H * K_D \tag{3.52}$$

H is the global horizontal solar radiation and K_D is the diffuse fraction. Several methods were proposed in literature to calculate the diffuse fraction among them,

3.6.1 Lieu and Jordan

Liu and Jordan (1960) proposed the first equation to calculate the diffuse fraction using the clearness index for the Blue Hill Massachusetts location as follow,

$$K_D = 1.39 - 4.027K_t + 5.531K_t^2 - 3.108K_t^3 \qquad for \qquad 0.30 < K_t \leq 0.70 \tag{3.53}$$

3.6.2 Frutos model (Frutos et al. 1985)

$$K_D = \begin{cases} 0.92 \\ 0.77 + 1.93K_t - 6.86K_t^2 + 4.27K_t^3 \\ 0.109 \end{cases} \qquad for \qquad \begin{cases} K_t < 0.166 \\ 0.166 \leq K_t \leq 0.8 \\ K_t > 0.8 \end{cases} \tag{3.54}$$

3.6.3 Page model

Page (1964) used the data of six locations between latitude 40°N and 40°S for calculating the diffuse fraction as follows,

$$K_D = 1 - 1.13K_t \tag{3.55}$$

3.7 Physical model

Satellite-derived solar radiation has become a valuable tool to quantify the solar irradiance at ground level for a large area. Thus, derived hourly values prove to be at least as good as the accuracy of interpolation from ground stations at a distance of 25 km (Zelenka et al. 1999). Several algorithms and models have been developed during the last two decades for estimating the solar irradiance at the Earth's surface from satellite images (Gautier et al. 1980; Hay, 1993).

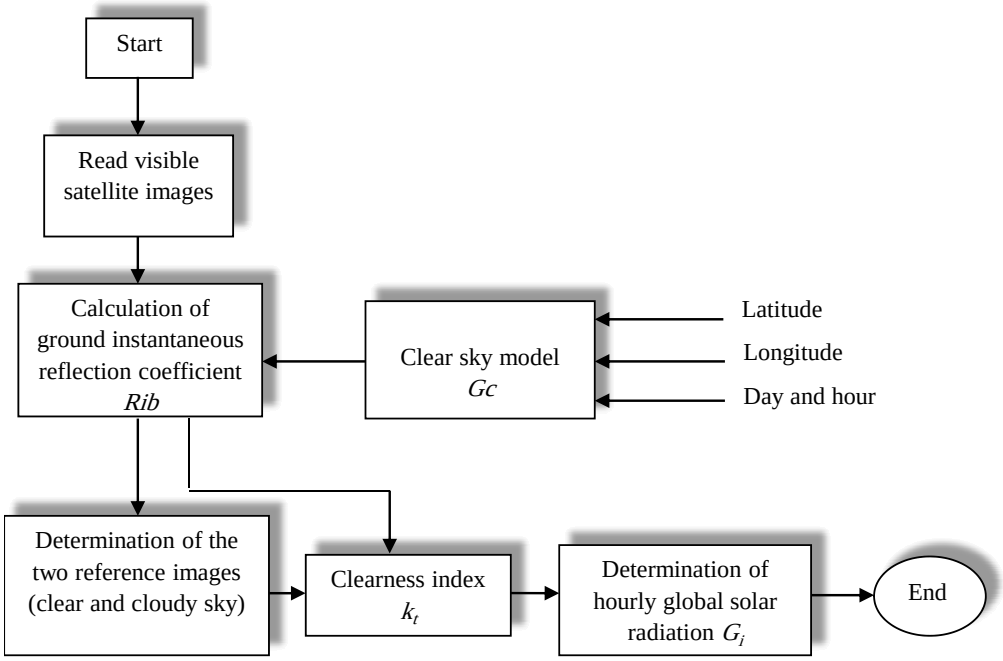

Figure 3.1: Diagram of the GISTEL model.

3.7.1 GISTEL model

GISTEL is a satellite methodology based on a simple physical model. It is used to estimate global solar irradiance from METEOSAT data. The adopted methodology has several steps summarized in the diagram of Fig.3.1.

In this work we proposed an improved GISTEL model by using the fuzzy logic method to obtain more precise results; it consists of the following steps,

3.7.1.1 Determination of the global solar radiation under clear sky

For the estimation of hourly solar radiation under a clear sky, the equation of the world organization of meteorology (W.M.O, 1981) is chosen as follows,

$$G_c = cor\,[1300 - 57T_L]\,(\sin(h_s))^{(36+T_L)/33} \tag{3.56}$$

$$cor = 1 + 0.034\cos(0.986\,(N_d - 3)) \tag{3.57}$$

Where , h_s is solar height, T_L is the Linked turbidity factor that used to quantify the effect of atmospheric components of solar radiation; the T_L values generally vary from 2 (very pure and dry sky) to 6 (polluted and humid sky). *cor* is the correction factor of the Sun-Earth distance given by Eq. (3.57) and N_d is the number of the days of the year.

3.7.1.2 Determination of the ground instantaneous reflection coefficients

Ground instantaneous reflection coefficients $Rb(x, y, d, h)$ for each pixel (x, y) of the visible MSG image of the day d and the hour h are given by Eq. (3.58). These coefficients represent the reflection of solar radiation on the surface.

$$Rb(x, y, d, h) = \frac{B(x, y, d, h) - Ba(x, y, d, h)}{K.Gc(x, y, d, h).T(x, y, d, h)} \tag{3.58}$$

Where, $B(x, y, d, h)$ represents the brightness of the (x, y) pixel, $Ba(x, y, d, h)$ the atmospheric brightness recorded by the satellite above the sea by a clear sky. This brightness was considered constant, and it is equal to 12 (Ben Djemaa and Delorme ,1992); K is the factor calibration of the visible channel sensor equal to 0.514. $T(x, y, d, h)$ is the transmission coefficient of the direct radiation from the ground to the satellite. It is given by Eq. (3.59),

$$T = \frac{(1390 - 31T_L)}{1367} \exp\left[-\frac{T_L}{12.6\sin(h_v + 2)}\right] \tag{3.59}$$

Where h_v is the height angle of the satellite, given by Eq. (3.60).

$$h_v = \arcsin\left(\frac{1.862\cos(\varphi)\cos(\phi) - 0.274}{\sqrt{3.41 - \cos(\varphi)\cos(\phi)}}\right) \tag{3.60}$$

3.7.1.3 Determination of the clear and cloudy reference images

To determine the two clear and cloudy reference images, a sequence of images is taken over a long period at 12 o'clock (generally, a period of one month). Taking the minimum values of the reflection coefficients obtained from these sequence images, the clear sky reference image can be obtained. On the other hand, the cloudy sky reference image is constructed by using the greatest values of the reflection coefficient obtained using the same sequence of images.

3.7.1.4 Calculation of the clearness index using fuzzy logic

The clearness index K_t is calculated for each image by comparing pixel by pixel and hour by hour the instantaneous reflection coefficients Rb with the two clear sky R_c and the cloudy sky R_n reflection coefficients. According to this comparison, three types of skies can be observed, namely clear sky, partially covered sky and completely covered sky (Ben Djemaa and Delorme,1992), as expressed in Eq. (3.61)

$$\begin{aligned}
Clear\,sky\ :\quad & Rb \leq Rc\ :\quad K_t = 1 \\
Partially\,covered\,sky\ :\quad & Rc < Rb < Rn\ :\ K_t = 1 - (1 - K_0)\frac{(Rb - Rc)}{(Rn - Rc)} \\
Completely\,covered\,sky\ :\quad & Rb \geq Rn\ :\quad K_t = K_0
\end{aligned} \tag{3.61}$$

Where K_0 is the index by a cloudy sky equals to 0.2.

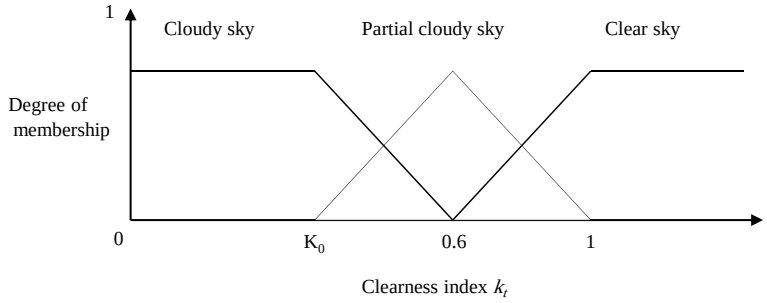

Figure 3.2: Fuzzy logic membership function.

However, Eq.(3.61) deals with fixed sky cases (only three) and do not consider all types of skies (for example : the case between clear sky and partially cloudy sky).Hence, to obtain more precise results a fuzzy logic approach is proposed in this thesis. Fuzzy logic methodology has the ability to translate human qualitative knowledge into formal algorithms; it deals with reasoning that is approximate rather than fixed. It consists of using expert rules that can sometimes produce a simple set of control for a dynamical system with less effort [See Appendix A.3]. Hence, three rules are introduced in this work to obtain logical values of the clearness index K_t as expressed in Fig. 3.2.

3.7.1.5 Calculation of the instantaneous global solar radiation

The instantaneous global solar radiation $G(x, y, d, h)$ for each pixel is obtained by multiplying the clearness index K_t by the global solar radiation obtained under clear sky $Gc(x, y, d, h)$. As expressed in Eq. (3.62) as

$$G(x, y, d, h) = K_t \times Gc(x, y, d, h) \tag{3.62}$$

3.8 Simulation results

In this part, we are interested to show the simulation results of the above-mentioned models for estimating hourly global solar radiation data. For this purpose, two locations have been chosen where the measured data are available. From the National Meteorological Office of Algeria, we choose the site of Bouzereah, Algeria (Lat : 36.87° N, Lon : 3 ° E, Alt : 358 m) that represents the north of Algeria and the site of Ghardaia ,Algeria (Lat: 32.4908° N, Lon : 3.6728° E, Alt: 467m) that locates in the south of Algeria. The performances of the simulated models are evaluated using the root mean square error (RMSE) and normalized root mean square error (NRMSE) expressed by the following equations,

$$RMSE = \left[< (I_{i,predicted} - I_{i,measured})^2 > \right]^{\frac{1}{2}} \tag{3.63}$$

$$NRMSE = \left(\frac{\left[< (I_{i,predicted} - I_{i,measured})^2 > \right]^{\frac{1}{2}}}{< I_{i,measured} >} \right) \tag{3.64}$$

RMSE and NRMSE provide information on the short-term performance of correlations by allowing a term-by-term comparison of the actual deviation between the predicted and measured values. The model that has the lowest NRMSE was considered the best model.

a) Semi-empirical model

Semi empirical models are used widely to estimate hourly solar radiation, especially in the case of clear sky. Hence, we compared the results of Lacis and Hansen (1974), Bird and Hulstrom (1981), Davies and Hay (1978) models. We have selected four days (06-01-2008 / 05-04-2008/ 24-06-2008 / 30-10-2008) for Ghardaia , and two days for Bouzereah (29-04-2006 / 05-08-2005).

The simulation results are shown in Fig.3.3 that represents the estimated hourly horizontal global solar radiation using different models. In addition, Table 3.4 shows the NRMSE error between measured and simulated solar radiation data using the mentioned models.

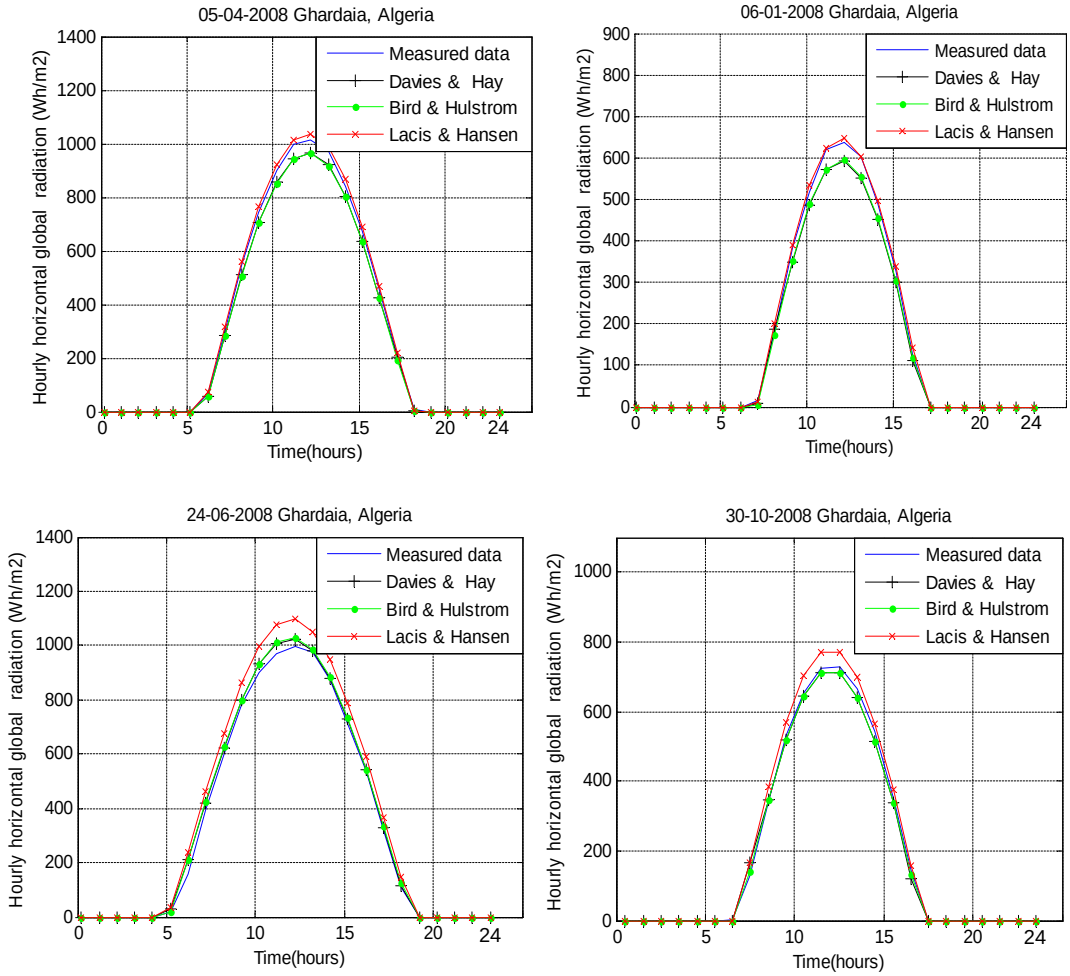

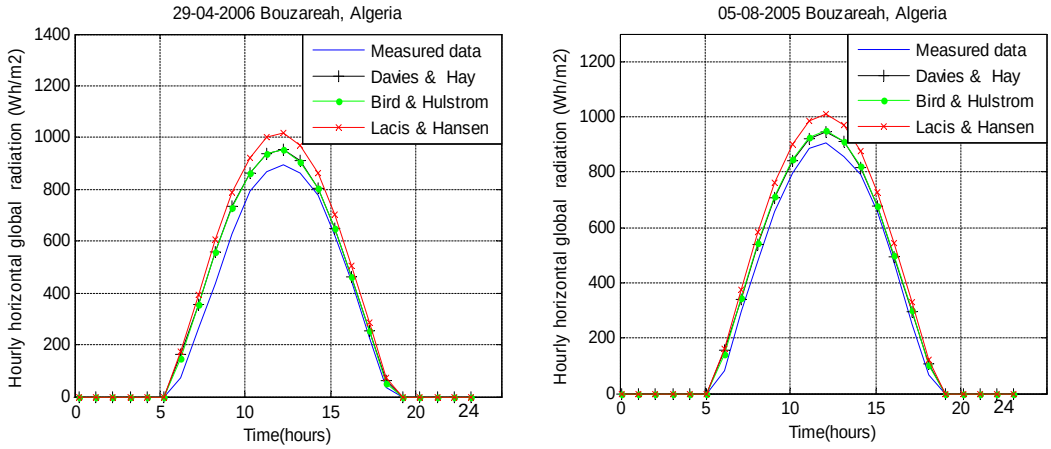

Figure 3.3: Measured and simulated hourly horizontal global solar radiations using Davies and Hay , Bird and Husltrom, and , Lacis and Hansen models for some days for the location of Ghardaia and Bouzareah.

Table 3.4: NRMSE between measured and simulated solar radiation data using Lacis and Hansen, Davis and Hay , and , Bird and Hulstrom models.

		Models			
	Days	Lacis and Hansen	Davis and Hoy	Bird and Hulstrom	Location
Direct solar radiation	06/01/2008		0.1683	0.1842	**Ghardaia**
	05/04/2008		0.0753	0.2934	
	24/06/2008		0.2771	0.1413	
	30/10/2008		0.2784	0.0863	
	29/04/2006		0.2246	0.1189	**Bouzareah**
	05/08/2005		0.107	0.0915	
Diffuse solar radiation	06/01/2008		0.1947	0.0729	**Ghardaia**
	05/04/2008		0.3028	0.6195	
	24/06/2008		0.6195	0.3028	
	30/10/2008		0.0729	0.1947	
	29/04/2006		0.3926	0.4955	**Bouzareah**
	05/08/2005		0.2668	0.7309	
Global solar radiation	06/01/2008	0.044	0.1457	0.1355	**Ghardaia**
	05/04/2008	0.0366	0.0871	0.0928	
	24/06/2008	0.1471	0.052	0.0539	
	30/10/2008	0.1074	0.07	0.0552	
	29/04/2006	0.2415	0.1598	0.1555	**Bouzareah**
	05/08/2005	0.1913	0.1034	0.105	

From Fig. 3.3 and Table 3.4, the three models are almost the same with the measured hourly global horizontal solar radiation data. However, they represent a small NRMSE error that depends on the location and the season. For the site of Ghardaia, which is characterised by the dry climate for the whole year that increases the probability of sandstorms, which have an influence on the turbidity. For the days of 06-01-2008 and 05-04-2008, Lacis and Hansen model gives the best results and the lowest NRMSE comparing with Davis and Hay , and Bird and Hulstrom models that is because these 2 days represent wet days (high value of water vapour) that influence the efficacy of other models. However , for days of 24-06-2008 and 30-10-2008, Lacis and Hansen model gives the highest NRMSE value comparing with other model that is, these days are totally dry that can present sandstorms which affect on the efficiency of Lacis and Hansen model.

For Bouzareah which located in the north of Algeria in front of the sea. That means the weather is wet with the presence of high levels of water vapour.

b) Inclined surface models

In this part, two models are selected to calculate the inclined solar radiation from the measured solar radiation on a horizontal surface. First, Liu and Jordan model is used to estimate the amount of the inclined global solar radiation and second, Temps and Coulson (1977) model is used for the inclined diffuse solar radiation estimation. Several days have been tested for both models (Liu and Jordan: 06-01-2008 and 28-06-2008 for Ghardaia, and or Temps and Coulson: 05-04-2008 for Ghardaia and 29-04-2006 for Bouzareah). The inclination angle is equal to the latitude of the location. The simulation results are shown respectively in Fig. 3.4 and Fig. 3.5.In addition, the NRMSE of the measured and estimated inclined data are presented in Table 3.5 .

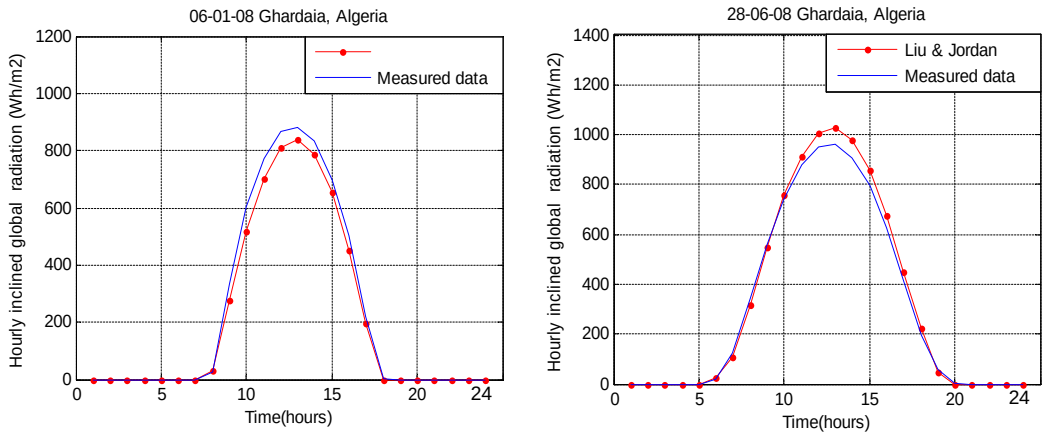

Figure 3.4: Measured and simulated hourly inclined global solar radiation using Liu and Jordan model.

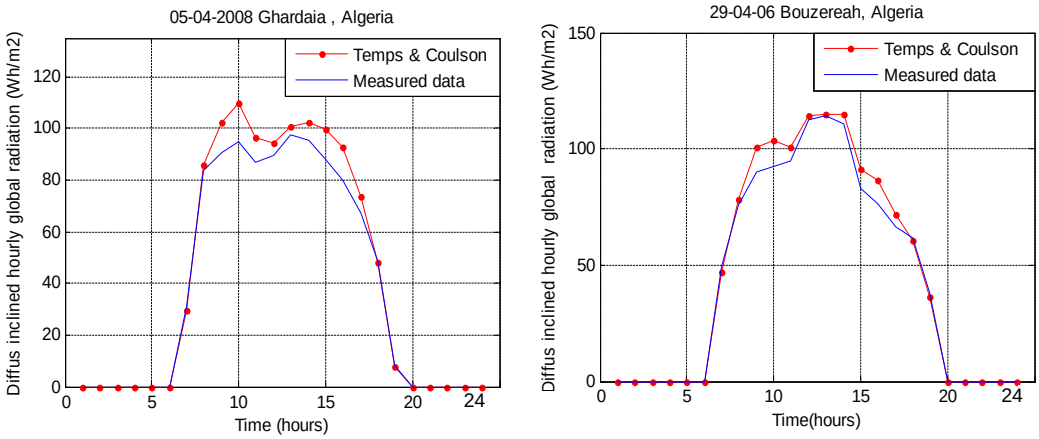

Figure 3.5: Measured and simulated diffuse inclined hourly global solar radiation using Temps and Coulson model.

Table 3.5: NRMSE between measured and simulated solar radiation data using Lacis and Hansen, Davis and Hay , and , Bird and Hulstrom models.

	Days	Model	NRMSE	Location
Inclined global radiation	06/01/2008	Liu and Jordan model	0.1534	Ghardaia
	24/06/2008		0.0922	Ghardaia
Inclined Diffuse radiation	05/04/2008	Temps and Coulson model	0.1403	Ghardaia
	29/04/2006		0.0965	Bouzareah

From Fig. 3.4, Fig. 3.5 and Table 3.5, it is clearly shown that the proposed models estimate in a good way the measured inclined data. However, they may represent some limitations because they depend on the physical mechanism of the atmospheric parameters.

c) Meteorological models

In this part, we used Angstrom (1924) , Garg (1983) and Hussain (1984) models to estimate the monthly average daily global solar radiation. The results are compared with the measured data for Ghardaia, 2002. The simulation results are shown in Fig.3.6. In addition, the NRMSE error between measured data and the simulated data using the three models are presented in Table 3.6. From these results, Garg model represents the best results with an NRMSE equal to 0.0230 compared with Hussain model (NRMSE = 0.0888) and Angstrom model (NRMSE = 0.1478). Angstrom model represents the highest NRMSE value that depends strongly on the empirical estimation of Angstrom parameters compared to Garg and Hussain models where its parameters (temperature and humidity) can determine precisely.

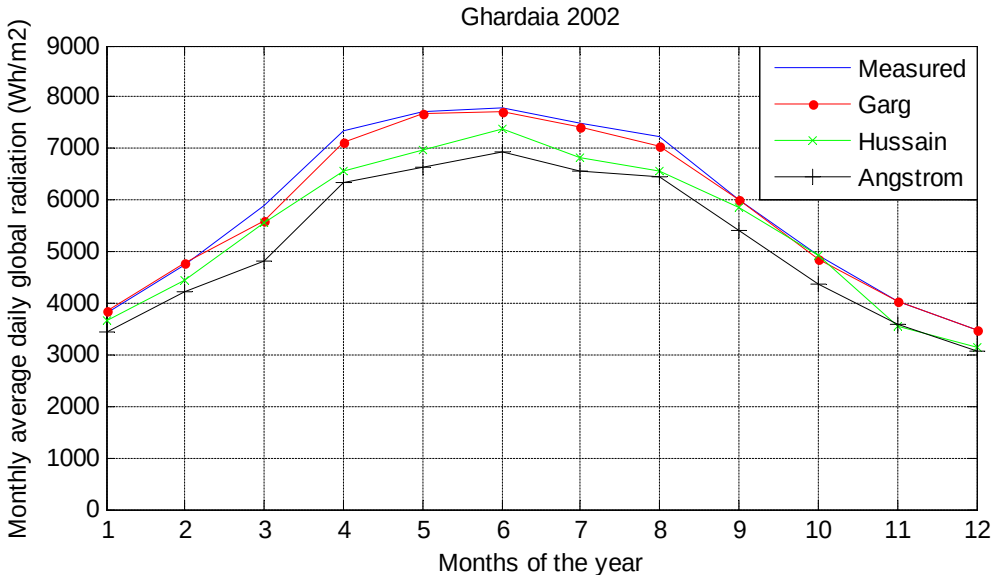

Figure 3.6: Measured and simulated monthly average daily global solar radiation using Garg, Hussain and Angstrom models.

Table 3.6: Relative error and NRMSE between measured and simulated monthly average daily global solar radiation using Garg, Hussain and Angstrom models.

	Relative error												**NRMSE**
Months	1	**2**	**3**	**4**	**5**	**6**	**7**	**8**	**9**	**10**	**11**	**12**	
Models													
Garg	0.92	0.74	5.37	3.35	0.45	0.9	0.94	2.44	0.1	1.43	0.12	1.02	0.023
Hussain	3.69	5.95	5.97	11.03	9.61	4.98	8.93	9.28	2.35	0.1	11.41	9.18	0.0888
Angstrom	10.1	11.1	18.5	13.9	13.7	10.8	12.6	10.7	10	11.4	10.5	11.2	0.1478

d) Physical models

The GISTEL methodology is presented in this part to estimate hourly solar radiation data for different sky conditions. To perform the GISTEL model, two different approaches with and without the fuzzy logic methods were used. We have chosen in our simulation two locations for validation purposes. For Ghardaia, the days of 22-11-2012 and 07-12-2012 and for Bouzereah, the days of 26^{th} March 2013 and 3^{rd} April 2013. The visible satellite images are taken from the Meteo Company B.V website: (http://www.sat24.com) as illustrated in Fig.3.7 which represents the satellite image for Algeria.

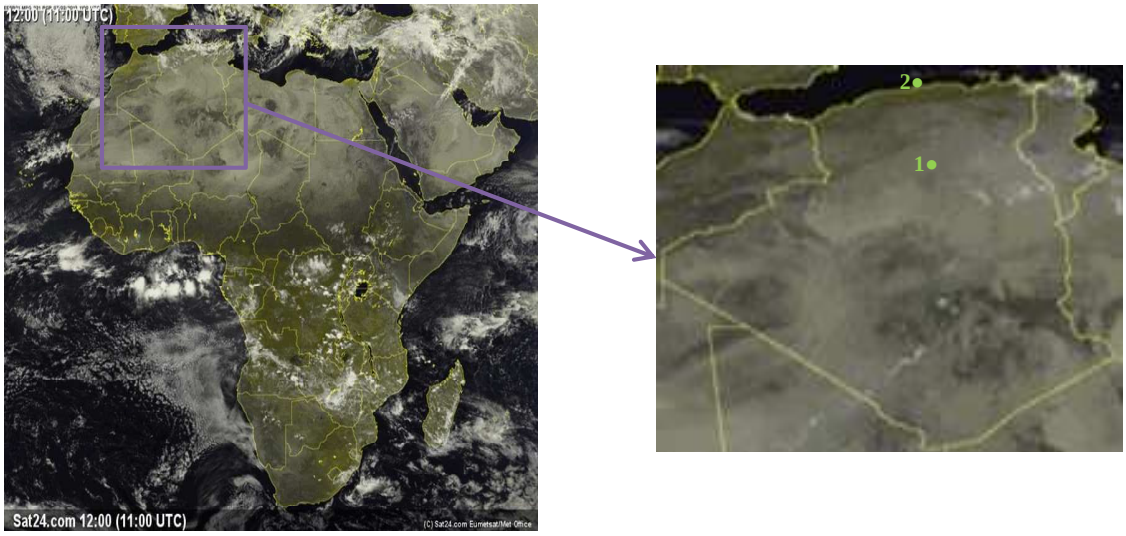

Figure 3.7: Satellite image for Algeria.

The first step of GISTEL methodology consists of determining the two reference images. For that, we used a sequence of images taken at 12 a.m. UTC for a period of one month. The clear sky and overcast sky reference images are shown in Fig.3.8.

The next step consists of determining the relation between the clearness index and global hourly solar radiation. Hence, visible images that represent sunny hours of the day are used to estimate the amount of the solar radiation using Eq. (3.62). The simulation results of the estimated hourly solar radiation using FL and without FL with the measured data are shown in Fig.3.9

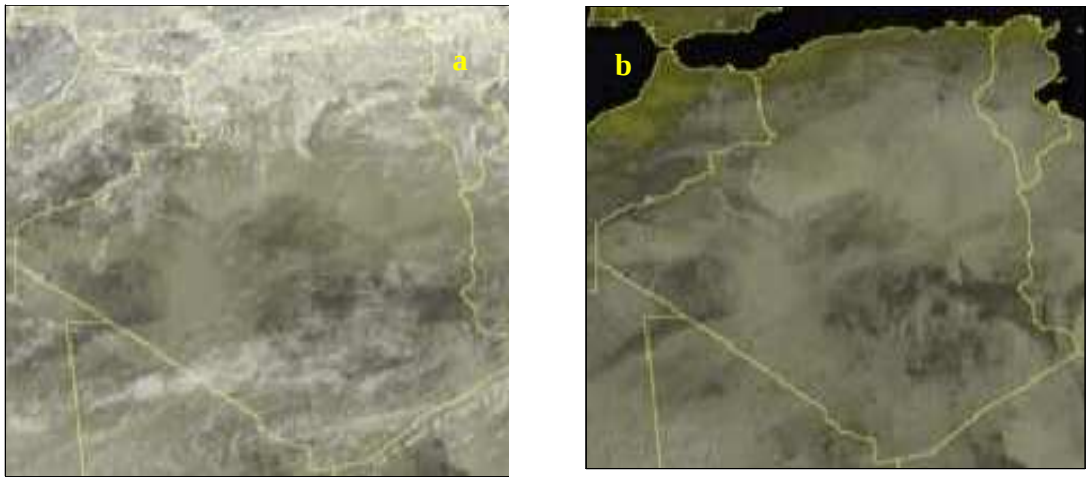

Figure 3.8: a) clear sky reference image . b) Overcast sky reference image.

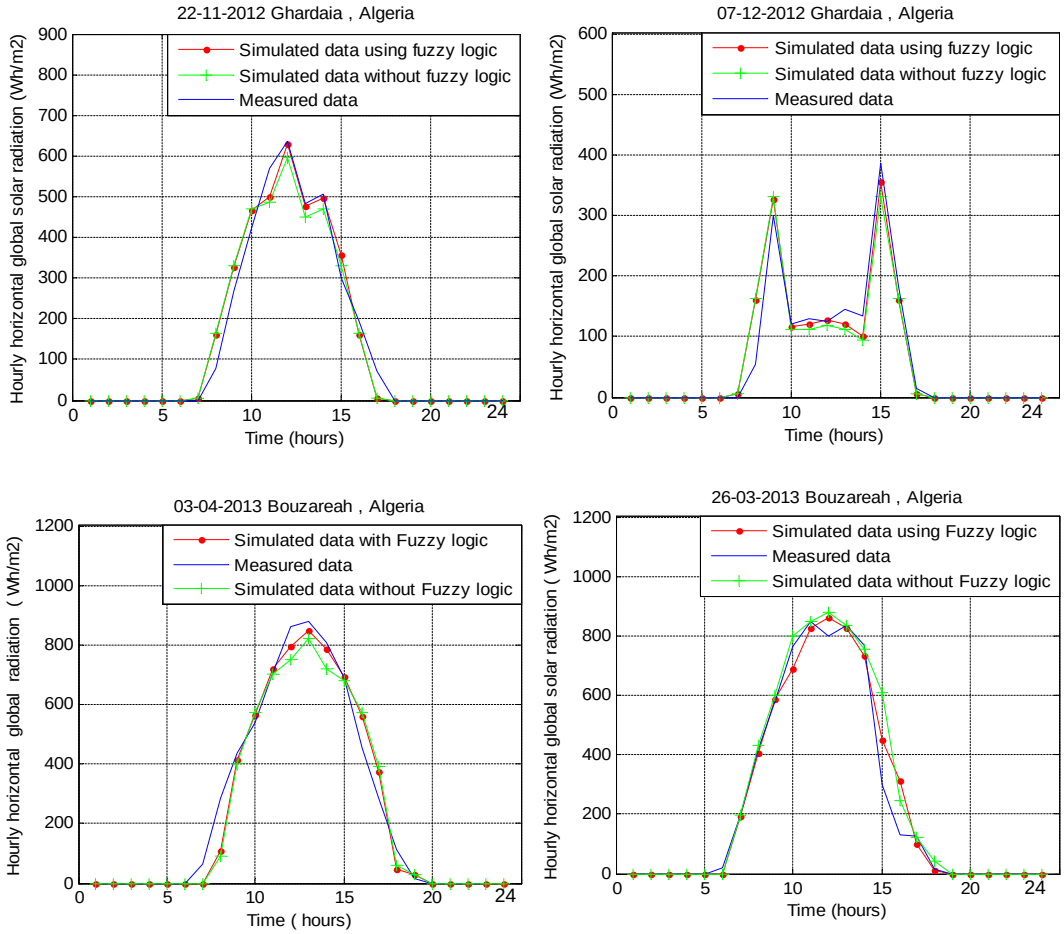

Figure 3.9: Estimated hourly solar radiation using FL and without FL with the measured data for Ghardaia and Bouzereah.

From Fig.3.9 we note that the simulated solar radiations are changed during the day; from low values in sunrise and sunset to high values at noon that leads to the fact that results obtained from the GISTEL model represent the real stat of a day. In addition, some fluctuations can occur due to the presence of clouds. The variation of the solar radiations depends on the clearness index K_t ; a clear day has a clearness index equal to 1, a cloudy day with $K_t = 0.2$ and a partially cloudy day between $0.2 < K_t < 1$. For more precise results, the clearness index should be calculated for a sequence of days.

For the validation of the simulation results of the estimation of hourly horizontal global solar radiation data with GISTEL model with and without the fuzzy logic model we calculated the NRMSE as represented in Table 3.7.

Table 3.7: NRMSE value of hourly solar radiation with and without FL.

		NRMSE	
Location	**Date**	**Without FL**	**With FL**
Ghardaia	22 Nov. 2012	0.2466	0.2184
	07 Dec. 2012	0.3408	0.2777
Bouzareah	26 Mar. 2013	0.2885	0.2185
	03 Apr. 2013	0.2488	0.2072

From Table 3.7, it is clearly shown that the simulated models with the fuzzy logic model are good enough, which represents an NRMSE error between 0.2 and 0.27 compared to the measured solar radiation data for all locations. Moreover, the NRMSE of the simulated hourly global horizontal solar radiation using the fuzzy logic method is lower than the simulated ones without using it, leads to a conclusion that the GISTEL model with fuzzy logic method is good for such similar problems.

3.9 Conclusion

The most important radiometric models are presented in this chapter. Semi-empirical models are used to calculate the various components of solar radiation at ground level using as input parameters: the astronomical, geographical and meteorological parameters. Meteorological models calculate the global radiation at ground level from the monthly average insolation. Physical models estimate the instantaneous solar radiation at ground level based on the data extracted from satellite images. Semi empirical and meteorological models have the advantage of being simple; they use mathematical equations not too heavy for the study of solar radiation and the estimation of the incident solar energy. They can be applied to any region and any day of the year. Nevertheless, the limitation of these models is that they are valid in situations of clear sky (most of them). Indeed, these models are sensitive to climatic disturbances such as sandstorms or clouds that significantly affect the estimate of the amount of incident solar energy. Thus, the direct use of one or the other of these models in this case can lead to erroneous values which can significantly impact the design of solar systems. However, complementary approach based on satellite images is essential. It helps to estimate the amount of solar radiation at any place in the world for all the sky cases (clear, partially cloudy and cloudy). It gives the best results compared with other models. But, it depends strongly on the satellite images which are not always available.

Another limitation of these models, which they take a lot of calculation time (for each hour we need to resolve equations). For that, we will present in next chapter two novel long-term forecasting models in order to predict the amount of solar radiation in the future.

Nomenclature

$B(x, y, d, h)$ Brightness of the pixel (x, y).

$Ba(x, y, d, h)$ Atmospheric brightness.

Cor Correction factor of the Sun-Earth distance.

D Diffuse radiation.

D_a Diffuse radiation from the aerosols diffusion.

D_i Diffuse solar radiation on titled surface.

D_m Diffuse radiation from the phenomena of multi reflection between the Ground and the atmosphere.

D_r Diffuse radiation from the Rayleigh diffusion.

F_c Dispersion coefficient in the atmosphere.

G Global solar radiation.

$G(x, y, d, h)$ Instantaneous global solar radiation of the pixel (x, y).

HR Relative humidity. hs Solar height.

h_v Height angle of the satellite.

I Direct horizontal solar radiation.

I_i Direct solar radiation on titled surface.

K Calibration factor of the visible channel sensor.

K_0 Index by a cloudy sky.

K_D Diffuse fraction.

K_t Clearness index.

$k_{\alpha\lambda}$ Mie scattering.

m_a Corrected air masses.

m_r Relative air masses.

N_d Number of the days of the year.

$NRMSE$ Normalized root mean square error .

$RMSE$ Root mean square error.

P Reel pressure at ground level (mbar).

R_b Inclination factor.

R_c Clear sky reflection coefficients.

R_i Reflected solar radiation on titled surface.

$Rb(x, y, d, h)$ Ground instantaneous reflection coefficients of the pixel (x, y).

R_n Cloudy sky reflection coefficients.

T Ambient temperature (°K) .

$T(x, y, d, h)$ Transmission coefficient of the pixel (x, y).

T_L Linked turbidity factor.

U_0 Thickness of condensable water.

α_0 Ozone absorption factor .

α_w Abortion water vapour factor.

ρ Ground albedo.

ρ_a' Clear sky albedo.

τ_0 Absorption by ozone.

τ_a Aerosols diffusion.

τ_g Absorption by gases.

τ_r Rayleigh diffusion.

τ_w Absorption by water vapour.

References

Ångström A. Solar and terrestrial radiation. Q J Roy Meteorol Soc 1924; 50:121-126.

Ben Djemaa A, Delorme C. A comparison between one year of daily global radiation from ground-based measurements versus METEOSAT images from seven locations in Tunisia. Sol Energy 1992;5:325–33.

Bird R E , Hulstrom R L . A Simplified Clear Sky Model for a Direct and Diffuse Insolation on Horizontal Surface, Solar Energy Research Institute. Goldon Colorado. 1981;642-761

Davies J A., et HAY J E . Calculation of the solar radiation incident on a horizontal surface, Proc. Canad. Sol. Radiat. Data workshop, 1st, 1978, Toronto, Ontario.

Frutos F , Ruiz V, Gutierrez J. Correlations between the solar diffuse and global radiation for Madrid. Revue Internationale Heliotechnique I.7 1985.

Garg H P , Garg S N Prediction of Global Solar Radiation from Bright Sunshine Hours and Other Meteorological Data, Energy Conversion and Management 1983; 23: 113- 118.

Gautier C , Diak G, Masse S. A simple physical model to estimate incident solar radiation at the surface from GOES satellite data. J. Appl. Meteor. 1980; 19:1005–1012.

Hay J E. An Assessment of Models which use Satellite Data to Estimate Solar Irradiance at the Earth's Surface. J. Climate Appl. Meteor. 1984; 23: 832–844.

Hussein M. Estimation of Global and Diffuse radiation Form Sunshine Duration and Atmospheric Water Vapor Content, Energy Conversion and Management 1984; 33: 217-220.

Katiyar K, Pandey C K. A Review of Solar Radiation Models—Part I. Journal of Renewable Energy. 2013.

Lacis A L , Hansen J E . A parameterization for Absorption of Solar Radiation in the Earth's Atmosphere. J. Atmospheric Science 1974; 31: 118-133.

Liu B Y H, Jordan R C . The interrelationship and characteristic distribution of direct, diffuse and total solar radiation. Sol. Energy 1960 ; 4: 1-19.

Mefti A, Bouroubi M.Y. Estimation et Cartographie de la Composante Globale du Rayonnement Solaire, Revue des Energies Renouvelables 1999 ; 219-224

Page J K . The estimation of monthly mean values of daily short wave radiation on vertical and inclined surface from sunshine records of latitude 40 degree N to 40 degree S. Proc. of UN-Conf. on New Sources of Energy. 1964; l:4 paper s/98. 378.

Temps R C , Coulsons K L . solar radiation incident upon slopes of different orientations. Sol. Energy 1977 ; 19: 179-184

W.M.O. Meteorological aspects of the utilization of solar radiation as an energy source. Technical note W.M.O. vol. 172; 1981. p. 57–85.

Zelenka A , Perez R , Seals R , Renné D. Effective accuracy of satellite-derived hourly irradiances. Theoretical and Applied Climatology 1999; 62: 199-207.

Chapter 4

Forecasting of solar radiation at ground level

4.1 Introduction

Solar energy is one of the most important renewable energies to generate electricity and meet our everyday needs. PV systems are used to convert this energy to a DC electrical power. However, sometimes it is not possible to estimate the PV system outputs in the long-term because they depend strongly on the input parameters such as the amount of solar radiation and temperature. Thus, solar radiation data should be measured continuously and accurately over the long-term. Unfortunately, in most areas of the world, solar radiation measurements are not easily available due to financial, technical or institutional limitations. Hence, forecasting is known as a solution that is important for the integration of photovoltaic plants into an electrical grid. Proper solar irradiance forecasting helps the grid operators to optimize their electricity production and /or to reduce additional costs by preparing an appropriate strategy. In this chapter, we present two forecasting methods to determine the amount of solar radiation on the long-term.

4.2 Forecasting solar radiation background

Solar radiation time series is a sequence of time ordered data values, measured at fixed time intervals. It analysis consists of determining the adequate model to represent the data for use it in varying ways, depending on the application target such as forecasting hourly solar radiation data. At first approximation, solar radiation time series presumes that past pattern will appear in the future. Then, a mathematical model will be determined to predict future values based on past values. However, forecasting solar radiation was known as a difficult problem, especially on hourly and small basis, due to the non-linearity and complexity of modelling of the solar radiation series (Zhang, 2003; André Luis et al., 2008; Wu and Chan, 2011). Hence, many studies had been conducted on this subject, such as stochastic models (Boland, 2008; Wu and Chan, 2011) and neural network methods (Markham and Rakes, 1998; Zhang et al., 1998; Mellit et al., 2009; Wu and Chan, 2011). These models treated the solar radiation sequence as a time series; they used mathematical models in the modelling phase to forecast future values.

Classical linear time series models like autoregressive moving average (ARMA) modelling (Box and Jenkins, 1970) have been widely used in modelling of linear time series (Wu and Chan, 2011). The popularity of the ARMA model is due to its statistical properties as well as the well-known Box–Jenkins methodology (Box and Jenkins, 1970). Even so, it was proven that they are inadequate in the analysis and prediction of solar radiation due to the non-stationarity (Box and Jenkins, 1970; Kwiatkowski et al., 1992; Wu and Chan, 2011) and nonlinearity of the solar radiation time series, especially for cloudy sky (Zhang, 2003; André Luis et al., 2008; Wu and Chan, 2011). In addition, stochastic models are based on the probability estimation that needs a full identification of the mathematical function, leads to a difficult forecasting of the solar radiation time series (Wu and Chan, 2011).Moreover, global solar radiation time series is a dynamical system that depends on some meteorological elements such as temperature, water vapour, suspend solids, cloud and water air condition that can represent nonlinear characteristics (Wu and Chan, 2011; Huang et al., 2013) .

To overcome this problem, nonlinear approaches, such as artificial neural networks (ANN), were considered a powerful tool for forecasting similar time series (Zhang, 2003; Mellit et al., 2009; Wu and Chan, 2011). The advantages of the ANN that is non-parametric. It does not require the knowledge of the internal system parameters that offer a compact solution for multiple variable problems (Denton, 1995; Markham and Rakes, 1998; Zhang, 2003,; Wu and Chan, 2011). Nonlinear Autoregressive (NAR) neural networks are considered a good solution for nonlinear time series forecasting. It is a simple multilayer perceptron neural network (MLP) with some modification that used only the past values of the time series to forecast future values. A good choice of the number of delays, neurons and training algorithm can resolve the problem of the non-linearity of the solar radiation time series.

However, single models presented a big forecasting error (Wu and Chan, 2011). For example, ARMA model showed good results for linear problems, but it could represent huge errors in the nonlinear problems; also, the outliers made the prediction by NAR networks difficult (Zhang, 2003; Diagne et al., 2009; Wu and Chan, 2011). Thus, hybrid methods combining different models have been widely used in literature to improve the forecast performance (Wu and Chan, 2011; Huang et al., 2013; Chen et al., 2013).

Pelikan et al. (1992), and Ginzburg and Horn (1994) proposed a model combining several feed forward neural networks, improving the time series forecasting accuracy. Wedding and Cios (1996) described a combining method using radial basis function networks and the Box–Jenkins models. Luxhoj et al. (1996) presented a hybrid econometric and an ANN approach for sales forecasting. Zhang (2003) proposed a method using a hybrid combination between ARMA and ANN models to predict time series, André Luis et al., (2008) used Zhang (2003) model and adjusted the model on the midpoint and an interval range series in the training set. Wu and Chan (2011) proposed a technique employing a combination of ARMA and time delay neural network (TDNN) for one-step ahead prediction based on Zhang (2003) model. In addition, many authors have already studied successfully the coupling between ANN and different traditional computing technologies such as fuzzy logic, wavelet-based analysis and genetic algorithm methods (Mellit et al., 2009; Diagne et al., 2009; Boata and Gravila, 2012; Chen et al., 2013). However, most of those models presented limitations, especially in long-term forecasting. In addition, no one of these methods will be capable of presenting information about the behaviour of the solar radiation time series in the future. Hence, two hybrid methods were presented in this chapter to overcome these problems.

First, a hybrid model of ARMA and NAR network for multi-step ahead prediction of solar

radiation time series for better performance in long-term forecasting. And second, a hybrid time series data mining (TSDM) and NAR neural network models for presenting information about the behaviour of the solar radiation time series in the future that ensures the accuracy of the forecasted model.

4.3 Forecasting hourly solar radiation using hybrid ARMA and NAR models

This section introduces the adopted hybrid methodology for multi-hour ahead forecasting of hourly global horizontal solar radiation time series as shown in Fig.4.1 It consists of three essential stages. First, Autoregressive Moving Average (ARMA) model is used to predict future values of the global solar radiation time series. However, because of the non- stationarity of hourly solar radiation time series, a phase of detrending is needed to stationarize the radiation data. Secondly, Nonlinear Autoregressive (NAR) neural network model is used for the prediction purposes. A hybrid method combining ARMA and NAR is introduced to produce better results taking into account the advantages of both models.

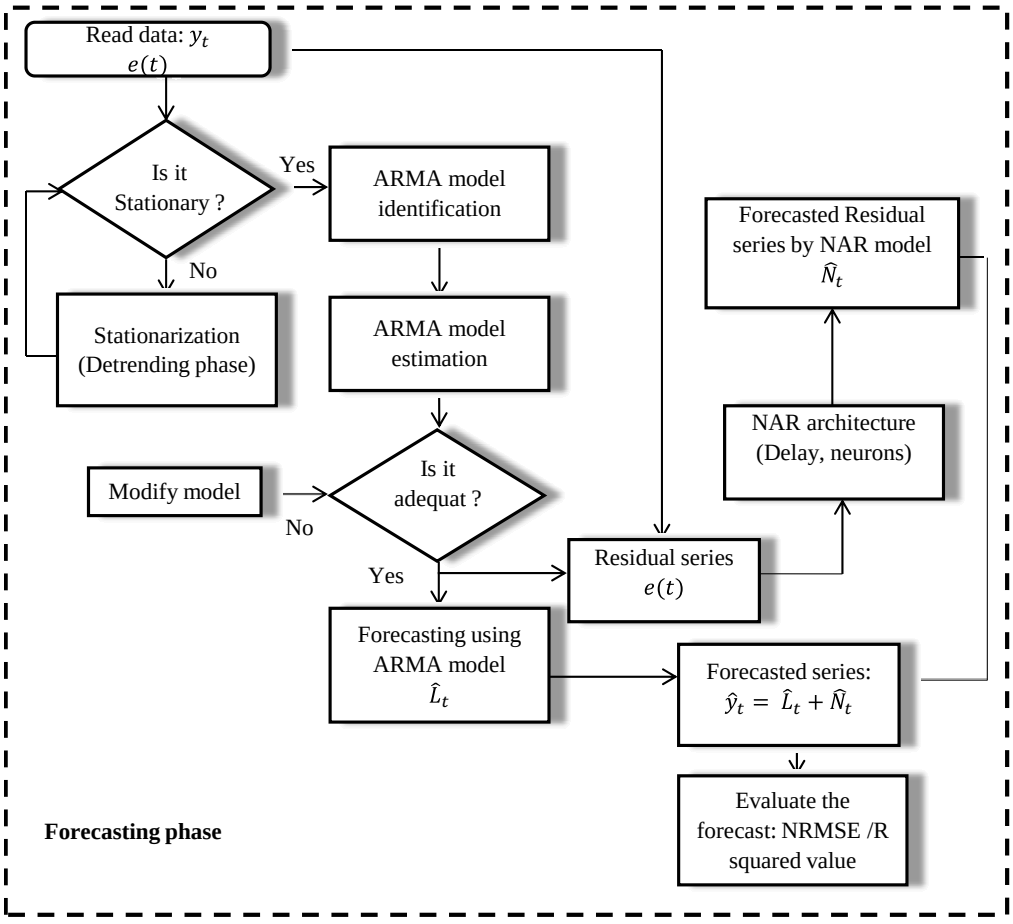

Figure 4.1: Flowchart of the proposed hybrid ARMA and NAR neural network models.

4.3.1 The ARMA model

ARMA model of order (p, q) can be viewed as linear filters for digital signal processing. It is of the form,

$$x_t = \sum_{i=1}^{p} \phi_i x_{t-i} + e_t + \sum_{j}^{q} \theta_j e_{t-j} \tag{4.1}$$

Where, $\phi_i (i = 1 \dots p)$ and $\theta_j (j = 1 \dots q)$ are constants representing the autoregressive AR, and the moving average MA parameters of order p, q, respectively. x_t is the actual value and e_t represents the Gaussian white noise with mean zero in time t. To find the parameters of Eq. (4.1), the Box and Jenkins (1970) method is then applied as follows.

4.3.1.1 Stationnarization

Time series modelling and forecasting requires explicitly a stationary time series (Makridakis et al., 1998; Voyant et al., 2013). The condition of stationarity (weakly- stationarity) implies a stable series, which means that the mean $\mu(t)$ and the covariance $cov(x_t, x_{t+h})$ stay constant over time, as expressed by the following equations,

$$E[x_t] = \mu(t) = \mu \tag{4.2}$$

$$cov[x_t, x_{t+h}] = E[(x_t - \mu)(x_{t+h} - \mu)] \tag{4.3}$$

Moreover, a strict stationary series needs a time invariant joint distribution of any observation of the processes. In addition, modelling and analysis of time series of classical models such as an ARMA model without testing the stationarity can present real practical problems (Ineichen, 2008). Hence, several methods were demonstrated in literature to check stationarity (non- stationarity). The most widely used one is the test of a unit root in the time series (Dickey and Fuller, 1981; Kwiatkowski et al., 1992). A unit root test is a test for a specific type of non- stationarity for autoregressive time series. The series is covariance stationary if and only if all the roots of the characteristic polynomials are outside the unit circle in the complex plane. In other words, if it exists a unit root, then the time series is not stationary. Otherwise, it is stationary. The most widely used method for testing unit root is the Augmented Dicky –Fuller (ADF) test (Dickey and Fuller, 1981), expressed by the following equation,

$$\Delta x_t = \alpha + \beta t + \gamma\ x_{t-1} + \sum_{j=1}^{p} (\delta_t \Delta x_{t-j}) + e_t \tag{4.4}$$

Where, α is a constant called a drift, β is the coefficient on a time trend, p is the lag order of the autoregressive process, γ is the coefficient presenting process root, δ_t represents the lag operator and et represents an independent identically distributes residual term with mean zero and variance $\sigma^2 = 0$.

The focus of testing is whether the coefficient γ equals to zero, what means that the original $x_1, x_2, \ldots x_n$ process has a unit root. Hence, the null hypothesis of $\gamma = 0$ (random walk process) was tested against the alternative hypothesis $\gamma < 0$ to obtain a stationary series.

The augmented Dickey–Fuller (ADF) statistic, used in the test, is a negative number. The stronger reject of the null hypothesis needs more negative test. In our simulation and using this stationarity test, we found that the solar radiation series is not stationary. Hence, a stationnarization step is needed. A phase of detrending was introduced to obtain a stationary series. In this phase, we simulated different models to fit the solar radiation time series. For each model, the residual series between simulated series and the original series had been tested using the ADF test. The most stationary series will be used in ARMA modelling. We have used in this work, the Jain model (Baig et al., 1991; Kaplanis, 2006), Baig et al. (1991), Kaplanis (2006), Kaplanis and Kaplani (2007), and high degree polynomial models were applied to remove trends of the solar radiation series as follow.

a) The Jain model

Jain (Baig et al., 1991; Kaplanis, 2006) proposed a Gaussian function to fit the recorded data and established the following relation for global radiation. Where,r_t is the ratio of hourly to daily global solar radiation, t is the true solar time in hours,m_d is the pick hour of the day and $\sigma^{"}$ is the standard deviation of the Gaussian curve.

$$r_t = \frac{1}{\sigma'' \sqrt{2\pi}} \exp\left[\frac{(t - m_d)^2}{2\sigma''^2}\right] \tag{4.5}$$

To simplify the calculation of the σ" values, Jain proposed the following equation

$$\sigma'' = 0.461 + 0.192 S_0 \tag{4.6}$$

Where, S_0 is the day length.

b) The Baig model

The Baig et al. (1991) model modified Jain's model to fit the recorded data during the starting and ending periods of a given day. In this model, r_t was estimated by,

$$r_t = \frac{1}{2\sigma'' \sqrt{2\pi}} \left\{ \exp\left[-\frac{(t - m_d)^2}{2\sigma''^2}\right] + \cos\left[180 \frac{(t - m)_d^2}{S_0 - 1}\right] \right\} \tag{4.7}$$

Several methods were found in the literature to estimate the standard deviation σ" using recorded data (Kaplanis, 2006). Bevington (1969) mentioned that the determination of σ"does not need any recorded data and it depends only on the day length, as expressed in Eq. (4.8),

$$\sigma'' = 0.246 S_0 \tag{4.8}$$

The r_t values are obtained to offer,

$$I_t = r_t.H_n \tag{4.9}$$

Where, I_t is hourly solar radiation and H_n is the daily solar radiation data.

c) Kaplanis model

Kaplanis (2006) proposed another model for estimating hourly global solar radiation that is,

$$r_t = \alpha^{'} + \beta^{'} \cos\left(\frac{\cos(2\pi(t - m_d)}{24}\right) \tag{4.10}$$

Where, α' and β' are parameters which have to be determined for any site and for any day (Kaplanis, 2006). However, this model presented some drawback in the estimation of solar radiation at noontime. Hence, Kaplanis and Kaplani (2007) proposed an improved model for more accuracy as presented in the following equation,

$$r_t = a + b\frac{e^{-\mu(N_d)\chi(t)}\cos(2\pi(t - m_d)/24)}{e^{-\mu(Nd)\chi(t=m_d)}} \tag{4.11}$$

where, a' and b' are determined in the same way as Eq. (4.10), $\mu(N_d)$ is the solar beam attenuation coefficient and$\chi(t)$ is the distance of the solar beam travels within the atmosphere at time t.

d) High order polynomial model

This model is represented as follows,

$$I_t = a_0t^0 + a_1t^1 + a_2t^2 + ... + a_nt^n \tag{4.12}$$

Nonlinear least squares regression analysis was used to fit Eq. (4.12) to the data for each hour of the day to obtain the values of the regression constants $a_0, a_1 \ldots a_n$ for each month of the year (Al-Sadah et al., 1990) . t represents the time.

4.3.1.2 Model identification

Model identification consists of specifying the appropriate structure, AR, MA or ARMA and orders of the model (Box and Jenkins, 1970). Identification is sometimes done by looking at the plots of the Autocorrelation function (ACF) and the Partial Autocorrelation function (PACF).

a) **Autocorrelation**

Measures the linear dependence or the correlation between x_t and x_{t-k}. (summarizes serial dependence)

$$\rho_k = \frac{Cov(x_t, x_{t-k})}{\sqrt{Var(x_t)Var(x_{t-k})}} = \frac{Cov(x_t, x_{t-k})}{Var(x_t)} \tag{4.13}$$

$$\rho_k = \frac{\sum_{t=k+1}^{n} (x_t - \overline{x})(x_{t-k} - \overline{x})}{\sum_{t=1}^{n} (x_t - \overline{x})^2} \tag{4.14}$$

Where $Var(xt) = Var(xt - k)$ for weakly stationarity process.

b) Partial Autocorrelation

Correlation between observations x_t and x_{t+k} after removing the linear relationship of all observations in that fall between x_t and x_{t+k}.

$$\begin{aligned} x_t &= \varphi_{0,1} + \varphi_{1,1}x_{t-1} + e_{1,t} \\ x_t &= \varphi_{0,2} + \varphi_{1,2}x_{t-1} + \varphi_{2,2}x_{t-2} + e_{2,t} \\ x_t &= \varphi_{0,3} + \varphi_{1,3}x_{t-1} + \varphi_{2,3}x_{t-2} + \varphi_{3,3}x_t + e_{3,t} \\ &\vdots \end{aligned} \tag{4.15}$$

Each $\varphi_{p,q}$ represent the lag-p of the PACF.

After determining the ACF and PACF functions, we can choose the (p, q) order of the ARMA model, as expressed in Table 4.1,

Akaike's Information Criterion (AIC) (Akaike, 1974) defined by Eq. (4.16), is another factor to decide ARMA (p, q) order. AIC provides a measure of the model quality by simulating the situation where the model is tested on a different data set. According to Akaike's theory, the most accurate model has the smallest AIC.

$$AIC = \log V + \frac{2d_e}{N_e} \tag{4.16}$$

Where V is the loss function, d_e is the number of estimated parameters and N_e is the number of values in the estimation data set.

Table 4.1: Different scenarios of choosing ARMA (p,q) parameters.

	AR (p)	**MA (q)**	**ARMA (p , q)**
ACF	Tails off	Cuts off	Tails off
PACF	Cuts off	Tails off	Tails off

4.3.1.3 Parameter estimation

Once the orders of ARMA model obtained, estimation of the model parameters is straightforward. The parameters are estimated using the maximum likelihood method (Box and Jenkins, 1970). This method requires an assumption on the distribution of the random vector $X = (X_1, \ldots, X_n)^T$. The estimates are usually found numerically using some iterative numerical optimisation routine.

The last step of the ARMA model building is the diagnostic checking of the model adequacy. The plotting of residuals examines the goodness of the obtained model.

4.3.2 The Nonlinear Autoregressive (NAR) neural network model

Artificial neural network (ANN) is a class of neural network represented by a mathematical model that is inspired by the biological nervous system; it is an intelligent system that has the ability to recognize time series patterns and nonlinear characteristics [See Appendix A.2]. Hence, it has been widely used for modelling dynamic nonlinear time series (Haykin, 1998). For that, various types of artificial neural networks were presented in literature among them Multilayer Perceptron (MLP), where the neurons are grouped into an input layer, one or more hidden layers and an output layer. Recurrent Neural Networks (RNN) such as layer recurrent networks (Haykin, 1998), Time Delay Neural Networks (TDNN) (Haykin, 1998; Wu and Chan, 2011) and NAR (Chow and Leung, 1996; Markham and Rakes, 1998).

In RNN, the outputs of a dynamic system depend not only on the present inputs, but also on the history of the systems stats and inputs. The NAR is a dynamic recurrent network based on a linear autoregressive model with feedback connections, including several layers of the network. The next value of the dependent output signal is regressed on previous values of the output signal. That it is used in multi-step ahead time series forecasting. The NAR model is based on the linear AR model, which is commonly used in time-series forecasting. The defining equation for the NAR network is,

$$\hat{y}(t) = f(y(t-1) + y(t-2) + \cdots + y(t-d)) \tag{4.17}$$

f is a nonlinear function, where the future values depend only on regressed d earlier values of the output signal. When using NAR network, the network performs only an one-step ahead prediction after it has been trained. Therefore, we need to use the closed loop network to perform a multi-step-ahead prediction and turn the network into a parallel configuration as shown in Fig. 4.2.

The output of the closed loop NAR network is expressed as follows

$$\hat{y}(t+p) = f(y(t-1) + y(t-2) + \cdots + y(t-d)) \tag{4.18}$$

Where p represents the forecasted steps in the future.

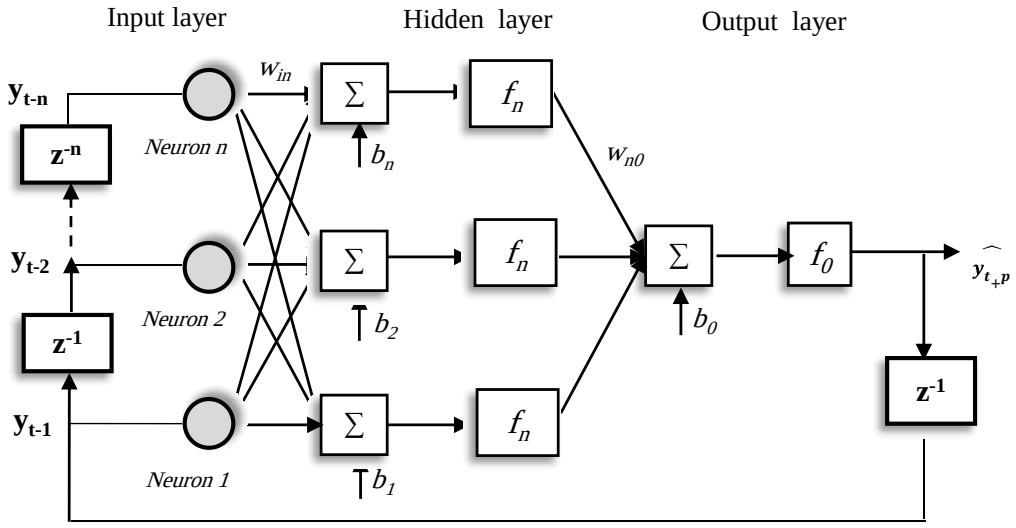

Figure 4.2: Structure of NAR neural network.

In addition, the RNN are based on training algorithms that used to adjust the weight values to get a desired output when certain inputs are given. Hence, various ways were presented to let a neural network learn such as supervised training where the input-output set is defined, and unsupervised learning that the output is undefined.

Back-propagation method is one of the most popular and widely used learning techniques for training RNN. It consists of minimizing the global quadratic error between the network output and the desired target by adjusting the weight values. The adjustment can be done using several algorithms such as Levemberg-Marquardt (Levenberg, 1944; MacQueen, 1967), Bayesian Regularization (MacKay, 1992) and scaled conjugate gradient (Moller, 1993) algorithms. The latter one is selected to train larger networks. Once the network is trained using the preselected inputs and outputs, all the synaptic weights are saved, and the network is ready to be tested on the new input information. Since the NAR network is very similar to a Multilayer Perceptron (MPL), a modified MLP neural network is applied in this work for predicting purposes.

4.3.3 The Hybrid ARMA and NAR Model

ARMA model represented linear models and has achieved great popularity since the publication of Box and Jenkins (1970). However, this method may not be adequate for nonlinear problems, contrary to the NAR networks that can solve the complexity of nonlinear systems. However, no one of them can use for both linear and nonlinear problems (Zhang, 2003; André Luis et al., 2008; Wu and Chan, 2011). Hence, the hybrid models were then applied taking the advantages of both ARMA and NAR models. We can simply detect the nonlinearity in a time series by using the surrogate data test for nonlinearity (Kugiumtzis, 2000). The hybrid model proposed in this work is based on Zhang (2003) model. It is assumed that time series is composed of a linear autocorrelation structure and a non-linear part,

$$y_t = L_t + N_t \tag{4.19}$$

Where, L_t denotes the linear part and N_t denotes the nonlinear part. The proposed method by Zhang (2003) consists of two stages. Firstly, ARMA model was used to predict future values at time t noted $\hat{L}_t$. The residual series between the time series and linear ARMA model series contains only nonlinear relationship. As expressed by the following equation,

$$v_t = y_t - \hat{L}_t \tag{4.20}$$

Where, v_t denote the residual at time t from the linear model.

Secondly, by modelling the residuals using NAR method, nonlinear relationships can be discovered. With n input nodes, the NAR model for the residuals will be,

$$v_t = f(v_{t-1}, v_{t-2}, ..., v_{t-n}) + e_t \tag{4.21}$$

Where, f is a nonlinear function determined by the neural network and e_t is the random error. The forecasted series from Eq. (4.20) is denoted $\hat{N}_t$. Then the combined forecast will be expressed by the next equation,

$$\hat{y}_t = \hat{L}_t + \hat{N}_t \tag{4.22}$$

4.4 Forecasting hourly solar radiation using hybrid *k*-means and NAR models

Stochastic models are based on the probability estimation that needs a full identification of the mathematical function, leads to a difficult forecasting of the solar radiation time series (Wu and Chan, 2011). Moreover, global solar radiation time series is a dynamical system that depends on some meteorological elements such as temperature, water vapor, suspend solids, cloud and water air condition that can represent nonlinear characteristics (Wu and Chan, 2011; Huang et al., 2013) . For that, we proposed a new hybrid method with the aim of forecasting hourly solar radiation time series taking into account the dynamic behaviour of this series. It based on the combination of one of the time series data mining technics namely the unsupervised k-means clustering algorithm and the nonlinear autoregressive neural network.

Data mining is the identification of interesting structure in the data, where the structure designates patterns of the data and relationships among regions of the data; it is a process of grouping similar elements gathered closely using unsupervised clustering methods such as k-means and c-means algorithms (Xu and Donald, 2005). Data mining techniques were used in a wide variety of fields for prediction. For example, in stock prices, meteorological data, customer behaviour, production control and other types of scientific data (Fu, 2011). Time Series Data Mining (TSDM) methodology (Sandberg and Xu, 1997) which is a fundamental contribution to the fields of time series analysis and data mining that allows a search, for valuable information on nonlinear problems such as solar radiation time series (Liao et al, 2012).

In addition , nonlinear autoregressive (NAR) approach, was considered a powerful tool for forecasting similar time series and understand the nonlinear characteristics of the solar radiation time series (Zhang, 2003; Mellit et al., 2009; Wu and Chan, 2011). Taking the advantages of both methods, the k-means approach (MacQueen, 1967) for clustering the solar radiation data to extract useful information and the NAR for forecasting purposes, a new method is proposed that combines an unsupervised k-means clustering algorithm and nonlinear autoregressive neural network.

At the first stage, the data obtained from the phase space reconstitution using Takens theorem (Takens, 1981) were clustered using k-means algorithm; clustering is a process of grouping an unlabelled set of examples into several clusters such that a similar pattern is associated with every cluster. The motivation of using the k-means approach in this work is due to its simplicity and also to the fact that the proposed methods do not require an advanced clustering algorithm. However, one of the vital issues of the k-means algorithm is the choosing of the appropriate number of clusters (Xu and Donald, 2005). Therefore, a silhouette function proposed by (Rousseeuw, 1987; Lletí et al., 2004) was used to obtain the best number of bunches.

At the second stage, the nonlinear autoregressive (NAR) neural network was applied for forecasting the solar radiation time series trying different architecture to get the best network structure. Combining those two methods presented better results for multi-step ahead prediction in long-term forecasting.

4.4.1 Methodology

The methodology of hybrid k-means and NAR neural network is shown in Fig.4.3 and it consists of the following steps,

1. Determine the minimum, appropriate, embedding dimension for phase space reconstruction for the time series (Kennel et al, 1992);

2. Identify regions of the reconstructed phase-space which has similar characteristics using k-means clustering algorithm;

3. For each cluster, train different NAR neural network to generate regional predictor for forecasting local regions;

4. Use the corresponding NAR neural network using different delay and neurons to generate a global prediction for the time series;

5. Reconstructed phase-space of the obtained time series from step 4, then use the appropriate k-means method to cluster the data using the same parameters used in step 1 and step 2;

6. To perform the forecast, assign each pattern from step 5 to the appropriate region obtained from step 3 using as a criterion the Euclidean distance:

- If the Euclidean distance between each region and the assigned pattern is small, then it is considered a better forecast, else return to step 4.

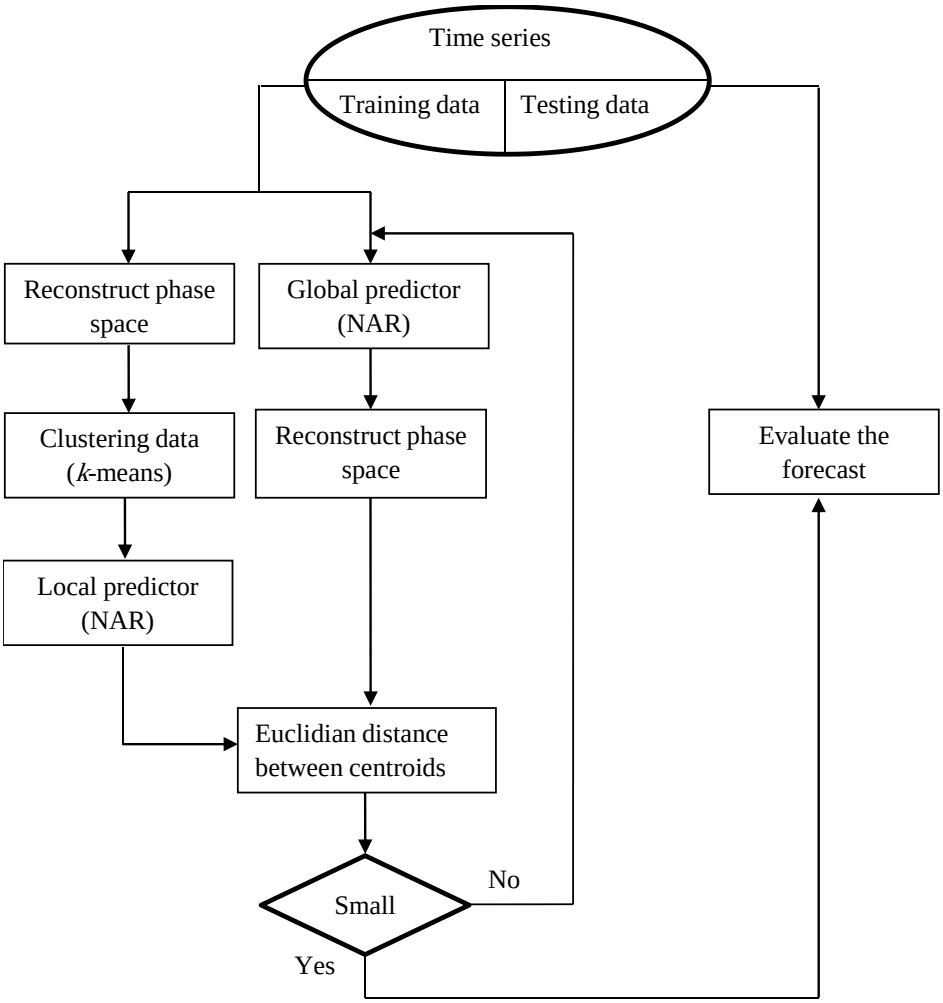

Figure 4.3: Flowchart of the proposed hybrid k-means and NAR neural network.

4.4.2 Phase space reconstruction (determining an appropriate embedding dimension)

Signals have been partitioned traditionally into two broadly defined classes, deterministic signals and stochastic processes. This classification, however, overlooks another important class of signals, known as chaotic signals that share attributes with both deterministic signals and stochastic processes (as the solar radiation time series). Chaotic signal generally has a very irregular waveform, but is generated by a deterministic mechanism.

One of the goals of time series analysis is to gain an understanding of the underlying dynamical system. However, this is a complicated task since the time series gives incomplete information about the dynamics. Only one variable is being measured in a time series, yet a dynamical system is often represented mathematically by several differential or difference equations. The task then becomes how to visualize the time series in such a way as to reveal the dynamics in the full phase space of the system.

Phase space reconstruction is devised using a delay coordinate embedding .From manipulations of the time series, delay coordinate embedding's allow to reconstruct vectors representing the dynamics in the phase space. The approach of phase-space reconstruction consists of embedding the time series into a higher-dimensional space to see the underlying dynamical system (Kennel et al, 1992). The most widely used version of embedding is a time delay embedding (Takens, 1981).

4.4.2.1 Time delay embedding

This method embeds a scalar time series $x(t_i)$ into m-dimensional space denoted $X(t_i)$, as expressed in Eq. (4.23),

$$X(t_i) = (x(t_i), x(t_i + \tau), ..., x(t_i + (m-1)\tau) \tag{4.23}$$

Where, $i = (1, 2, \ldots, M)$, τ is the delay time, m is the embedding dimension, and M is the number of embedded points in the m-dimensional space gave by Eq. (4.24). N is the total number of points in the time series and $X(t_i)$ is the embedded time series into an m-dimensional space

$$M = N - (m-1)\tau \tag{4.24}$$

Research shows that the reconstructed phase-space with appropriate m and τ has the same quality of the original dynamical system. Several methods were presented in the literature to provide an estimation of optimal embedding dimension and time delay for better phase space reconstitution of the original time series (Takens, 1981; Kim et al., 1999; Ragulskis and Lukoseviciute, 2009). In this work, the mutual information method proposed by Fraser and Swinney (1986) is used to set the delay coordinates. This method is summarized as follows.

a) Determine of time delay (τ)

The current methods to determine the time delay τ include autocorrelation function and the mutual information method. That can be used to analyse linear or nonlinear systems. The description of this method will be discussed in what follows.

a.1) Mutual information method

a.1.1) Definition

Mutual information is a measure of the dependence between two variables. If the two variables are independent, the mutual information between them is zero. If not, then they are strongly dependent. The difference between mutual information and the correlation function is that the first measures of the general dependence, while, the correlation function measures the linear dependence, and mutual information is a better quantity than the correlation function to measure the dependence. To understand how the mutual information method works. We

have to introduce first the concept of entropy (Fraser and Swinney , 1986).

a.1.2) ENTROPY

The average amount of information gained from a measurement that specifies is defined to be the entropy $H(X)$, which is a measure of uncertainty of a random variable. With support χ and probability mass function $p(x) = P_r\{X = x\}, x \in \chi$, the entropy $H(X)$ of a discrete random variable X is defined by

$$H(X) = -\sum_{x\in\chi} p(x)\log p(x) \tag{4.25}$$

a.1.2.1) Joint entropy and conditional entropy

We have defined the entropy of a single random variable in the previous section. We now extend the definition to a pair of random variables. There is nothing really new in this definition because (X, Y) can be considered a single vector-valued random variable.

Definition: The joint entropy $H(X, Y)$ of a pair of discrete random variables (X, Y) with a joint distribution $p(x, y)$ is defined as

$$H(X,Y) = -\sum_{x\in\chi}\sum_{y\in\gamma} p(x,y)\log p(x,y) \tag{4.26}$$

We also define the conditional entropy of a random variable given another as the expected value of the entropies of the conditional distributions, averaged over the conditioning random variable.

Definition: the conditional entropy is defined as:

$$\begin{aligned} H(Y\,|X\,) &= -\sum_{x\in\chi} p(x)H(Y\,|X=x\,) \\ &= -\sum_{x\in\chi} p(x)\sum_{y\in\gamma} p(y\,|x\,)\log p(y\,|x\,) \\ &= -\sum_{x\in\chi}\sum_{y\in\gamma} p(x,y)\log p(y\,|x\,) \end{aligned} \tag{4.27}$$

The naturalness of the definition of joint entropy and conditional entropy is exhibited by the fact that the entropy of a pair of random variables is the entropy of one plus the conditional entropy of the other.

Theorem: (Chain rule)

$$H(X,Y) = H(X) + H(Y\,|X\,) \tag{4.28}$$

a.1.3) Mutual information

Consider two random variables X and Y with a joint probability mass function $p(x, y)$ and marginal probability mass functions $p(x)$ and $p(y)$.The mutual information $I(X, Y)$ is the relative entropy between the joint distribution and the product distribution:

$$I(X,Y) = \sum_{x\in\chi}\sum_{y\in\gamma} p(x,y)\log\frac{p(x,y)}{p(x)p(y)} \tag{4.29}$$

The method of mutual information is a way to determine useful delay coordinates for plotting attractors. The idea of delay coordinates is simple. If we can only observe one variable from a system, $X(t)$ and we want to reconstruct a higher-dimensional attractor, we can consider $(X(t), X(t+\tau), \ldots, X(t+n\tau))$ producing a $(n+1)$ dimensional coordinate which can be plotted. It is important to choose a good value for τ, the delay. If the delay is too short, then $X(t)$ is very similar to $X(t+\tau)$ and when plotted all the data stays near the line $X(t) = X(t+\tau)$. If the delay is too long, then the coordinates are essentially independent and no information can be gained from the plot.

The method of mutual information for finding the delay τ was proposed by Fraser and Swinney (1986). This method is expressed as follows,

- Calculate the mutual information of $x(t)$ and $x(t-\tau)$ for given τ

$$I(x(t), x(t-\tau)) = \sum_{x\in\chi}\sum_{y\in\gamma} p(x(t), x(t-\tau))\log\frac{p(x(t), x(t-\tau))}{p(x(t))p((t-\tau))} \tag{4.30}$$

- Draw the mutual information function $I(t)$ for given τ;
- The optimum time delay τ is the first minimum of the mutual information function.

b) Determine of embedding dimension (m)

To determine the optimal embedding dimension m, different methods such as the box–counting dimension (Mandelbrot, 1967), false nearest neighbours (Kennel et al, 1992), small-window solution (Kugiumtzis, 1996) and C–C methods (Kim et al., 1999) were proposed in literature. We have chosen in our work the false nearest neighbour method because of its simple implementation and accuracy.

b.1) False nearest Neighbours method

It consists of learning how many dimensions are sufficient to embed a particular time series (Kennel et al, 1992); for a given embedding dimension, this method determines the nearest neighbour of every point in a given dimension, then checks to see if these are still close neighbours in one higher dimension. The percentage of False Nearest Neighbours should drop to zero when the appropriate embedding dimension has been achieved.

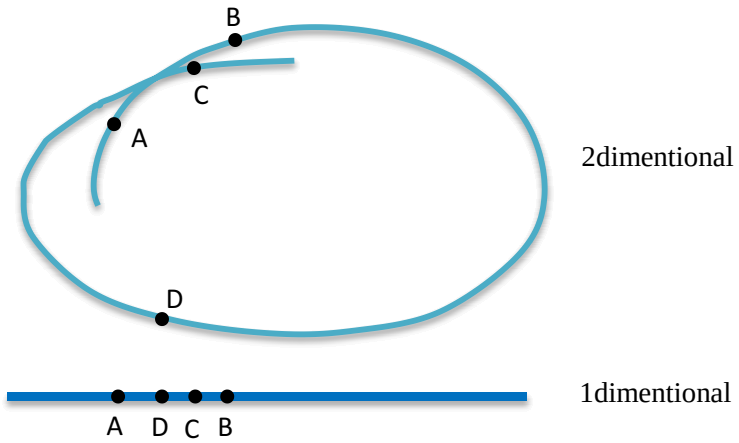

Figure 4.4: An example of false nearest neighbours.

The following example explains the false nearest neighbour method. Consider Fig.4.4, each of the points A, B, C and D in Fig.4.4 resides on a one-dimensional curve. Embedded in 2 dimensions, point C is the closest neighbour to point A. In a one-dimensional embedding, point D is incorrectly identified as the nearest neighbour. Yet neither C nor D is the closest neighbour to A on this curve. Only in three dimensions are there no self-crossings of this curve, and point B is shown to be the nearest neighbour of A.

Points A, B, C, and D lie on a one-dimensional curve. In two dimensions, points A and C appear to be nearest neighbours. In one dimension, point D appears to be the nearest neighbour of A. In three dimensions the curve would not intersect itself, and it could be seen that B is the nearest neighbour to A.

Explicitly, the original criteria for identification of false nearest neighbours are as follows:

Consider each vector $(\bar{Y_i}) = (X_i, X_{i+\tau}, X_{i+2\tau}, \ldots X_{i+(m-1)\tau})$, in a delay coordinate embedding of the time series with delay τ and embedding dimension m. Look for its nearest neighbour $(\bar{Y_j}) = (X_j, X_{j+\tau}, X_{j+2\tau}, \ldots X_{j+(m-1)\tau})$. The nearest neighbour is determined by finding the vector $(\bar{Y_j})$ in the embedding which minimizes the Euclidean distance expressed in the following equation

$$R_i = \left\| \overline{Y_i} - \overline{Y_j} \right\| \tag{4.31}$$

Now consider each of these vectors under a $m+1$ dimensional embedding;

$$\begin{aligned} \overline{Y_i'} &= (X_i, X_{i+\tau}, X_{i+2\tau}, ..., X_{i+(m-1)\tau}, X_{i+m\tau}) \\ \overline{Y_j'} &= (X_j, X_{j+\tau}, X_{j+2\tau}, ..., X_{j+(m-1)\tau}, X_{j+m\tau}) \end{aligned} \tag{4.32}$$

In a $(m+1)'$dimensional embedding, these vectors are separated by the Euclidean distance,

$$R'_{\prime_i} = \left\| \overline{Y_i'} - \overline{Y_j'} \right\| \tag{4.33}$$

The first criterion proposed by Kennel et Al. (1992) to identify a false nearest neighbour.

Criterion 1

$$\sqrt{\left(R'_{\prime_i} - R^{2'}_{\prime_i}\right) R^{2'}_{\prime_i}} = \frac{|X_{i+m\tau} - X_{j+m\tau}|}{R_n} > R_{TOL} \tag{4.34}$$

T_{tol} is a unit less tolerance level for which Kennel et al. (1992) suggests a value of approximately. This criterion is meant to measure if the relative increases in the distance between two points when going from i to $i+1$ dimension is large. A value 15 was suggested based upon empirical studies of several systems, although values between 10 and 40 were consistently acceptable.

Criterion 2

$$\frac{R'_{\prime_i}}{R_A} > A_{TOL} \tag{4.35}$$

This was introduced to compensate for the fact that portions of the attractor may be quite sparse. In those regions, near neighbours are not actually close to each other. Here, R_A is a measure of the size of the attractor, for which Kennel et al.(1992) use the standard deviation of the data,

$$R_A = \sqrt{< (x - < x >) >} \tag{4.36}$$

If either Eq.(4.34) or Eq. (4.35) hold $(\bar{Y_j})$, then is considered a false nearest neighbour of $(\bar{Y_i})$. The total number of false nearest neighbours is found, and the percentage of nearest neighbours, out of all nearest neighbours, is measured. An appropriate embedding dimension is one where the percentage of false nearest neighbours identified by either method falls to 0.

4.4.3 *k*-means algorithm

k-means is one of the quickest and simplest unsupervised learning algorithm to perform clustering; the method consists of classifying a given data into fixed k clusters (MacQueen, 1967; Spath, 1985). The main idea is to define k centroids for each cluster; those centroids should be placed as much as possible far away from each other. In the first step, each point of the data set is connected to the nearest cluster centroid by calculating the squared Euclidian distance between data point $x_i(j)$ and the cluster centre c_j, as expressed by Eq. (4.37)

$$\left\| x_i^{(j)} - c_j \right\|^2 \tag{4.37}$$

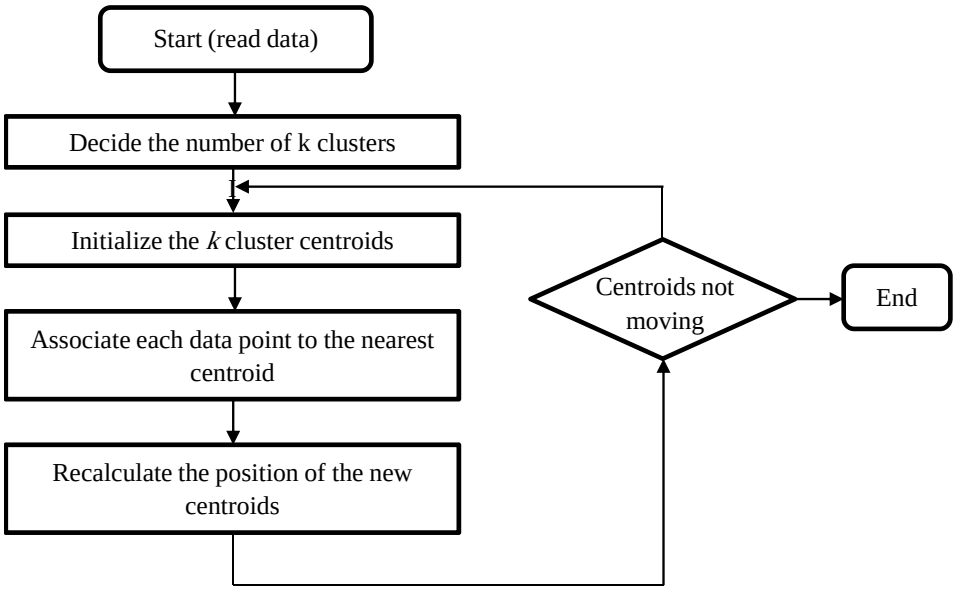

Figure 4.5: Flowchart of k-means algorithm.

The second step consists of re-calculating the location of the new k centroid. Repeating the first and second steps until the centroids no longer move produced a separation of the objects into groups from which the objective function J expressed in Eq. (4.38) is minimized.

$$J = \sum_{j=1}^{k} \sum_{i=1}^{n} \left\| x_i^{(j)} - c_j \right\|^2 \tag{4.38}$$

A summary of k-means algorithm is shown in Fig. 4.5.

4.4.3.1 Selection of the number of clusters

The k-means algorithm is based on the selection of the optimum number of clusters (Spath, 1985; Xu and Donald, 2005). The choosing of many clusters does not necessarily imply having a better quality of information. On the other hand, a small number of clusters produce unclear results that could muddle the pattern recognition up.

The Silhouette function (Rousseeuw, 1987) expressed in Eq. (4.39) provides a measure of the cluster separation that can be used for interpretation and validation of clustered data. The motivation of using this technique that is simple to read, and provides a graphical representation that allows the testing of various sets of clusters. It consists of calculating the average dissimilarity $a(i)$ of the i^{th} datum within the same cluster. This criterion can be interpreted as how well-matched the i^{th} datum to those clusters are assigned to it. The next step, is to determine the average dissimilarity of the i^{th} data with the data of another cluster. Then, the lowest average is denoted by $b(i)$.

$$s(i) = \frac{b(i) - a(i)}{\max\{a(i), b(i)\}} \tag{4.39}$$

From this equation, it is clearly shown that if $s(i)$ is close to 1 then $a(i) << b(i)$, which means that the values of $a(i)$ are too small, which indicate that the i^{th} datum is well matched for its cluster. Furthermore, a large $b(i)$ implies that i^{th} datum is badly matched to its neighbouring cluster. Thus, a $s(i)$ close to 1 means that the datum is appropriately clustered. If $s(i)$ is close to minus one, then by the same logic, we can see that i would be more appropriate if it is clustered in its neighbouring cluster. An $s(i)$ near zero means that the datum is on the border of two natural clusters.

A successful clustering has a high mean silhouette value $s(i)$. Lletí et al. (2004) considered a 0.6 silhouette value for all clusters as a good result. However, in real-time series, it is almost impossible to achieve this. Hence, a compromise among silhouette plots and averages is used to determine the natural number of clusters within data set.

4.5 Simulation results

Our goal of the simulation is to select the best model for multi-hour ahead forecasting of the future values of hourly global solar radiation data, using two different hybrid models. To evaluate the quality of the proposed model, the root mean square error (RMSE) and normalized root means square error (NRMSE) are chosen as the forecasting accuracy measures. Lewis (1982) was considered that if the NRMSE values are between 0.2 and 0.5, the forecasted model is considered good model. Wu and Chan (2011) , and Kostylev and Pavlovski (2011) found that the best performing model on an hourly time scale had an NRMSE of 0.17 for mostly clear days and 0.32 for mostly cloudy days. In addition, the R squared value gave by Eq. (4.40) was used as metric to judge the goodness of the forecast.

$$R^2 = 1 - \left(\frac{\sum_{i=1}^{n} \left(I_{i,measured} - I_{i,predicted}\right)^2}{\sum_{i=1}^{n} \left(I_{i,measured} - \overline{I_{i,measured}}\right)^2} \right) \tag{4.40}$$

Moreover, an important task of the proposed method is chosen the proper training and testing data set to avoid the overheating problem. Hence, the k-fold cross validation method (Kohavi, 1995) has been used to check the performances. In this method, the data set is divided into k subsets, each time, one of the k subsets is used as the test set and the other *k-1* subsets are put together to form a training set. Then, the average error across all k trials is computed until we reached the best training and testing data set (Klipp et al., 2008).

4.5.1 Forecasting using hybrid ARMA and NAR

We use in this part, hourly global horizontal solar radiation time series for the year of 2010 for the site of Oran, Algeria (35.6911° N, 0.6417° W). The data were collected from the National Meteorological Office of Algeria. We ignored data between 6:00 and 20:00 o'clock because there is no solar radiation measured during this period.

Using the k-fold cross validation method the data are divided into two sets, training set (from 1^{st} January 2010 to 31^{st} October 2010) that represent 4530 hours, and test data set

(from 1^{st} November 2010 to the 31^{st} December 2010) that represent 915 hours (prediction horizon) .The training data set is used exclusively for model development then the test sample is used to evaluate the established model.

4.5.1.1 Stationnarization phase

In this phase, the trends obtained from Jain (Baig et al., 1991; Kaplanis, 2006), Baig et al. (1991), Kaplanis (2006), Kaplanis and Kaplani (2007) and high degree polynomial models are simulated against the measured data to find the suitable model for being used in the prediction phase. For that, the monthly hourly average global solar radiation time series is then applied to the site of Oran, 2010. Fig. 4.6 shows the monthly average hourly global horizontal solar radiation of January 2010 in W/m^2 against the estimated models. We ignored data between 6:00 and 20:00 o'clock because there is no solar radiation measured during this period.

For choosing the proper model, we have to check the stationarity of the series. Thus, the Augmented Dickey and Fuller (ADF) test was applied to the residual series between measured and simulated data from different models. If the test result is below the critical values that means we should reject the null hypothesis and the time series is stationary. Otherwise, it is not stationary. The statistical power is the probability tests to reject a false null hypothesis (Dickey and Fuller, 1981). The test results are presented in Table 4.2.

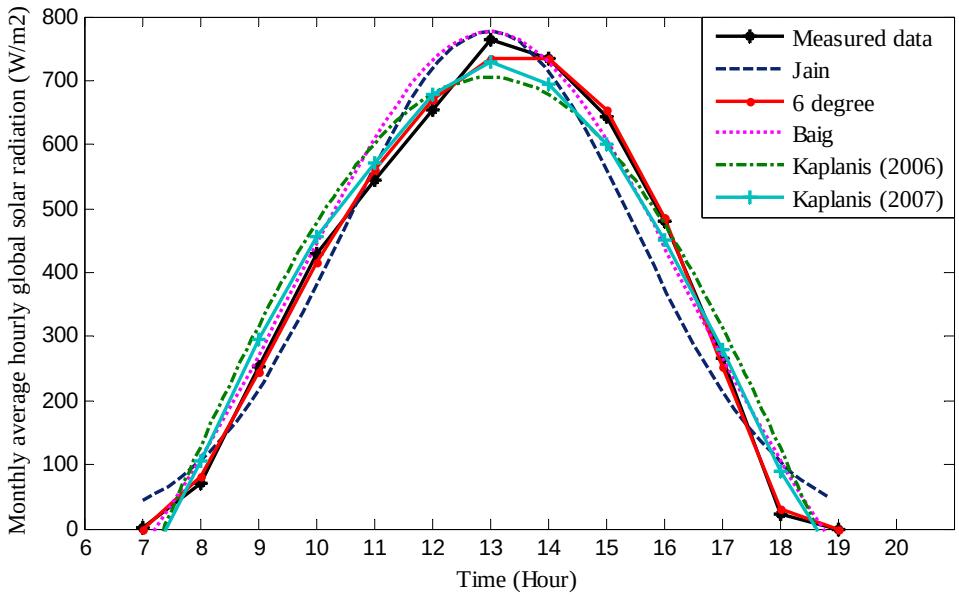

Figure 4.6: Comparison between the measured monthly average hourly global horizontal solar radiation data of January 2010 from the site of Oran, Algeria, and the Jain (Baig et al., 1991; Kaplanis, 2006), Baig et al. (1991), Kaplanis (2006), Kaplanis and Kaplani (2007) and 6 degree polynomial models.

Table 4.2: ADF test test for the detrending models.

Detrending models	Statistical power	Significant level	Test results	Critical value
Jain's model	0.0428	0.05	-2.0389	-1.958
Baig's model	0.0126	0.05	-2.658	-1.958
S.Kaplanis (2006) model	0.0117	0.05	-2.6918	-1.958
Kaplanis and Kaplani (2007) model	0.0097	0.05	-3.4307	-1.958
6 degree polynomial model	0.001	0.05	-4.3232	-1.958

Table 4.3: The RMSE and NRMSE between actual data and the other different models.

	Error (RMSE)	Error (NRMSE)
Jain's model	55.2255	0.149
Baigs's model	42.8663	0.1146
S.Kaplanis(2006) model	37.1987	0.1013
Kaplanis and Kaplani (2007) model	22.581	0.0735
6 degree polynomial model	13.3939	0.0358

The performances of the five simulated models to predict monthly average hourly global solar radiation from mean daily global solar radiation are evaluated using the root mean square error (RMSE) and normalized root mean square error (NRMSE), The results of the statistical comparison of the simulated models are presented in Table 4.3.

From Fig. 4.6 and Table 4.3, it is clearly shown that Jain's model fits the monthly hourly average global solar radiation series, but it presents a big NRMSE error versus other models that equal to 0.1490 especially at the beginning and at the end of the series. Hence, since Baig's model is based on Jain's model, it was used to overcome this error. However, it still represents some lags with NRMSE equal to 0.1146.For the Kaplanis (2006) model, it used a different method than Jain and Baig models, but still had a big NRMSE equal to 0.1013. Using the improved approach by Kaplanis and Kaplani (2007), the NRMSE was reduced to 0.0735. The 6-degree polynomial model seems the best choice to fit the solar radiation time series, which represents the lowest NRMSE error equal to 0.0358.

In addition, from the results of Table 4.2, we can see that the test results are below the critical values. Therefore, the residual series of all those models was considered stationary. The statistical power of 6-degree polynomial model is the highest one, which implies that the residual series between this model and measured data has the lowest probability to incorporate a unit root. Hence, it is considered the most stationary residual series.

Since higher degree polynomial model provided the best performance in both detrending and fitting phases, we used this model for ARMA model in the detrending phase for predicting future values.

4.5.1.2 Forecasting phase

The hybrid ARMA-NAR method was applied to do the forecasting. First, ARMA model is used for predicting hourly global solar radiation time series, then the residual between ARMA and measured series is forecasted using NAR model. The obtained forecast is added to the one of ARMA models.

In the detrending phase, we used a 6-degree polynomial model to get a stationary residual series. From the autocorrelation, partial correlation and the AIC test of the residual series we established that the ARMA (5, 7) is the suitable model to use it in the simulation. In addition, different algorithms of training and sets of delays and neurons were tested in the simulation of the nonlinear autoregressive neural network model. We found that the use of 31 delays and 10 neurons in the hidden layer with the Lavenberg-Marquardrt training method gives the fastest convergence with the smallest forecasting error.

The simulation results of the hybrid model to forecast hourly global solar radiation for the year of 2010 are presented in Fig. 4.7 (a); the blue line represents the measured hourly global horizontal solar radiation and the red dot one is the forecasted series by the hybrid model. In addition, Figs. 4.7 (b-c) represent the comparison results for the months of November 2010 and December 2010 respectively, and Fig.4.7 (d) for the first two weeks of November 2010. The blue line represents measured data, and the red dot line is the forecasted data.

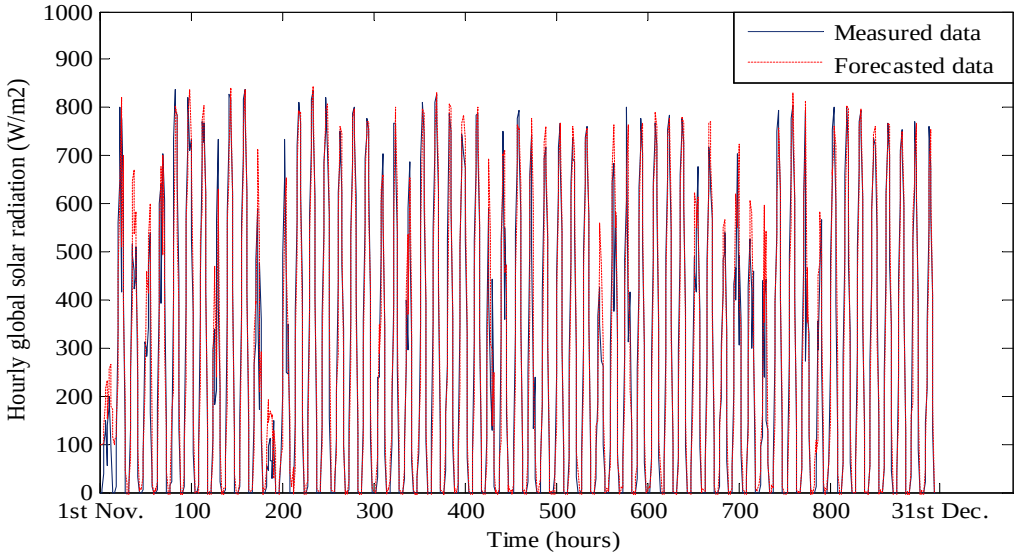

(a) : Comparison between measured hourly global horizontal solar radiation data (from 1^{st} November 2010 to 31^{st} December 2010) and the forecasted using hybrid model.

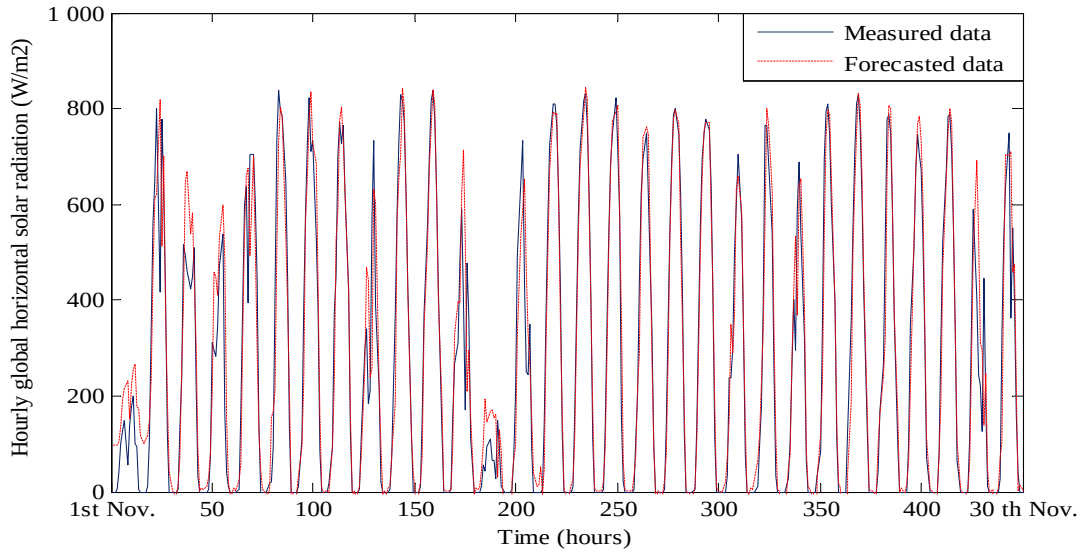

(b) : Comparison between measured hourly global horizontal solar radiation (from 1^{st} November 2010 to the 30^{th} November 2010) and forecasted by proposed model.

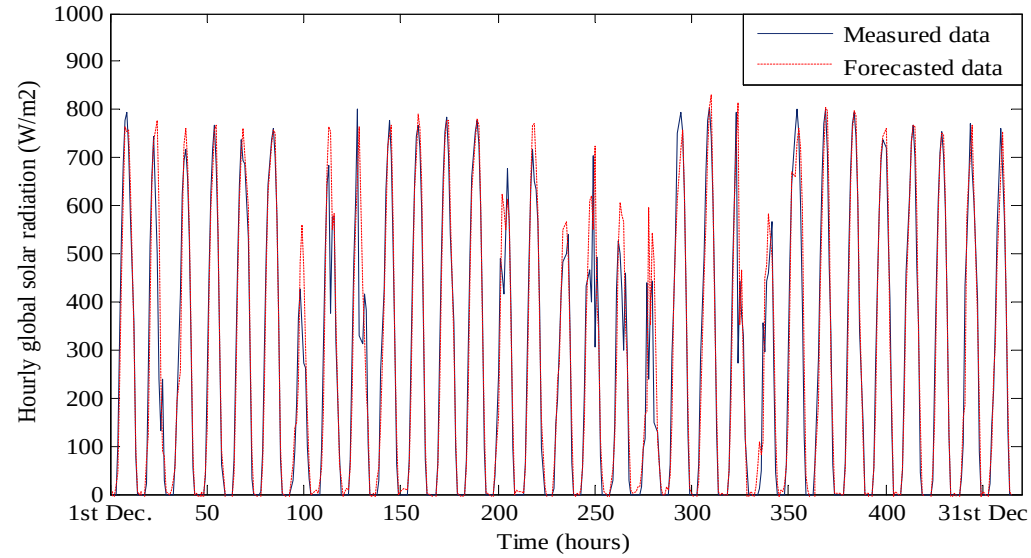

(c) :Comparison between measured hourly global horizontal solar radiation (from 1^{st} December 2010 to the 31^{st} December 2010) and forecasted by proposed model.

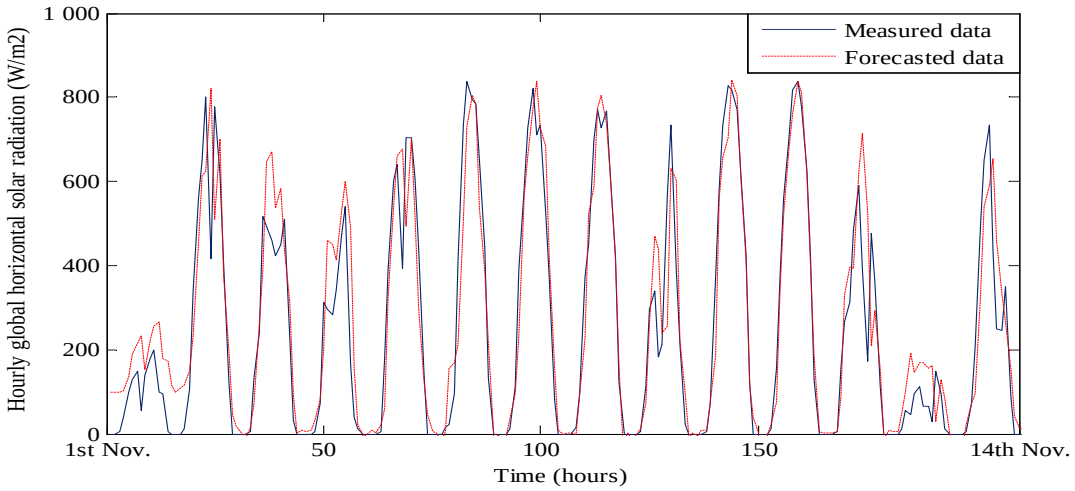

(d) : Comparison between measured hourly global horizontal solar radiation (from 1^{st} November 2010 to the 14^{th} November 2010) and forecasted by proposed model.

Figure 4.7: *(a - d),* Comparison between measured and forecasted solar radiation data for different periods

The comparisons and performance of the forecasting hourly global horizontal time series using a hybrid model have been evaluated by calculating the RMSE errors between the actual data and forecasted one for the period of 1^{st} November 2010 to 31^{st} December 2010 (915 hour-step ahead).

Moreover, the quadratic error between measured and simulated hourly global solar radiation using the proposed method is demonstrated in Fig. 4.8.

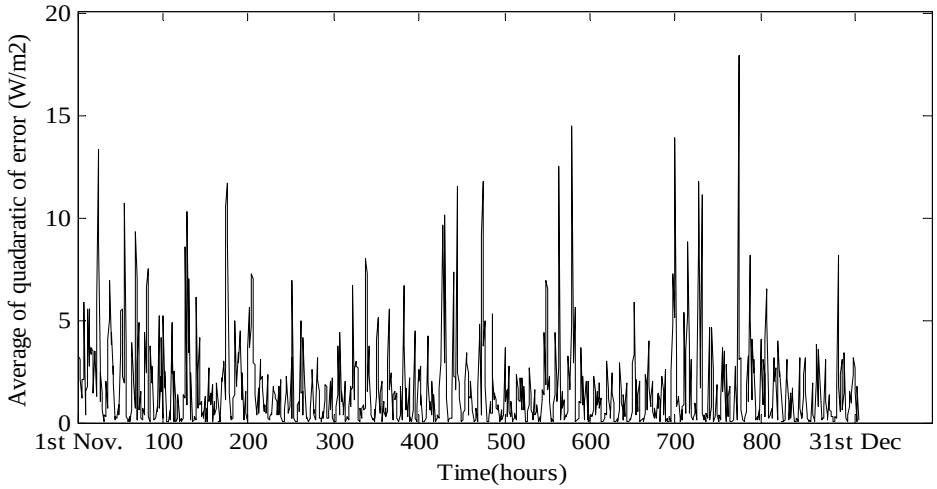

Figure 4.8: The average of quadratic error between measured global horizontal solar radiation (from 1^{st}November to 31^{st} December 2010) and the forecasted using hybrid model.

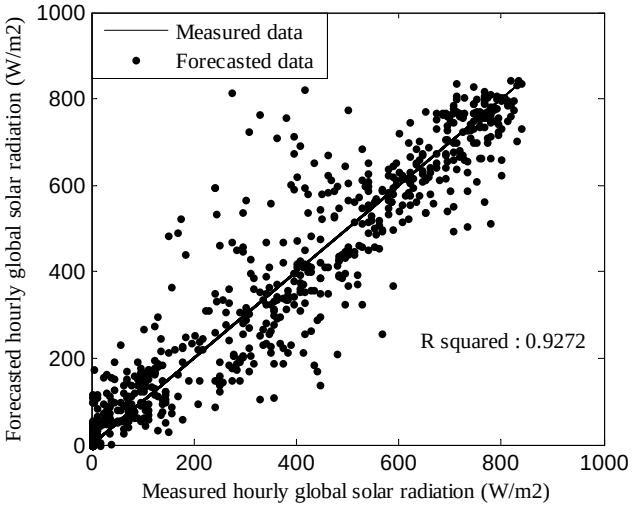

Figure 4.9: The measured hourly global horizontal from (1^{st} November 2010 to 31^{st} December 2010) versus forecasted time series using the hybrid model.

In addition, Fig. 4.9 represents the measured time series versus the forecasted one.

From Figs. 4.7 (a-d), Fig. 4.8 and Fig.4.9 it is clearly shown that the hybrid model forecasted in good manner the measured solar radiation time series. From Fig.4.7 (a), the total RMSE is equal to 71.82 W/m^2 and the NRMSE is 0.2103. With an R-squared value equal to 0.9272. Nevertheless, we can ensure that the comparison between forecasted and measured solar radiation time series presents some lag due to the presence of clouds.

4.5.2 Forecasting using hybrid k-means and NAR models

In this part, we are interested in multi-hour ahead forecasting of hourly global solar radiation time series using a combination of clustering techniques and nonlinear autoregressive neural networks. We use hourly solar radiation for Oran, 1996. The data were collected from the National Meteorological Office of Algeria for the site of Oran. We used only the data from sunrise to the sunset of the day. Using the k-fold cross validation method the data were divided into two sets, training set (from 1^{st} January 1996 to 31^{st} October 1996) that represent 4530 hours, and test data set (from 1^{st} November 1996 to the 31^{st} December 1996) that represent 915 hours.

The first step in the analysis and prediction of this time series is the choice of an appropriate time delay τ and the determination of the embedding dimension, m. To select τ an established approach is to use the value that yields the first minimum of the mutual information function; a time delay of 1 and an embedding dimension equal to 2 were found experimentally using mutual information and false nearest neighbour methods to be the right choices for this time series.

The next step is to apply the k-means algorithm for clustering high dimensional training data set obtained from phase space reconstitution in the previous step. At each step, different numbers of clusters were examined; the silhouette function was calculated for the determina-

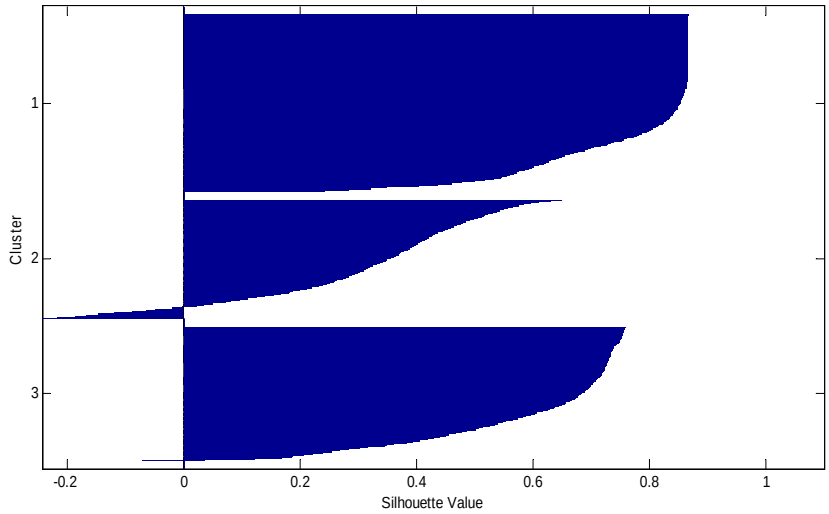

Figure 4.10: Silhouette values with 3 clusters for hourly global horizontal solar radiation data for Oran, Algeria (from1st January 1996 to 31st October 1996).

tion of the right number of clusters. The metric used is the squared Euclidean distance. We had plotted different silhouette functions for hourly global horizontal solar radiation with a different number of clusters, and we established that the choosing of 3 clusters to be the best choice as shown in Fig. 4.10.

From Fig.4.10, it is clearly shown that most of the mean silhouette values are high. However, it is nearly impossible to arrive at a value of 0.6 for all clusters and not having negative values as the case of the second cluster. Thus, the appropriate number of clusters is usually taken when the graphical representation provides satisfactory results that mean when most of the silhouette values are high as expressed in Lletí et al. (2004). The obtained 3 cluster groups the solar radiation time series into three categories, high values of solar radiation, which represents the noon hours, medium values that represents the day hours from 9 to 11 o'clock (or sky with medium clouds) and low solar radiation value, which represents hours of sunrise and sunset (or the presence of clouds).

After that, the NAR method with different architectures was applied to generate local predictor for each cluster that provides what we called regions for the three clusters in the future (these regions represent future windows for the forecasted data).Then, the NAR method with different time delay and neurons was applied to create a global predictor of the data. The use of 25 delays with 13 neurons was found as the right choice for forecasting purpose. A comparison between the centroids of the global forecasted series and centroids of the regions can show the goodness of the forecast; the two centroids of each cluster region and forecasted series should be near each other.

The results of phase space reconstitution of the forecasted regions and clusters for hourly global horizontal solar radiation at time t and $t+1$ considering a time delay of 1 and embedding dimension of 2 are presented in Fig.4.11.

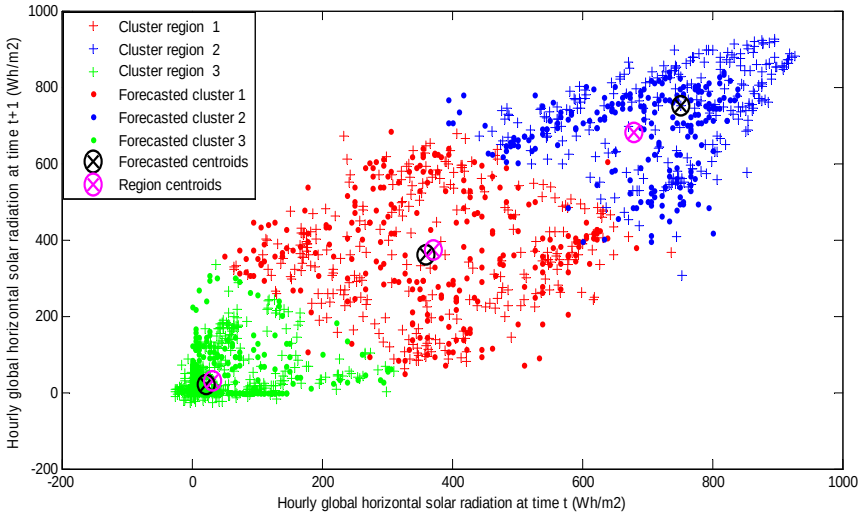

Figure 4.11: Space phase reconstitution for the forecasted regions and clusters of hourly global horizontal solar radiation testing data (from 1^{st} November 1996 to the 31^{st} December 1996).

The plotted points represent the phase space of the solar radiation time series at time t and $t+1$. We can visualize clearly the three kinds of clusters with low, medium and high solar radiation values. In addition, most of the points of each forecast cluster are in the right regions, the centroids are near each other, which means that the obtained forecast is acceptable.

The comparison between the forecasted hourly global horizontal solar radiation data tested one is shown in Fig.4.12 (a). In addition, Figs. 4.12 (b-c) represent the comparison results for the months of November 1996 and December 1996 respectively. The blue line represents measured data, and the red one is the forecasted data.

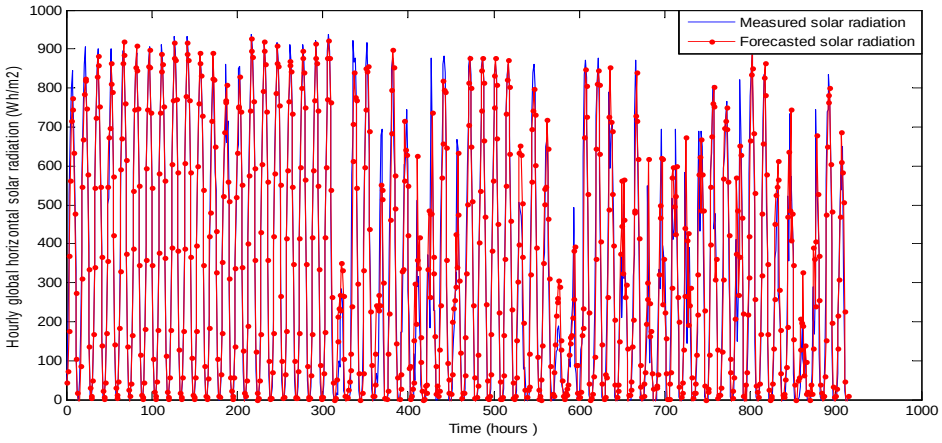

(a) : Comparison between measured hourly global horizontal solar radiation (from 1^{st} November 1996 to the 31^{st} December 1996) and forecasted by proposed model.

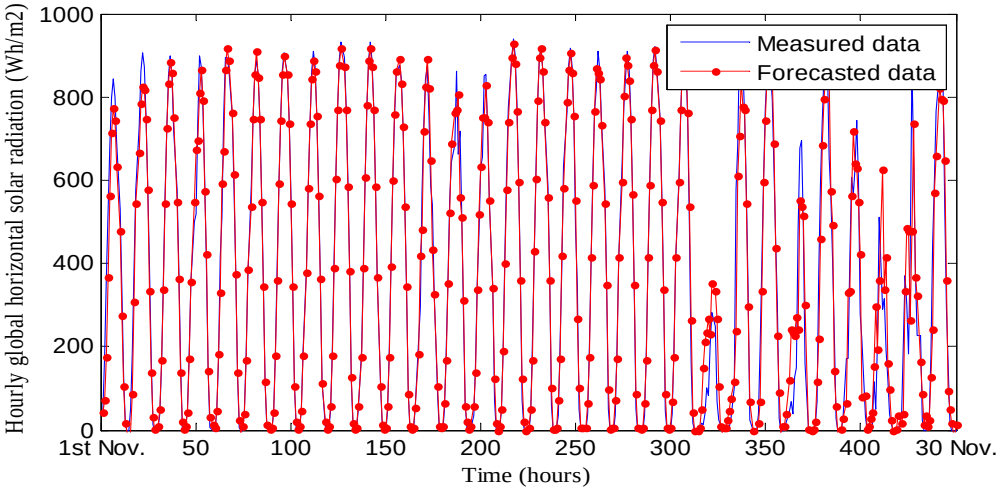

(b) : Comparison between measured hourly global horizontal solar radiation (from 1^{st} November 1996 to the 30^{st} November 1996) and forecasted by proposed model.

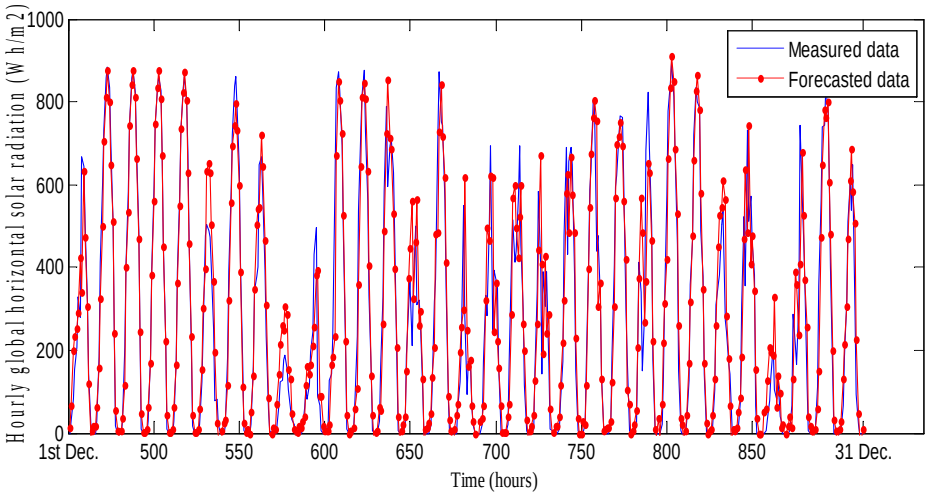

(c) : Comparison between measured hourly global horizontal solar radiation (from 1st December 1996 to the 31st December 1996) and forecasted by the proposed model.

Figure 4.12: (a - c) Comparison between measured and forecasted solar radiarion data using hybrid k- means and NAR models.

Moreover, the performance of the forecasted hourly global horizontal time series has been evaluated by calculating the RMSE errors between the actual data and forecasted one for the period of 1^{st} November 1996 to 31^{st} December 1996. The quadratic error between measured and simulated hourly global solar radiation using the proposed method are presented in Fig. 4.13. In addition, Fig. 4.14 represents the measured time series versus the forecasted one.

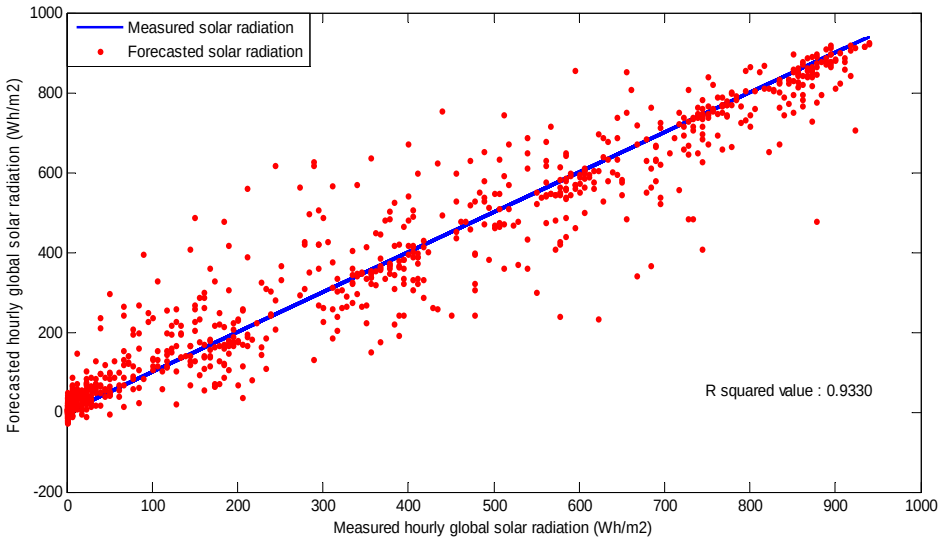

Figure 4.14: The measured hourly global horizontal from (1^{st} November 1996 to 31^{st} December 1996) versus forecasted time series using the proposed model.

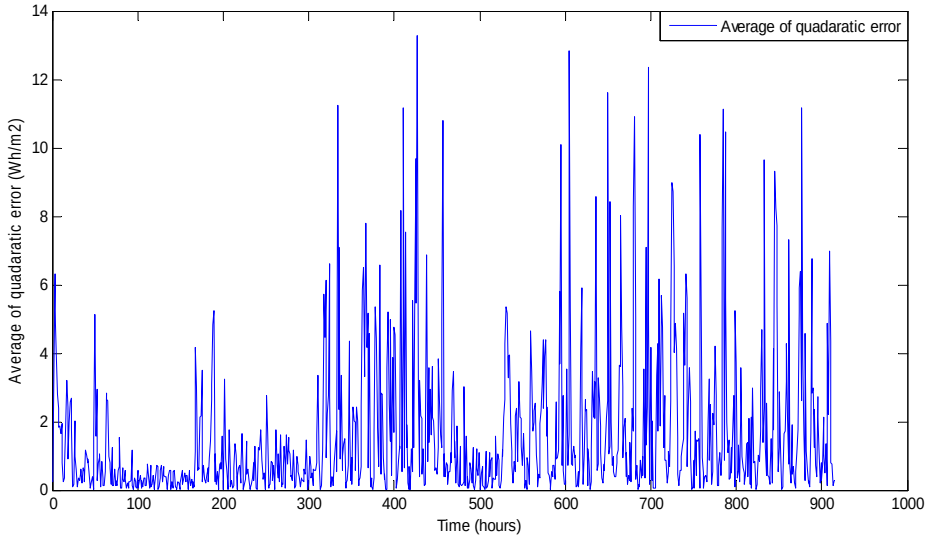

Figure 4.13: The quadratic error between measured global horizontal solar radiation (from 1^{st} November to 31^{st} December 1996) and the forecasted using the proposed model.

From Fig. 4.13, the total RMSE is equal to 64.34 Wh/m^2 and the NRMSE is 0.2003, which can be viewed as good forecasted values compared with an NRMSE equal to 0.3184 by using the baseline ARMA model. In addition, from Fig. 4.14, the R-squared value is equal to 0.9330. Most of the points of the forecasted and measured series are near each to other.

However, it presents some lags due to the total covered days that present a lot of clouds. Finally, from the simulation results, this methodology is conceived to be such a good method to perform the forecast results.

4.6 Conclusion

In this chapter, we introduced two hybrid models for multi-step ahead forecasting of hourly global horizontal solar radiation time. First, hybrid ARMA and NAR neural network was used. According to the fact that solar radiation series has linear and nonlinear components, the ARMA model was good to forecast the linear behaviour of the solar radiation time series. Also, NAR network proved to be a suitable method to capture the non-linearity of the series. But, no one of them was suitable to extract full characteristics of global solar radiation series. Hence, the hybrid model is a good method to forecast such similar problems.

Second, a hybrid method based on the k-means clustering methods and NAR neural networks was used. The obtained experimental results showed that the clustering of the input space is an important task to interpret the behaviour of the series. Moreover, identifying forecasted regions using NAR network provides additional information about future patterns that can simplify the analysis of the global forecast of the series. In addition, the proposed method does not need a complicate clustering algorithm.

Hence, as a conclusion, the time series data mining method is considered such a good way of forecasting such similar problems. Nevertheless, this method presents some limitations for the total covered sky where the presence of clouds is heavy, also the calculation time, especially in the preparation phase of the NAR network.

The next chapter will discuss the application of the obtained results on the stand- alone PV systems sizing, estimation of the DC outputs and fault detection of the PV systems.

Nomenclature

$a(i)$	Average dissimilarity.
ACF	Autocorrelation function .
PACF	Partial Autocorrelation function.
AIC	Akaike's Information Criterion.
$b(i)$	Lowest average dissimilarity.
c_j	Cluster centre.
Cov	Covariance function.
d_e	Number of estimated parameters.
e_t	Gaussian white noise.
$H(X)$	Entropy.
$H(Y \mid X)$	Conditional entropy.
H_n	Daily solar radiation.
$I(X, Y)$	Mutual information.
I_t	Hourly solar radiation.
J	Objective function .
L_t	Linear part of the time series.
$\hat{L}_t$	Predicted series from linear part.
m	Embedding dimension.
M	Number of embedded points in the m-dimensional space.
MPL	Multilayer Perceptron.
m_d	Pick hour of the day.
N_e	Number of values in the estimation data set.
N_t	Nonlinear part of the time series
$\hat{N}_t$	Forecasted series from nonlinear part.
p	Lag order of the autoregressive process.
$p(x)$	Probability mass function.
R^2	R- squared value.

R_A	Size of the attractor.
r_t	Ratio of hourly to daily global solar radiation.
$s(i)$	Silhouette function.
t	Time.
T_{tol}	A unit less tolerance level.
V	Loss function.
Var	Variance function
v_t	Residual at time t from the linear part of the time series.
$X_{(ti)}$	Embedded time series into an m-dimensional space.
$x_{(ti)}$	Scalar time series.
α	Constant called a drift.
β	Coefficient on a time trend.
γ	Coefficient presenting process root.
δ_t	Lag operator .
ϕ_I	Autoregressive AR parameters.
θ_j	Moving average MA parameters.
τ	Delay time.
$\mu(t)$	Mean of a time series.
$\mu_{(N_d)}$	Solar beam attenuation coefficient.
σ"	Standard deviation of the Gaussian curve.
$\chi(t)$	Distance of the solar beam travels within the atmosphere at time t.

References

Akaike H.. A new look at the statistical model identification. In: IEEE Trans. Autom. Control 1974, 6: 716–723.

Al-Sadah F H, Ragab F M , Arshad M K . Hourly solar radiation over Bahrain. Energy 1990, 15 : 395-402.

André Luis S , Maia Francisco de A T , de Carvalho Teresa B L . Forecasting models for interval-valued time series. Neurocomputing 2008, 71: 3344–3352.

Baig A , Achter P , Mufti A. A novel approach to estimate the clear day global radiation. Renew. Energy 1991, 1: 119–123.

Bevington P R, 1969 . *Data reduction and error analysis for the physical sciences.* McGraw Hill Book Co, pp. 336 .

Boata, R S T , Gravila P . Functional fuzzy approach for forecasting daily global solar radiation. Atmos. Res. 2012, 112:79-88.

Boland J W, 2008. *Time series and statistical modelling of solar radiation, Recent Advances in Solar Radiation Modelling.* Viorel Badescu (Ed.), Springer-Verlag, pp. 283-312.

Box G E P , Jenkins, G , 1970. *Time Series Analysis, Forecasting and Control. Holden -Day*, San Francisco, CA.

Chen S X , Gooi H B , Wang M Q. Solar raidaiton forecast based on fuzzy logicand neural network.Renew. Energy 2013, 60 :195–201.

Chow T W S , Leung C T . Non-linear autoregressive integrated neural network model for short term load forecasting. IEE proc. Generation transmission and distribution 1996, 143: 500-506.

Denton J W. How good are neural networks for causal forecasting?. J. Bus. Forecasting. 1995, 14: 17–20.

Diagne M , David M , Lauret P , Boland J , Schmutz N .Review of solar irradiance forecasting methods and a proposition for small-scale in solar grids. Renew. Sust. Energ. Rev. 2009, 13: 406–419.

Dickey D A , Fuller W A. Likelihood ratio statistics for autoregressive time series with a unit root. Econometrica 1981, 49: 1057–1072.

Fraser M , Swinney . Independent coordinates for strange attractors from mutual information. Phys. Rev. 1986, 33: 1134-1140. Fu T. A review on time series data mining, Engineering

Applications of Artificial Intelligence 2011, 24 : 164–181.

Ginzburg I , Horn D . Combined neural networks for time series analysis. Adv. Neural Inf. Process. Systems . 1994, 6: 224–231.

Haykin S. 1998. Neural Networks: *A Comprehensive Foundation*, 2nd ed. Prentice Hall.

Huang J , Korolkiewicz M , Agrawal M , Boland J. Forecasting solar radiation on an hourly time scale using a coupled autoregressive and dynamical system (CARDS) model, Sol. Energy 2013, 87:136-149.

Ineichen P . A broadband simplified version of the Solis clear sky model. Sol. Energy 2008, 82: 758-762.

Kaplanis S . New methodologies to estimate hourly global solar radiation; comparisons with existing models. Renew. Energy . 2006, 31: 781–790.

Kaplanis S, Kaplani E. A model to predict expected mean and stochastic hourly glob. Renew. Energy 2007, 32 : 1414-1425.

Kennel M B , Brown R, Abarbanel H D . Determining embedding dimension for phase space reconstruction using a geometrical construction, Physical Review 1992, 45 : 3403-3411.

Kim H S, Eykholt R, Salas J D. Nonlinear dynamics, delay times, and embedding windows. Physica D 1999, 127 : 48–60.

Applications for the PV systems

Klipp E , Herwig R , Kowald A , Wierling C , Lehrach H, 2008 . Systems Biology in Practice: Concepts, Implementation and Application. John Wiley & Sons, pp. 327.

Kohavi R. "A study of cross-validation and bootstrap for accuracy estimation and model selection". Proceedings of the Fourteenth International Joint Conference on Artificial Intelligence 2, 1995, 12: 1137–1143.

Morgan Kaufmann, San Mateo, CA. Kostylev V , Pavlovski A . Solar Power Forecasting Performance – Towards Industry Standards, Proceedings of the 1st International Workshop on the Integration of Solar Power into Power Systems, 2011, Aarhus, Denmark.

Kugiumtzis D. State space reconstruction parameters in the analysis of chaotic time series—the role of the time window length. Physica D 1996, 95: 13–28.

Kugiumtzis, D . Surrogate data test for nonlinearity including nonmonotonic transforms. Phys.Rev E Stat Phys. Plasmas Fluids Relat.Interdiscip Topics 2000, 62, no.1.

Kwiatkowski D , Phillips P C B, Schmidt P , Shin Y. Testing the Null Hypothesis of Stationarity against the Alternative of a Unit Root. J. Econometrics. 1992, 54: 159–178.

Levenberg K . A method for the solution of certain problems in least squares. Q. Appl.Math. 1944, 5: 164–168.

Lewis C D , 1982. *International and business forecasting methods.* London: Butter- worths.

Liao S , Chu P , Hsiao P. Data mining techniques and applications – A decade review from 2000 to 2011. Expert Systems with Applications 2012, 39 : 11303–11311.

Lletí R , Ortiz M C , Sarabia L A , Sánchez M S. Selecting variables for k-means cluster analysis by using a genetic algorithm that optimises the silhouettes. Analytica Chimica Acta 2004, 515 : 87–100.

Luxhoj J T , Riis J O . Stensballe B. A hybrid econometric-neural network modeling approach for sales forecasting. Int. J. Prod. Econ . 1996, 43 : 175–192.

MacKay D J C . Bayesian interpolation, Neural Computation 1992. 4: 415-447.

MacQueen J.B . Some Methods for classification and Analysis of Multivariate Observations. Proceedings of 5th Berkeley Symposium on Mathematical Statistics and Probability 1, 1967. University of California Press, pp. 281–297

Makridakis S , Wheelwright S C , Hyndman R J , 1998. Forecasting: Methods and Applications. 3rd ed., New York, ISBN: 0471532339.

Mandelbrot B B , 1967. *How long is the coastline of Britain? Statistical self-similarity and fractional dimension.* Science 155. pp 636.

Markham I S , Rakes T R ,. The effect of sample size and variability of data on the comparative performance of artificial neural networks and regression. Comput. Oper. Res. 1998, 25: 251–263.

Mellit S A , Kalogirou L , Hontoria S S . Artificial intelligence techniques for sizing photovoltaic systems: A review article. Renew. Sust. Energ. Rev. 2009, 13: 406–419.

Moller M F. A scaled conjugate gradient algorithm for fast supervised learning. Neural Networks 1993, 4: 525-533.

Pelikan E , de Groot C , Wurtz D. Power consumption in West-Bohemia: improved forecasts with decorrelating connectionist networks. Neural Netw. World 1992, 2: 701–712.

Ragulskis M., Lukoseviciute K. Non-uniform attractor embedding for time series forecasting by fuzzy inference systems. Neurocomputing 2009, 72: 2618–2626.

Rousseeuw J . Silhouettes: a Graphical Aid to the Interpretation and Validation of Cluster Analysis. Computational and Applied Mathematics 1987, 20:53–65.

Sandberg I, Xu L. Uniform approximation of multidimensional myopic maps, IEEE Transactions on Circuits and Systems I: Fundamental Theory and Applications 1997, 44 : 477–485.

Spath H . Cluster Dissection and Analysis: Theory, FORTRAN Programs, Examples, translated by J. Goldschmidt. Halsted Press, 1985, New York, 226 pp.

Takens F . Detecting strange attractors in turbulence, Dynamical Systems and Turbulence (D. A. Rand and L. S. Young, eds.), Lecture Notes in Mathematics 898, 1981. pp. 366-381.

Voyant C, Muselli M , Paoli C , Nivet M . Hybrid methodology for hourly global radiation forecasting in Mediterranean area. Renew. Energy 2013, 53: 1–11.

Wedding D K , Cios K J. Time series forecasting by combining RBF networks, certainty factors, and the Box–Jenkins model. Neurocomputing 1996, 10: 149–168.

Wu J , Chan K C . Prediction of hourly solar radiation using a novel hybrid model of ARMA and TDNN. Sol. Energy 2011, 85: 808-817.

Xu R, Donald C . Survey of Clustering Algorithm , IEEE Transactions on Neural Networks 2005, 16: 46-51.

Zhang G, Patuwo E B , Hu MY . Forecasting with artificial neural networks: the state of the art. Int. J. Forecasting 1998, 14: 35–62.

Zhang G. Time series forecasting using a hybrid ARIMA and neural network model. Neurocomputing 2003, 50: 159–175.

Chapter 5

Applications for the PV systems

5.1 Introduction

Solar energy is used widely in two large categories; grid connected and stand-alone photovoltaic (SAPV) systems. Recent applications in remote areas and space applications need a continuous source of power. Stand-alone PV (SAPV) systems could assure this power if the optimal sizing is reached especially in small scales. Hence, this chapter deals with the application of the estimated and forecasted solar radiation to use them in the sizing of stand-alone PV systems .

5.2 Description of PV systems

PV systems are devised into two categories, grid connected systems and stand-alone systems. The difference between these systems is that the first is connected to the grid and the other is not as shown in Fig. 5.1.

Grid connected systems are interconnected with the network of power lines (the network of cables through which electricity is transported from power stations to other places). It consists of an inverter that converts the DC power produced from PV panels into AC power injected into the grid. It can deliver the electricity to the network at any time when required. In a grid connected system no battery or other storage is needed.

Stand-alone PV systems produce power independently of the grid utility. They are used to supply electricity to a single system. They usually included with one or more batteries to store the produced electricity. They are used widely in remote areas, water pumping, highway lighting, weather stations, remote homes... etc.

5.3 Stand-alone PV system components

In this thesis, we are interested in the application of the proposed methods to the stand- alone PV system. Hence, we present in what follows the principal parts of this system (panels, battery and the load profile).

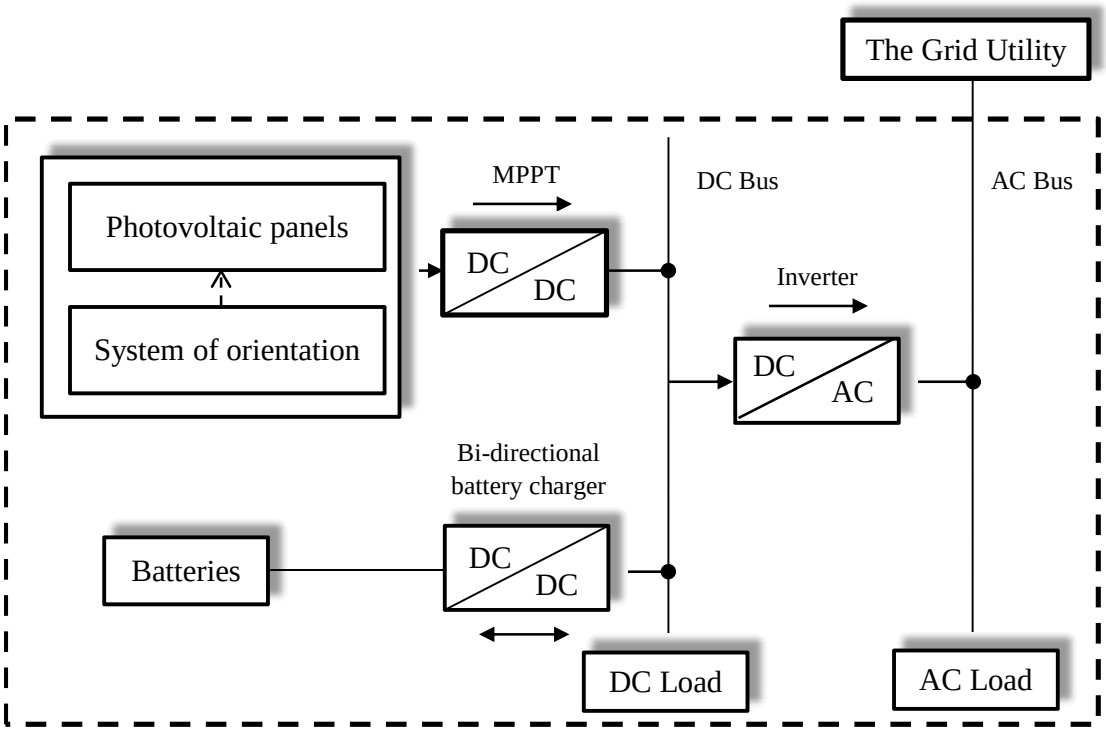

Figure 5.1: Description of a PV system.

5.3.1 PV Panels

Solar cells represent the elementary power conversion unit. It converts the solar radiation reaches the surface of the cell into electrical energy by the photovoltaic process. The equivalent circuit of a double diodes PV cell is shown in Fig.5.2. It consists of two diodes in parallel with a current source, and two resistors.

For extracting the DC output powers, the output currents and voltages of the PV systems have been calculated using a double diode PV model as expressed in Eq. (5.1).

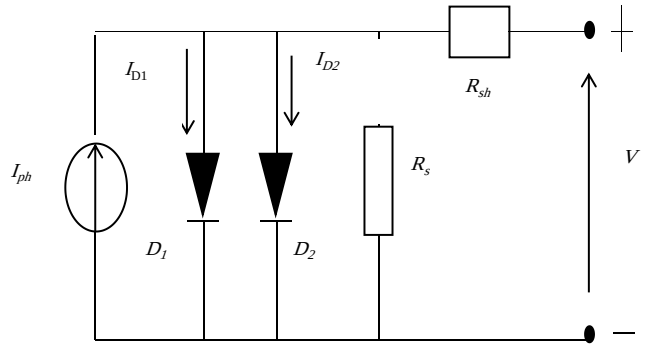

Figure 5.2: Two diode PV cell model.

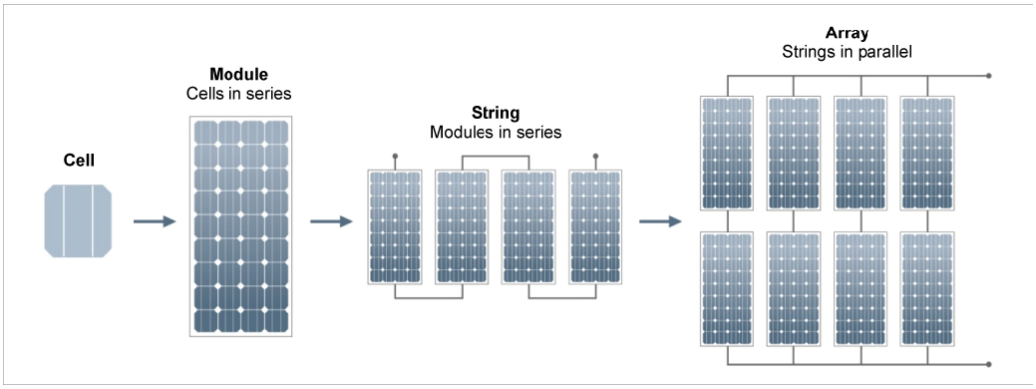

Figure 5.3: Photovoltaic cells, modules, strings and arrays

$$I = I_{ph} - I_{01}\left(\exp\left(\frac{V + R_s I}{n_1 V_t} - 1\right)\right) - I_{02}\left(\exp\left(\frac{V + R_s I}{n_2 V_t} - 1\right)\right) - \frac{V + R_s I}{R_{sh}} \tag{5.1}$$

Where, I_{ph} is the current generated by the incident light. I_{01}, I_{02} are the reverse saturation currents of the diodes D_1 and D_2 respectively.V_t is the thermal voltage. n_1, n_2 are the ideality factors of diodes D_1 and D_2. $R_s$and R_{sh} are the series and shunt resistance respectively. V and I are the output PV module voltage and current respectively.

Photovoltaic cells are modular. That is, one can be used to make a very small amount of electricity, or many can be used together to make a large amount of electricity. A 10 centimetre diameters PV cell can make about one Watt of power if the Sun is directly overhead and the conditions are clear because each photovoltaic cell produces only about one-half volt of electricity.

Cells are often mounted together in groups called modules. Each module holds about 40 photovoltaic cells, by being put into modules; the current from several cells can be combined. PV cells can be strung together in a series of modules or strung together in a parallel placement to increase the electrical output. When multiple PV cell modules are put together, they can form an arrangement called an array or array field (Fig.5.3). Photovoltaic modules and arrays produce direct current (DC) electricity. They can be connected in both series and parallel electrical arrangements to produce any required voltage and current combination.

5.3.2 Batteries

Rechargeable batteries are widely used in stand-alone photovoltaic systems to store the DC output power from the PV array surplus and supply the load in case of low renewable energy production. The most common type used is regulated Lead–acid battery because of its low cost, maintenance-free operation and high efficiency characteristics.

Although the battery installation cost is relatively low compared to that of PVs, the lifetime cost of the battery is greatly increased because of limited service time (Posadillo and Lopez Luque, 2008). The expected battery lifetime is reduced if there is low PV energy availability for prolonged periods or improper charging control, both resulting in a low battery state of charge (SOC) levels for a long time periods. The overall system cost can be reduced by the

use of proper battery charging/discharging control techniques (MPPT), which achieve high battery SOC and, consequently, longer lifetime.

5.3.3 Maximum Power Point Tracking (MPPT)

The MPPT control (Maximum Power Point Tracking) is a functional component of a PV system; it allows the optimal operating point of the PV generator, in different conditions. Whether analogical or digital control, the control principle is the same; it is based on an automatic variation of the duty cycle α to the appropriate value, in order to exploit the maximum power output of PV generator. Many MPPT algorithms have been developed by researchers around the world such as Perturb and observe, incremental conductance, fuzzy logic, neural network ... etc. (Eltawil and Zhao, 2013; Kamarzaman and Tan, 2014).

5.4 Optimal sizing of stand-alone PV systems

Accurate sizing is one of the most important aspects to take into consideration when designing a (SAPV) system; it consists of finding the best compromise between the reliability and the cost that the system (PV panels and batteries) can feed the load at any time. Several methods were proposed in literature for obtaining the optimal sizing based on the concept of the loss of load probability (LLP). LLP is a parameter used to characterize the system design. It is defined as the relationship between the energy deficit and the energy demand, as referred to the load. In statistical terms, the LLP value refers to the probability that the system will be unable to meet load demands (Posadillo and Lopez Luque, 2008). The main reason of this failure is the stochastic characteristics of the solar radiation that affect the sizing process. Kaplani and Kaplanis (2012), Chen (2012) and Cabral et al. (2010) improved that the fluctuation observed in the daily solar radiation affects highly the reliability of the PV system sizing. Hence, it is an important task to study earlier the dynamic behaviour of the solar radiation time series before any sizing processes. In addition, the failures can occur due to losses in the cables, in the battery storage, the ageing of the components, the degradation of the PV panel's performance and the charge / discharge effects of the batteries.

Several methods were demonstrated in literature to calculate the sizing parameters for a constant LLP (Khatib et al., 2013). Among them, intuitive methods (Charma et al., 1995; Sidrach-de-Cardona and Mora Lopez, 1998), where the size of the system is taken in such a way to ensure the load demand without gives a relation between the number of panels, batteries and the LLP. Analytical methods (Barra et al., 1984; Bartoli et al. ,1984; Hontoria et al., 2005), based on the graphical information obtained from of the iso-probability curves, and the numerical methods (Ambrosone et al. 1985; Egido and Lorenzo, 1992; Mellit,2010) which based on a detailed simulation of the PV system in small scales (daily, hourly... etc.). In the numerical methods, the produced energy from the PV generator and the stat of the charge of the batteries are calculated at each time t. The advantages of the numerical methods are the precision and the simplicity of choosing different elements of the system (Egido and Lorenzo, 1992; Mellit, 2010; Posadillo and Lopez Luque, 2008; Lucio et al. 2012). Several algorithms had been proposed in literature to calculate LLP values based on numerical methods. They are based on the measured monthly or daily solar radiation data over a long time, taking into account the worst month of the year (Egido and Lorenzo, 1992; Posadillo and Lopez Luque,

2008; Lucio et al. 2012). However, they present major drawbacks as the length and non-occurrence of the used solar radiation data (only in daily or monthly basis), where the most of solar radiation applications need hourly solar radiation data Posadillo and Lopez Luque, 2008; Labed and Lorenzo, 2004; Lorenzo and Narvarte, 2000) . In addition, choosing of the worst month in the year does not give all the information on the dynamic characteristics of the measured solar radiation (maybe it exists bad weather outside the worst month) that limited the importance of the sizing in daily basis. For that, we proposed a modified numerical algorithm based only on the classified hourly solar radiation using a clustering algorithm for obtaining the lowest solar radiation data over a one-year period that ensures the optimal sizing in hourly basis. The novelty of the proposed method compared to other methods presented in the literature (Posadillo and Lopez Luque, 2008; Khatib et al., 2013; Fadaee and Radzi, 2012; Sidrach-de-Cardona and Mora Lopez, 1998; Barra et al., 1984; Bartoli et al. ,1984; Hontoria et al., 2005; Ambrosone et al. 1985; Egido and Lorenzo, 1992; Mellit,2010; Lucio et al. 2012),is that assure first, the full identification of the dynamic characteristics of hourly solar radiation time series, and second, the optimal sizing of the system is guaranteed in small scales by using only one year hourly solar radiation data.

At first stage, time series data mining was applied to hourly solar radiation data. It consists of grouping similar elements into clusters that have the same characteristics (Liao et al., 2012; Sandberg and Xu, 1997). For this purpose, several methods were proposed in literature based on unsupervised clustering methods such as k-means and fuzzy c–means (FCM) algorithm (MacQueen, 1967; Xu, 2005; Dunn, 1974; Bezdek, 1981; Takens, 1981). We have chosen in this work the FCM algorithm which based on the fuzzy method that gives good results. Before that, phase space reconstruction is needed to overcome the nonlinearity of the solar radiation data. The motivation of using the FCM algorithm that it is a powerful tool which presents more precise results comparing with k-means algorithm (Mingoti and Lima, 2006). Nevertheless, it depends strongly on the initialization parameters (initial number of clusters), Hence, the sub-clustering method (Chiu, 1994) was used to decide the right number of clusters.

In the second phase, the low solar radiation data obtained from the clustering processes are used to determine the iso-probability curves using the numerical method. For each hour, the LLP is calculated and compared to the desired LLP (1% in our example). After that, an economic study of the system is achieved by minimizing the total cost of the system to get satisfactory results (Wissem et al., 2012; Hongxing et al., 2009; Dufo-Lopez et al., 2011) . We used the genetic algorithm (GA) method as optimizing technique for the search of the optimal solution. Finally, a general decision is selected that insured the minimization of an objective function that guaranteed the minimum cost of the pairs of panels and batteries which give a LLP equal to 1% for a desired hourly load is reached.

5.4.1 Methodology

We will present in this work a basic configuration for optimal sizing of the stand-alone PV systems based on hourly global solar radiation time series classification and the genetic algorithm for the economic cost optimization as shown in the flowchart in Fig. 5.4.

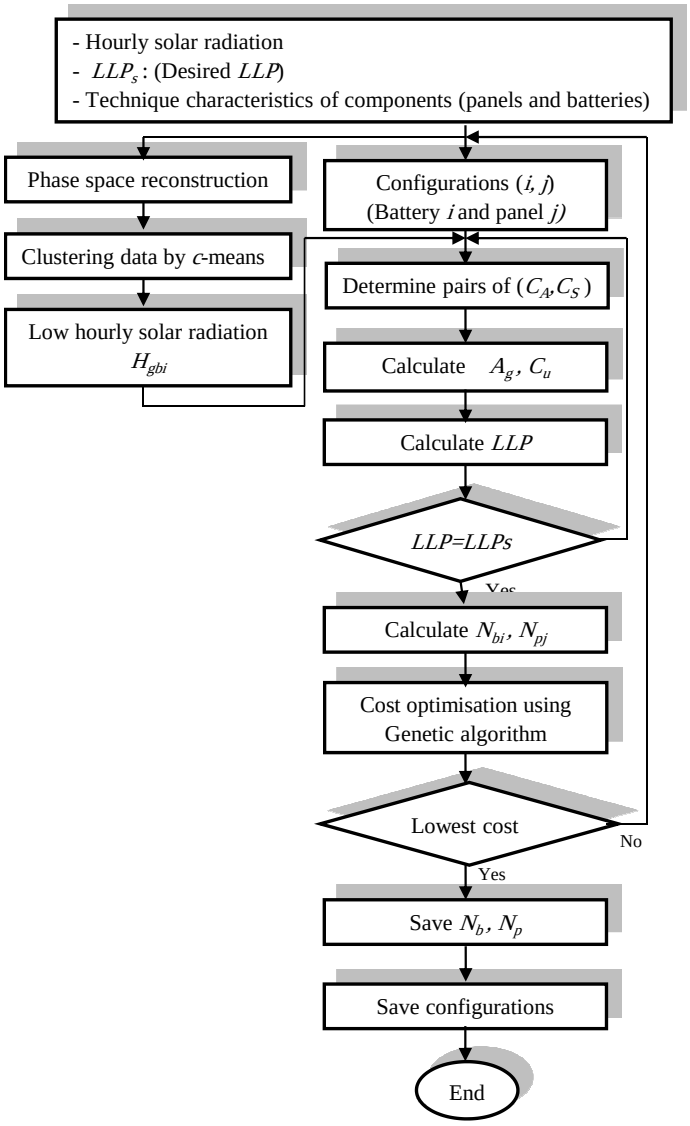

Figure 5.4: Flowchart of the proposed hybrid k-means and NAR methodology.

The developed methodology consists of the following steps:
Step 1 : Classification phase;

- Reconstruction of the phase space of hourly global solar radiation by determining the optimal embedding dimension,
- Classification of hourly global solar radiation using fuzzy c-means clustering algorithm.

Step 2 : Sizing phase (iso-reliability curves);

- Calculating of the stand-alone PV system dimensional parameters, the capacity of the PV panel array C_A and the capacity of the storage system C_S;

- Estimation of the loss of load probability LLP (plotting of the iso-reliability lines).

Step 3 : Economic optimization phase;

- Initialize the cost of the components (PV panels, Batteries, other costs... etc.),
- Finding the minimum system costs versus optimal system reliability using the GA optimization method.

5.4.1.1 Classification phase : fuzzy c –means clustering algorithm

The FCM algorithm introduced by Dunn (1974) and modified by Bezdek (1981) is used widely in the clustering methods. It consists of separating the data point into c clusters with respect to some given criterion for the optimization of an objective function. However, due to the presence of nonlinearity in some time series such as hourly global solar radiation time series, it is more useful to represent the time series in higher-dimensional space to understand the underlying dynamical of the system (MacQueen, 1967). Hence, phase space reconstruction [presented in chapter 4] was used to simplify the analysis of the time series.

After determining the optimal embedding dimension, the reconstructed phase space of the solar radiation data is clustered using the fuzzy c-means algorithm. In this method, as in the fuzzy logic approach, each point belongs to a cluster with some degree of belonging defined by a membership grade. The FCM algorithm minimizes an objective function J_{FCM} that calculated the weighted within-group sum of squared errors as expressed in Eq. (5.2)

$$J_{FCM} = \sum_{k=1}^{n} \sum_{i=1}^{c} (u_{ik})^q d^2 (x_k, v_i) \tag{5.2}$$

Where, n is the length of the data, c is the number of clusters defined by the c-means algorithm, u_{ik} is the degree of membership of x_k in the ith cluster, q is a weighting exponent on each fuzzy membership, it is a real number greater than 1 (typically q =2 (Chiu,2012)), $X = (x_1, x_2, \ldots, x_n)$ is the data in the m-dimensional vector space, v_i is the centre of the cluster i, $d^2(x_k, v_i)$ is the distance measured between data x_k and cluster centrev_i.

The summary of the FCM algorithm is illustrated by the following steps (Dunn,1974; Bezdek , 1981),

(1) Initialize the values c, q and the error ε ;

(2) Initialize the cluster centre matrix $V^{(t=0)} = \left[v_i^{(t=0)}\right]$ and the membership matrix $U^{(t=0)} = \left[u_{ik}^{(t=0)}\right]$;

(3) Increase the time t and calculate the new c cluster centres $V^{(t)}$;

$$V^{(t)} = \frac{\sum_{k=1}^{n} \left((u_{ik})^{(t)}\right)^q x_k}{\sum_{k=1}^{n} \left((u_{ik})^{(t)}\right)^q} \tag{5.3}$$

(4) Calculate the new membership values $U^{(t+1)}$;

$$U^{(t+1)} = \left[u_{ik}^{(t+1)}\right] \frac{1}{\sum_{j=1}^{c} \left(\frac{d_{ik}}{d_{jk}}\right)^{2/(q-1)}} \tag{5.4}$$

Where , $d_{ik} = \|x_k - v_i\|$and $1 \leq k \leq n$, $1 \leq i \leq c$;

(5) If $\left\|U^{(t)} - U^{(t+1)}\right\| < \varepsilon$ stop. Otherwise, increase t and go to step (3).

The FCM algorithm depends strongly on the position of the initialization points. Hence, an important task in the FCM algorithm is choosing the correct number of clusters to avoid the problem of falling in a local minimum. Several techniques are proposed in the literature to solve this problem, such as sub-clustering method (Chiu, 1994) and mountain method proposed in (Yager and Filev , 1994). In this study, we used the sub-clustering technique to decide the number of clusters. This method is an iterative process which supposed that each point is a potential cluster centre according to its location to other data points. The algorithm is summarized as follows (Chiu, 1994) :

- Choose a point that has the probability to be the highest potential cluster centre;
- Delete all the points which are inside the radius of the first cluster centre (the radius is defined by the neighbourhoods of the centre), and recalculate the potential of the other points to determine the next cluster centre;
- Repeat this step until all the data are within the radius of a cluster centre.

5.4.1.2 The sizing phase (iso-probability curves)

Sizing of the stand-alone PV systems consists of determine the reliability performance based on two dimensional parameters, the PV generator capacity C_A which means the number of loads fed only by the PV array and the battery storage capacity C_S indicates the number of days (hours) where the batteries are fully charged and with no energy income could feed the load (the hours where the load is supplied only by the batteries and not from the PV array) (Khatib, 2013; Jakhrani et al., 2012; Posadillo and Lopez Luque, 2008). These two parameters are defined by the following equations,

$$C_A = \frac{\eta_t A_G \overline{H_{g\beta_i}}}{L_t} \tag{5.5}$$

Where A_G is the used PV array area in (m2), $\overline{H_{g\beta_i}}$ is the global mean hourly solar radiation received on inclined surface in (Wh/m^2). L_t is the load value at time t in (W) and η_t is the total panels' efficiency gave by the following equation,

$$\eta_t = \eta_p(1 - B.(T_c - T_r)) \tag{5.6}$$

Where, η_p is the efficiency of a solar cell at a referenced solar radiation (i.e. 1000 W/m^2), B

is the temperature coefficient is between (0.004-0.006), T_c is the cell temperature in °C and T_r is the reference temperature of the panel (generally equal to 25 °C with air mass AM= 1.5).

$$C_S = \frac{C_U}{L_t} \tag{5.7}$$

$$C_U = N_b V_B C_B DOD \tag{5.8}$$

Where, C_U is the maximum battery useful capacity in (Wh), N_b is the number of batteries, V_B is voltage for the unity of storage, C_B is the nominal battery capacity in (Ah) and DOD is the maximum depth of discharge.

The objective of the sizing is the measure of the degree of the reliability in which the system (photovoltaic generator plus batteries) can supply the load demand at any time *t*. For that, the load loss of probability *LLP* defined as the ratio between the energy deficit and energy demand for a specified load during the total operation time of the installation as expressed in the following equation

$$LLP = \frac{\int_t \text{Energy deficit}}{\int_t \text{Energy demand}} \tag{5.9}$$

At each time *t*, the numerical method is applied to each configuration (panels and batteries) in an iterative way until the desired *LLP* is obtained. Once this task is completed, the parameters are saved and the reliability condition is reached. The summary of the modified algorithm based on numerical methods (Egido and Lorenzo, 1992; Mellit, 2010) is given by the following steps,

Step 1: Initialization of the data;

$LLP \leftarrow 0.01$, $L_t \leftarrow$Load at time t , $Err \leftarrow 10^{-4}$, $\eta_t \leftarrow$the panels' efficiency, $LLP_s \leftarrow 0.01$, $H_{g\beta_i} \leftarrow$the classified hourly solar radiation data on inclined surface (lowest hourly solar radiation obtained from the fuzzy *c*-means algorithm), $C_S \leftarrow 1$.

Step 2: Calculate the useful PV array area A_G and the maximum useful battery capacity C_u;

$SOC \leftarrow 0$, $E^{Aux} \leftarrow 0$, $A_G = \frac{C_A L_t}{\eta_t \overline{H}_{g\beta_i}}$, $C_U = C_S L_t$.

Step 3: calculate the state of the charge of the battery at the time *t*.

$$SOC_t = \min\left(SOC_{t-1} + \frac{\eta_t A_G H_{g\beta_i}}{C_U}; 1\right) \tag{5.10}$$

The energy supplied by the auxiliary generator E^{AUX}, keep the battery fully charged if the

load requirements is bigger than the energy stored in the batteries, that

$$SOC_t \geq \frac{1}{C_S} \Rightarrow E_t^{Aux} = 0$$

$$SOC_t \leq \frac{1}{C_S} \Rightarrow E_t^{Aux} = (1 - SOC_t).L_t.C_S \quad and \quad SOC_t = 1 \quad (5.11)$$

The LLP value is calculated over the number of available hours by the following equation,

$$LLP = \frac{\sum_{t=1}^{N_t} E_t^{Aux}}{\sum_{t=1}^{N_t} L_t} \quad (5.12)$$

Step 4: if $LLP > LLP_s$ then $C_A \leftarrow C_A + 0.05$ and go to step 5; Otherwise $C_A \leftarrow C_A - 0.05$ and go to step 5.

Step 5: if $(ABS(LLP - LLP_s)) > Err$ go to step 3; else, go to the next step.

Step 6: saving pairs C_A, C_S.

Step 7: if the values of C_A, C_S are changes go to step 2; otherwise stop.

5.4.1.3 System Cost optimization

In the economic study, we are interesting to minimize the total cost of the stand- alone PV system. Thus, the Genetic Algorithm (GA) optimization method was used to select the best configuration for selecting the lowest cost. After the determination of the output power as well as the dimensional parameters C_A and C_S (number of panels and batteries) for a specified LLP value, it remains the calculation of the actualized total cost C_t of the system by the following equation (Wissem et al., 2012; Hongxing et al., 2009; Dufo-Lopez et al. ,2011; Avril, 2010)

$$C_t = A_f C_c + C_m + C_r \quad (5.13)$$

Where, A_F is the actualization factor expressed by,

$$A_f = \frac{A_r}{(1 - (1 + A_r)^{-L_F})} \quad (5.14)$$

A_r is the actualization rate; it is equal to 8% for this kind of system (Wissem et al., 2012).
L_F represents the system lifetime (lifetime of the panels, generally 25 years).
C_c is the total components cost defined by,

$$C_c = N_p C_p + N_b C_b + C_a \quad (5.15)$$

where, C_p, C_p, C_b, N_p and N_b,are the prices and the numbers of panels and batteries respectively. C_a represents the additional costs include the cost of civil work, the command system and cable costs.

The maintenance cost C_m is given by,

$$C_m = C_{m(1)}.(1 + E_f)^{L_F} \tag{5.16}$$

$C_{m(1)}$ is the maintenance cost of one year, E_f is the annual expansion factor is equal generally to 1.5%.

The total replacement cost C_r of the system is determined as follow,

$$C_r = C_{r'}.R_f \tag{5.17}$$

Where, C_r is the system cost and R_f is the replacement factor given by,

$$R_f = \frac{A_r}{((1 + A_r)^{nb} - 1)} \tag{5.18}$$

Where, n_b is the battery lifetime.

After the determination of the cost objective function, the next step consists of applying the GA for the minimization of the cost function. The GA is an artificial intelligence method used for the optimization problems based on the natural genetic that mimics biological evolution [See Appendix A.4].

5.5 Results and discussion

In this section, we will discuss the obtained results from application of solar radiation. Namely, the results of sizing stand-alone PV systems, estimation of output DC parameters and faults detection.

5.5.1 Sizing of stand-alone PV systems

Our goal of the simulation is to minimize the total cost of the stand-alone PV system while ensuring the desired reliability in hourly scale during the day with a variable load requirement during a day. Three load profiles have been chosen in the simulation phase as expressed in Fig. 5.5.

The methodology consists of selecting the lowest values of the solar radiation during one year period and trying different sets of panels and batteries to find the best configurations.

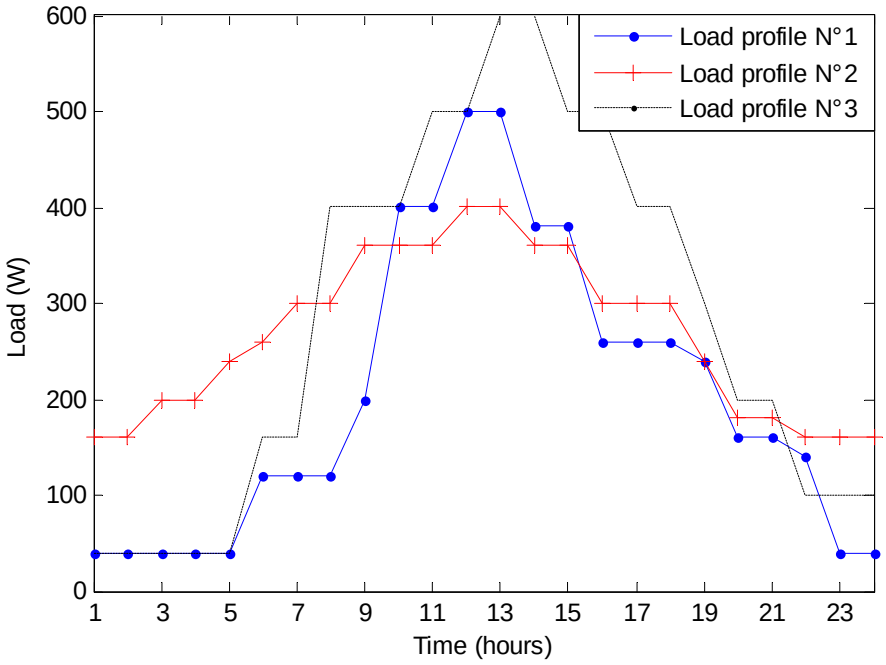

Figure 5.5: Different load profiles.

The technical characteristics and costs of panels, batteries and other components are listed in Tables 5.(1-3),

Table 5.1: Characteristics of the used photovoltaic panels.

Type	Power (W)	Dimension(mm)	Cell type (η)		Price($)
			Monocrystalline	Polycrystalline	
1.CHSM6610P	250	1626×994×45		15.2	248
2. ZJP-260W	260	1956×992×36		13.4	208
3. Panasonic HIT power240	240	1579×798×35	21.6		545
4. GH_M_003	260	1956×992×36	17		336

Table 5.2: Characteristics of the used batteries.

Type	Nominal capacity(AH)	Voltage(V)	Price($)
1.UB4D AGM	200	12	345
2.PVX-1040T	104	12	282
3.Trojan J305G	315	12	253

Table 5.3: Characteristics of the other used components

Other components	
Array installation cost ($/Wp)	(0.6$/Wp)
Array life	25 Years
Battery life	10 years
Annual operation & maintenance cost	1% of initial capital cost
Civil work cost	20% of initial capital cost
Other costs	10% of initial capital cost

5.5.1.1 Solar radiation classification using the FCM algorithm

The first phase of the proposed methodology is the choice of the global inclined hourly solar radiation data. We had collected these data from the national meteorological station in Algeria for the site of Ghardaia (longitude: 32.4833° N, latitude: 3.6667° E) for the year of 2012 with an inclination angle equal to 32°. Firstly, and using the FCM algorithm, the lowest hourly solar radiation data set was selected for use it in the sizing phase. The phase space reconstruction of hourly solar radiation was reached using the time delay embedding method. We found that a time delay of one and embedding dimension equal to two to be the suitable choice for the reconstructed phase space.

Next, the FCM algorithm is applied to the results obtained from the last step. Using the sub-clustering method, we found that the number of clusters is 3. The simulation results of the reconstructed phase space as well as the three subsets obtained from the FCM clustering algorithm of the solar radiation are shown in Fig.5.6 and Fig.5.7 respectively.

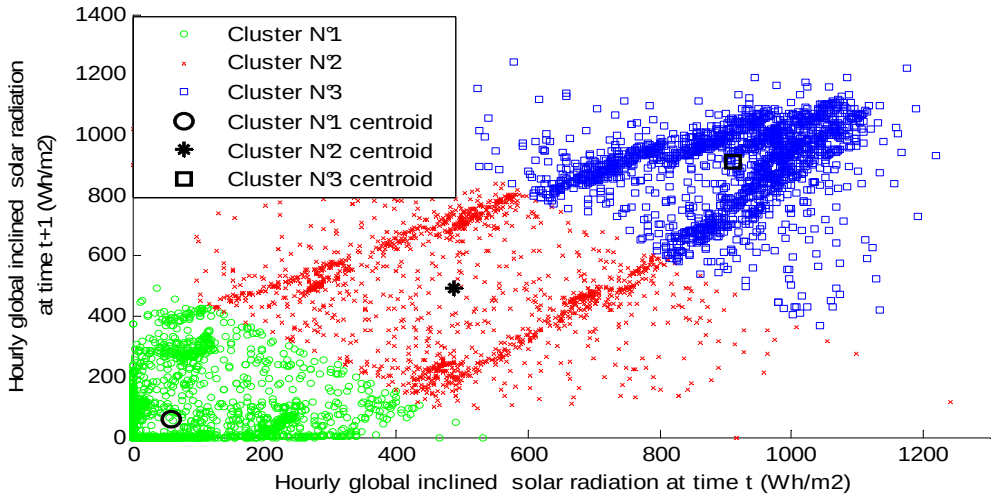

Figure 5.6: Space phase reconstitution of hourly global inclined solar radiation (Ghardaia, 2012).

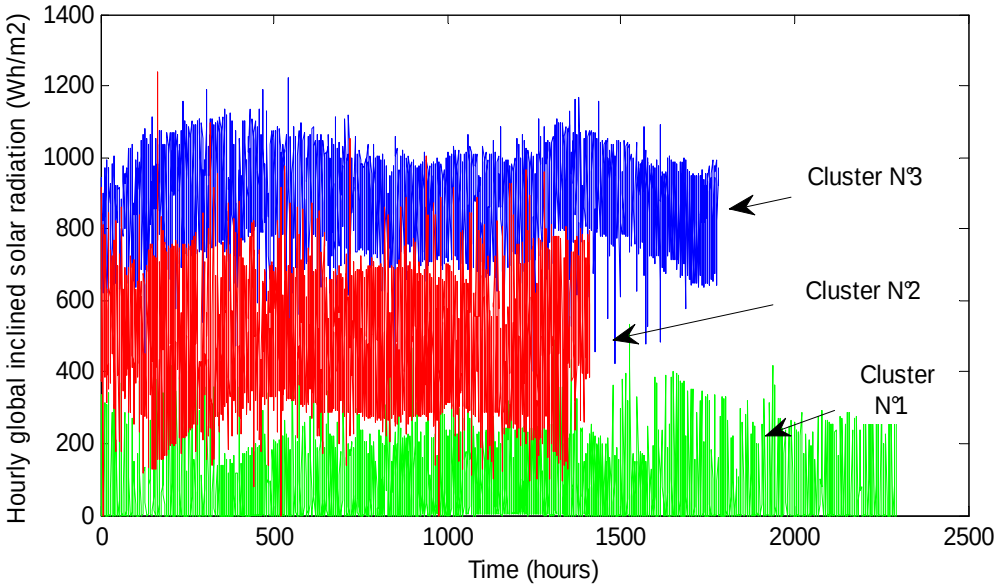

Figure 5.7: Clustered hourly global inclined solar radiation using FCM algorithm.

Fig.5.6 represents the reconstructed phase space of the inclined hourly solar radiation at time t and $t+1$. And, Fig.5.7 represents the amount of solar radiation in Wh/m^2 of the resulted clusters. From these figures it is clearly shown that the solar radiation time series had been grouped into three clusters, high values solar radiation (cluster N°3) which represent the sunny hours of the year (or noon hours during clear sky days), medium solar radiation values (cluster N°2) that represent the hours for partly cloudy skies (or hours from 9 AM to 11 AM and from 2 PM to 4 PM) and low solar radiation data (cluster N°1) that illustrate the case of cloudy skies (or the hours of sunshine and sunset). From these results it is clearly shown that cluster N°1 is the most appropriate to use it in the sizing phase because it represents the lowest hourly solar radiation values during the year.

5.5.1.2 Reliability sizing curves (iso-reliability curves)

In the second stage, the numerical method is applied to the obtained solar radiation data from the previous step to get the iso-probability curves for a specific reliability level. The results are given in Figs. 5.8 (a-c). They represent the number of panels against the number of batteries for a constant LLP equal to 1% for the load profile N°1.

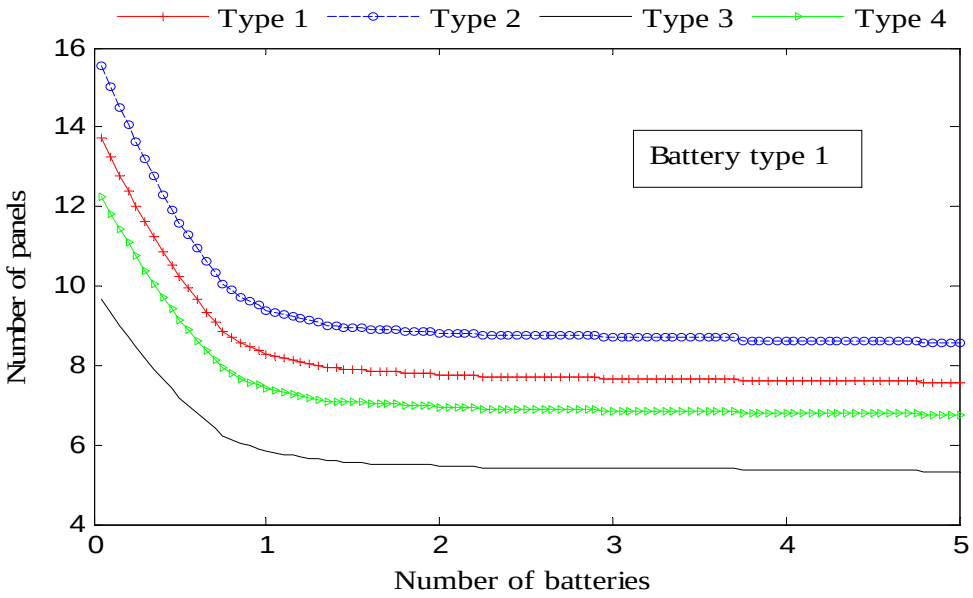

(a) : Sizing curve of the four type of panels for the battery type 1 for a LLP =1%.

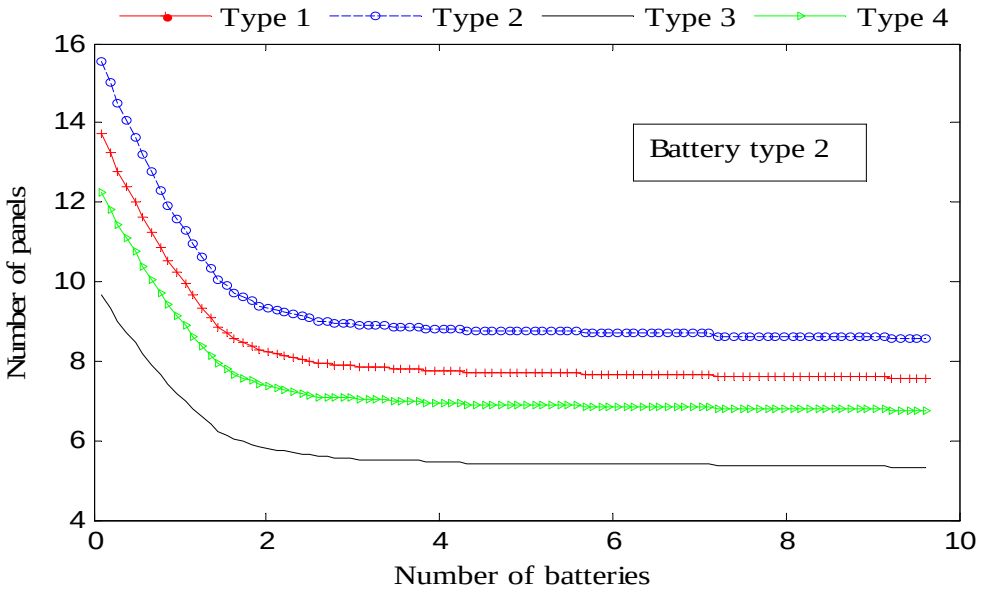

(b) : Sizing curve of the four type of panels for the battery type 2 for a LLP =1%.

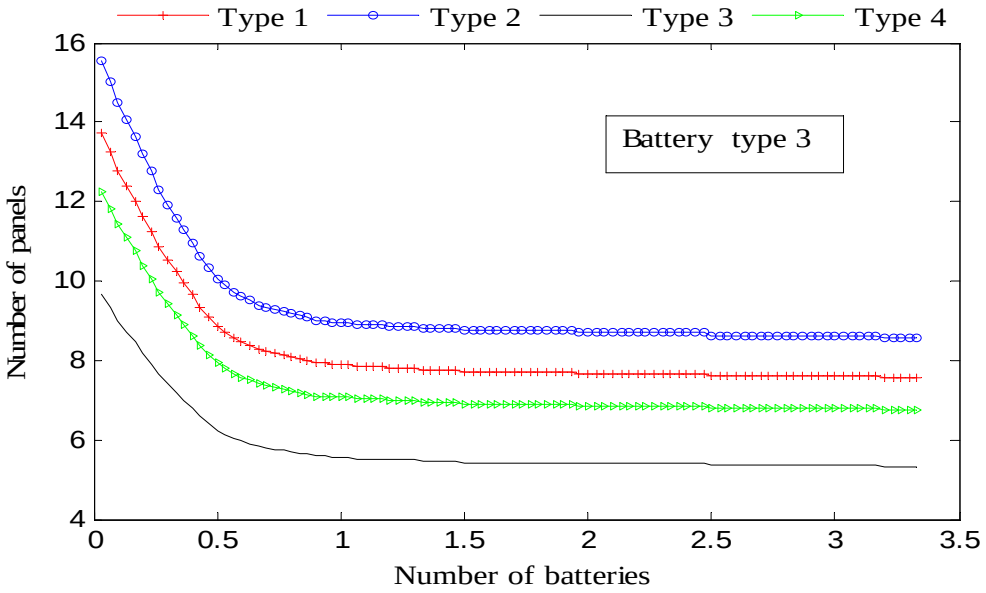

(c) : Sizing curve of the four type of panels for the battery type 3 for a LLP =1%.

Figure 5.8: (a - c) Sizing curve of the diffrent type of panels and batteries.

From these figures, it is clearly indicated that the panel type 3 gives the best results. It ensures the desired *LLP* compares with other type of panels. In addition, we can discover that the surface (dimension) of panels has an influence on the obtained results, more the surface is high more the number of panels is low (in the case of constant efficiency). Moreover, comparing the results that have the same surface of the panels (type 2 and 4), we discover that the type 4 gives better results; that it's because of the efficiency of the panel type 4 which is higher than the one of type 2. Furthermore, comparing the types of batteries for a specified type of panels (such as comparing the results of panels type 3 with the three types of batteries), we can see clearly that the battery type 3 gives the best results. This is because that the nominal capacity of battery type 3 is the higher one.

However, these conclusions do not reflect the goodness of the results, especially the economic point of view. A good technical choice that insures the desired *LLP* value does not imply that it is the lowest cost comparing with other configurations. Hence, an additional economic study is discussed to choose the optimal one.

5.5.1.3 Economic optimization with GA

After the technical study, it is more useful to calculate the cost of each pair (panels and batteries) basing on the actualized total cost for choosing the best configuration. Hence, we have compared the configuration already studies in the previous step. The simulation results are represented in Fig.5.9 (a-c) that expresses the total cost of the system for each type of panels and batteries.

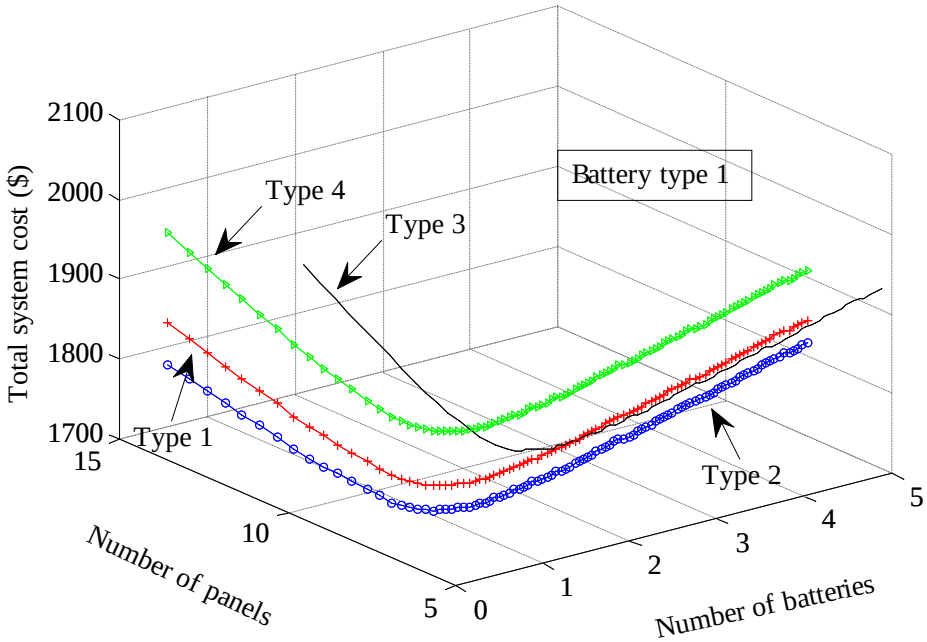

(a) : Total system cost versus the number of panels and batteries for the four types of panels and the battery type 1.

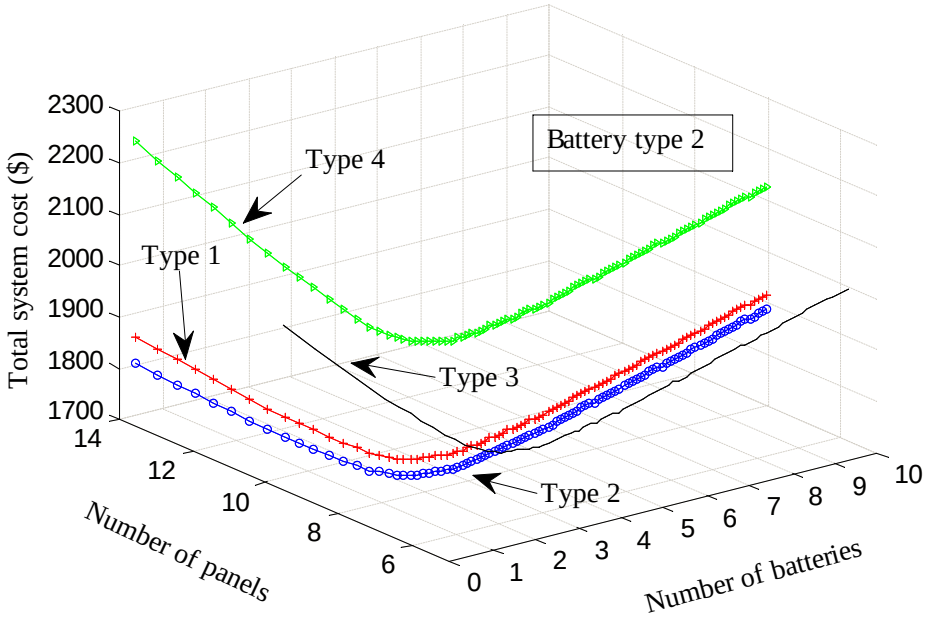

(b) : Total system cost versus the number of panels and batteries for the four types of panels and the battery type 2.

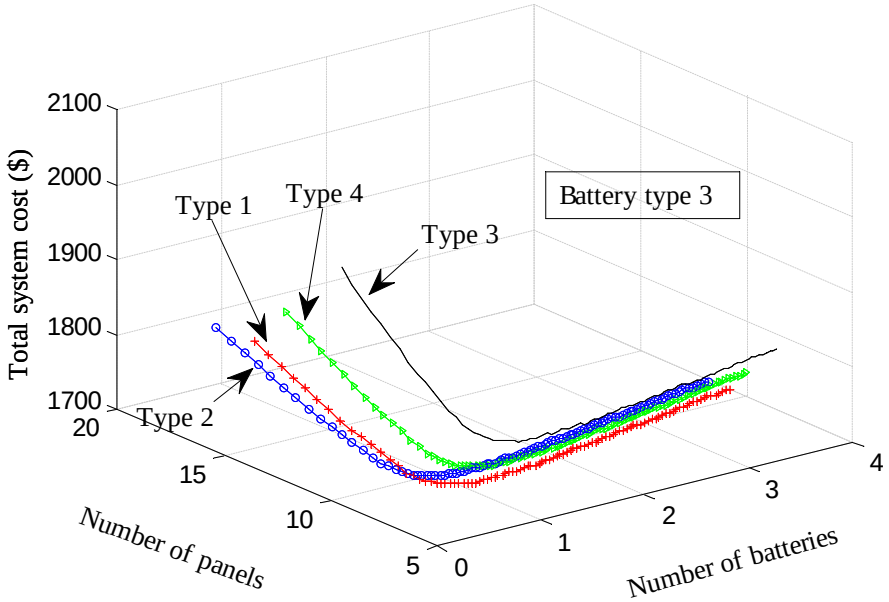

(c) : Total system cost versus the number of panels and batteries for the four types of panels and the battery type 3.

Figure 5.9: Total system cost versus the number of panels and batteries.

From these figures, it is clearly shown that the panel type 2 gives the lowest cost values for each type of batteries. Contrary to the results obtained from the sizing curves which indicate that the panels type 3 is the best choice.

Moreover, to determine the best optimal solution that ensures the best configuration of the system, the GA optimizing method is applied to the obtained results. For each type of panels and batteries, the total cost of the system was calculated. Then, the lowest value between them is chosen to be the best values. The comparison between all the results obtained from GA for each type of panels and batteries as illustrated in Table 5.4.

From Table 4, the battery type 1 shows the lowest configuration comparing with other batteries. In addition, the use of eight panels of type 2 and 1 battery of type 1 is considered the optimal configuration of the systems that give the lowest cost values which insure also a desired LLP for the load profile N°1.

Table 5.4: The total cost results obtained from the GA optimization for all types of panels and batteries.

Batteries	Panels			
	Type1	Type2	Type3	Type4
Type 1 : Cost, (Nb ,Np)	1737 $, (1, 8)	1706 $, (1, 8)	1824 $, (1, 6)	1804 $, (1, 8)
Type 2 : Cost, (Nb ,Np)	1756 $, (2, 8)	1724 $, (2, 8)	1845 $, (2, 6)	1985 $, (2, 8)
Type 3 : Cost, (Nb , Np)	1716 $, (1, 8)	1714 $, (1, 9)	1801 $, (1, 6)	1749 $, (1, 7)

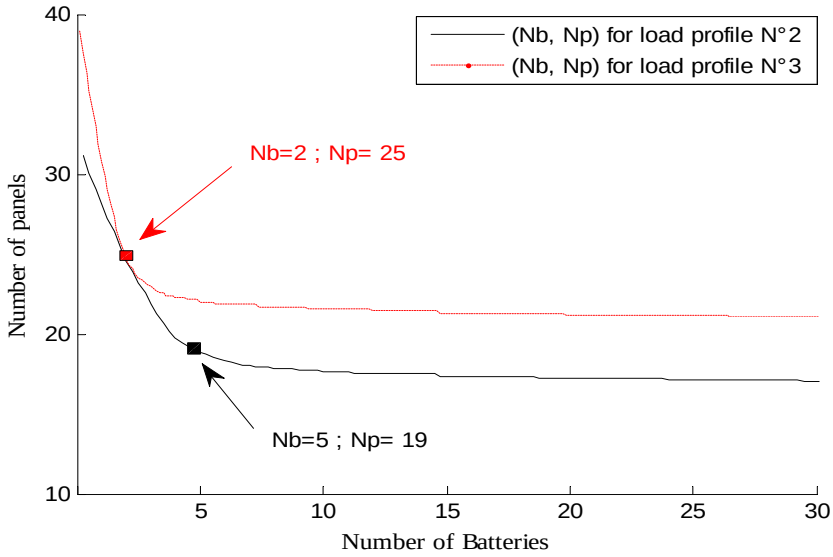

Figure 5.10: Sizing curve of the panel type 2 and the battery type 1 for a LLP =1% and the load profile N°2 and N°3.

In the same way, we have applied the proposed methodology for the load profiles N°2 (highest consummation during the night) and N°3 (highest consummation during the day). We found that the use of the panel number 2 with the battery number 1 give the best results. The simulation results are shown in Fig. 5.10 which represents the number of panels against the number of batteries for a constant LLP equal to 1% for load profile N°2 (black line) and N°3 (red dot line).

The last step is comparing the optimal sizing parameters (panels and batteries) for showing the importance of installing PV systems in the south of Algeria. Hence, we have simulated the proposed algorithm for two different climatic regions in Algeria (Oran : north, Ghardaia : south). The load profile N°1 was selected for both locations for a desired LLP=1%. The simulation results of the number of panels against a number of panels for Ghardaia (in red) and Oran (in blue) are shown in Fig. 5.11.

From this figure, it is clearly shown that the number of panels used in Ghardaia is less than Oran. Precisely, the number of panels used for Oran equal to 1.2 the number used for Ghardaia which means that the installation of stand-alone PV system in the south of Algeria are more suitable than their installation in the north.

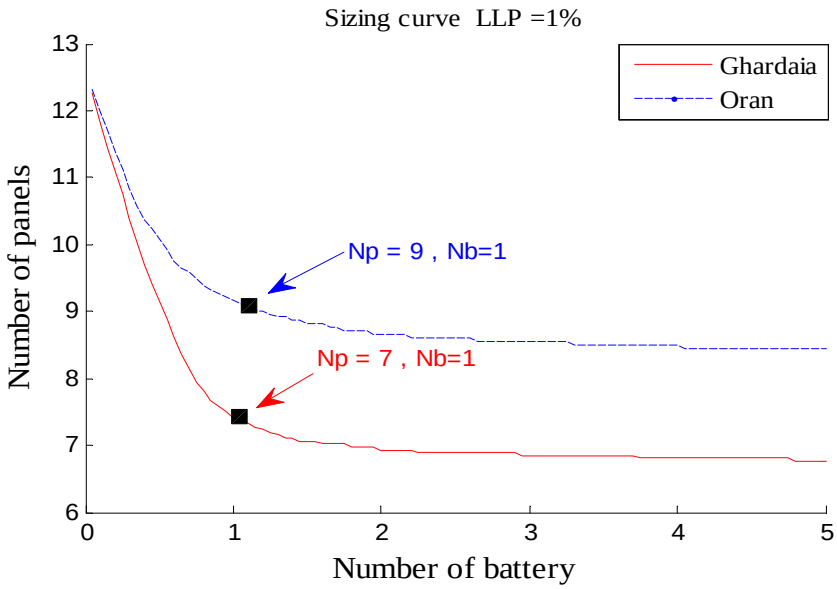

Figure 5.11: Sizing curve (LLP = 1% ; load profile N°1) for Ghardaia and Oran.

5.6 Conclusion

The models presented in previous chapters can be used in multiple applications such as sizing of stand-alone PV systems. From the results of the stand-alone sizing we can note clearly that the sizing in hourly is more efficacious and give better results that in a daily basis. Moreover, we discover that the centre of the Algerian Sahara is the most suitable place to install PV system contrary to the north of the country. Finally, the proposed models to estimate and forecast solar radiation give good results when they used in some useful applications in the field of PV systems.

Nomenclature

A_f	Actualization factor.
A_g	Used photovoltaic array area, m2.
A_r	Actualization rate.
B	Temperature coefficient.
c	Number of clusters.
C_A	Capacity of the photovoltaic panel array.
C_B	Nominal battery capacity, Ah.
C_b	Price of the battery, $.
C_c	Total components cost, $.
C_m	Maintenance cost, $.
$C_{m(1)}$	Maintenance cost of one year, $.
C_p	Price of one panel, $.
C_r	Total replacement cost, $.
C_r'	System cost, $.
C_S	Capacity of the storage system.
C_t	Actualized total cost, $.
C_U	Maximum battery useful capacity, Wh.
d	Standard deviation.
$d^2(x_k, v_i)$	Distance measure between data and cluster centre.
DOD	Maximum depth of discharge.
E^{AUX}	Auxiliary generator.
E_f	Annual expansion factor.
Err	Error.
FCM	Fuzzy c –means.
GA	Genetic algorithm.
$H_{g\beta i}$	Hourly global solar radiation received on inclined surface, Wh/m^2.
$\overline{H_{g\beta i}}$	Mean hourly global solar radiation received on inclined surface, Wh/m^2.

I	Output PV module current.
I_{01}, I_{02}	Reverse saturation currents of the diodes D1 and D2 respectively.
I_{ph}	Current generated by the incident light.
J_{FCM}	Objective function.
L_F	System life time, year.
LLP	Load of loss probability.
$LLPs$	Desired LLP.
L_t	Load at time t, W.
MPPT	Maximum Peak Power Tracking.
n_1, n_2	Ideality factors of diodes D1 and D2.
n_b	Battery life time, year.
N_b	Number of batteries.
N_p	Number of panels.
q	Weighting exponent on each fuzzy membership.
R_f	Replacement factor.
R_ss	Series resistance.
R_{sh}	Shunt resistance.
SAPV	Stand-alone photovoltaic systems .
SOC	State of charge.
T_c	Cell temperature, °C.
T_r	Reference temperature of the panel, °C.
$U(t)$	Membership matrix.
u_{ik}	Degree of membership.
V	Output PV module voltage.
$V(t)$	Cluster centre matrix.
V_B	Voltage for the unit of storage, V.
v_i	Centre of the i^{th} cluster .
V_t	Thermal voltage.

ε	Small error.
η_p	Efficiency of a solar cell at a referenced solar radiation.
$\eta.$	Total panels efficiency.
τ	Delay time.

References

Ambrosone G, Catalonotti S, Coscia U, Troise G. Comparison between power and energy methods of analyses of photovoltaic plants. Sol Energy 1985;34:1–8.

Avril S, Arnaud G, Florentin A, Vinard M. Multi-objective optimization of batteries and hydrogen storage technologies for remote photovoltaic systems. Energy 2010; 35: 5300-5308.

Barra L, Catalanotti S, Fontana F, Lavorante F. An analytical method to determine the optimal size of a photovoltaic plant. Sol Energy 1984;33:509–14.

Bartoli B, Cuomo V, Fontana F, Serio C, Silvestrini 5. The design of photovoltaic plants: an optimization procedure. Appl Energy 1984;18:37–47.

Bezdek JC. Pattern Recognition with Fuzzy Objective Function Algorithms. New York: Plenum Press, 1981.

Cabral CVT, Filho DO, Diniz ASAC, Martins JH, Toledo OM, Machado Neto B. stochastic method for stand-alone photovoltaic system sizing. Sol Energy 2010; 84 : 1628–1636.

Charma VK, Golangelo A, Spagna G. Photovoltaic technology: basic concepts, sizing of a stand-alone photovoltaic system for domestic applications and preliminary economic analysis. ENERG CONVERS MANAGE. 1995; 36: 161-174.

Chen SG. An efficient sizing method for a stand-alone PV system in terms of the observed block extremes. APPL ENERG 2012; 91: 375-384.

Chiu S. Fuzzy Model Identification Based on Cluster Estimation. J INTELL FUZZY SYST 1994; 3: 267–278

Dufo-Lopez R, Bernal-Agustin JL, Yusta-Loyo JM, Dominguez-Navarro JA, Ramirez-Rosado IJ, Lujano J, Aso I. Multi-objective optimization minimizing cost and life cycle emissions of stand-alone PV–wind–diesel systems with batteries storage. APPL ENERG 2011; 88:4033–4041.

Dunn JC. A Fuzzy Relative of the ISODATA Process and its Use in Detecting Compact Well Separated Clusters. J CYBERNETICS 1974; 3: 32–57.

Egido M, Lorenzo E. The sizing of stand-alone PV-systems: a review and a proposed new method. SOL ENERG MAT SOL C 1992; 26: 51-69.

Eltawil M A, Zhao Z. MPPT techniques for photovoltaic applications. RENEW SUST ENERG REV 2013; 25: 793-813.

Fadaee M, Radzi M.A.M. Multi-objective optimization of a stand-alone hybrid renewable energy system by using evolutionary algorithms: A review. RENEW SUST ENERG REV

2012; 16: 3364– 3369.

Hongxing Y, Wei Z, Chengzhi L. Optimal design and techno-economic analysis of a hybrid solar–wind power generation system. APPL ENERG 2009; 86 :163–169.

Hontoria L, Aguilera J, Zufiria P. A new approach for sizing stand alone photovoltaic systems based in neural networks. Sol Energy 2005;78:313–319.

Jakhrani AQ , Othman A, Ragai A, Rigit H, Samo SR, Kamboh SA. A novel analytical model for optimal sizing of standalone photovoltaic systems. Energy 2012; 46: 675-682.

Kamarzaman NA, Tan CW. comprehensive review of maximum power point tracking algorithms for photovoltaic systems. RENEW SUST ENERG REV 2014; 37: 585-598

Kaplani E, S. Kaplanis S. A stochastic simulation model for reliable PV system sizing providing for solar radiation fluctuations. APPL ENERG 2012; 97: 970-981.

Khatib T, Azah M, Sopian K. A review of photovoltaic systems size optimization techniques. RENEW SUST ENERG REV 2013; 22 : 454–465.

Labed S, Lorenzo E. The impact of solar radiation variability and data discrepancies on the design of PV systems. Renew Energy 2004;29:1007–22.

Liao S, Chu P, Hsiao P. Data mining techniques and applications – A decade review from 2000 to 2011. Expert Syst Appl 2012; 39:11303–11311.

Lorenzo E, Narvarte L. On the usefulness of stand-alone PV sizing methods. Prog Photovoltaics Res Appl 2000;8:391–409.

Lucio H, Valdes R, Rodrıguez LR. Loss-of-load probability model for stand-alone photovoltaic systems in Europe. Sol Energy 2012; 86: 2515–2535.

MacQueen JB. Some methods for classification and analysis of multivariate observations. In: Proceedings of 5th Berkeley symposium on mathematical statistics and probability 1. University of California Press; 1967. p. 281–297.

Mellit A, ANN-based GA for generating the sizing curve of stand-alone photovoltaic systems. ADV ENG SOFTW 2010; 41: 687-693.

Mingoti SA,Lima JO. Comparing SOM neural network with Fuzzy c-means, k-means and traditional hierarchical clustering algorithms. EUR J OPER RES 2006; 174: 1742-1759.

Posadillo R, Lopez Luque R. Approaches for developing a sizing method for stand-alone PV systems with variable demand. RENEW ENERG 2008;33: 1037–1048.

Sandberg I, Xu L. Uniform approximation of multidimensional myopic maps, IEEE T CIRCUITS SYST: Fundamental Theory and Applications 1997; 44, no. 6: 477–485.

Sidrach-de-Cardona M, Mora Lopez Ll. A simple model for sizing stand-alone photovoltaic systems. SOL ENERG MAT SOL C 1998 ;55 : 199-214.

Takens F. Detecting strange attractors in turbulence, Dynamical Systems and Turbulence In: Rand DA, Young LS. Editors. LECT NOTES MATH 1981; 898: p. 366-381.

Wissem Z, Gueorgui K, Hédi K. Modeling and technical economic optimization of an autonomous photovoltaic system. Energy 2012; 37 : 263-272.

Xu R, Donald. Survey of Clustering Algorithm, IEEE T NEURAL NETWOR 2005; 16: no. 3, 46-51.

Yager, R.R.; Filev, D.P.*Approximate clustering via the mountain method.* IEEE T SYST MAN CYB 1994; 24: 1279 – 1284.

General conclusion and perspectives

Various applications of thermal energy systems and photovoltaic conversion of solar energy require a detailed study of solar radiation received at ground level. Any investigation in the field of solar energy needs adequate and proper information on the evolution of the solar radiation during a given period for a specific geographical location. Evaluation of solar radiation is used to simulate the behaviour of the solar energy systems. Thus, it is an important task to give accurate models in order to guarantee the optimal functioning of any solar energy system. At the top of the atmosphere, the solar radiation can be predicted with great accuracy since it mainly depends on geographical and astronomical parameters. On the ground, the prediction is more difficult due to the interaction of the direct solar radiation in the atmosphere in the presence of aerosols, water vapor, cloud and other surfaces. Therefore, this influence must be determined by studying of the components of sunlight as well as the data measured at ground radiometric stations. However, the density of meteorological network is low across the countries over the world. Taking the example of Algeria, with an area of 2,381,741 km^2, less than 60 radiometric stations give information about sunshine duration and less than 6 stations give information about the amount of solar radiation. Hence, theoretical methods are used to estimate the incident solar energy in the areas where there are no measurements. The data obtained is used in different applications such as optimal sizing PV systems.

In this thesis, we proposed a range of models and algorithms for estimating and forecasting solar radiation using geographical, astronomical and meteorological parameters as well as the measured data in order to use them in some useful applications in the field of solar energy. Some of these models are proposed in the literature by various scientific researche and proven to be valid for several locations in the world. And, other models are proposed in this thesis as original scientific papers, namely in the estimation of solar radiation using a novel satellite image approach (based on GISTEL model), forecasting using two new hybrid models (ARMA and NAR models, k-means and NAR models) and some applications such as sizing of stand-alone PV systems, fault detections and estimation of the outputs of the PV systems. These models are tested for the territory of Algeria, where there are some measured solar radiation data collected in some locations (Ghardaia, Bouzareah and Oran). The comparison is made generally between measured and simulated data by these models.

Before that, the solar zones of the country were made by applying the Kriging interpolation method for the monthly sunshine duration measured at 56 meteorological stations for 10 years. It allowed us to extract from these two information: the amount of sunshine received at a site and its evolution during the year. This, helps to distinguish six energetic zones in Algeria.

Secondly, we show the possibility to study the evolution of various astronomical parameters (declination, height, solar azimuth, sunrise and sunset ...), and solar components (direct, diffuse and global) received on any day with a collecting area of any location, whether hori-

zontal or inclined by simply entering data (day, month, geographical settings and sometimes some weather parameters). A comparative study has been elaborated to the different models for estimating the amount of solar radiation. Semi-empirical models and meteorological show good accuracy in clear sky weather. However, they are limited in the case of cloudy sky. Physical models, which based on satellite image processing (improved GISTEL model), give good results in cloudy sky conditions compared with other models.

In addition, we present in this thesis two novel forecasting models based on hybrid methodology. First, we introduced a hybrid model that combined both ARMA and NAR models for multi-step ahead forecasting of hourly global horizontal solar radiation time. Combining linear and nonlinear components of any solar radiation time series seem to be the best method for forecasting such similar problems. Second, we presented a time series forecasting methodology based on hybrid k-means and NAR models. The obtained experimental results showed that the clustering is quite good to interpret the behaviour of the series. It gives some information about the future regions and the behaviour of the forecasted time series using NAR model. Both of the two hybrid methods are novel. However, they may need some heavy calculation.

Finally, we apply the developed models for sizing stand-alone photovoltaic systems. We have proved using a novel algorithm the importance of sizing in our PV system application, especially in the economic point of view. We found that it would be more appropriate to use hourly solar radiation data rather than daily data for optimal sizing. In addition, we showed that southern Algeria is very favourable compared to the north by the nature of its solar resources for the implementation of photovoltaic power plants. Moreover, the outputs of a PV system can be determined by using the obtained forecasted series of the proposed models in this thesis. In addition, other applications can be studied based on the developed model such as fault detection in PV array, which is improved to be simple and useful using only input solar radiation data and other simple calculation algorithms.

In conclusion, the goal of this thesis is reached. This work represents an important advance in the understanding and effective use of solar radiation modelling for the sustainable exploitation of the huge solar potential in the Algerian Sahara. However, the actual outcome of this great goal requires broad consultation involving politicians, industrialists and scientists.

Perspectives

The future of renewable energies will be part of our life. Climate change concerns high prices of fossil fuels and increasing political support are driving renewable energy prospects. This thesis is considered a powerful support for each research in the field of solar radiation quantification; it gives a detailed description of several models of solar radiation studying from the top of the atmosphere to the ground level. The results obtained from it can be used in solar power generators ranging from small standalone to large grid-connected systems.

Future works can improve the results of this thesis. Testing other models, whether for estimation or forecasting could be the complementary part of this thesis. Other satellite approaches can be used as comparative studies with the GISTEL model used in our thesis. In addition, hybrid model showed a good utility and accuracy. Hence, future works can test other hybrid methods combining classical and artificial intelligence techniques for best results. Moreover, we applied our results only on stand-alone PV systems. Other works can apply the proposed models in grid connected systems. There are many applications of the models

studied in this thesis. We choose only two of them (fault detection and estimation of PV system outputs) and future researchers can test other types of applications. In fact, two PhD thesis are proposed which based on the quantification of solar radiation. The first one is the monitoring of PV systems based on the estimation of solar radiation. And, the second is testing the MPPT technics of PV systems under shadow. Moreover, the practical part of this thesis already begins in the laboratory of the University of Laghouat, that use essentially the model elaborated in order to obtain optimal and efficacy PV system installation.

Appendix A

A.1 Artificial Intelligence Techniques

(AI) is defined as the study and design of intelligent agents. An intelligent agent is an autonomous entity that perceives its environment, directs its activity toward achieving goals and takes actions that maximize its chances of success. AI methods are highly successful in dealing with incomplete or uncertain input data. Most important, they are often capable to solve problems where the existing dependencies are too complex or insufficiently known to be programed in a traditional, rigid manner. There are several approaches developed in AI such as: Genetic Algorithms (GA), Expert Systems (ES), Artificial Neural Networks (ANN), Fuzzy Logic (FL), and some hybrid systems that combine the above techniques. Several approaches for forecasting solar irradiance at different time horizon based on AI techniques have been reported. These approaches can be categorized in three groups:

- The models in the first group estimate solar irradiance based on meteorological parameters;
- The second group includes models which predict the actual solar irradiance based on past observed data;
- Models from the third group combine the defining approaches of the first and second group.

A.2 Artificial neural networks

One type of network sees the nodes as 'artificial neurons'. These are called artificial neural networks (ANNs). An artificial neuron is a computational model inspired in the natural neurons. Natural neurons receive signals through synapses located on the dendrites or the membrane of the neuron. When the signals received are strong enough (surpasses a certain threshold), the neuron is activated and emits a signal through the axon. This signal might be sent to another synapse, and might activate other neurons.

The complexity of real neurons is highly abstracted when modelling artificial neurons. These basically consist of inputs (like synapses), which are multiplied by weights (strength of the respective signals), and then computed by a mathematical function which determines the activation of the neuron. Another function (which may be the identity) computes the output of the artificial neuron (sometimes in dependence of a certain threshold). ANNs combine artificial neurons in order to process information.

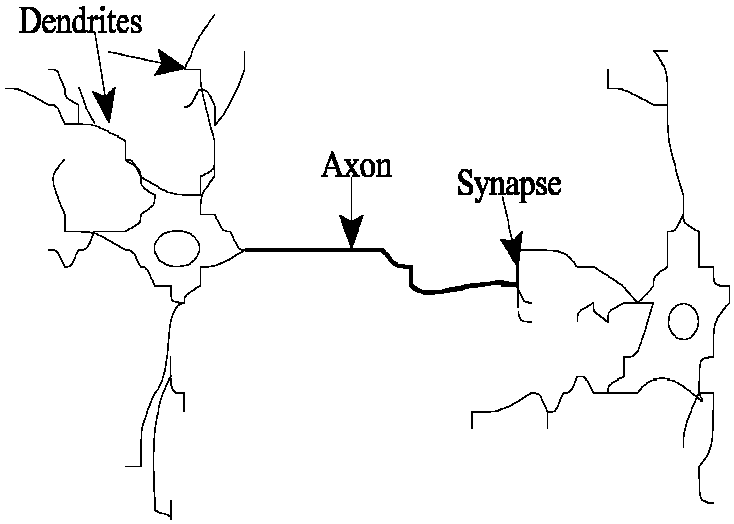

Figure A.1: Natural neuron.

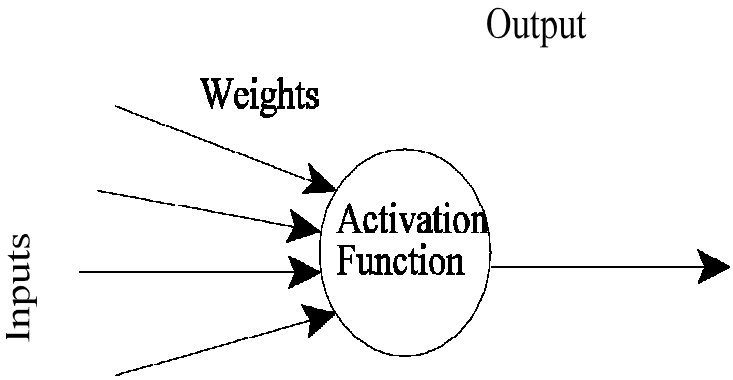

Figure A.2: Artificial neuron.

$$Output = Activation function\left(\sum inputs * weights\right)$$

Using mathematical notation, the output of a neuron can be written as follows

$$y = f\left(b + \sum_i w_i x_i\right) \tag{A.1}$$

Here, b is the bias for the neuron. The bias input to the neuron algorithm is an offset value that helps the signal to exceed the activation function's threshold.

A.2.1 Activation Function

The activation function, denoted $f(v)$, defines the output of the neuron in terms of the local field v. Three basic types of activation functions are as follow:

a) Threshold Function (or Heaviside Function)

A neuron employing this type of activation function is normally called McCulloch-Pitts model. The model has an all-or-none property.

$$f(v) = \begin{cases} 1 & if \quad v \geq 0 \\ 0 & if \quad v < 0 \end{cases} \tag{A.2}$$

b) Piecewise-Linear Function

This form of activation function may be viewed as an approximation to a non-linear amplifier. The following definition assumes the amplification factor in the linear region is unity.

$$f(v) = \begin{cases} 1 & if \quad v \geq 1/2 \\ v & if \quad -1/2 < v < 1/2 \\ 0 & if \quad v < -1/2 \end{cases} \tag{A.3}$$

c) Sigmoid Function

This is the most common form of activation function used in artificial neural networks. An example of a sigmoid function is the logistic function, defined by:

$$f(v) = \frac{1}{1 + \exp(-av)} \tag{A.4}$$

Where $a > 0$ is the slope parameter. In the limit as $a \to \infty$, the sigmoid function simply becomes the threshold function. However, unlike the threshold function, the sigmoid function is continuously differentiable (differentiability is an important feature when it comes to network learning).

A.2.2 Architectures of Neural Networks

a) Single-Layer Feed-Forward Networks

The simplest form of a layered network, consisting of an input layer of source nodes that project onto an output layer of neurons. The network is strictly feed forward, no cycles of the information are allowed. Fig.A.3 shows an example of this type of network. The designation of single-layer refers to the output layer of neurons; the input layer is not counted since no computation is performed there.

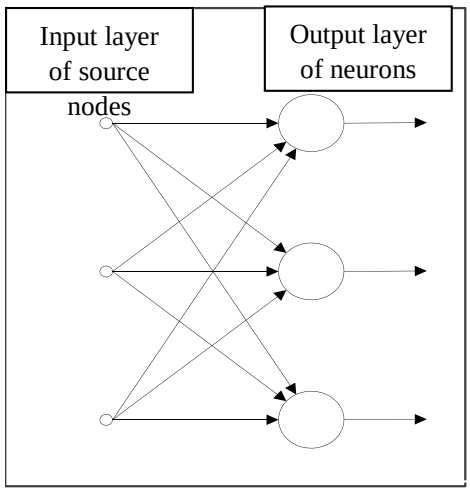

Figure A.3: Single-Layer Feed-Forward Neural Network.

b) Multi-Layer Feed-Forward Networks

The Multi-Layer Perceptron (MLP) extends the Perceptron model with hidden layers between input and output layers. It is a feed-forward network, typically trained with back-propagation. Conceptually, the MLP architecture consists of an input layer, one or more hidden layers of neurons with non-linear activation functions and the output layer. Hidden layers are not exposed to input vectors, as input and output layers are. A MLP network is illustrated in Fig.A.4.

c) Recurrent Networks

A recurrent neural network has a similar architecture to that of a multi-layer feed-forward neural network, but contains at least one feedback loop. This could be self-feedback, a situation

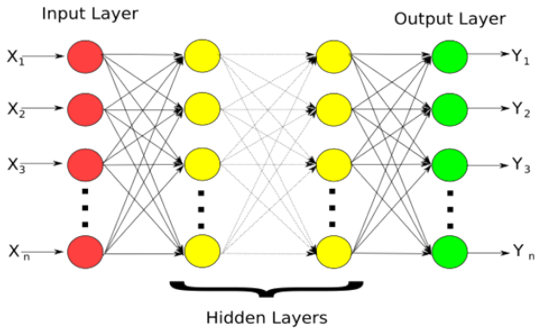

Figure A.4: Example of a MLP network

where the output of a neuron is fed-back into its own input, or the output of a neuron could be fed to the inputs of one or more neurons in the same or preceding layers.

A.2.3 Learning

A crucial part of the working of a neural network is the learning step. There are various ways to let a network learn, for example, supervised training (show the network the right output to an input), reinforcement learning (giving the network feedback on its given output) or unsupervised learning (the network can learn what is good and bad all by itself).

A.2.3.1 Back-propagation

Back-propagation has been, by far, the most popular and widely used learning technique for training ANN. The goal of the training process is to obtain a desired output when certain inputs are given. Since the error is the difference between the actual output $y(k)$ and the desired output $y_d(k)$, the error depends on the weights w_{ij}, and we need to adjust the weights in order to minimize the global quadratic error ε. We can define the error function for the output of each neuron:

$$\varepsilon = (y_d(k) - y(k))^2 \tag{A.5}$$

We take the square of the difference between the output and the desired target because it will be always positive, and because it will be greater if the difference is big, and lesser if the difference is small. The error of the network will simply be the sum of the errors of all the neurons in the output layer

$$\varepsilon = \frac{1}{2}\sum_k (y_d(k) - y(k))^2 \tag{A.6}$$

The back propagation algorithm now calculates how the error depends on the output, inputs, and weights. After we find this, we can adjust the weights using the method of gradient descendent

$$\Delta w_{ij} = -\alpha \frac{\partial \varepsilon}{\partial w_{ij}} \tag{A.7}$$

This formula can be interpreted in the following way: the adjustment of each weight w_{ij} will be the negative of a constant α multiplied by the dependence of the i previous weight on the error of the network, which is the derivative of ε in respect to w_{ij}.we use this until we find appropriate weights (the error is minimal) in the layer m.

$$\Delta w_{ij}^m = -\alpha \frac{1}{2}\frac{\partial}{\partial w_{ij}^m}\left(\sum_k \left(y_d(k) - y^{m+1}(k)\right)\left(y_d(k) - y^{m+1}(k)\right)\right) \tag{A.8}$$

$$= -\alpha \sum_k \left(y_d(k) - y^{m+1}(k)\right)\frac{\partial y^{m+1}(k)}{\partial w_{ij}^m} \tag{A.9}$$

With

$$\frac{\partial y^{m+1}(k)}{\partial w_{ij}^{l}} = \frac{\partial}{\partial w_{ij}^{m+1}} f^{m+1}(x^{m+1}(k)) \tag{A.10}$$

$$x^{m+1}(k) = \sum_{ij} w_{ij}^{m+1} y_{ij}^{m}(k) \tag{A.11}$$

We obtain

$$\Delta w_{ij}^{m} = \alpha \sum_{k} \left(y_d(k) - y^{m+1}(k)\right) w_{ij}^{m+1} f^{(m+1)'}(x^{m+1}(k)) f^{m'}(x_{ij}^{m}(k)) y_{ij}^{m-1}(k) \tag{A.12}$$

Now we introduce the elementary error :

$$\begin{aligned} \delta^{m+1}(k) &= \left(y_d(k) - y^{m+1}(k)\right) f^{(m+1)'}(x^{m+1}(k)) \\ \Delta w_{ij}^{m} &= \alpha \sum_{k} \delta^{m+1} y_{ij}^{m} \end{aligned} \tag{A.13}$$

Generally we have :

$$\delta^{m}(k) = \left\{ \sum_{k} \delta^{m+1}(k) w_{ij}^{m+1}(k) \right\} f^{m'}(x_{ij}^{m}(k)) \tag{A.14}$$

And

$$\Delta w_{ij}^{m} = \alpha \sum_{k} (y_d(k) - y^{m}(k)) f^{m'}(x_{ij}^{m}(k)) y_{ij}^{m-1}(k) \tag{A.15}$$

A summary of the technique is given below:

- Feed the MLP with a training sample;
- Compare the output to the desired output from that sample and calculate the error in each neuron (this is the local error);
- The local error is assumed to be caused by the neurons of the previous level, proportionally to the weight value of each neuron connection arriving to the level under investigation;
- Adjust the weights arriving to each neuron to minimize the local error;
- Repeat the steps above to the previous level (backwards) using as error the neurons' contribution to the local error of the previous step.

A.3 Fuzzy Logic

In classical logic, every proposition must either be True or False, excluding the middle. Fuzzy logic (FL) introduced in 1965 by Zadeh is designed to allow computers to make use of the distinctions among data with shades of grey. That means it studies the middle between the True and False. The main advantage of fuzzy logic is their ability to describe the knowledge in a descriptive human-like manner as simple logical rules using linguistic variables only.

A.3.1 Fuzzy logic concept

The Fuzzy logic is based on three essential steps as shown in Fig.A.5.

A.3.1.1 Fuzzification

It is a coding process that consists of converting numerical values of a linguistic variable into a membership function value.

a. Linguistic variables

Linguistic variables are the input or output variables of the system whose values are words or sentences from a natural language, instead of numerical values. A linguistic variable is generally decomposed into a set of linguistic terms. For example, let the sky be linguistic the variable which represents the sky cases. To qualify the sky, terms such as " clear" , "cloudy" , "partially" cloudy are used in real life. These are the linguistic values of the sky. Each member of this decomposition is called a linguistic term and can cover a portion of the overall values of the day case.

b. Membership Functions

Membership functions are used in the fuzzification and defuzzification steps of a FL, to map the non-fuzzy input values to fuzzy linguistic terms and vice versa. A membership func-

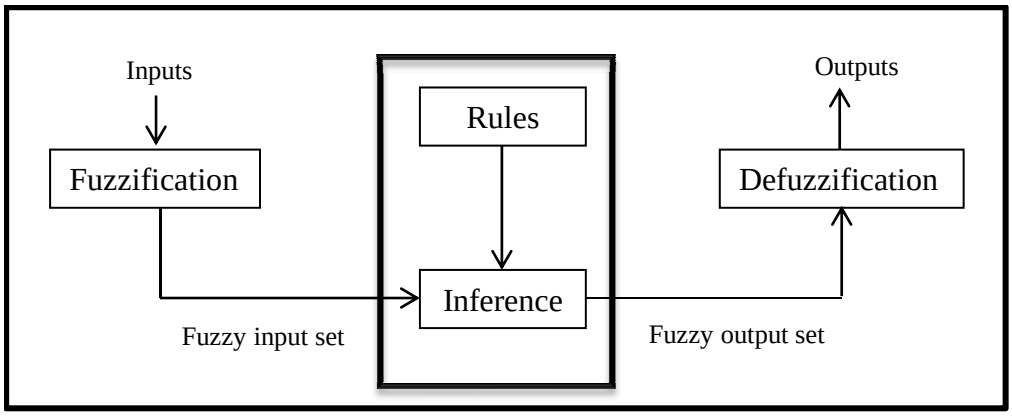

Figure A.5: Fuzzy logic concept.

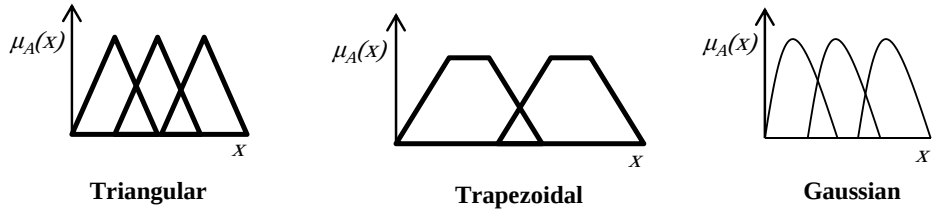

Figure A.6: Different forms of the membership function.

tion is used to quantify a linguistic term. It can be defined as follows. If X is a collection of objects, the associated fuzzy set A is defined as

$$A \equiv \{(x, \mu_A(x)) : x \in X\} \tag{A.16}$$

Where, $\mu_A(x)$ is the membership function showing the degree of affiliation of the element x to the fuzzy set A. Different forms of the membership function are used in literature, among them, triangular, trapezoidal, and Gaussian shapes as shown in Fig. A.6. In addition, one value can belong to multiple sets at the same time.

A.3.1.2 Inference rules

In fuzzy logic, the output variables are controlled by a rule base between different membership functions. Generally, these rules expressed in the form of IF-THEN rule. The following example shows how this rule is worked. Let x the membership function values of the fuzzy set A (the linguistic terms of A areA_1 and A_2) and y the membership function values of the fuzzy set B (the linguistic terms of B are B_1 and B_2) . And let z the resulting command associated with the output fuzzy set C (the linguistic terms of C are C_1, C_2, C_3 and C_4).

The construction of the fuzzy rules can be expressed as follows,

- Rule 1: **IF** x is A_1 **And** y is B_1 **Then** z is C_1
  OR
- Rule 2: **IF** x is A_2 **And** y is B_1 **Then** z is C_2
  OR
- Rule 3: **IF** x is A_1 **And** y is B_2 **Then** z is C_3
  OR
- Rule 4: **IF** x is A_2 **And** y is B_2 **Then** m is C_4

- The fuzzy operator AND is used in the computation in the conclusion between two membership functions.

- The fuzzy operator OR is used between all the rules to obtain the final result.

-The set of rules is called rule matrix.

a. Operations on Fuzzy Sets

To build a fuzzy set theory, some logical operation (such as And, Or, and complement) between the elements of the sets must be defined through the membership functions as follow

Fuzzy intersection (AND)

$$\mu_{A\cap B}(x) = \min\left(\mu_A(x), \mu_B(x)\right), \quad \forall x \in X \tag{A.17}$$

Fuzzy intersection (OR)

$$\mu_{A\cup B}(x) = \max\left(\mu_A(x), \mu_B(x)\right), \quad \forall x \in X \tag{A.18}$$

Fuzzy complement (NON)

$$\mu_{\overline{A}} = 1 - \mu_A(x), \quad \forall x \in X \tag{A.19}$$

A.3.1.3 Deffuzification

This is the decoding phase, which consists of converting the output fuzzy set results from the inference process into a crisp (numerical) values. Several defuzzification methods are proposed in the literature. The most popular is the centre of gravity method. It is expressed by the following equation

$$y = \frac{\sum\limits_i c_i \int \mu_{y_i}(x)dx}{\sum\limits_i \int \mu_{y_i}(x)dx} \tag{A.20}$$

c_i is the centre of the membership function (generally, the value of the variable x where the membership function reaches its peak) and the integral $\int \mu_{yi}\left(x\right) dx$ represents the surface under the membership function $\mu_{yi}(x)$ corresponding to the attribute i of the output linguistic variable y.

A.4 Genetic algorithms

Genetic Algorithms (GAs) are adaptive heuristic search algorithm based on the evolutionary ideas of natural selection and genetics. The basic techniques of the GAs are designed to simulate processes in natural systems necessary for evolution. GAs offer a new and powerful approach to the optimization problems, and their use is made possible by the increasing availability of high performance computers at relatively low costs.

The main idea of GAs is the optimization of an objective function. The Algorithm starts with a set of solutions (represented by chromosomes) called a population. Each candidate solution has a set of properties (its chromosomes or genotype) which can be mutated and altered. Solutions from one population are taken and used to form a new population. This is motivated by a hope that the new population will be better than the old one.

The steps of the GA are shown in Fig. A.7, and summarized as follow,

1. *Initialization*: initial randomly the individuals as parents from the current population to produce children for the next generation.
2. *Selection*: using a fitness function (objective function) which indicates the quality of the represented solution, a selection of the new generation was achieved based on the optimum fitness function values of the current individuals.
3. *Crossover and mutation*: in this step, a pair of parents was selected to generate new children solutions, which share many characteristics of their parents due to the crossover and mutation of the chromosomes of the parents. During the processes, each new child has a new pair of parents until a new population of solutions of the proper size is generated.
4. *Generalization* : the generalization process is repeated until the optimum solution is reached.

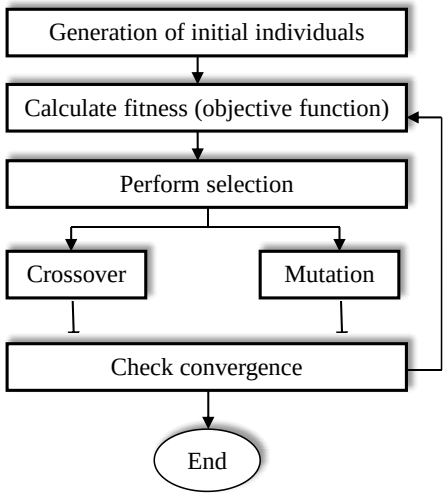

Figure A.7: The principle structure of the GA method.

Energy Conversion and Management 75 (2013) 561–569

Contents lists available at SciVerse ScienceDirect

Energy Conversion and Management

journal homepage: www.elsevier.com/locate/enconman

Forecasting hourly global solar radiation using hybrid *k*-means and nonlinear autoregressive neural network models

Khalil Benmouiza [a,1], Ali Cheknane [b,*]

[a] Département de Physique, Faculté des Sciences, Université Abou-Beker Belkaid de Tlemcen, BP 119, Tlemcen 13000, Algerie
[b] Laboratoire des Semiconducteurs et Matériaux Fonctionnels, Université Amar Telidji de Laghouat, Algérie, BP 37G, Laghouat 03000, Algerie

ARTICLE INFO

Article history:
Received 14 May 2013
Accepted 5 July 2013

Keywords:
Forecasting solar radiation
Artificial neural networks
Clustering
Phase space reconstitution

ABSTRACT

In this paper, we review our work for forecasting hourly global horizontal solar radiation based on the combination of unsupervised *k*-means clustering algorithm and artificial neural networks (ANN). *k*-Means algorithm focused on extracting useful information from the data with the aim of modeling the time series behavior and find patterns of the input space by clustering the data. On the other hand, nonlinear autoregressive (NAR) neural networks are powerful computational models for modeling and forecasting nonlinear time series. Taking the advantage of both methods, a new method was proposed combining *k*-means algorithm and NAR network to provide better forecasting results.

1. Introduction

The generation of the energy in our modern industrialized society is still mainly based on a very limited resource. Some projections show that the global energy demands will almost triple by 2050 [10]. Thus, the search for alternative energy resources has become an important issue for our time. Solar energy is becoming a very attractive solution since it is considered an essentially inexhaustible and broadly available energy.

For an efficient conversion and utilization of solar power, solar radiation data should be measured continuously and accurately over the long-term. However, the measurement of solar radiation is not available for all countries in the world due to some technical and fiscal limitations. Hence, several studies were proposed in the literature to find mathematical and physical models to estimate and forecast the amount of solar radiations such as stochastic prediction models based on time series methods [14,36,39,40] and artificial neural network approaches [11,2,4].

Classical linear time series models like autoregressive moving average modeling [3] have been widely used in modeling of linear time series [36]. Even so, it was proven that they are inadequate in the analysis and prediction of solar radiation due to the non-stationary and nonlinearity of the solar radiation time series, especially for cloudy sky [39,1,36]. In addition, stochastic models are based on the probability estimation that needs a full identification of the mathematical function, leads to a difficult forecasting of the solar radiation time series [36]. Moreover, global solar radiation time series is a dynamical system that depends on some meteorological elements such as temperature, water vapor, suspend solids, cloud and water air condition that can represent nonlinear characteristics [36,12,38] .

To overcome this problem, nonlinear approaches, such as artificial neural networks (ANN) was considered a powerful tool for forecasting similar time series [39,28,36]. The advantages of the ANN that it does not require the knowledge of the internal system parameters that offer a compact solution for multiple variable problems [11,2,36,4]. However, single models presented a big forecasting error [36]. Thus, hybrid methods combining different models have been widely used in the literature to improve the forecast performance [36,12,5]. Nevertheless, no one of those methods will be capable of presenting information about the behavior of the solar radiation time series in the future. Hence, it was used the Time Series Data Mining (TSDM) methodology [33] which is a fundamental contribution to the fields of time series analysis and data mining that allows a search, for valuable information on nonlinear problems such as solar radiation time series [21].

Data mining is the identification of interesting structure in the data, where the structure designates patterns of the data and relationships among regions of the data; it is a process of grouping similar elements gathered closely using unsupervised clustering methods such as *k*-means and *c*-means algorithms [37]. Data mining techniques were used in a wide variety of fields for prediction. For example, in stock prices, meteorological data, customer behavior, production control and other types of scientific data [9].

Taking the two advantages of both methods, the *k*-means approach [25] for clustering the solar radiation data to extract useful

* Corresponding author. Tel.: +213 (0)29 93 21 17; fax: +213 (0)29 93 26 98.
E-mail addresses: benkhalil3@gmail.com (K. Benmouiza), cheknanali@yahoo.com, a.cheknane@mail.lagh-univ.dz (A. Cheknane).
[1] Tel.: +213 (0)778 73 85 56.

0196-8904/$ - see front matter © 2013 Elsevier Ltd. All rights reserved.
http://dx.doi.org/10.1016/j.enconman.2013.07.003

information and the ANN for forecasting purposes, a new method was proposed in this paper that combines an unsupervised *k*-means clustering algorithm and nonlinear autoregressive neural network.

At the first stage, the data obtained from the phase space reconstitution using Takens theorem [35] were clustered using *k*-mean algorithm; clustering is a process of grouping an unlabelled set of examples into several clusters such that a similar pattern is associated with every cluster. The motivation of using the *k*-means approach in this paper is due to its simplicity and also to the fact that the proposed methods do not require an advanced clustering algorithm. However, one of the vital issues of the *k*-means algorithm is the choosing of the appropriate number of clusters [37]. Therefore, a silhouette function proposed by [32,23] was used to obtain the best number of bunches.

At the second stage, the nonlinear autoregressive (NAR) neural network that is a multilayer perceptron neural network (MLP) with some modification was applied for forecasting the solar radiation time series trying different architecture to get the best network structure. Combining those two methods presented better results for multi-step ahead prediction in long term forecasting.

The remaining part of this paper is organized as follows. Section 2 presented the methodology used in this work for forecasting the solar radiation time series using time series data mining technique, a background of space phase reconstitution, *k*-means clustering algorithm and NAR network methods were also viewed. In Section 3, we simulated the forecasting results of the proposed method and comparing the results with the measured ones. The last section was devoted to the conclusion and discussion of future works.

2. Methodology

A time series is a collection of time ordered observations $x(t_i)$, each one being entered at a specific time t called a period [30]. Modeling and forecasting of the time series are an importation task to extract useful information from the data [7]. Hence, in this paper, a proposed method that relies on principles of time series analysis, unsupervised clustering, artificial neural networks and evolutionary optimization methods were proposed as presented in Fig. 1. The methodology can be outlined in the following steps:

(1) Determine the minimum, appropriate, embedding dimension for phase space reconstruction for the time series [15];
(2) Identify regions of the reconstructed phase-space which has similar characteristics using *k*-means clustering algorithm;
(3) For each cluster train different NAR neural network to generate regional predictor for forecasting local regions;
(4) Use the corresponding NAR neural network using different delay and neurons to generate a global prediction for the time series;
(5) Reconstructed phase-space of the obtained time series from step 4, then use the appropriate *k*-means method to cluster the data using the same parameters used in step 1 and step 2;
(6) To perform the forecast, assign each pattern from step 5 to the appropriate region obtained from step 3 using as a criterion the Euclidean distance:
- If the Euclidean distance between each region and the assigned pattern is small, then it was considered a better forecast, else return to step 4.

2.1. Determining an appropriate embedding dimension

Phase space reconstruction provides a simplified, multidimensional representation of a nonlinear time series that simplifies further analysis. The approach of phase-space reconstruction consists of embedding the time series into a higher-dimensional space to see the underlying dynamical system [15]. The most widely used version of embedding is a time delay embedding [35]. This method

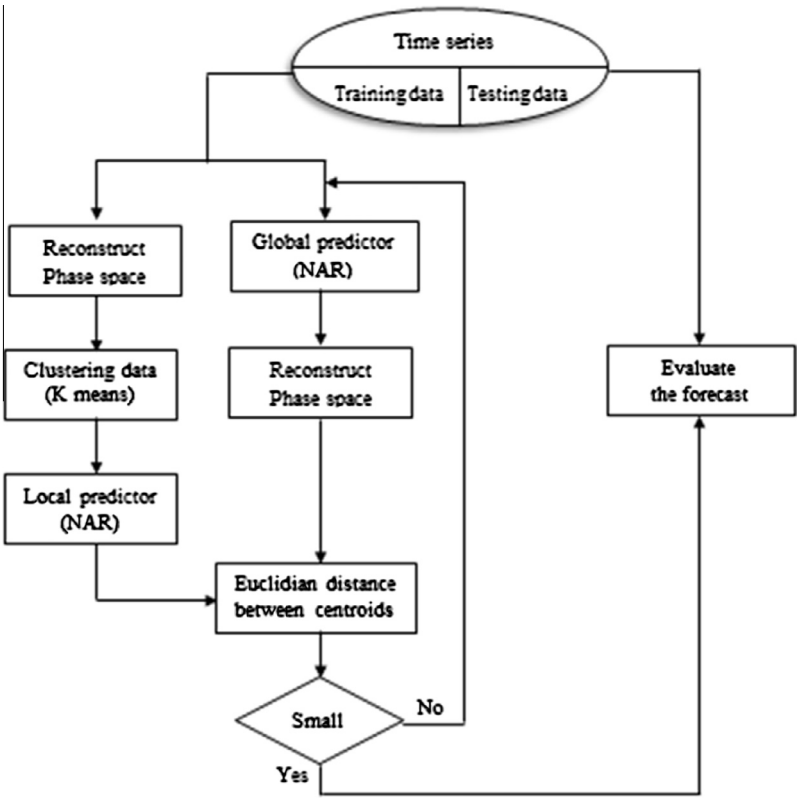

Fig. 1. The proposed methodology for time series data mining forecasting.

embeds a scalar time series $x(t_i)$ into a m-dimensional space denoted $X(t_i)$, as expressed in the following equation,

$$X(t_i) = (x(t_i), x(t_i + \tau), \cdots, x(t_i + (m-1)\tau) \quad (1)$$

where $i = (1, 2, \ldots, M)$, τ is the delay time, m is the embedding dimension, and M is the number of embedded points in the m-dimensional space given by Eq. (2). N is the total number of points of the time series and $X(t_i)$ is the embedded time series into an m-dimensional space.

$$M = N - (m-1)\tau \quad (2)$$

Several methods were presented in the literature to provide an estimation of optimal embedding dimension and time delay for better phase space reconstitution of the original time series [35,16,31]. In this paper, the mutual information method proposed by Fraser and Swinney [8] was used to set the delay coordinates. This method is summarized as follows,

- Calculating of the mutual information $I(x(t), x(t-\tau))$ of $x(t)$ and $x(t-\tau)$ for a given τ as expressed in the following equation,

$$I(x(t), x(t-\tau)) = \sum_{x \in \chi} \sum_{y \in \gamma} p(x(t), x(t-\tau)) \times \log \frac{p(x(t), x(t-\tau))}{p(x(t)) p((t-\tau))} \quad (3)$$

  $p(x(t), x(t-\tau))$, is the joint probability mass function for the marginal probability mass functions $x(t)$ and $x(t-\tau)$.
- Drawing of the mutual information function $I(t)$ for given τ,
- The optimum time delay τ is the first minimum of the mutual information function.

A small value of the delay leads to a $x(t)$ very similar to $x(t+\tau)$ then all the data stay near one other. On other hands, big delay leads to an independent coordinates and no information can be gained from the plotted data.

To determine the optimal embedding dimension m, different methods such as the box-counting dimension [26], false nearest neighbors [15], small-window solution [18] and C–C methods [16] were proposed in the literature.

In this paper, false nearest model was employed because of simple implementation and accuracy. It consists of learning how many dimensions are sufficient to embed a particular time series [15]; for a given embedding dimension, this method determines the nearest neighbor of every point in a given dimension, then checks to see if these are still close neighbors in one higher dimension. The percentage of False Nearest Neighbors should drop to 0 when the appropriate embedding dimension has been achieved.

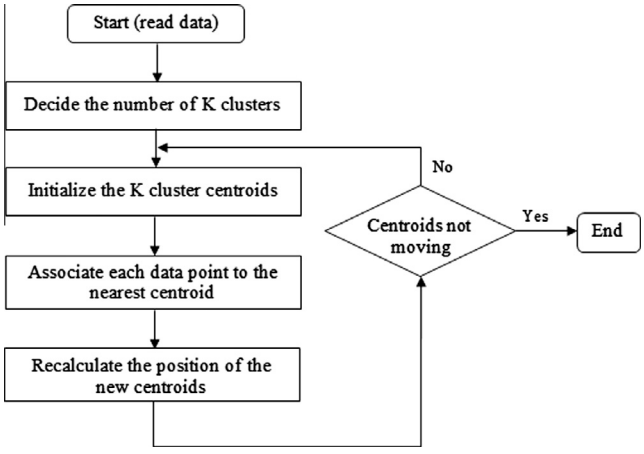

Fig. 2. k-Means clustering algorithm.

2.2. k-Means algorithm

k-Means is one of the quickest and simplest unsupervised learning algorithms to perform clustering; the method consists of classifying a given data into fixed k clusters [25,34]. The main idea is to define k centroids for each cluster; those centroids should be placed as much as possible far away from each other. In first step, each point of the data set is connected to the nearest cluster centroid by calculating the squared Euclidian distance between data point $x_i^{(j)}$ and the cluster centre c_j, as expressed by the following equation

$$\|x_i^{(j)} - c_j\|^2 \quad (4)$$

The second step consists of re-calculating the location of the new k centroid. Repeating the first and second steps until the centroids no longer move produced a separation of the objects into groups from which the objective function J expressed in Eq. (5) is minimized.

$$J = \sum_{j=1}^{k} \sum_{i=1}^{n} \|x_i^{(j)} - c_j\|^2 \quad (5)$$

A summary of k-means algorithm is shown in Fig. 2,

2.2.1. Selection of the number of clusters

The k-means algorithm is based on the selection of the optimum number of clusters [34,37]. The choosing of many clusters does not necessarily imply having a better quality of information. On the other hand, a small number of clusters produce unclear results that could muddle the pattern recognition up.

The Silhouette function [32] expressed in Eq. (6) provides a measure of the cluster separation that can be used for the interpretation and validation of clustered data. The motivation of using this technique that is simple to read, and provides a graphical representation that allows the testing of various sets of clusters. It consists of calculating the average dissimilarity $a(i)$ of the ith data within the same cluster. This criterion can be interpreted as how well-matched the ith data to those clusters are assigned to it. The next step, is to determine the average dissimilarity of the ith data with the data of another cluster, then the lowest average is denoted by $b(i)$.

$$s(i) = \frac{b(i) - a(i)}{\max\{a(i), b(i)\}} \quad (6)$$

From this equation, it is clearly shown that if $s(i)$ is close to 1 then $a(i) \ll b(i)$, which means that the values of $a(i)$ are too small, which indicate that the ith data is well matched for its cluster. Furthermore, a large $b(i)$ implies that i is badly matched to its neighboring cluster. Thus, a $s(i)$ close to 1 means that the datum is appropriately clustered. If $s(i)$ is close to minus one, then by the same logic, we can see that i would be more appropriate if it was clustered in its neighboring cluster. An $s(i)$ near zeromeans that the datum is on the border of two natural clusters.

A successful clustering has a high mean silhouette value $s(i)$. Letí et al. [23] considered a 0.6 silhouette value for all clusters as a good result. However, in real-time series, it is almost impossible to achieve this. Hence, a compromise among silhouette plots and averages was used to determine the natural number of clusters within a data set.

2.3. Nonlinear autoregressive neural network (NAR)

Artificial neural network (ANN) is a class of neural network represented by a mathematical model that is inspired by the biological nervous system; it is an intelligent system that has the ability to recognize time series patterns and nonlinear characteristics.

Hence, it has been widely used for modeling dynamic nonlinear time series [13,22].

ANN combines artificial neurons to process information; it is made up by simple neurons that are connected in a network by weighted links. Each input is multiplied by those weights that computed by a mathematical function which defines the activation of the neuron. Another activation function computes the output of the artificial neuron that depends on a certain threshold.

Using mathematical notation, the output of a neuron can be written as the following equation,

$$y = f\left(b + \sum_i w_i x_i\right) \tag{7}$$

here b is the bias for the neuron; the bias input to the neuron algorithm is an offset value that helps the signal to exceed the activation function's threshold. f is the activation function, w_i are the weights, x_i are the inputs and y represents the output.

Various types of artificial neural networks were presented in literature among them Multi-Layer Perceptron (MLP), where the neurons are grouped into an input layer, one or more hidden layers and an output layer. Recurrent Neural Networks (RNN) such as layer recurrent networks [13], Time Delay Neural Networks (TDNN) [13,36] and NAR [6,27]. In RNN, the outputs of a dynamic system depend not only on the present inputs, but also on the history of the states systems and the inputs. The NAR is a recurrent dynamic network based on a linear autoregressive model with feedback connections, including several layers of the network. It is commonly used in multi-step ahead time series forecasting; it uses past values of the actual time series to predict next values as determined by the following equation,

$$\hat{y}(t) = f(y(t-1) + y(t-2) + \cdots + y(t-d)) \tag{8}$$

f is a nonlinear function, where the future values depend only on regressed d previous values of the output signal as shown in Fig. 3. The combined history of the inputs and outputs of the system forms an intermediate inputs vector to be shown in the neural network model that could be any of the standard feed forward neural networks like MLP networks.

In addition, the RNN are based on training algorithms that used to adjust the weight values to get a desired output when certain inputs are given. Hence, various ways were presented to let a neural network learn such as supervised training where the input–output set is defined, and unsupervised learning that the output is undefined.

Back-propagation method is one of the most popular and widely used learning techniques for training RNN. It consists of minimizing the global quadratic error between the network output and the desired target by adjusting the weight values. The adjustment can be done using several algorithms such as Levemberg–Marquardt [19,25], Bayesian Regularization [24] and scaled conjugate gradient [29] algorithms. The latter one was selected to train larger networks. Once the network is trained using the preselected inputs and outputs, all the synaptic weights are saved, and the network is ready to be tested on the new input information. Since the NAR network is very similar to a Multilayer Perceptron (MPL), a modified MLP neural network was applied in this paper for predicting purposes.

3. Simulation results

In our simulation, we are interested in multi-hour ahead forecasting of the hourly global solar radiation time series using a combination of clustering techniques and nonlinear autoregressive neural networks. Hence, two global horizontal solar radiation time series were selected in this paper for simulation purposes. In all cases, the evaluation of the accuracy of the prediction methodology is accomplished by calculating the root mean square error (RMSE) expressed by Eq. (9) and the normalized root mean square error (NRMSE) given by Eq. (10),

$$\mathrm{RMSE} = \left[< (I_{i,predicted} - I_{i,measured})^2 >\right]^{\frac{1}{2}} \tag{9}$$

$$\mathrm{NRMSE} = \left(\frac{\left[< (I_{i,predicted} - I_{i,measured})^2 >\right]^{\frac{1}{2}}}{< I_{i,measured} >}\right) \tag{10}$$

RMSE and NRMSE provide information on the short-term performance of the correlations by allowing a term-by-term comparison of the actual difference between the predicted and measured values. An NRMSE value between 0.2 and 0.5 was considered by Lewis [20] to be as a good prediction model. Kostylev and Pavlovski [17] found that the best performing model on an hourly time scale had an NRMSE of 0.17 for mostly clear days and 0.32 for mostly cloudy days. Furthermore, Wu and Chan [36] found that the NRMSE error will be big in the case of cloudy skies.

In addition, a comparison between the introduced naïve autoregressive and moving average (ARMA) predictors was used to evaluate the goodness of the proposed method. ARMA model has been widely used in papers for forecasting solar radiation time series [36]. It consists of modeling a time series of its past values, as expressed in the following equation,

$$x_t = \sum_{i=1}^{p} \varphi_i x_{t-i} + e_t + \sum_{j}^{q} \theta_j e_{t-j} \tag{11}$$

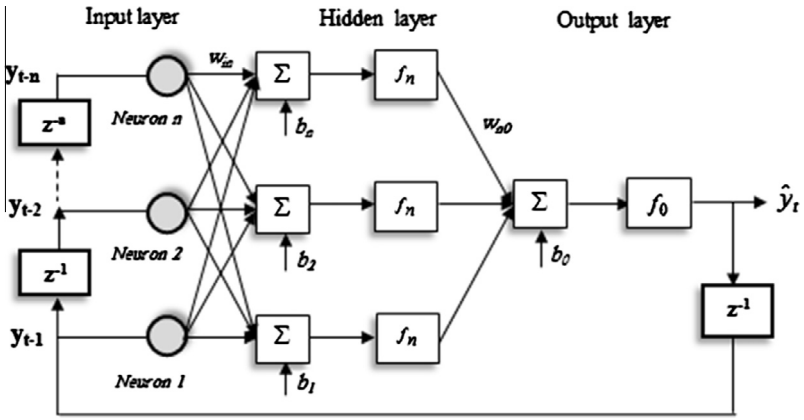

Fig. 3. Structure of NAR network.

where $\phi_i(i = 1 \ldots p)$ and $\theta_j(j = 1 \ldots q)$ are the constants representing the autoregressive AR, and the moving average MA parameters of order p, q, respectively. x_t is the actual value and e_t represents the Gaussian white noise with the mean zero in time t. The Box Jenkins methodology [3] was used to define the parameters of Eq. (11).

First, the average monthly global horizontal solar radiation time series between the years 1994 to 1996 was used. This time series takes the average of solar radiation for each hour during a month. The data were compiled from the National Meteorological Office of Algeria for the site of Oran, as shown in Fig. 4. The data set was divided into two samples of training data (from January 1994 to June 1996) and testing data (from July 1996 to December 1996), the training data set was used exclusively for model development then the test sample was used to evaluate the established model.

The first step in the analysis and prediction of this time series is the choice of an appropriate time delay, τ and the determination of the embedding dimension, m. To select τ an established approach is to use the value that yields the first minimum of the mutual information function; a time delay of 1 and an embedding dimension equal to 2 were used in the simulation.

The next step is to apply the k-means algorithm for clustering the high dimensional training data set obtained from phase space reconstitution in the previous step. At each step, different numbers of clusters were examined; the silhouette function was calculated for the determination of the right number of clusters. The metric used was squared Euclidean distance. We had plotted difference silhouette functions for the average monthly global horizontal solar radiation with a different number of clusters, and we established that the choosing of three clusters to be the best choice as shown in Fig. 5.

From Fig. 5, it is clearly shown that the most of the mean silhouette values are high. However, it is nearly impossible to arrive at a value of 0.6 for all clusters and not having negative values as the case of the first cluster. Thus, the appropriate number of clusters is usually taken when the graphical representation provides satisfactory results that mean when most of the silhouette values are high as expressed in Lletí et al. [23].

The obtained three cluster groups the solar radiation time series into three categories, high values of solar radiation which represent the noon hours, medium values that represent the day hours from 9 to 11 o'clock (or sky with medium clouds) and low solar radiation values, which represent hours of sunrise and sunset (or the presence of clouds).

After that, the NAR method with different architectures was applied to generate local predictor for each cluster that provides what we called regions for the three clusters in the future, which give more information about the doings of the global forecast of the time series in the future.

Second step consists of getting a global forecast of the hourly global solar radiation time series using different parameters of

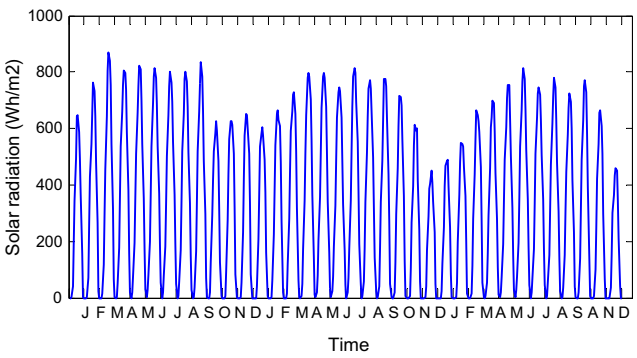

Fig. 4. Measured monthly global horizontal solar radiation data for Oran, Algeria.

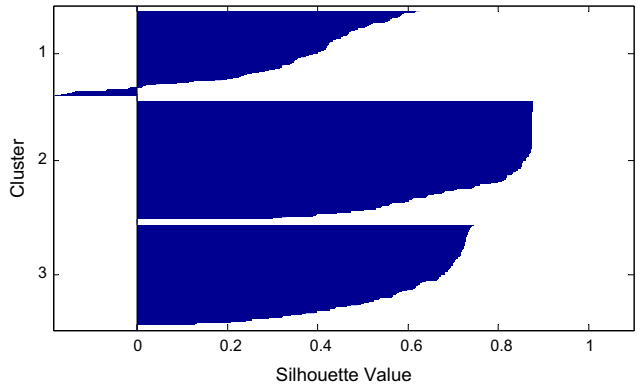

Fig. 5. Silhouette values with three clusters for the monthly horizontal solar radiation data for Oran, Algeria (from January 1994 to June 1996).

the NAR network. Using the same number of clusters and embedding parameters, a phase space of this forecasted series was used. A comparison between the centroids of the global forecasted series and centroids of the regions can show the goodness of the forecast; the two centroids of each cluster region and forecasted series should be near each other.

The results were shown in Fig. 6 which represents the phase space of the clustered regions presented by the sign of (+), and forecasted clusters represented by dots. According to Eq. (1), the plotted points represent the phase space of the solar radiation time series at time t and $t + 1$, that can visualize clearly the three kinds of clusters with low, medium and high solar radiation values. From this figure, it was shown that the most of the points of each forecasted cluster belonging to the appropriate regions. In addition, the centroids are close to each cluster that means that the forecasted series is quite good compared with the measured one.

Moreover, Fig. 7(a) shows the comparison results of the tested time series and forecasted one by the technique of k-means approach and NAR network and Fig. 7(b) represents the forecasted results using the ARMA model. The blue line is representing the testing monthly global horizontal solar radiation series between July 1996 to December 1996, and the red dot line is the forecasted series.

It's clearly shown that the forecasted series using the proposed method is virtually the same as the tested on with an RMSE equal to 60.24 W h/m^2 and NRMSE equal to 0.1985, which it was considered as a good forecast value compared to ARMA model that represents an NRMSE equal to 0.3078.

To understand more how this technique is working, we plotted a phase space of the hourly global horizontal solar radiation time

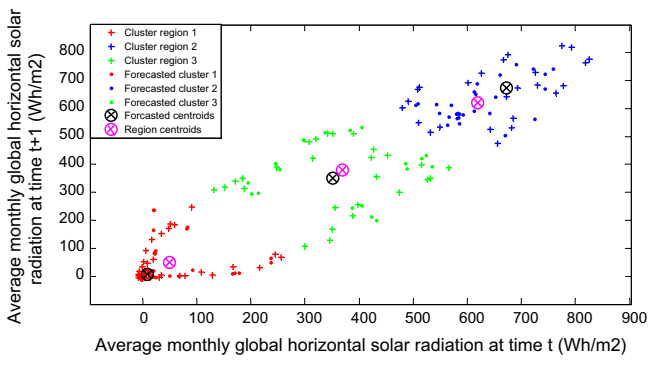

Fig. 6. Space phase reconstitution for forecasted regions and clusters of the monthly global horizontal solar radiation testing data (from July 1996 to December 1996).

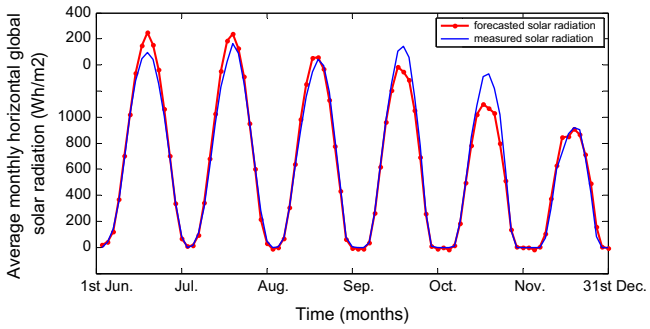

Fig. 7a. Comparison between measured monthly global horizontal solar radiation data (from July 1996 to December 1996), and forecasted by the proposed model.

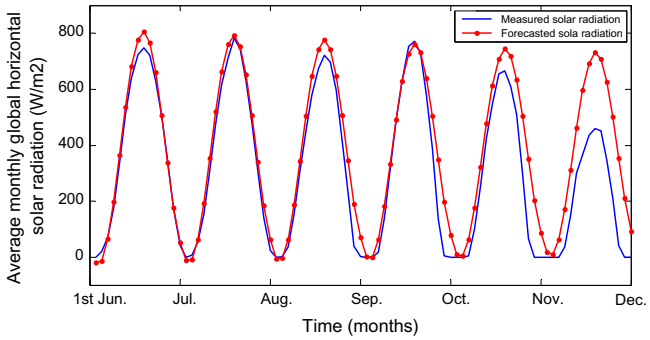

Fig. 7b. Comparison between measured monthly global horizontal solar radiation data (from July 1996 to December 1996), and forecasted by ARMA model.

series at time t and $t+1$, but with wrong NAR network parameters, as shown in Fig. 8. It can observe from this figure that the points of the clusters are mixed with each other. In addition, the centroids are too far from each other, especially for the cluster 2 and 3, leading to the fact that the obtained forecast is not good comparing by the test one as shown in Fig. 9, which represented the forecasted average monthly global solar radiation series in red and the tested series in blue, representing an NRMSE error equals to 0.5532 that is not good forecast value.

In the same way, we used this methodology for more complicated solar radiation time series that provides forecasts at one-hour time step, which used widely in a lot of solar radiation application. Hence, an hourly global horizontal solar radiation time series for the year of 1996 was then applied.

The data were collected from the National Meteorological Office of Algeria for the site of Oran. We used only the data from sunrise to the sunset of the day. The data were divided into two sets, training set (from 1st January 1996 to 31st October 1996) that represent 4530 h, and test data set (from 1st November 1996 to the 31st December 1996) that represent 915 h. An example of one month from each season were shown in Figs. 10(a)–(d) that represent the hourly global horizontal solar radiation for months of January, April, July and October 1996 respectively.

A phase space reconstitution with time delay of 1 and embedding dimension equal to 2 were found experimentally using mutual information and false nearest neighbor methods to be the right choices for this time series. In addition, a plotting of the silhouette function with a different number of clusters was tested. We established that the use of three clusters to be the appropriate

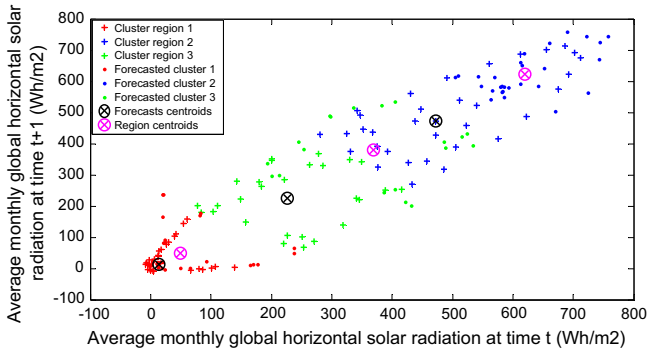

Fig. 8. Space phase reconstitution for forecasted regions and clusters of the monthly global horizontal solar radiation testing data (from July 1996 to December 1996) using wrong parameters.

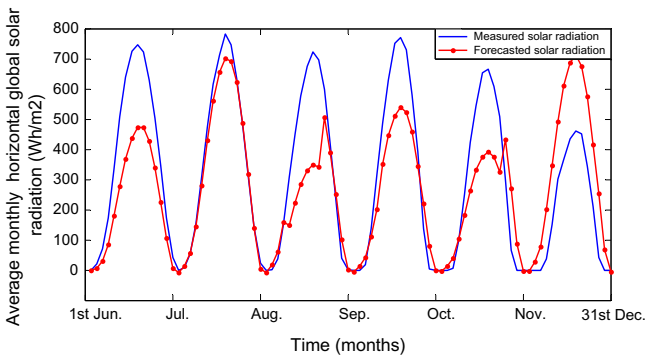

Fig. 9. Comparison between measured monthly global horizontal solar radiation data (from July 1996 to December 1996), and forecasted by proposed model using wrong parameters.

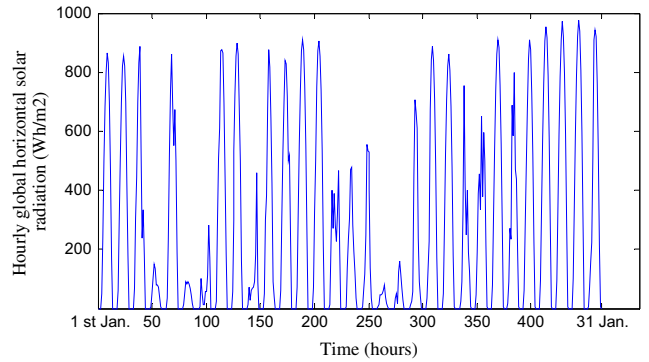

Fig. 10a. Measured hourly global horizontal solar radiation time series for January 1996.

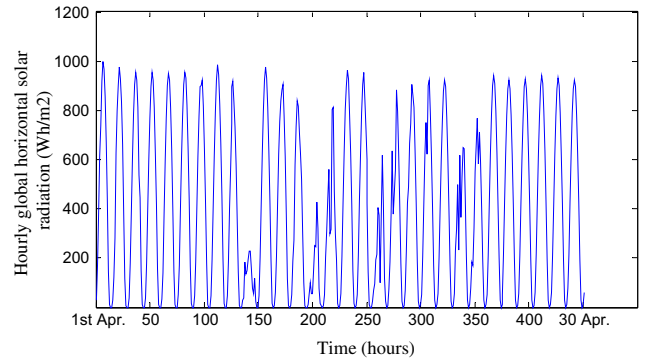

Fig. 10b. Measured hourly global horizontal solar radiation time series for April 1996.

choice as represented in Fig. 11, which represented the silhouette function of the hourly global horizontal solar radiation time series. It is clearly shown that the three clusters are well separated with the most of the points are above 0.6, except some negative ones in the second cluster that we can consider to be normal for such nonlinear time series.

For calculating the hourly global solar radiation time series, the *k*-means algorithm was then applied to clustering the training data. A local predictor was applied for obtaining future regions; those regions represent future windows for the forecasted data. Then, the NAR method with different time delay and neurons was applied to create global predictor of the data. The use of 25 delays with 13 neurons was found as the right choice for forecasting purpose. The results of phase space reconstitution of the forecasted regions and clusters for the hourly global horizontal solar radiation at time t and $t+1$ considering a time delay of 1 and embedding dimension of 2 was presented in Fig. 12.

From Fig. 12, the most of the points of each forecast cluster are in the right regions, the centroids are near each other, which mean that the obtained forecast is acceptable. The comparison between the forecasted hourly global horizontal solar radiation data and the tested data is shown in Fig. 13(a).

In addition, Figs. 13(b) and (c) represent the comparison results for the months of November 1996 and December 1996 respectively. The blue line represents measured data, and the red one is the forecasted data.

Moreover, the performance of the forecasted hourly global horizontal time series has been evaluated by calculating the RMSE errors between the actual data and forecasted one for the period of 1st November 1996 to 31st December 1996. The quadratic error between measured and simulated hourly global solar radiation using the proposed method was presented in Fig. 14. In addition, Fig. 15 represents the measured time series versus the forecasted time series.

From Fig. 14, the total RMSE was equal to 64.34 W h/m^2 and the NRMSE was 0.2003, which can be viewed as good forecasted values compared with an NRMSE equal to 0.3184 by using the baseline ARMA model.

In addition, from Fig. 15, the R squared value calculated by Eq. (12) is equal to 0.9330. The most of the points of the forecasted and measured series are near each to other. However, it presents some lags due to the total covered days that present a lot of clouds. Finally, from the simulation results, this methodology was conceived to be such a good method to perform the forecast results.

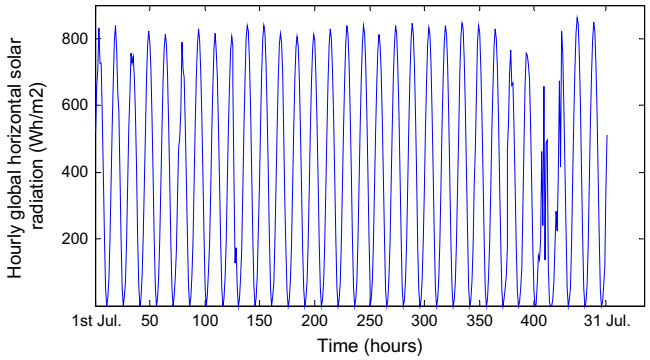

Fig. 10c. Measured hourly global horizontal solar radiation time series for July 1996.

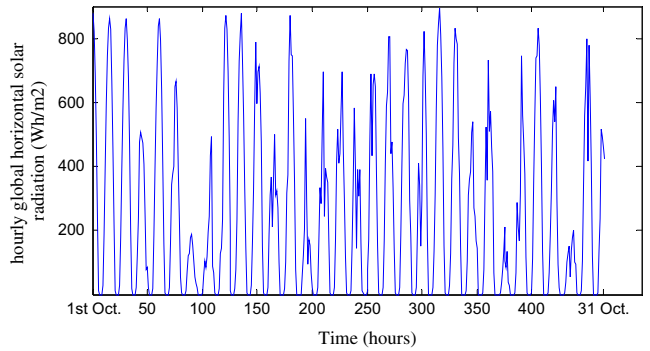

Fig. 10d. Measured hourly global horizontal solar radiation time series for October 1996.

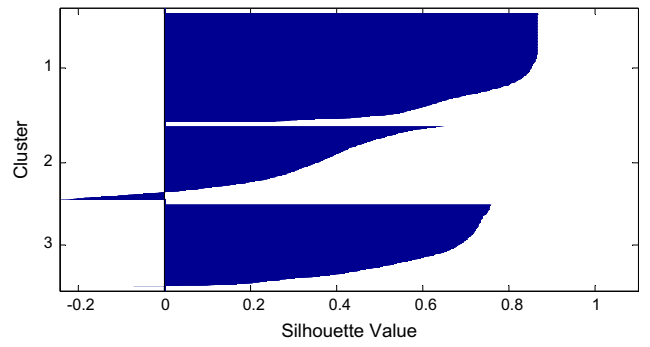

Fig. 11. Silhouette values with 3 clusters for the hourly global horizontal solar radiation data for Oran, Algeria (from 1st January 1996 to 31st October 1996).

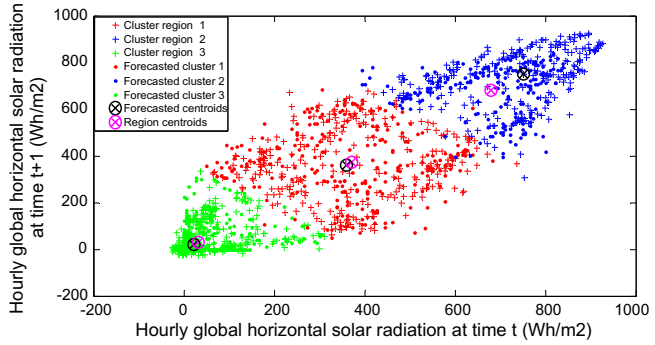

Fig. 12. Space phase reconstitution for the forecasted regions and clusters of the hourly global horizontal solar radiation testing data (from 1st November 1996 to the 31st December 1996).

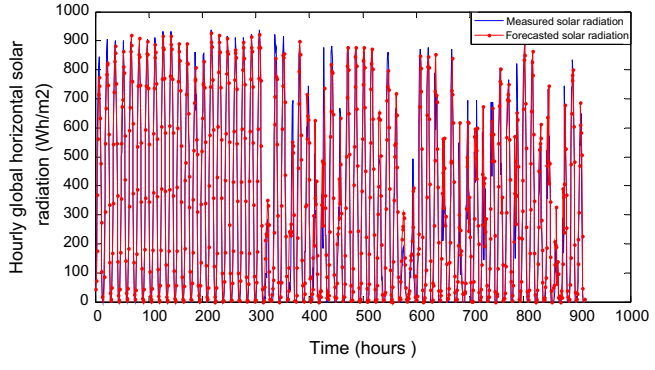

Fig. 13a. Comparison between measured hourly global horizontal solar radiation (from 1st November 1996 to the 31st December 1996) and forecasted by the proposed model.

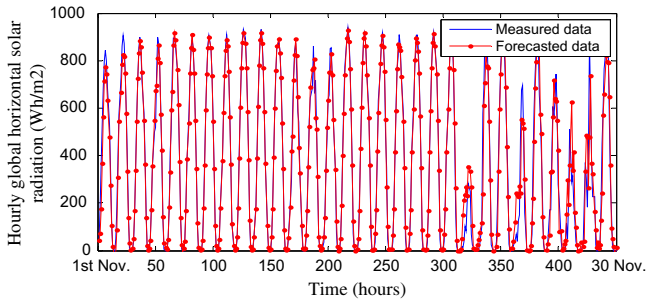

Fig. 13b. Comparison between measured hourly global horizontal solar radiation (from 1st November 1996 to the 31st November 1996) and forecasted by the proposed model.

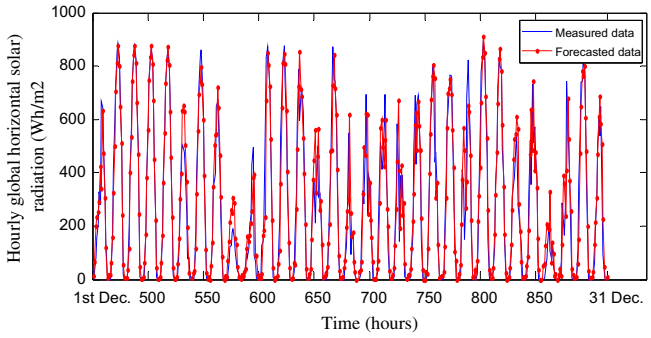

Fig. 13c. Comparison between measured hourly global horizontal solar radiation (from 1st December 1996 to the 31st December 1996) and forecasted by the proposed model.

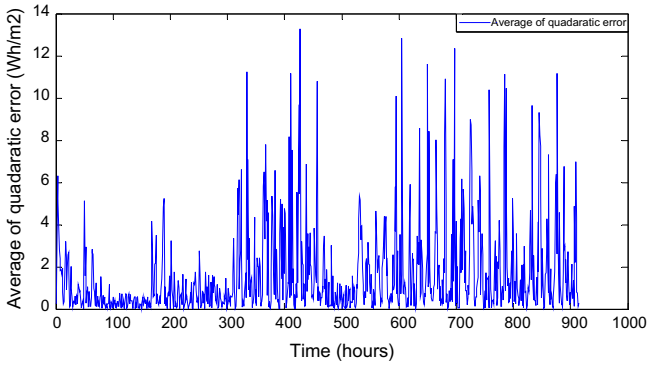

Fig. 14. the quadratic error between measured global horizontal solar radiation (from 1st November to 31st December 1996) and the forecasted using the proposed model.

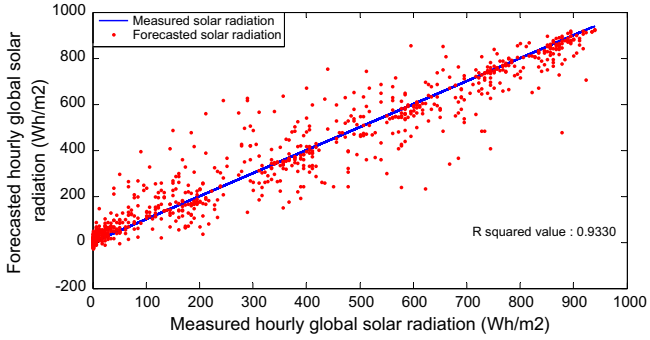

Fig. 15. The measured hourly global horizontal from (1st November 1996 to 31st December 1996) versus forecasted time series using the proposed model.

$$R^2 = \left(\frac{\left[\sum_{i=1}^{n} \left(I_{i,measured} - \bar{I}_{i,measured} \right)^2 \right]}{\left[\sum_{i=1}^{n} \left(I_{i,predicted} - \bar{I}_{i,measured} \right)^2 \right]} \right) \quad (12)$$

4. Conclusion

In this paper, we presented a time series forecasting methodology based on the clustering methods and artificial neural networks. The methodology consists of three essential stages. First, phase space reconstitution of the hourly global solar radiation time series was reached by finding the appropriate time delay using mutual information method, and the minimum embedding dimension is defined using false nearest neighbor method. Secondly, the unsupervised *k*-means clustering algorithm was then applied for grouping the input data into *k* clusters, which have similar characteristics. For choosing of the right number of clusters, the silhouette plot which represents a graphical representation of the separation of the heads of each cluster from another one was then used. Subsequently, a different NAR neural network was prepared on each cluster to act as a local predictor for the corresponding subspace of the input space. In addition, another NAR network was used to act as a global predictor for the solar radiation time series. The methodology was applied to generate multi-step ahead forecasts for the hourly global horizontal solar radiation time series. The obtained experimental results showed that the clustering of the input space is an important task to interpret the behavior of the series. Moreover, identifying forecasted regions using NAR network provides additional information about future patterns that can simplify the analysis of the global forecast of the series. In addition, the proposed method does not need a complicate clustering algorithm. Hence, as a conclusion of this work, the time series data mining method was considered such a good way of forecasting such similar problems. Nevertheless, this method presents some limitations for the total covered sky where the presence of clouds is heavy, also the calculation time, especially in the preparation phase of the NAR network. Hence, future works, will be focused on testing different clustering algorithms and different artificial neural networks to improve the forecasting performance that improves the reliability in the case of covered sky.

Acknowledgement

The authors would like to thank the University of Laghouat for the financial aspect of the present work.

References

[1] Maia André Luis S, de Carvalho ATFrancisco, Teresa BL. Forecasting models for interval-valued time series. Neurocomputing 2008;71:3344–52.
[2] Azadeh A, Maghsoudi A, Sohrabkhani S. An integrated artificial neural networks approach for predicting global radiation. Energy Convers Manage 2009;50:1497–505.
[3] Box GEP, Jenkins G. Time series analysis. Holden-Day (San Francisco, CA): Forecasting and Control; 1970.
[4] Celik AN, Muneer T. Neural network based method for conversion of solar radiation data. Energy Convers Manage 2013;67:117–24.
[5] Chen SX, Gooi HB, Wang MQ. Solar radiation forecast based on fuzzy logic and neural networks. Renew Energy 2013;60:195–201.
[6] Chow TWS, Leung CT. Non-linear autoregressive integrated neural network model for short term load forecasting. IEE Proc Gen Trans Distribut 1996;143:500–6.
[7] Faraway JJ, Chatfield C. Time series forecasting with neural networks: a case study. Statistics Group Research Report 9506, University of Bath; 1995.
[8] Fraser M, Swinney L. Independent coordinates for strange attractors from mutual information. Phys Rev A 1986;33:1134–40.
[9] Fu T. A review on time series data mining. Eng Appl Artif Intell 2011;24:164–81.
[10] Gelman R. 2011 Renewable energy data book (Revised Book). Efficiency Renew Energy (EERE) 2013.

[11] Huang Y. Advances in artificial neural networks-methodological development and application. Algorithms 2009;2:973–1007.
[12] Huang J, Korolkiewicz M, Agrawal M, Boland J. Forecasting solar radiation on an hourly time scale using a Coupled AutoRegressive and Dynamical System (CARDS) model. Sol Energy 2013;87:136–49.
[13] Haykin S. Neural networks: a comprehensive foundation. 2nd ed. Prentice Hall; 1998.
[14] Kaplanis S. New methodologies to estimate the hourly global solar radiation; comparisons with existing models. Renew Energy 2006;31:781–90.
[15] Kennel MB, Brown R, Abarbanel HD. Determining embedding dimension for phase space reconstruction using a geometrical construction. Phys Rev A 1992;45(6):3403–11.
[16] Kim HS, Eykholt R, Salas JD. Nonlinear dynamics, delay times, and embedding windows. Physica D 1999;127:48–60.
[17] Kostylev V, Pavlovski A. Solar power forecasting performance – towards industry standards, In: Proceedings of the 1st international workshop on the integration of solar power into power systems, Aarhus, Denmark; 2011
[18] Kugiumtzis D. State space reconstruction parameters in the analysis of chaotic time series—the role of the time window length. Physica D 1996;95:13–28.
[19] Levenberg K. A method for the solution of certain problems in least squares. Q Appl Math 1944;5:164–8.
[20] Lewis CD. International and business forecasting methods. London: Butter-Worths; 1982.
[21] Liao S, Chu P, Hsiao P. Data mining techniques and applications – a decade review from 2000 to 2011. Expert Syst Appl 2012;39:11303–11.
[22] Ljung L. System identification: theory for the user. 2nd ed. Prentice Hall PTR; 1998.
[23] Lletí R, Ortiz MC, Sarabia LA, Sánchez MS. Selecting variables for *k*-means cluster analysis by using a genetic algorithm that optimises the silhouettes. Anal Chim Acta 2004;515:87–100.
[24] MacKay DJC. Bayesian interpolation. Neural Comput 1992;4(3):415–47.
[25] MacQueen JB. Some methods for classification and analysis of multivariate observations. In: Proceedings of 5th Berkeley symposium on mathematical statistics and probability 1. University of California Press; 1967. p. 281–297.
[26] Mandelbrot BB. How long is the coastline of Britain? Statistical self-similarity and fractional dimension. Science 1967;155:636.
[27] Markham IS, Rakes TR. The effect of sample size and variability of data on the comparative performance of artificial neural networks and regression. Comput Oper Res 1998;25:251–63.
[28] Mellit A, Kalogirou SA, Hontoria L, Shaari S. Artificial intelligence techniques for sizing photovoltaic systems: a review. Renew Sustain Energy Rev 2009;13(2):406–19.
[29] Moller MF. A scaled conjugate gradient algorithm for fast supervised learning. Neural Networks 1993;4:525–33.
[30] Pandit SM, Wu SM. Time series and system analysis, with applications; 1983.
[31] Ragulskis M, Lukoseviciute K. Non-uniform attractor embedding for time series forecasting by fuzzy inference systems. Neurocomputing 2009;72:2618–26.
[32] Rousseeuw J. Silhouettes: a graphical Aid to the interpretation and validation of cluster analysis. Comput Appl Math 1987;20:53–65.
[33] Sandberg I, Xu L. Uniform approximation of multidimensional myopic maps. IEEE Trans Circ Syst I: Fund Theory Appl 1997;44(6):477–85.
[34] Spath H. Cluster dissection and analysis: theory, Fortran programs, examples translated by J. Goldschmidt. New York: Halsted Press; 1985. 226 pp.
[35] Takens F. Detecting strange attractors in turbulence, Dynamical Systems and Turbulence In: Rand DA, Young LS. editors, Lecture notes in mathematics. vol. 898; 1981. p. 366-381.
[36] Wu J, Chan KC. Prediction of hourly solar radiation using a novel hybrid model of ARMA and TDNN. Sol Energy 2011;85:808–17.
[37] Xu R, Donald C. Survey of clustering algorithm. IEEE Trans Neural Networks 2005;16(3):46–51.
[38] Zeng Z, Yang H, Zhao R, Meng J. Nonlinear characteristics of observed solar radiation data. Sol Energy 2013;87:204–18.
[39] Zhang G. Time series forecasting using a hybrid ARIMA and neural network model. Neurocomputing 2003;50:159–75.
[40] Boland JW. Time series and statistical modelling of solar radiation, Recent Advances in Solar Radiation Modelling, Viorel Badescu (Ed.), Springer-Verlag 2008; 283-312.

Theor Appl Climatol
DOI 10.1007/s00704-015-1469-z

ORIGINAL PAPER

Small-scale solar radiation forecasting using ARMA and nonlinear autoregressive neural network models

Khalil Benmouiza[1] · **Ali Cheknane**[2]

Received: 7 January 2015 / Accepted: 12 April 2015

Abstract This paper aims to introduce an approach for multi-hour forecasting (915 h ahead) of hourly global horizontal solar radiation time series and forecasting of a small-scale solar radiation database (30- and 1-s scales) for a period of 1 day (47,000 s ahead) using commonly and available measured meteorological solar radiation. Three methods are considered in this study. First, autoregressive–moving-average (ARMA) model is used to predict future values of the global solar radiation time series. However, because of the non-stationarity of solar radiation time series, a phase of detrending is needed to stationarize the irradiation data; a 6-degree polynomial model is found to be the most stationary one. Secondly, due to the nonlinearity presented in solar radiation time series, a nonlinear autoregressive (NAR) neural network model is used for prediction purposes. Taking into account the advantages of both models, the goodness of ARMA for linear problems and NAR for nonlinear problems, a hybrid method combining ARMA and NAR is introduced to produce better results. The validation process for the site of Ghardaia in Algaria shows that the hybrid model gives a normalized root mean square error (NRMSE) equals to 0.2034 compared to a NRMSE equal to 0.2634 for NAR model and 0.3241 for ARMA model.

✉ Ali Cheknane
cheknanali@yahoo.com; a.cheknane@mail.lagh-univ.dz

Khalil Benmouiza
benkhalil3@gmail.Com

[1] Unité de Recherche des Matériaux et Energies Renouvelables, Department of Physics, Faculty of Science, Abou Bekr Belkaid University, BP 119, Tlemcen 13000, Algeria

[2] Laboratoire des Semiconducteurs et Matériaux Fonctionnels, Université Amar Telidji de Laghouat, Bd des Martyrs, BP 37G, Laghouat 03000, Algérie

1 Introduction

Solar energy is one of the most important renewable energies to generate electricity and meet our everyday needs. PV systems are used to convert this energy to a DC electrical power. However, sometimes it is not possible to estimate the PV system outputs in long-term because they depend strongly on the input parameters such as the amount of solar radiation and temperature. Thus, the solar radiation data should be measured continuously and accurately over the long-term. Unfortunately, in most areas of the world, solar radiation measurements are not easily available due to financial, technical, or institutional limitations. Therefore, many studies have carried out to develop methods to estimate the amount of the solar radiation (Zhang et al. 1998; Zhang 2003; Kaplanis 2006; Kaplanis and Kaplani 2007; Boland 2008; Wu and Chan 2011; Pandey and Soupir 2012; Badescu et al. 2013). In addition, forecasting of solar radiation is important for the integration of photovoltaic plants into an electrical grid. Proper solar irradiance forecasting helps the grid operators to optimize their electricity production and /or to reduce additional costs by preparing an appropriate strategy (Diagne et al. 2009). Forecasts of solar radiation can be either in short or long term. Forecasts for the near future can be done using relatively simple procedures with a good accuracy. In the other side, forecasts for the far future need more complicated models. This is known as a difficult problem, due to the non-linearity and complexity of modeling of the solar radiation series (Zhang 2003; André Luis et al. 2008; Wu and Chan 2011; Mellit et al. 2013; Khatib et al. 2012; Peled and Appelbaum 2013). Hence, many studies have been conducted

Published online: 25 April 2015

on this subject such as stochastic models (Boland 2008; Wu and Chan 2011) and neural network methods (Markham and Rakes 1998; Zhang et al. 1998; Mihalakakou et al 2000; Mellit et al. 2009; Wu and Chan 2011). These models treated the solar radiation sequence as a time series; they used mathematical models in the modeling phase to forecast future values.

The autoregressive–moving-average (ARMA) model is commonly used in time series prediction, the popularity of the ARMA model is due to its statistical properties as well as the well-known Box–Jenkins methodology (Box and Jenkins 1970). However, ARMA model requires a stationary time series, while most real-time series are not stationary (Box and Jenkins 1970; Kwiatkowski et al. 1992; Wu and Chan 2011). We found using the augmented Dickey–Fuller (ADF) test (Dickey and Fuller 1981) that the solar radiation time series is not stationary. Hence, we need a detrending phase to make the time series stationary (Wu and Chan 2011). Therefore, Jain model (Baig et al. 1991; Kaplanis 2006), Baig et al. (1991), Kaplanis (2006), Kaplanis and Kaplani (2007), and high-degree polynomial models are tested in this paper to remove the trends of the solar radiation series. A test of stationarity of the residual series using the ADF test was applied to get the best model to use it in the simulation. The choice of the suitable order of ARMA model is reached using autocorrelation and partial correlation of the residual series as well as the Akaike Information Criterion (AIC) (Akaike 1974).

On the other hand, time series prediction using neural network approach is non-parametric, in the sense that it is not necessary to know any information about the process that generates the signal (Denton 1995; Markham and Rakes 1998; Zhang 2003). Among them, nonlinear autoregressive (NAR) neural networks which used only the past values of the time series to forecast future values. A good choice of the number of delays, neurons, and training algorithm can resolve the problem of the non-linearity of the time series.

However, both ARMA and NAR models present limitations in the forecasting phase. ARMA model shows good results for linear problems, but it could represent huge errors in the nonlinear problems; also, the outliers made the prediction by NAR networks difficult (Zhang 2003; Diagne et al. 2009; Wu and Chan 2011). Hence, hybrid models are proposed taking the advantages of the two models to provide better prediction results. Pelikan et al. (1992), and Ginzburg and Horn (1994) proposed a model combining several feed forward neural networks, improving the time series forecasting accuracy. Wedding and Cios (1996) described a combining method using radial basis function networks and the Box–Jenkins models. Luxhoj et al. (1996) presented a hybrid econometric and an ANN approach for sales forecasting. Zhang (2003) proposed a method using a hybrid combination between ARMA and ANN models to predict time series, André Luis et al. (2008) used Zhang (2003) model and adjusted the model on the midpoint and an interval range series in the training set. Wu and Chan (2011) proposed a technique employing a combination of ARMA and time delay neural network (TDNN) for one-step ahead prediction based on Zhang (2003) model. In addition, many authors have already studied successfully the coupling between ANN and different traditional computing technologies such as fuzzy logic, wavelet-based analysis (Peled and Appelbaum 2013) and genetic algorithm methods (Mellit et al. 2009; Diagne et al. 2009; Boata and Gravila 2012; Chen et al. 2013). However, most of these models present limitations especially in long-term forecasting. Hence, in this paper, we propose a hybrid model of ARMA and NAR network for multi-step ahead prediction of solar radiation time series for better performance in long-term forecasting.

The follow-up of this paper is organized as follows. In Section 2, we present the proposed methodology as well as backgrounds of the ARMA, NAR, and the hybrid models. A comparison between the detrending models to get the most stationary series is also seen. In Section 3, we have presented the data used in the simulation and comparison results. In Section 4, we simulate the forecasting results of the hybrid model and compared them with other models. The last section is devoted to the conclusion and discussion of future works.

2 Background

This section introduces the adopted methodology in this paper as shown in Fig. 1. It consists of forecasting hourly solar radiation using hybrid ARMA and NAR neural network model. Also, a review of ARMA, NAR, and the proposed hybrid model is discussed.

2.1 The ARMA model

ARMA model of order (p, q) can be viewed as linear filters for digital signal processing. It is of the form,

$$x_t = \sum_{i=1}^{p} \phi_i x_{t-i} + e_t + \sum_{j}^{q} \theta_j e_{t-j} \tag{1}$$

where, $\phi_i (i = 1 \ldots p)$ and $\theta_j (j = 1 \ldots q)$ are constants representing the autoregressive AR, and the moving average MA parameters of order p, q, respectively. x_t is the actual value and e_t represents the Gaussian white noise with mean zero in time t. To find the parameters of Eq. (1), the Box and Jenkins (1970) method is applied as expressed in what follows.

2.1.1 Stationarization

Time series modeling and forecasting requires explicitly a stationary time series (Makridakis et al. 1998; Voyant et al.

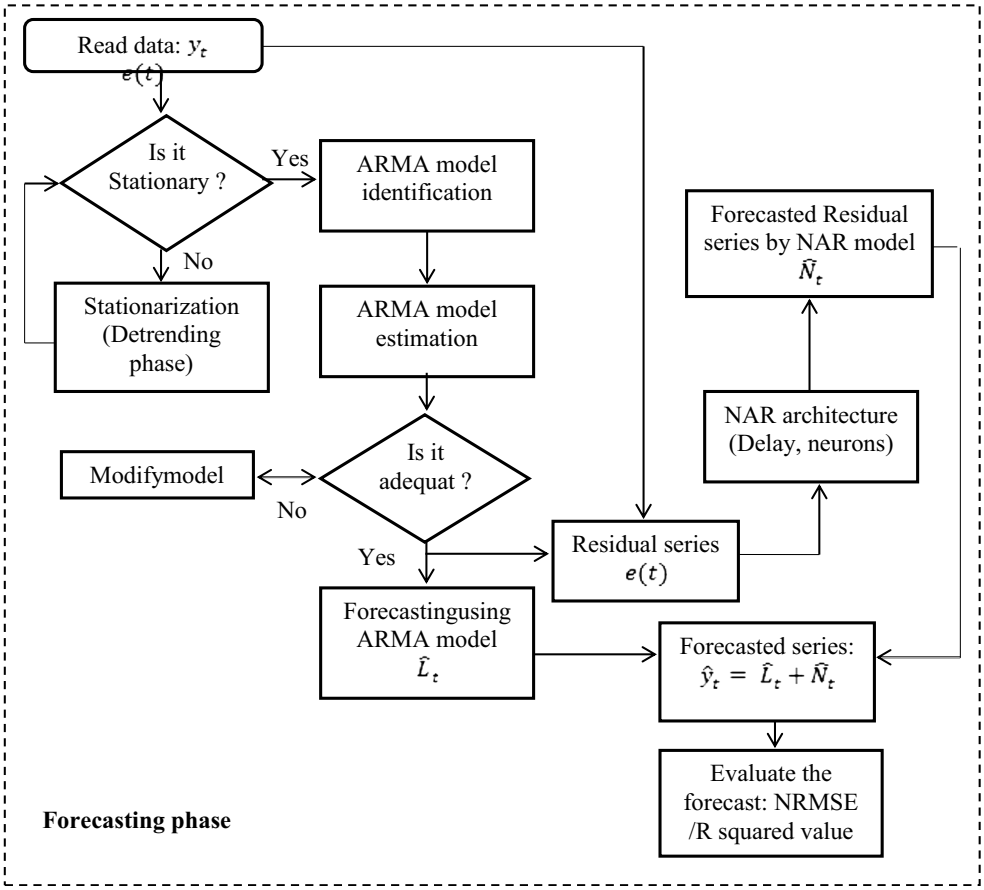

Fig. 1 The flowchart of the proposed methodology

2013). The condition of stationarity (weakly stationarity) implies a stable series. Which means that the mean $\mu\ (t)$ and the covariance $cov(x_t,x_{t+h})$ stay constant over time, as expressed by the following equations:

$$E[x_t] = \mu(t) = \mu. \tag{2}$$

$$\mathrm{cov}\lfloor x_t, x_{t+h}\rfloor = E\lfloor(x_t-\mu)(x_{t+h}-\mu)\rfloor \tag{3}$$

Moreover, a strict stationary series needs a time invariant joint distribution of any observation of the processes. In addition, modeling and analysis of time series of classical models such as ARMA model without testing the stationarity can present real practical problems (Ineichen 2008).

Hence, several methods are demonstrated in the literature to check the stationarity (non-stationarity). The most widely used one is the test of a unit root in the time series (Dickey and Fuller 1981; Kwiatkowski et al. 1992). A unit root test is a test for a specific type of non-stationarity for autoregressive time series. The series is covariance stationary if and only if all the roots of the characteristic polynomials are outside the unit circle in the complex plane. In other words, if it exists a unit root, then the time series is not stationary. Otherwise, it is stationary.

The most widely used method to test unit root is the ADF test (Dickey and Fuller 1981), expressed by the following equation,

$$\Delta x_t = \alpha + \beta t + \gamma x_{t-1} + \sum_{j=1}^{p}\left(\delta_t \Delta x_{t-j}\right) + e_t \tag{4}$$

where, α is a constant called a drift, β is the coefficient on a time trend, p is the lag order autoregressive process, γ is the coefficient presenting process root, δ_t represent the lag operator and e_t represents an independent identically distributes residual term with mean zero and variance $\sigma^2=0$.

The focus of testing is whether the coefficient γ equals to zero, what means that the original $x_1, x_2, \ldots x_n$ process has a unit root. Hence, the null hypothesis of $\gamma=0$ (random walk process) is tested against the alternative hypothesis $\gamma<0$ to obtain a stationary series.

The ADF statistic, used in the test, is a negative number. The stronger reject of the null hypothesis needs more negative test. In our simulation and using this stationarity test, we found that the solar radiation series is not stationary. Hence, a stationarization step is needed. A phase of detrending is introduced to obtain a stationary series. In this phase, we simulated different models to fit the solar radiation time series. For each model, the residual series between simulated series and the

original series had been tested using the ADF test. The most stationary series will be used in ARMA modeling. In this paper, the Jain model (Baig et al. 1991; Kaplanis 2006), Baig et al. (1991), Kaplanis (2006), Kaplanis and Kaplani (2007) and high-degree polynomial models are applied to remove trends of the solar radiation series as follow.

The Jain model The Jain model (Baig et al. 1991; Kaplanis 2006) proposed a Gaussian function to fit the recorded data and established the following relation for global irradiation.

Where, r_t is the ratio of hourly to daily global solar radiation, t is the true solar time in hours, m is the time of pick solar radiation hour of the day, and σ is the standard deviation of the Gaussian curve.

$$r_t = \frac{1}{\sigma\sqrt{2\pi}} \exp\left[\frac{(t-m)^2}{2\sigma^2}\right] \tag{5}$$

The Baig model The Baig et al. (1991) model modified Jain's model to fit the recorded data during the starting and ending periods of a given day. In this model, r_t was estimated by:

$$r_t = \frac{1}{2\sigma\sqrt{2\pi}} \left\{ \exp\left[-\frac{(t-m)^2}{2\sigma^2}\right] + \cos\left[180\frac{(t-m)^2}{S_0-1}\right] \right\} \tag{6}$$

where, S_0 is the length of the day (from sunrise to sunset), n_j is the number of the day at the site with latitude φ. δ is the sun declination.

$$S_0 = \frac{2}{15}\cos^{-1}[-\tan(\varphi)\tan(\delta)] \tag{7}$$

Several methods are found in the literature to estimate the standard deviation σ using recorded data (Kaplanis 2006). Bevington (1969) mentioned that the determination of σ does not need any recorded data and it depends only on the day length, as expressed in Eq. (8):

$$\sigma = 0.246 S_0 \tag{8}$$

The r_t values are obtained to offer:

$$I_t = r_t \cdot H_n \tag{9}$$

Where, I_t is hourly solar radiation and H_n is the daily global solar radiation data.

Kaplanis model Kaplanis (2006) proposed another model to estimate hourly global solar radiation that is:

$$r_t = \alpha + \beta\cos\left(\frac{\cos(2\pi(t-m)}{24}\right) \tag{10}$$

where, α and β are parameters which have to be determined for any site and for any day (Kaplanis 2006). However, this model presented some drawback in the estimation of solar radiation at noontime. Hence, Kaplanis and Kaplani (2007) proposed an improved model for more accuracy as presented in the following equation:

$$r_t = a + b\frac{e^{-\mu(nj)\chi(t)}\cos(2\pi(t-m)/24)}{e^{-\mu(nj)\chi(t=m)}} \tag{11}$$

Where, a and b are determined in the same way as Eq. (10), $\mu(nj)$ is the solar beam attenuation coefficient and $\chi(t)$ is the distance of the solar beam travels within the atmosphere at time t.

High-order polynomial model This model is represented as follows:

$$I_t = a_0 h^0 + a_1 h^1 + a_2 h^2 + \ldots + a_n h^n \tag{12}$$

Least squares regression analysis was used to fit Eq. (12) to the data for each hour of the day to obtain the values of the regression constants a_0, a_1 ... a_n for each month of the year and h is the time (Al-Sadah et al. 1990).

The trends obtained from these models are simulated against the measured data to find the suitable model to be used in the prediction phase. For that, the monthly average hourly global solar radiation time series is then applied. The data are collected from the National Meteorological Office (ONM) of Algeria for the site of Oran (35.6911° N, 0.6417° W). Figure 2 shows the monthly average hourly global horizontal solar radiation of January 2010 in watt per square meter against the estimated models. We ignored data between 6:00 and 20:00 o'clock because there is no solar radiation measured during this period.

To choose the proper model, we have to check the stationarity of the series. Thus, the ADF test is applied to the residual series between measured and simulated data from different models. If the test result is below the critical values that means we should reject the null hypothesis and the time series is stationary.

Otherwise, it is not stationary. The statistical power is the probability tests to reject a false null hypothesis (Dickey and Fuller 1981). The test results are presented in Table 1. The performances of the five simulated models to predict monthly average hourly global solar radiation from mean daily global solar radiation are evaluated using the root mean square error (RMSE) and normalized root mean square error (NRMSE),

$$\mathrm{RMSE} = \left[\left\langle \left(I_{i,predicted} - I_{i,measured}\right)^2 \right\rangle\right]^{\frac{1}{2}} \tag{13}$$

RMSE and NRMSE provide information in the short-term performance of correlations by allowing a term-by-term comparison of the actual deviation between the predicted and

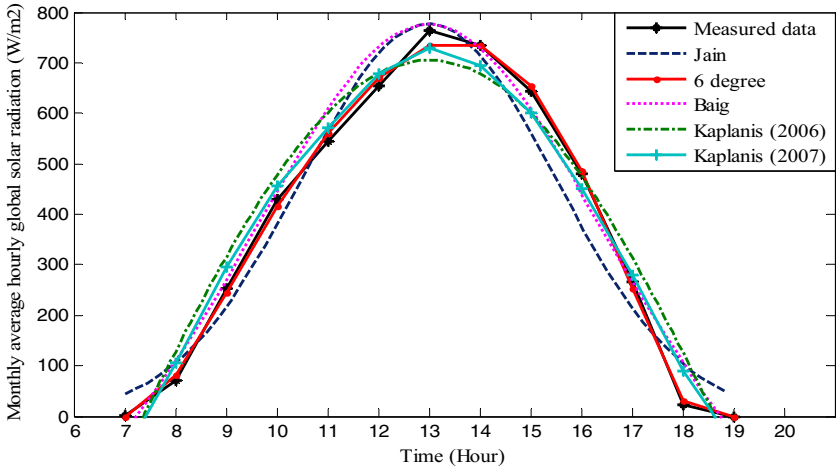

Fig. 2 Comparison between the measured monthly average hourly global horizontal solar radiation data of January 2010 for the site of Oran, Algeria, and the Jain (Baig et al. 1991; Kaplanis 2006), Baig et al. (1991), Kaplanis (2006), Kaplanis and Kaplani (2007), and 6-degree polynomial models

measured values. The model that has the lowest NRMSE is considered the best model.

$$\mathrm{NRMSE} = \left(\frac{\left[\left\langle \left(I_{i,predicted} - I_{i,measured} \right)^2 \right\rangle \right]^{\frac{1}{2}}}{\left\langle I_{i,measured} \right\rangle} \right) \tag{14}$$

The results of the statistical comparison of the simulated models are presented in Table 2,

From Fig. 2 and Table 2, it is clearly shown that Jain's model fits the monthly average hourly global solar radiation series, but it presents a big NRMSE error versus other models that equal to 0.1490 especially at the beginning and at the end of the series. Hence, since the Baig's model is based on Jain's model, it was used to overcome this error. However, it still represents some lags with NRMSE equal to 0.1146.

For the Kaplanis (2006) model, it used a different method than Jain and Baig models, but still had a big NRMSE equal to 0.1013. Using the improved approach by Kaplanis and Kaplani (2007), the NRMSE is reduced to 0.0735. The 6-degree polynomial model seems the best choice to fit the solar radiation time series, which represents the lowest NRMSE error equal to 0.0358.

In addition, from the results of Table 1, we can see that the test results are below the critical values. Therefore, the residual series of all these models is considered stationary. The statistical power of 6-degree polynomial model is the highest one, which implies that the residual series between this model and measured data has the lowest probability to incorporate a unit root. Hence, it is considered the most stationary residual series.

Since higher degree polynomial model provides the best performance in both detrending and fitting phases, we used this model for ARMA model in the detrending phase to predict future values.

2.1.2 Model identification

Model identification consists of specifying the appropriate structure, AR, MA, or ARMA and orders of the model (Box and Jenkins 1970). Identification is sometimes done by looking at the plots of the autocorrelation function (ACF) and the partial autocorrelation function (PACF). After determining the ACF and PACF functions, we can choose the (p,q) order of the ARMA model, as expressed in Table 3,

Table 1 The ADF test for the detrending models

Detrending models	Statistical power	Significant level	Test results	Critical value
Jain's model	0.0428	0.05	−2.0389	−1.9580
Baig's model	0.0126	0.05	−2.6580	−1.9580
Kaplanis (2006) model	0.0117	0.05	−2.6918	−1.9580
Kaplanis and Kaplani (2007) model	0.0097	0.05	−3.4307	−1.9580
6-Degree polynomial model	0.001	0.05	−4.3232	−1.9580

Table 2 The RMSE and NRMSE between actual data and the other different models

	Error (RMSE)	Error (NRMSE)
Jain's model	55.2255	0.1490
Baig's model	42.8663	0.1146
Kaplanis (2006) model	37.1987	0.1013
Kaplanis and Kaplani (2007) model	22.5810	0.0735
6-degree polynomial model	13.3939	0.0358

Table 3 Different scenarios of choosing ARMA (*p*,*q*) parameters

	AR (*p*)	MA (*q*)	ARMA (*p*, *q*)
ACF	Tails off	Cuts off	Tails off
PACF	Cuts off	Tails off	Tails off

Akaike's Information Criterion (AIC) (Akaike 1974) defined by Eq. (15), is another factor to decide ARMA (*p*,*q*) order. AIC provides a measure of the model quality by simulating the situation where the model is tested on a different data set. According to Akaike's theory, the most accurate model has the smallest AIC.

$$\mathrm{AIC} = \log V + \frac{2d}{N} \tag{15}$$

Where V is the loss function, d is the number of estimated parameters and N is the number of values in the estimation data set.

2.1.3 Parameter estimation

Once the orders of ARMA model obtained, estimation of the model parameters is straightforward. The parameters are estimated using maximum likelihood method (Box and Jenkins 1970). The last step of the ARMA model building is the diagnostic checking of the model adequacy. The plotting of residuals examines the goodness of the obtained model.

2.2 The nonlinear autoregressive (NAR) model

Recurrent neural networks have been widely used for modeling of nonlinear dynamical systems (Haykin 1998; Ljung 1998). Among various types of the recurrent neural networks, time delay neural networks (TDNN) (Haykin 1998; Wu and Chan 2011), layer recurrent networks (Haykin 1998) and NAR (Markham and Rakes 1998; Chow and Leung 1996). TDNN is a straightforward dynamic network that consists of a feed-forward network with a tapped delay line at the input layer which the dynamics appear only in the input layer of a static multilayer feed-forward network. However, the NAR is a dynamic recurrent network, with feedback connections including several layers of the network. The next value of the dependent output signal is regressed on previous values of the output signal. The main advantage of using the NAR network comparing with the TDNN is that the input to the feed-forward network is more accurate which, provide more precise result for multi-step ahead prediction.

The NAR model is based on the linear AR model, which is commonly used in time-series forecasting. The defining equation for the NAR network is:

$$\hat{y}(t) = f(y(t-1) + y(t-2) + \cdots + y(t-d)) \tag{16}$$

f is a nonlinear function, where the future values depend only on regressed d earlier values of the output signal as expressed in Fig. 3.

When using NAR network, the network performs only a one-step ahead prediction after it has been trained. Therefore, we need to use the closed loop network to perform a multi-step-ahead prediction and turn the network into a parallel configuration. The output of the closed loop NAR network is expressed as follows:

$$\hat{y}(t+p) = f(y(t-1) + y(t-2) + \cdots + y(t-d)) \tag{17}$$

where p represents the forecasted steps in the future.

A crucial part of a neural network working is the training step. Because of the very similarity structure between NAR network and the Multilayer Perceptron (MLP), the back propagation method with some modification is then applied; training typically starts with random weights on its synapses. It is exposed to a training set of input data. The output of the

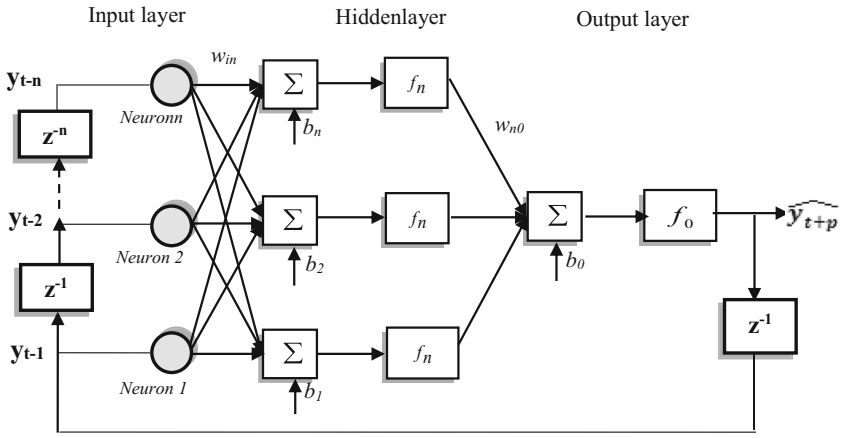

Fig. 3 Structure of NAR network

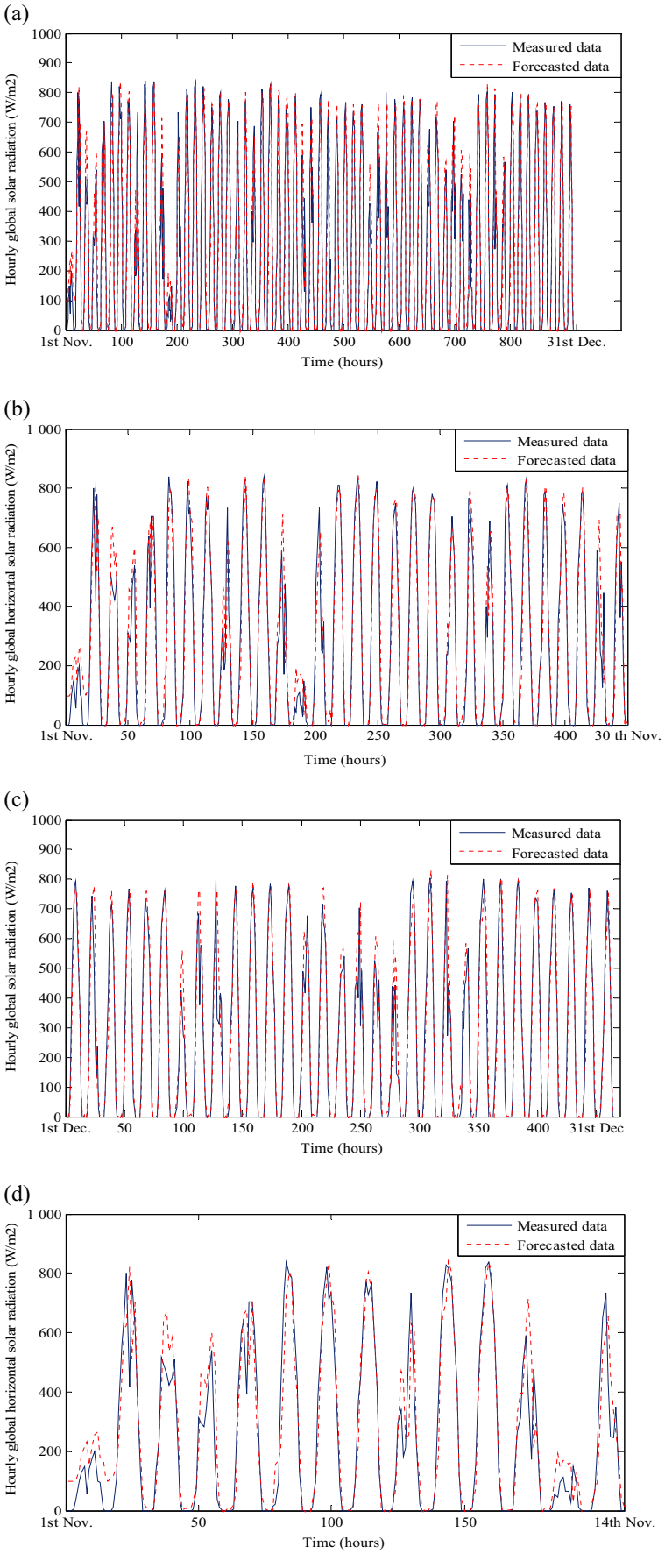

Fig. 4 **a** Comparison between measured hourly global horizontal solar radiation data (from 1 November 2010 to 31 December 2010) and the forecasted using hybrid model. **b** Comparison between measured hourly global horizontal solar radiation (from 1 November 2010 to the 30 November 2010) and forecasted by proposed model. **c** Comparison between measured hourly global horizontal solar radiation (from 1 December 2010 to the 31 December 2010) and forecasted by proposed model. **d** Comparison between measured hourly global horizontal solar radiation (from 1 November 2010 to the 14 November 2010) and forecasted by proposed model

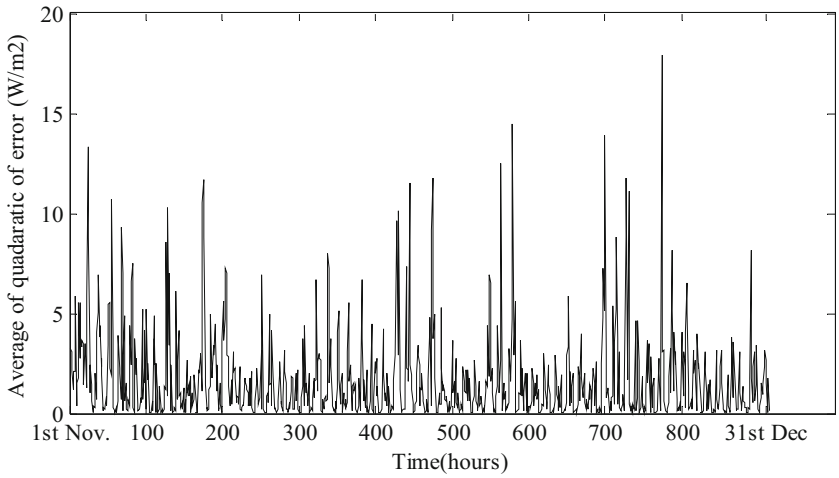

Fig. 5 The average of quadratic error between measured global horizontal solar radiation (from 1 November to 31 December 2010) and the forecasted using hybrid model

network is compared to the example (supervised training) and a learning procedure alters the network interconnections (weights).

Several training algorithms available in the literature, algorithms such as the Levenberg-Marquardt (Levenberg 1944; MacQueen 1967), and Bayesian Regularization (MacKay 1992), proved to be too computationally intensive to train larger networks. After a heuristic search, the scaled conjugate gradient algorithm presented in Moller (1993) is selected to train larger networks. Once the network is trained using the preselected inputs and outputs, all the synaptic weights are frozen and the network is ready to be tested on the new input information.

2.3 The hybrid model

ARMA model represented linear models and has achieved great popularity since the publication of Box and Jenkins (1970). However, this method may not be adequate for nonlinear problems, contrary of the NAR networks that can solve the complexity of nonlinear systems. However, not one of them can use for both linear and nonlinear problems (Zhang 2003; André Luis et al. 2008; Wu and Chan 2011). Hence, a hybrid models is applied taking the advantages of both ARMA and NAR models. We can simply detect the nonlinearity in a time series by using the surrogate data test for nonlinearity (Kugiumtzis 2000). The proposed hybrid model in this work is based on Zhang (2003) model. It is assumed that time series is composed of a linear autocorrelation structure and a non-linear part:

$$y_t = L_t + N_t \tag{18}$$

where, L_t denotes the linear part and N_t denotes the nonlinear part. The proposed method by Zhang (2003) consists of two stages. Firstly, ARMA model is used to predict future values at time t noted . The residual series between the time series and linear ARMA model series contains only nonlinear relationship. As expressed by the following equation:

$$v_t = y_t - \widehat{L}_t \tag{19}$$

where, v_t denote the residual at time t from the linear model.

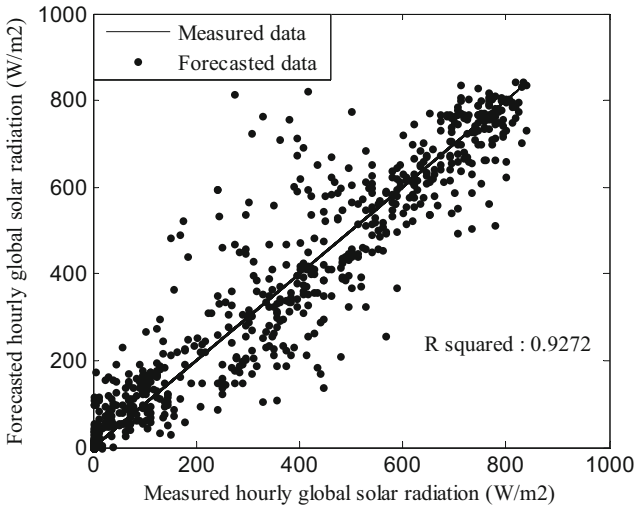

Fig. 6 The measured hourly global horizontal from (1 November 2010 to 31 December 2010) versus forecasted time series using hybrid model

Table 4 The RMSE and NRMSE error for the site of Ghardaia, 2012; London, 2005; and Almeria, 2012

Location and year	Training/ testing data set	ARMA (p,q) order	NRMSE		
			ARMA model	NAR model	Hybrid model
Ghardaia, 2012	(6222/1655)	(4,6)	0.3241	0.2634	0.2034
London, 2005	(3816/1068)	(3,5)	0.3338	0.2862	0.2154
Almeria, 2010	(7196/1564)	(6,5)	0.3001	0.2313	0.1910

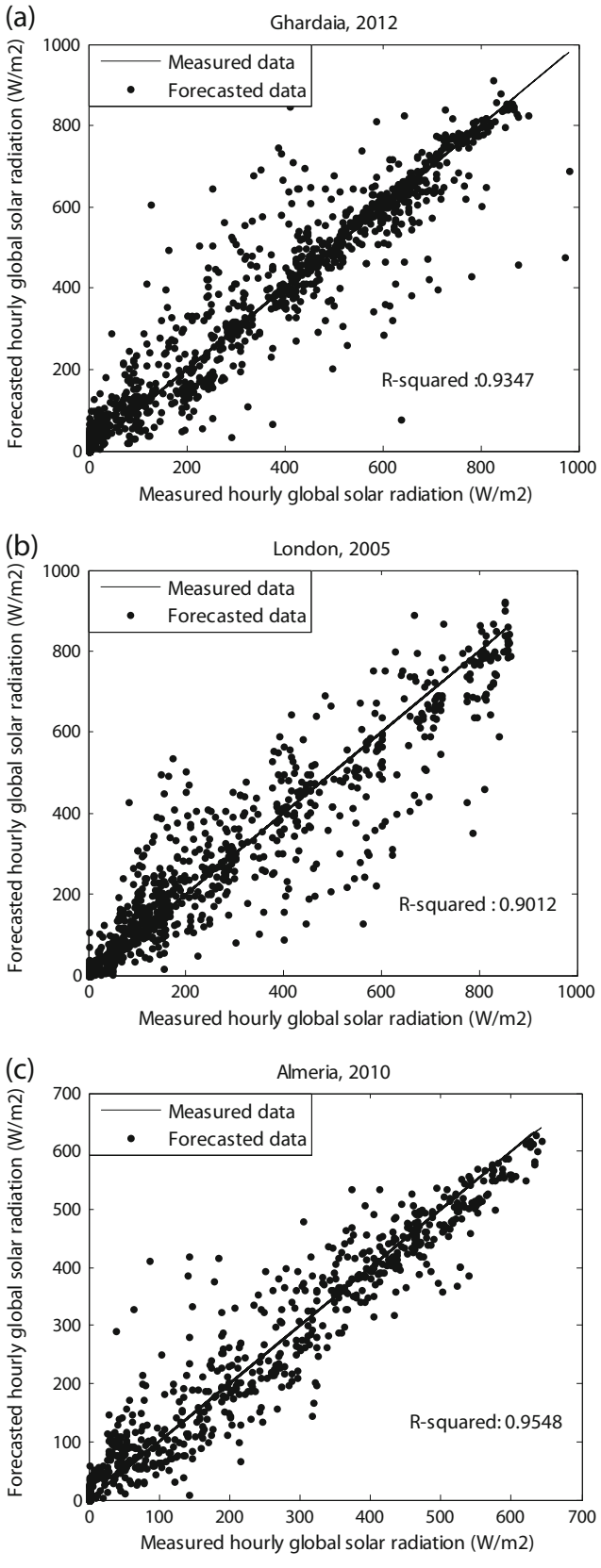

Fig. 7 **a** The measured test hourly global horizontal from versus forecasted time series using hybrid model for the site of Ghardaia, 2012. **b** The measured test hourly global horizontal from versus forecasted time series using hybrid model for the site of London, 2005 **c** The measured test hourly global horizontal from versus forecasted time series using hybrid model for the site of Almeria, 2010

Secondly, by modeling the residuals using NAR method, nonlinear relationships can be discovered. With n input nodes, the NAR model for the residuals will be:

$$v_t = f(v_{t-1}, v_{t-2}, \ldots, v_{t-n}) + e_t \tag{20}$$

where, f is a nonlinear function determined by the neural network and e_t is the random error. The forecasted series from Eq. (20) is denoted . Then the combined forecast will be expressed by the next equation:

$$\widehat{y}_t = \widehat{L}_t + \widehat{N}_t \tag{21}$$

In our simulation, we noted that the residual series v_t is often a random process that makes difficulties in the prediction of future values. The use of a 1D interpolation of v_t can solve this problem. Interpolation is a method of constructing new data point within a range of known data points. The obtained series of interpolation is then used to be forecasted by the NAR network.

3 Data selection

Our goal of the simulation is to select the best model for multi-hour ahead forecasting of the future values of hourly global solar radiation data. To evaluate the quality of the proposed model, the root mean square error (RMSE) and normalized root means square error (NRMSE) are chosen as the forecasting accuracy measures. Lewis (1982) considered that if the NRMSE values are between 0.2 and 0.5, the forecasted model is considered good model. Wu and Chan (2011) and Kostylev and Pavlovski (2011) found that the best performing model on an hourly time scale had an NRMSE of 0.17 for mostly clear days and 0.32 for

Table 5 Comparison between the NRMSE of the forecasting models taken from Wu and Chan (2011)) and Huang et al. (2013) and the proposed ARMA + NAR model

Models	NRMSE
ARMA + TDNN (Wu and Chan 2011)	0.3
vs. ARMA + NAR	0.1835
CARDS (Huang et al. 2013)	0.165
vs. ARMA + NAR	0.1339

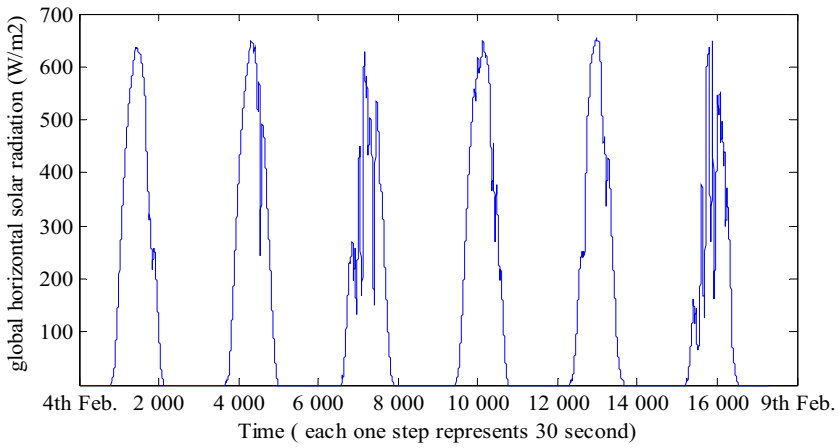

Fig. 8 The measured 30-s global horizontal solar radiation (from 4 February 2005 to 9 February 2005) for the site of Oran, Algeria

mostly cloudy days. In addition, the *R*-squared value gave by Eq. (22) is used as metric to judge the goodness of the forecast.

$$R^2 = 1 - \left(\frac{\sum_{i=1}^{n} \left(I_{i,measured} - I_{i,predicted} \right)^2}{\sum_{i=1}^{n} \left(I_{i,measured} - \overline{I_{i,\text{measured}}} \right)^2} \right) \tag{22}$$

Moreover, an important task of the proposed method is chosen the proper training and testing data set to avoid the over fitting problem. Hence, the *k*-fold cross validation method (Kohavi 1995) has been used to check the performances. In this method, the data set is divided into k subsets, each time, one of the k subsets is used as the test set and the other $k-1$ subsets are put together to form a training set. Then, the average error across all k trials is computed until we reached the best training and testing data set (Klipp et al. 2008).

In the simulation phase, we tested several hourly global horizontal solar radiation time series in this work for different climatic locations in the world. From the National Meteorological Office of Algeria, we choose the site of Oran, Algeria (35.6911° N, 0.6417° W) for the year of 2010 and the site of Ghardaia, Algeria (32.4908° N, 3.6728° E) for the year of 2012. From the Soda service website (http://www.soda-is.com/eng/index.html), the site of London, England (51.5171° N, 0.1062° W) for the year of 2005 and from GeoModelSolar S.R.O. (data calculated from Meteosat MSG and MFG satellite data (2012 EUMETSAT) and data (2012 ECMWF and NOAA) by SolarGIS method) the site of Almeria, Spain (36.8300° N, 2.4300° W) for the year of 2010.

In addition, to evaluate the performance of the proposed methodology to forecast hourly solar radiation against the methods presented in literature, a comparison part between ARMA and NAR approach and other methods is needed. For that, two models that based in hybrid methodology are

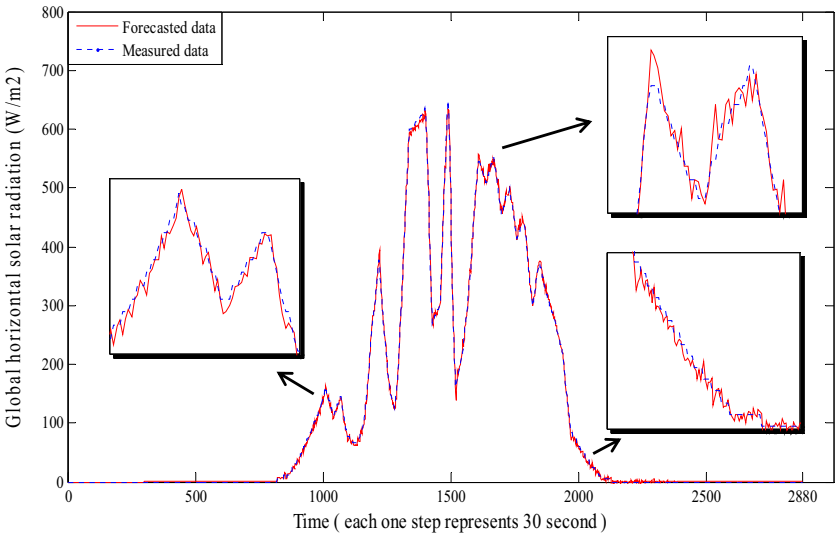

Fig. 9 The measured test 30-s global horizontal solar radiation (9 February 2005) versus forecasted series using hybrid model for the site of Oran, Algeria

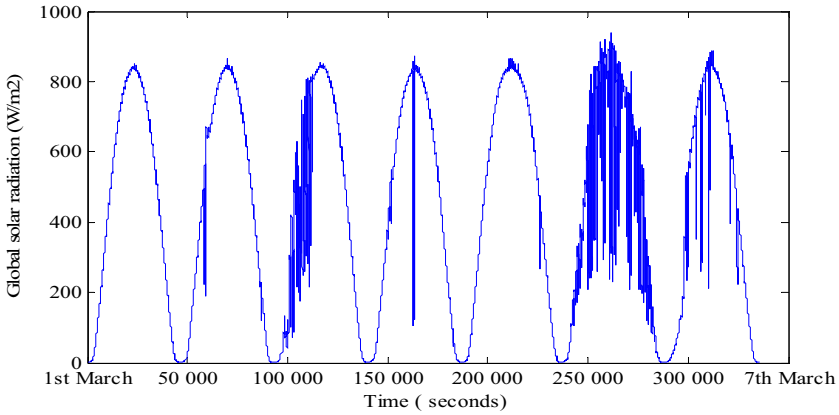

Fig. 10 The measured secondly global horizontal solar radiation (from 1 March 2013 to 7 March 2013) for the site of Sohar, Oman

selected. First, the hybrid model (ARMA and TDNN) proposed by Wu and Chan (2011). In this method, Al-Sadah et al. (1990) model is used to fit the monthly mean solar radiation series. Moreover, the hybrid model of ARMA with TDNN is selected for the forecasting purpose. Secondly, we have chosen the model developed by Huang et al. (2013), a coupled autoregressive and dynamical system (CARDS) model is used to forecast the solar radiation. In addition, the Fourier series is used to fit the solar radiation time series.

For the comparison between the method of this paper and other models, we used the same sample data used in Wu and Chan (2011) (Singapore, 2010; testing day: 2 February) and Huang et al. (2013) (Mildura, 2001; testing day: 25 January) .

4 Results and discussion

The first time series used in the simulation is for the site of Oran, Algeria (35.6911° N, 0.6417° W) for the year of 2010. We ignored data between 5:00 and 21:00 o'clock because there is no solar radiation measured during this period. Using the *k*-fold cross validation method the data are divided into two sets, training set (from 1 January 2010 to 31 October 2010) that represent 4,530 h, and test data set (from 1 November 2010 to the 31 December 2010) that represent 915 h (prediction horizon) . The training data set is used exclusively for model development then the test sample is used to evaluate the established model.

The hybrid ARMA-NAR method is applied to do the forecasting. First, ARMA model is used to predict hourly global solar radiation time series, then the residual between ARMA and measured series is forecasted using NAR model. The obtained forecast is added to the one of ARMA models.

In the detrending phase, we used a 6-degree polynomial model to get a stationary residual series. From the autocorrelation, partial correlation, and the AIC test of the residual series, we established that the ARMA (5, 7) is the suitable model to use it in the simulation.

In addition, different algorithms of training and sets of delays and neurons were tested experimentally in the simulation of the nonlinear autoregressive neural network model.

We found that the use of 31 delays and 10 neurons in the hidden layer with the Levenberg-Marquardt

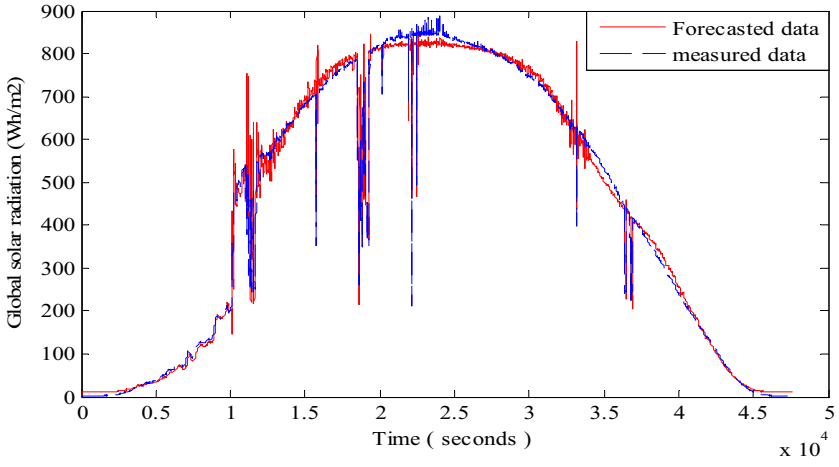

Fig. 11 The measured secondly global horizontal solar radiation (7 March 2013) versus forecasted series using hybrid model for the site of Sohar, Oman

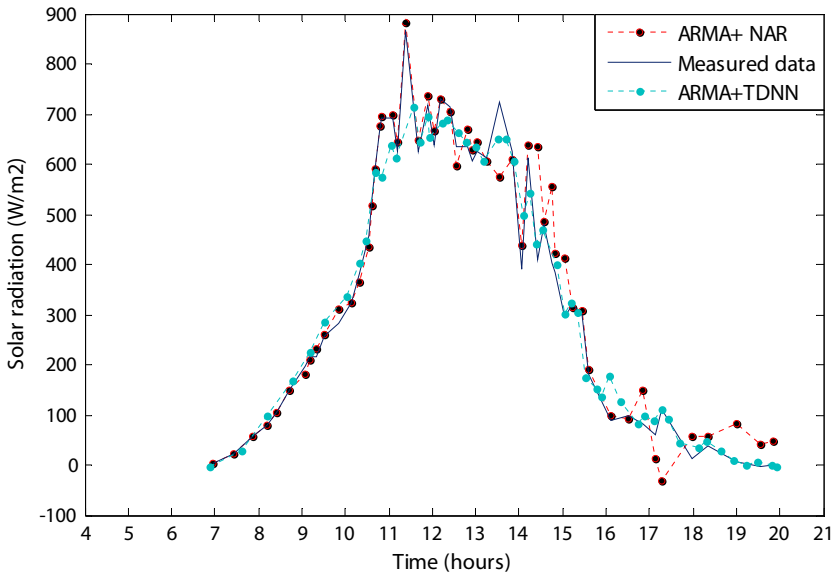

Fig. 12 Comparison between the 2nd February solar radiation data of Singapore 2010 taken from Wu and Chan (2011), the forecasting model using ARMA + TDNN (Wu and Chan 2011) and the proposed ARMA + NAR model

training method gives the fastest convergence with the smallest forecasting error.

The simulation results of the hybrid model to forecast hourly global solar radiation for the year of 2010 are presented in Fig. 4a; the blue line represents the measured hourly global horizontal solar radiation and the red dot one is the forecasted series by hybrid model. In addition, Fig. 4b–c represents the comparison results for the months of November 2010 and December 2010, respectively, and Fig. 4d for the first 2 weeks of November 2010. The blue line represents measured data, and the red dot line is the forecasted data.

The comparisons and performance of the forecasting hourly global horizontal time series using a hybrid model have been evaluated by calculating the RMSE errors between the actual data and forecasted one for the period of 1 November 2010 to 31 December 2010 (915-h-step ahead).

Moreover, the quadratic error expressed in Eq.(23) between measured and simulated hourly global solar radiation using the proposed method is demonstrated in Fig. 5. In addition, Fig. 6 represents the measured time series versus the forecasted one.

$$\mathrm{err} = \left(\frac{\left(I_{i,predicted} - I_{i,measured}\right)^2}{n} \right) \tag{23}$$

Where err is the quadratic error and n is the number of simples.

From Figs. 4a–d, 5, and 6 it was clearly shown that the hybrid model forecasted in good manner the measured solar radiation time series. From Fig. 4a, the total RMSE is equal to 71.82 W/m^2 and the NRMSE is 0.2103. With an R-squared value equal to 0.9272. Nevertheless, we can ensure that the comparison between forecasted and measured solar radiation time series presents some lag due to the presence of clouds.

In a same manner, we applied the hybrid method for the sites of Ghardaia (2012), London (2005), and Almeria (2010). The results of the k-fold cross validation as well as the RMSE and NRMSE errors between the measured and forecasted

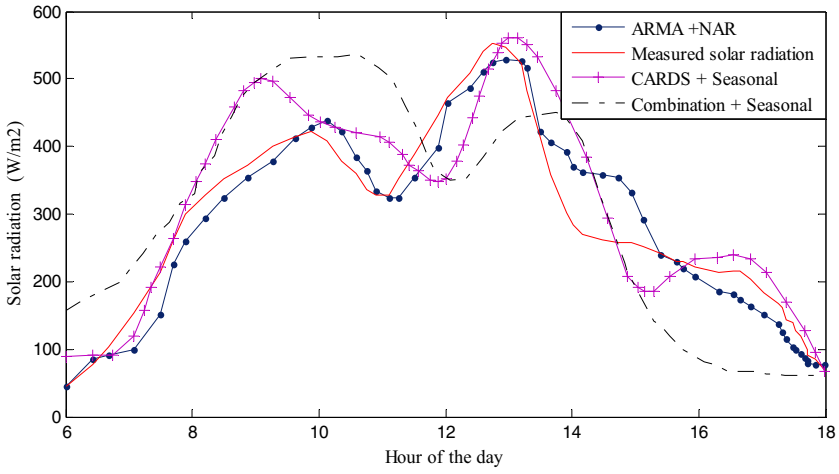

Fig. 13 Comparison between the 25 January solar radiation data of Mildura taken from Huang et al. (2013, p.146), the forecasting model using CARDS+ Seasonal (Huang et al. 2013), Combination + Seasonal (Huang et al. 2013) and the proposed ARMA + NAR model

series are represented in Table 4. Moreover, the simulation results of the proposed hybrid model versus measured hourly solar radiation for the sites of Ghardaia, London, and Almeria are shown in Fig. 7a–c, respectively.

From the results of Fig. 7a–c and Table 5, the hybrid model is considered the suitable method to forecast such similar problems. The NRMSE error had the lowest values comparing with single ARMA and NAR models. In addition, the *R*-squared value was found to be high for all tested locations.

The above-mentioned models are simulated based on hourly scales. However, the uncertainty of solar radiation time series increases in small scales (less than 1 min time step). Hence, it is an important task to test the proposed hybrid model in small scales. For that, two small step solar radiation data are used . First, a sequence of 30-s solar radiation data for the site of Oran, Algeria (from 4 February to 9 February) was used as shown in Fig. 8. The data are divided into training dataset (from 4 February to 8 February) and testing dataset (9 February) (Fig. 9).

And second, a sequence of 1-s solar radiation data for a desert zone in Sohar, Oman (From 1 March to 7 March 2013) is used as shown in Fig. 10. We ignored the data between 19 o'clock and 6 o'clock because there is no solar radiation data measurement in this period. In addition, data are divided into training dataset (from 1 March to 6 March) and testing dataset (9 February).

The simulation results of the forecasted data compared with measured data are shown in Fig. 9. (Oran, Algeria) and Fig. 11 (Sohar, Oman). From Fig. 9, it is clearly shown that the hybrid model is good with an NRMSE equal to 0.1935. In addition, from Fig. 11 the hybrid model forecast in good manner with an NRMSE equal to 0.1767. However, forecasted data represent some fluctuations compared with measured data that are because it simulated in small scales, which reduce the forecasting accuracy.

4.1 Comparison with other models

For the comparison between the method of this paper and other models, we used the same sample data used in Wu and Chan (2011) (Singapore, 2010; testing day: 2 February) and Huang et al. (2013) (Mildura, 2001; testing day: 25 January) .

Figures 12 and 13 show the simulation between the forecasting results using the ARMA and NAR method and other models. According to these figures and results of Table 5 we can see that the hybrid model provides better results with an NRMSE equal to 0.1835 against an average NRMSE of 0.3 for ARMA and TDNN model, and NRMSE of 0.1339 compared with the best NRMSE of the CARDS model that equals to 0.165. Finally, these results show the robustness and the accuracy of the proposed method in this paper.

5 Conclusion

In this paper, we introduced a hybrid model for multi-step ahead forecasting of hourly global horizontal solar radiation time. Firstly, ARMA model is applied to a stationary residual series that obtained from a detrending phase, the ADF test is used to choose the most stationary residual series. We concluded that the high polynomial degree fitting gives better results. Secondly, the NAR model is applied for the forecasting purpose that gives satisfactory results than the ARMA model. However, it takes much calculation time than the first model. The last approach is based on a hybrid method that combined both ARMA and NAR models. According to the fact that solar radiation series has linear and nonlinear components, the ARMA model was good to forecast the linear behavior of the solar radiation time series. Also, NAR network proved to be a suitable method to capture the non-linearity of the series. But, no one of them was suitable to extract full characteristics of global solar radiation series. Hence, as a conclusion of this works, the hybrid model is a good method to forecast such similar problems.

However, those models present a limitation in the forecasting in extremely bad weather condition, thus future works will be focused to test other hybrid models that can improve the reliability for the very cloudy sky.

Acknowledgments The authors would like to thank the University of Laghouat for the financial aspect of the present work. Also, the authors would like to thank Dr. Tamer Khatib and Dr. Hussian Kazem for providing experimental data used for further validation of the proposed model. These data were obtained from an experiment done in the frame of the research project no. ORG SU EI 11 010. Funded by the research council of the Sultanate of Oman.

References

Akaike H (1974) A new look at the statistical model identification. IEEE Trans Autom Control 6:716–723

Al-Sadah FH, Ragab FM, Arshad MK (1990) Hourly solar radiation over Bahrain. Energy 15:395–402

André Luis S, de Maia Francisco AT, de Carvalho Teresa BL (2008) Forecasting models for interval-valued time series. Neurocomputing 71:3344–3352

Badescu V, Gueymard C, Cheval S, Oprea C, Baciu M, Dumitrescu A, Iacobescu F, Milos I, Rada C (2013) Accuracy analysis for fifty-four clear-sky solar radiation models using routine hourly global irradiance measurements in Romania. Renew Energy 55:85–103

Baig A, Achter P, Mufti A (1991) A novel approach to estimate the clear day global radiation. Renew Energy 1:119–123

Bevington PR (1969) Data reduction and error analysis for the physical sciences. McGraw Hill Book Co, New York, p 336

Boata RST, Gravila P (2012) Functional fuzzy approach for forecasting daily global solar irradiation. Atmos Res 112:79–88

Boland JW (2008) Time series and statistical modelling of solar radiation. In: Badescu V (ed) Recent advances in solar radiation modelling. Springer-Verlag, Berlin, pp 283–312

Box GEP, Jenkins G (1970) Time series analysis, forecasting and control. Holden -Day, San Francisco

Chen SX, Gooi HB, Wang MQ (2013) Solar radiation forecast based on fuzzy logic and neural network. Renew Energy 60:195–201

Chow TWS, Leung CT (1996) Non-linear autoregressive integrated neural network model for short term load forecasting. IEE Proc Gener Transm Distrib 143:500–506

Denton JW (1995) How good are neural networks for causal forecasting? J Bus Forecast 14:17–20

Diagne M, David M, Lauret P, Boland J, Schmutz N (2009) Review of solar irradiance forecasting methods and a proposition for small-scale in solar grids. Renew Sust Energ Rev 13:406–419

Dickey DA, Fuller WA (1981) Likelihood ratio statistics for autoregressive time series with a unit root. Econometrica 49:1057–1072

Ginzburg I, Horn D (1994) Combined neural networks for time series analysis. Adv Neural Inf Process Syst 6:224–231

Haykin S (1998) Neural networks: a comprehensive foundation, 2nd edn. Prentice Hall, Upper Saddle River

Huang J, Korolkiewicz M, Agrawal M, Boland J (2013) Forecasting solar radiation on an hourly time scale using a coupled autoregressive and dynamical system (CARDS) model. Sol Energy 87:136–149

Ineichen P (2008) A broadband simplified version of the Solis clear sky model. Sol Energy 82:758–762

Kaplanis S (2006) New methodologies to estimate the hourly global solar radiation; comparisons with existing models. Renew Energy 31: 781–790

Kaplanis S, Kaplani E (2007) A model to predict expected mean and stochastic hourly global solar radiation $I(h;n_j)$ values. Renew Energy 32:1414–1425

Khatib T, Mohamed A, Sopian K (2012) A review of solar energy modeling techniques. J Renew Sustain Energy Rev 16:2864–2869

Klipp E, Herwig R, Kowald A, Wierling C, Lehrach H (2008) Systems biology in practice: concepts, implementation and application. John Wiley & Sons, West Sussex, p 327

Kohavi R (1995) A study of cross-validation and bootstrap for accuracy estimation and model selection. Proceedings of the Fourteenth International Joint Conference on Artificial Intelligence 2 (12): 1137–1143. Morgan Kaufmann, San Mateo, CA

Kostylev V, Pavlovski A (2011) Solar power forecasting performance—towards industry standards. Proceedings of the 1st International Workshop on the Integration of Solar Power into Power Systems, Aarhus, Denmark

Kugiumtzis D (2000) Surrogate data test for nonlinearity including nonmonotonic transforms. Phys Rev E Stat Phys Plasmas Fluids Relat Interdiscip Topics 62(1):R25–R28

Kwiatkowski D, Phillips PCB, Schmidt P, Shin Y (1992) Testing the null hypothesis of stationarity against the alternative of a unit root. J Econom 54:159–178

Levenberg K (1944) A method for the solution of certain problems in least squares. Q Appl Math 5:164–168

Lewis CD (1982) International and business forecasting methods. Butterworths, London

Ljung L (1998) System identification: theory for the user, 2nd edn. Prentice Hall PTR, Upper Saddle River

Luxhoj JT, Riis JO, Stensballe B (1996) A hybrid econometric-neural network modeling approach for sales forecasting. Int J Prod Econ 43:175–192

MacKay DJC (1992) Bayesian interpolation. Neural Comput 4:415–447

MacQueen JB (1967) Some methods for classification and analysis of multivariate observations. Proceedings of 5th Berkeley Symposium on Mathematical Statistics and Probability 1. University of California Press, Berkeley, pp 281–297

Makridakis S, Wheelwright SC, Hyndman RJ (1998) Forecasting: methods and applications, 3rd edn. John Wiley & Sons, New York

Markham IS, Rakes TR (1998) The effect of sample size and variability of data on the comparative performance of artificial neural networks and regression. Comput Oper Res 25:251–263

Mellit SA, Kalogirou L, Hontoria SS (2009) Artificial intelligence techniques for sizing photovoltaic systems: a review article. Renew Sust Energ Rev 13:406–419

Mellit A, Massi Pavan A, Benghanem M (2013) Least squares support vector machine for short-term prediction of meteorological time series. Theor Appl Climatol 111:297–307

Mihalakakou G, Santamouris M, Asimakopoulos DN (2000) The total solar radiation time series simulation in Athens, using neural networks. Theor Appl Climatol 66:185–197

Moller MF (1993) A scaled conjugate gradient algorithm for fast supervised learning. Neural Netw 4:525–533

Pandey PK, Soupir ML (2012) A new method to estimate average hourly global solar radiation on the horizontal surface. Atmos Res 115:83–90

Peled A, Appelbaum J (2013) Evaluation of solar radiation properties by statistical tools and wavelet analysis. Renew Energy 59:33–38

Pelikan E, de Groot C, Wurtz D (1992) Power consumption in West-Bohemia: improved forecasts with decorrelating connectionist networks. Neural Netw World 2:701–712

Voyant C, Muselli M, Paoli C, Nivet M (2013) Hybrid methodology for hourly global radiation forecasting in Mediterranean area. Renew Energy 53:1–11

Wedding DK, Cios KJ (1996) Time series forecasting by combining RBF networks, certainty factors, and the Box–Jenkins model. Neurocomputing 10:149–168

Wu J, Chan KC (2011) Prediction of hourly solar radiation using a novel hybrid model of ARMA and TDNN. Sol Energy 85:808–817

Zhang G (2003) Time series forecasting using a hybrid ARIMA and neural network model. Neurocomputing 50:159–175

Zhang G, Patuwo EB, Hu MY (1998) Forecasting with artificial neural networks: the state of the art. Int J Forecast 14:35–62

Energy Conversion and Management 80 (2014) 298–304

Contents lists available at ScienceDirect

Energy Conversion and Management

journal homepage: www.elsevier.com/locate/enconman

Improving the performance of PV systems by faults detection using GISTEL approach

Mohammed Tadj [a,1], Khalil Benmouiza [b,2], Ali Cheknane [a,*], Santiago Silvestre [c]

[a] Laboratoire des Semi-conducteurs et Matériaux Fonctionnels, Université Amar Telidji de Laghouat, BP 37G, Laghouat 03000, Algeria
[b] Department of Physics, Faculty of Science, Abou Bekr Belkaid University, Tlemcen, BP 119, Tlemcen 13000, Algeria
[c] MNT Group, Electronic Engineering Department, UPC-BarcelonaTech, Campus Nord UPC, Jordi Girona 1-3, 08034 Barcelona, Spain

ARTICLE INFO

Article history:
Received 8 October 2013
Accepted 17 January 2014
Available online 15 February 2014

Keywords:
Estimation of solar radiation
GISTEL model
Fault detection
Satellite images
PV systems

ABSTRACT

In this paper, we present a new approach for detecting the faults in the photovoltaic systems based on the satellite image approach for estimating solar radiation data and DC output power calculations for detecting the failures. At first stage, the estimation of the hourly global horizontal solar radiation data has been evaluated by using the GISTEL (Gisement solaire par télédetection: Solar Radiation by Teledectection) model improved by the fuzzy logic technique. Thus, the results were compared with the ground solar radiation measurements. On the other hand, the comparison between the simulated and measured output DC powers was reached to find the nature of the faults in the PV array.

The results showed a good accuracy and the simple implementation of the proposed approach. The estimation of the hourly solar radiation presents an NRMSE <0.22 using GISTEL model improved by fuzzy logic comparing with the estimation without fuzzy logic with an NRMSE = 0.2885 for clear sky and NRMSE = 0.2852 comparing with NRMSE = 0.3121 for cloudy sky.

1. Introduction

Solar energy is one of the most important renewable energies for generating electricity and meeting our daily needs. However, the efficiency of the photovoltaic (PV) panels was considered low [1] due to financial and technical problems that can increase the installation cost. Hence, the methods for estimating the amount of the solar radiation and monitoring of the PV systems become very important tasks [2]. To ensure a proper monitoring of photovoltaic plants, it is necessary to adopt specific techniques related with the type and accuracy of the information provided as well as their prices [3]. The measurement of the solar irradiation is one of those techniques. To this end, different ways were proposed in the literature to estimate the solar radiation data; such as ground models [4–6] and satellite image processing models [7–10]. In addition, several studies have been carried out on the detection of different failures in PV systems [11–15].

The results from these models showed that the optimal determination of the solar radiation estimation models, and failure detection techniques lead to an efficient PV system. Drews et al. [12] developed a procedure to detect failures in grid connected PV systems based on the average hourly solar radiation satellite data using Heliosat method and PV simulation. Firth et al. [13] have used empirical models for failure detection in PV systems. However, these methods based on the average solar radiation data, where in this paper we proposed a satellite approach model to get the hourly solar radiation. In addition, Chouder and Silvestre [14] have present an automatic supervision and faults detection of PV systems based on capture losses and the analysis of several parameters such as thermal losses and miscellaneous losses that complicate the procedure and increase the calculation time. And generally, those methods used complicated algorithms and mathematical models, and sometimes provide bad results. For this purpose, we had proposed in this paper a new simple method based on the extraction of the hourly global horizontal solar radiation data from satellite images for a specific location combined with an algorithm for detecting the faults in the PV system.

The precision of the estimated solar radiation is necessary to improve the performance of the proposed model, for that, the GISTEL (Gisement Solaire par Télé detection) proposed by [16] was used. It consists of the processing of the Meteosat second generation images MSG-2. An algorithm based on a relationship between the clearness indexes determined from the Meteosat images and the global solar irradiation received on the ground under clear

* Corresponding author. Fax: +213 93 26 98.
E-mail addresses: mohtej@gmail.com (M. Tadj), benkhalil3@gmail.com (K. Benmouiza), a.cheknane@mail.lagh-univ.dz, cheknanali@yahoo.com (A. Cheknane).
[1] Tel.: +213 553 00 90 11.
[2] Tel.: +213 778 73 85 56.

http://dx.doi.org/10.1016/j.enconman.2014.01.030
0196-8904/

sky was used. Moreover, a hybrid model was proposed in this paper that combined the basic method of GISTEL and the fuzzy logic approach in order to obtain more precise results.

Second, for detecting the failures in the PV array, we have proposed a procedure based on the analysis of the measured and simulated DC output powers. The DC powers are used here leading to the fact that the failure detection algorithm deals only with the DC part of the PV system. The next step consists in the determination of the current and the voltage ratios that indicates the nature of the faults. Moreover, the proposed method allows the determination of the false detection of failures. The evaluation of the proposed method was reached using the root mean square error RMSE and normalized root mean square NRMSE errors.

The remaining part of this paper is organized as follows. Section 2 presented the methodology used in this work for the detection of failures in PV systems; a background of the GISTEL model has been viewed. In addition, the mechanisms of detection of the faults have also been shown. In Section 3, we had simulated the results obtained from the GISTEL model and compared them to the measured solar radiation data. Moreover, a comparison between the simulated results of the proposed approach and the obtained ones in the case of the absence of failure in the PV array has been also carried out. The last section is devoted to the conclusion and discussion of future works.

2. Methodology

The detecting of failures in PV arrays was known as an important task for optimal sizing of the PV system to get the maximum of output power [14,17]. The failures in the PV system augment the power losses in the case of the presence of faults [18]. Hence, in this work, a proposed simulation method based on the Matlab/Simulink environment has been used for detecting the faults. This method consists of two main parts. First, the GISTEL model was applied to estimate the hourly horizontal global solar radiation time series, and then the obtained results were compared to the measured ones. At the second stage, a comparison of the output power from GISTEL and the measured data were used to detect the failures. The proposed method was presented in Fig. 1.

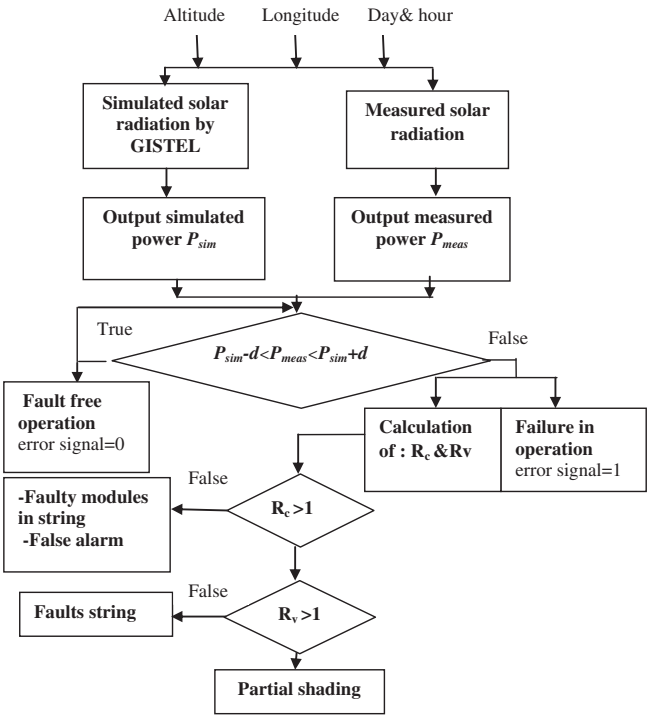

Fig. 1. Flowchart of the fault detection procedure.

2.1. GISTEL model

GISTEL is a satellite methodology based on a simple physical model. It is used to estimate global solar irradiance from Meteosat data. The adopted methodology has several steps that we have summarized by the diagram of Fig. 2.

1. For estimating the global solar radiation (Gc) under a clear sky, the world organization of meteorology (W.M.O.) [19] model given by Eq. (1) is used; this model depends on the solar height (hs) and the linked turbidity factor (TL) used to quantify the effect of atmospheric components of solar radiation, the TL values generally vary from 2 (very pure and dry sky) to 6 (polluted and humid sky).

$$G_c = cor[1300 - 57T_L](\sin(h_s))^{(36+T_L)/33} \quad (1)$$

where cor is the correction factor of the earth–sun distance given by Eq. (2) and nj *is* the number of the days of the year.

$$cor = 1 + 0.034\cos(0.986(nj - 3)) \quad (2)$$

2. The ground instantaneous reflection coefficients $Rib(x, y, d, h)$ for each pixel (x, y) of the visible MSG image of the day d and the hour h are given by Eq. (3). Those coefficients represent the reflection of solar radiation on the surface.

$$Rib(x, y, d, h) = \frac{Bi(x, y, d, h) - Bia(x, y, d, h)}{K \cdot Gc(x, y, d, h) \cdot Ti(x, y, d, h)} \quad (3)$$

where Bi (x, y, d, h) represents the brightness of the (x, y) pixel, Bia (x, y, d, h) the atmospheric brightness recorded by the satellite above the sea by a clear sky. This brightness was considered constant, and it is equal to 12 [9]; K is the factor calibration of the visible channel sensor equal to 0.514. Ti (x, y, d, h) *is* the transmission coefficient of the direct irradiation from the ground to the satellite. It is given by Eq. (4),

$$Ti = \frac{(1390 - 31T_L)}{1367}\exp\left[-\frac{T_L}{12.6\sin(h_v + 2)}\right] \quad (4)$$

where h_v is the height angle of the satellite, given by Eq. (5).

$$h_v = \arcsin\left(\frac{1.862\cos(\varphi)\cos(\theta) - 0.274}{\sqrt{3.41 - \cos(\varphi)\cos(\theta)}}\right) \quad (5)$$

θ and φ are respectively the latitude and the longitude.

3. For determining the two clear and cloudy reference images, a sequence of images was taken over long period at 12 h UTC. Taking the minimum values of the reflection coefficients obtained from those sequence images, the clear sky reference image can be obtained. On the other hand, the cloudy sky reference image is constructed by using the greatest values of the reflection coefficient obtained using the same sequence of images.
4. The clearness index k_t is calculated for each image by comparing pixel by pixel and hour by hour the instantaneous reflection coefficients Rib with the two clear sky R_c and the cloudy sky R_n reflection coefficients. According to this comparison three types of skies can be observed namely clear sky, partially covered sky and completely covered sky [9], as expressed in Eq. (6)

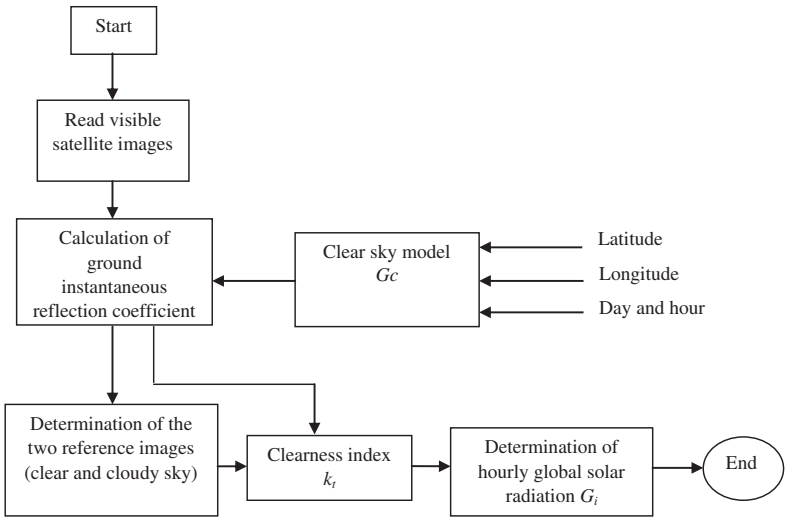

Fig. 2. The different steps of the GISTEL model.

$$\begin{aligned}&\text{Clear sky}: Rib \le Rc : k_t = 1\\ &\text{Partially covered sky}: Rc < Rib < Rn : k_t = 1 - (1 - K_0)\frac{(Rib - Rc)}{(Rn - Rc)}\\ &\text{Completely covered sky}: Rib \ge Rn : k_t = K_0\end{aligned} \tag{6}$$

where K_0 is the index by a cloudy sky equals to 0.2. However, for obtaining more precise results a fuzzy logic approach is proposed in this paper. Fuzzy logic methodology has the ability to translate human qualitative knowledge into formal algorithms; it deals with reasoning that is approximate rather than fixed. It consists of using expert rules that can sometimes produce a simple set of control for a dynamical system with less effort. Hence, three rules are introduced in this work to obtain logical values of the clearness index k_t as expressed in Fig. 3.

5. Finally the instantaneous global solar radiation $Gi(x, y, d, h)$ for each pixel is obtained by multiplying the clearness index k_t by the global solar radiation obtained under clear sky $Gc(x, y, d, h)$. As expressed in Eq. (7) as

$$Gi(x, y, d, h) = k_t \times Gc(x, y, d, h) \tag{7}$$

2.2. Detection of the faults

For extracting the DC output powers, the output currents and voltages of the PV systems have been calculated using a double diode PV model as expressed in Eq. (8).

$$I = I_{ph} - I_{01}\left(\exp\left(\frac{V + R_s I}{n_1 V_t} - 1\right)\right) - I_{02}\left(\exp\left(\frac{V + R_s I}{n_2 V_t} - 1\right)\right) - \frac{V + R_s I}{R_{sh}} \tag{8}$$

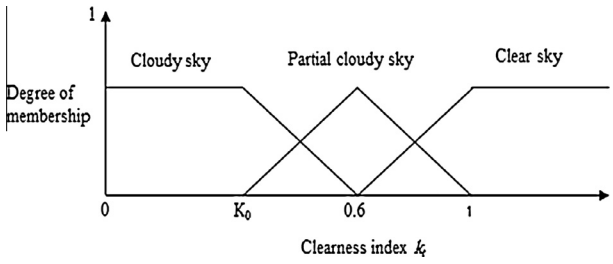

Fig. 3. Fuzzy logic membership functions.

where I_{ph} is the current generated by the incident light. I_{01}, I_{02} are the reverse saturation currents of the diodes D1 and D2 respectively. V_t is the thermal voltage. n_1, n_2 are the ideality factors of diodes D1 and D2. R_s and R_{sh} are the series and shunt resistance respectively. V and I are the output PV module voltage and current respectively. Fig. 4 represents the used electrical model of PV system with two diodes.

From Eq. (8), the simulated P_{sim} and measured P_{meas} powers are given by Eqs. (9) and (10) respectively. The measurements of voltages and currents have been made respectively using electronic Amperemeter and Voltmeter.

$$P_{meas} = V_{meas} \cdot I_{meas} \tag{9}$$

$$P_{sim} = V_{sim} \cdot I_{sim} \tag{10}$$

The detection of faults is based on the comparison between P_{sim} and P_{meas}. However, due to the calculation errors between simulated and measured outputs, upper and lower boundaries have been established as given by Eq. (11). This equation allows the determination whether the measured DC output power is inside the predetermined boundaries or outside of them. If yes, then no failure is detected. Otherwise, a failure in the PV system can be occurred.

$$P_{sim} - 2d < P_{meas} < P_{sim} + 2d \tag{11}$$

where d is the standard deviation calculated from simulated output DC powers for clear sky.

The next step consists of calculating the current and the voltage ratios given by Eqs. (12) and (13) respectively [14].

$$R_c = \frac{I_{PV\_sim}}{I_{PV\_meas}} \tag{12}$$

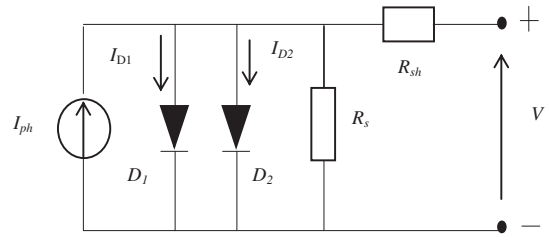

Fig. 4. The electrical model of PV system with double diodes.

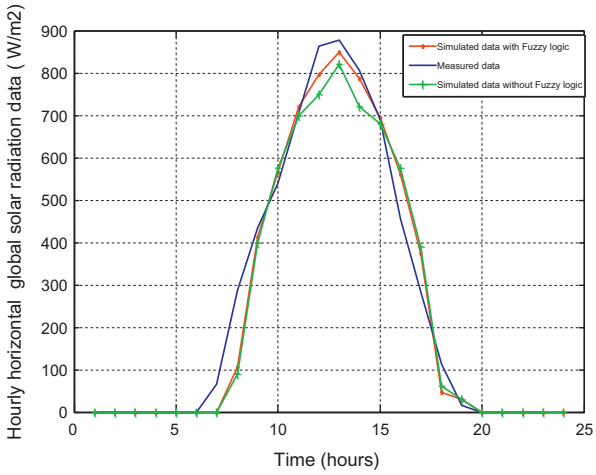

Fig. 5. Measured and simulated of the hourly global horizontal solar radiation with FL and without FL method for the day of 3rd March 2013 for the site of Bouzerah, Algeria.

$$R_v = \frac{V_{PV\_sim}}{V_{PV\_meas}} \tag{13}$$

From the analysis of R_C and R_v ratios, the failure can be determined as expressed in Fig. 1. If the measured output DC power is outside the lower and upper boundaries a failure due to faults may be observed in the PV array. The nature of the failure was determined by the calculation, first, the values of R_c. And second, the values of R_v. If both R_c and R_v are bigger that 1, then the nature of faults is the shadowing. Otherwise, other types of failures were determined like string faults.

3. Simulation results and discussion

In our simulation we are interested in detecting the faults in a PV array. Hence, two phases are applied. First, the estimation of hourly global solar radiation time series was determined using GISTEL model. On the other hand, a PV system formed by 2 strings with 4 PV panels in each one, which delivers a power equal to 600 Wp for DC output power calculation was then used. For the estimation of the hourly solar radiation different day that represent the stat of the sky (clear, partially cloudy and cloudy) have been used. However; just one day is used to detect faults (generally the clearest sky day).

In order to perform the GISTEL methodology, two different approaches with and without the fuzzy logic methods were used. We had chosen in our simulation two locations for validation purposes. First, two random days for the locations were selected, the first ones are from the site of Bouzareah in Algeria (36.78° N, 3° E) for the days of 3rd of February 2013 and the 26th of February 2013; the data were collected from the National Meteorological Office (ONM) of Algeria. The second location is for Almeria in Spain (36.84° N, 2.4° W); the data were collected from the GeoModel Solar S.R.O., M. Marecka 3, Bratislava, Slovakia for the days of 15th February 2011 and the 20th February 2011. Moreover, the satellite images for each hour were obtained from the Meteo Company B.V website: (http://www.sat24.com) for both locations of Bouzereah and Almeria.

Figs. 5–8 show the simulation results of the hourly global horizontal solar radiation time series of the above-mentioned locations; in all figures the blue line[3] represents the measured hourly

[3] For interpretation of color in Figs. 1 and 5–8, the reader is referred to the web version of this article.

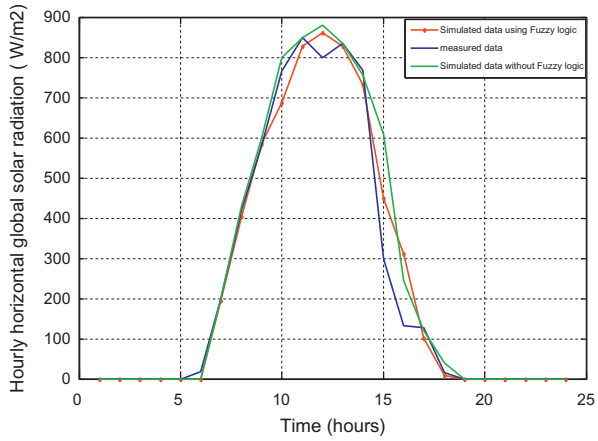

Fig. 6. Measured and simulated of the hourly global horizontal solar radiation with FL and without FL method for the day of 26th March 2013 for the site of Bouzerah, Algeria.

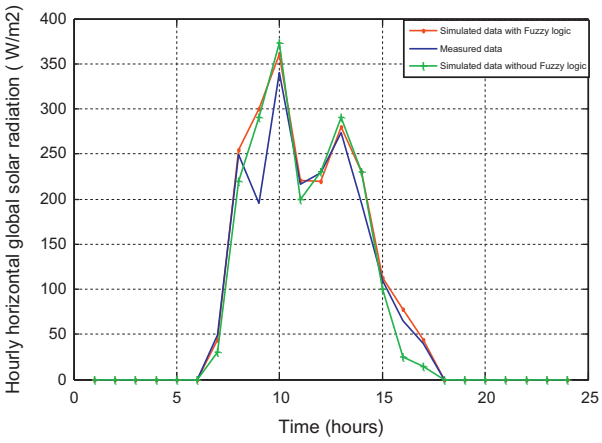

Fig. 7. Measured and simulated of the hourly global horizontal solar radiation with FL and without FL method for the day of 15th February 2011 for the site of Almeria, Spain.

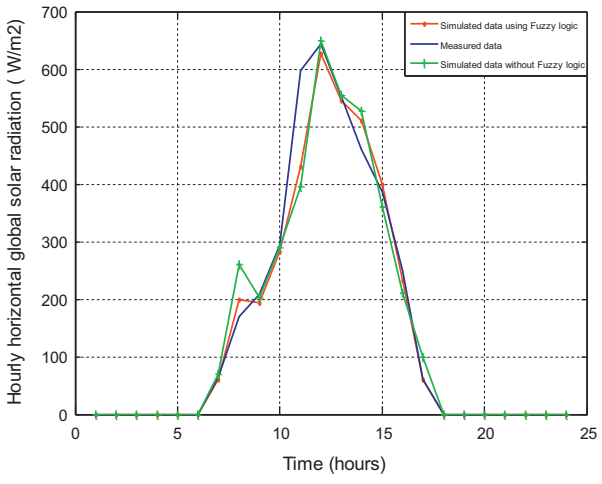

Fig. 8. Measured and simulated of the hourly global horizontal solar radiation with FL and without FL method for the day of 20th February 2011 for the site of Almeria, Spain.

solar radiation data, the red dot line present the simulated data using the fuzzy logic approach and the green dot line presents the simulated data without fuzzy logic method.

In addition, for comparing the simulation of the hourly horizontal global solar radiation by the mentioned methods, the RMSE and NRMSE represented in Eqs. (14) and (15) were used to judge the validity of the models.

$$\mathrm{RMSE} = \left[\frac{1}{n}\sum_{i=1}^{n}(I_{i,predicted} - I_{i,measured})^2\right]^{\frac{1}{2}} \quad (14)$$

$$\mathrm{NRMSE} = \left(\frac{\left[\frac{1}{n}\sum_{i=1}^{n}(I_{i,predicted} - I_{i,measured})^2\right]^{\frac{1}{2}}}{\frac{1}{n}\sum_{i=1}^{n}(I_{i,measured})}\right) \quad (15)$$

From Figs. 5–8, we note that the simulated solar radiations are changed during the day; from low values in sunrise and sunset to high values at noon that leads to the fact that the results obtained from the GISTEL model were representing the real stat of a day. In addition, some fluctuations can be occurring due to the presence of clouds.

The variation of the solar radiations depends on the clearness index it; a clear day has a clearness index equal to 1, a cloudy day with $k_t = 0.2$ and a partially cloudy day between $0.2 < k_t < 1$.

For the validation of the simulation results of the estimation of hourly horizontal global solar radiation data with GISTEL model with the fuzzy logic model and without it, the RMSE and the NRMSE represented in Table 1 were used.

From Table 1, it is clearly shown that the simulated models with the fuzzy logic model are good enough, that represents an NRMSE error between 0.2 and 0.28 comparing to the measured solar radiation data for all locations. Moreover, from Table 1, the NRMSE of the simulated hourly horizontal global solar radiation using the fuzzy logic method is lower than the simulated ones without use it, leads to a conclusion that the GISTEL model with the fuzzy logic method is good for such similar problems.

After determining the global solar radiation time series, we move onto the detection of the failures in the PV system. Thus, the simulation consists of two steps. First, the simulation PV system outputs without faults and second with faults.

3.1. PV outputs without faults

In this stage, we have simulated the outputs of the system without any faults to present the normal functioning of the proposed method. Hence, the output powers for the simulated solar radiation data from GISTEL model and measured one for the day of 26th March 2011 for the site of Bouzereah Algeria were calculated as shown in Fig. 9.

From Fig. 9 it is clearly shown that the measured and simulated output DC powers are near each other, which mean that the GISTEL model can be used to calculate the output power.

Next, to show the correct functionality of the PV array (no detection of fault), the upper and lower boundaries of the simulated output DC power expressed in Eq. (11) were calculated. The results are shown in Fig. 10. Those two boundaries plotted in red line can be used to indicate fault detection of failures; any output DC power outside the upper and lower boundary is considered as a fault.

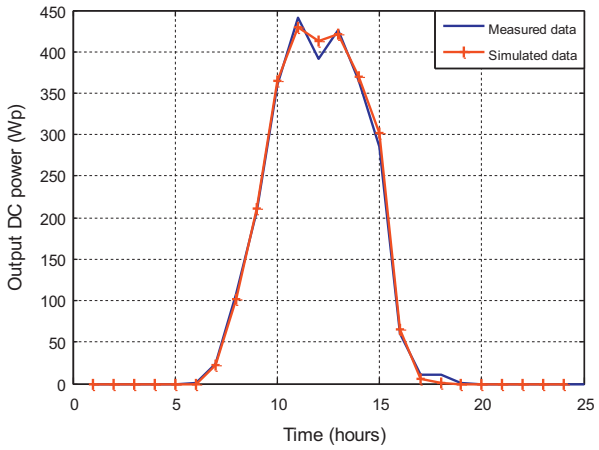

Fig. 9. Measured and simulated PV output DC power without faults.

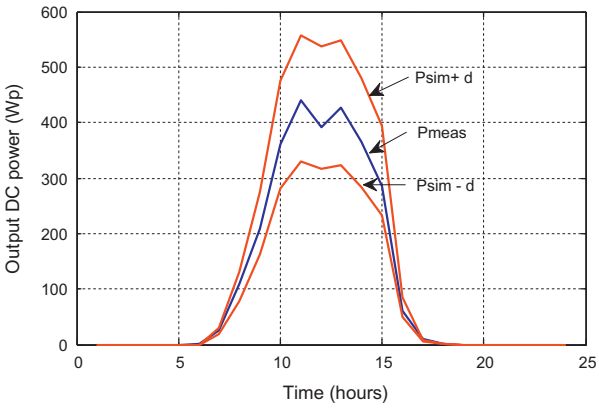

Fig. 10. Output DC powers evolution between lower and upper boundaries without faults.

Moreover, the values of the current and voltage ratios were simulated in Fig. 11. The blue line represents the current ratio and the red one represents the voltage ratio. Those two ratios indicate the nature of the failure as shown in Fig. 1. If the R_c and R_v values are near to 1, then no fault is detected. Else, the faults can be occurred.

3.2. PV system outputs with shading faults

This step consists of showing how the fault can be detected using just the DC output powers simulated and measured. Hence, the same day was used in the simulation, but with the presence

Table 1
The RMSE and NRMSE between actual data and simulated data with and without fuzzy logic method (FL) method.

	Date	Error (RMSE)		Error (NRMSE)	
		With FL	Without FL	With FL	Without FL
Bouzereah (Algeria)	26 March 2013	52.8788	69.8051	0.2185	0.2885
	03 April 2013	52.9886	63.6144	0.2072	0.2488
Almeria (Spain)	15 February 2011	23.3158	25.5123	0.2852	0.3121
	20 February 2011	36.9515	49.0828	0.2407	0.3197

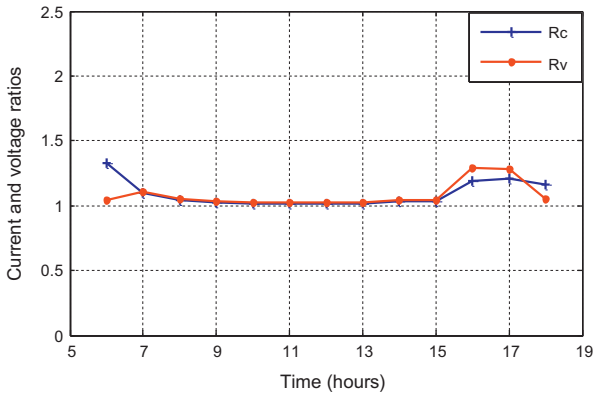

Fig. 11. Evolution of current and voltage ratios without faults.

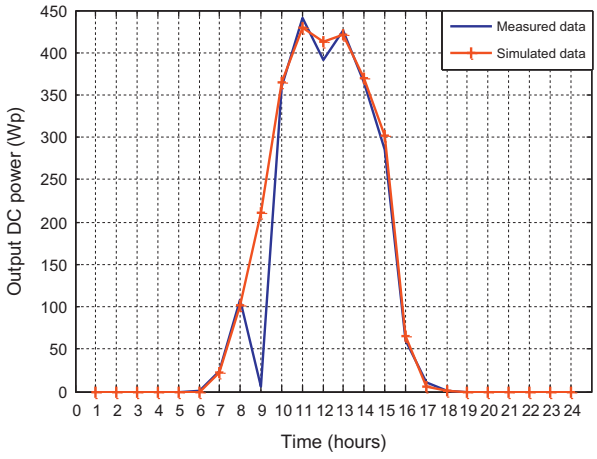

Fig. 12. Measured and simulated PV output DC power with faults between of 8 o'clock and 10 o'clock.

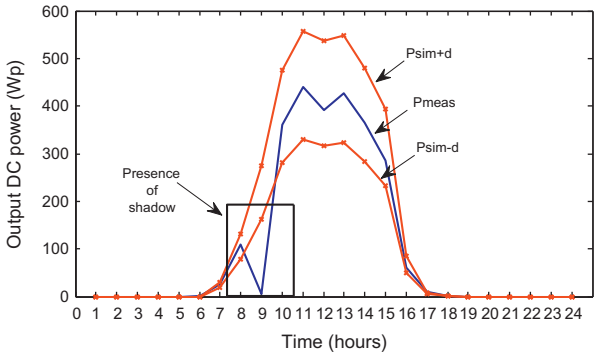

Fig. 13. Output DC powers evolution between lower and upper boundaries with faults.

of shadow (buildings and trees etc.) in the period from 8 o'clock to 10 o'clock as shown in Figs. 12 and 13.

From Figs. 12 and 13, the measured DC output power is outside upper and lower boundaries between 8 o'clock and 10 o'clock. This shows clearly the presence of faults in the PV array. Next, to know the nature of this fault, the current and voltage ratios have been simulated as shown in Fig. 14.

The simulated values of R_C and R_V are bigger than 1 between the period from 8 o'clock to 10 o'clock. Moreover, using the propped method from Fig. 1, we have both R_C and R_V above 1 that means that the nature of the fault is the shadow.

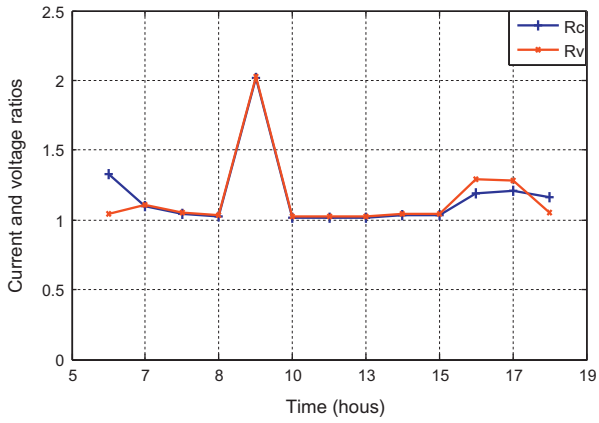

Fig. 14. Evolution of current and voltage ratios with faults.

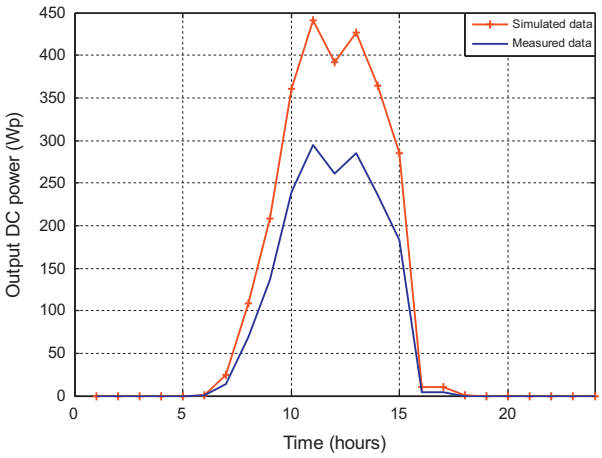

Fig. 15. Measured and simulated PV output DC power with a constant string faults.

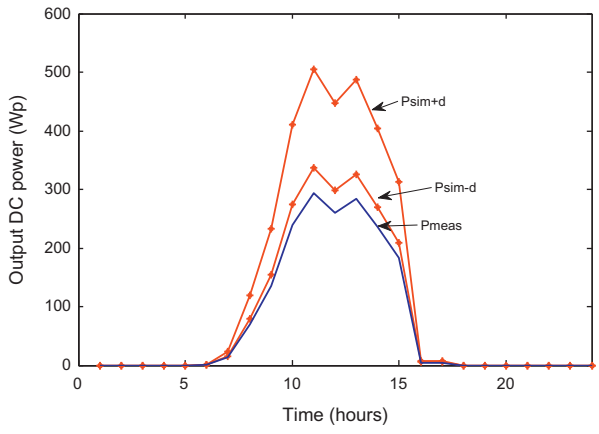

Fig. 16. Output DC powers evolution between lower and upper boundaries with a constant strings faults.

3.3. PV system outputs with string faults

The occurrence of constant faults in PV system indicates the existence of a problem in the strings. The simulated output DC power is very less than the measured one. As illustrated in Fig. 15.

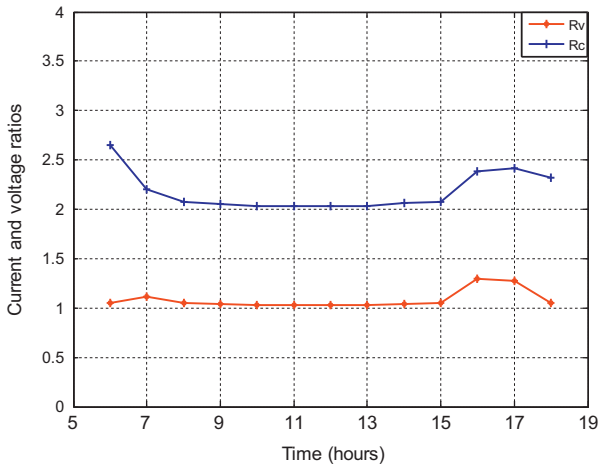

Fig. 17. Evolution of current and voltage ratios with a constant string faults.

Fig. 16 shows the deviation of the measured output DC power out of the upper and lower boundaries, that indicate the existence of losses in the PV system plant. In addition, Fig. 17 shows the evolution of current and voltage ratios with a constant string faults.

The current ratio is bigger than one and the value of the voltage ratio is equal to 1 which means that the fault is in the string as illustrated in the flowchart of Fig. 1.

4. Conclusion

In this paper, we proposed a new approach for detecting the failures in the photovoltaic systems, based on the output DC power analysis considering the amount of the solar radiation. The methodology used in this work consists, firstly on the estimation of the hourly global horizontal solar radiation data using a modified GISTEL model. The objective of this approach is the processing of the visible satellite images by calculating the transmission coefficients for each pixel of the image. A comparison between those coefficients and the ones obtained from the clear, partial and totally cover sky have been reached, which allows determining the clearness index that used for the estimation of the hourly solar radiation. In addition, a combination of the base GISTEL model and a fuzzy logic approach was used in this model in order to obtain more precise results. At the second stage, we have proposed a simple algorithm that can be used for detecting the faults in the PV systems. The calculation of the DC output powers for both measured and simulated PV systems allow detecting the faults. Moreover, the calculation of the ratios between simulated and measured voltages and currents lead to an identification of the type of faults in the PV array. The obtained experimental results showed the accuracy of this approach. In addition, the proposed method does not need a complicate calculation and based only on few input parameters.

References

[1] Kim JM, Dutta PS. Optical efficiency–concentration ratio trade-off for a flat panel photovoltaic system with diffuser type concentrator. Sol Energy Mater Sol Cells 2012;103:35–40.
[2] Huld T, Muller R, Gambardella A. A new solar radiation database for estimating PV performance in Europe and Africa. Sol Energy 2012;86:1803–15.
[3] Ismail MS, Moghavvemi M, Mahlia TMI. Characterization of PV panel and global optimization of its model parameters using genetic algorithm. Energy Convers Manage 2013;73:10–25.
[4] Badescu V, Gueymard C, Cheval S, Oprea C, Baciu M, Dumitrescu A, et al. Accuracy analysis for fifty-four clear-sky solar radiation models using routine hourly global irradiance measurements in Romania. Renew Energy 2013;55:85–103.
[5] David M, Lauret P, Boland J. Evaluating tilted plane models for solar radiation using comprehensive testing procedures, at a southern hemisphere location. Renew Energy 2013;51:124–31.
[6] Hove T, Manyumbu E. Estimates of the Linke turbidity factor over Zimbabwe using ground-measured clear-sky global solar radiation and sunshine records based on a modified ESRA clear-sky model approach. Renew Energy 2013;52:190–6.
[7] Pillot B, Muselli M, Poggi P, Haurant P, Hared I. Solar energy potential atlas for planning energy system off-grid electrification. Energy Convers Manage 2013;69:131–47.
[8] Cano D, Monget JM, Albuisson M, Guillard H, Regas N, Wald L. A method for the determination of the global solar radiation from meteorological satellite data. Sol Energy 1986;37:31–9.
[9] Ben Djemaa A, Delorme C. A comparison between one year of daily global irradiation from ground-based measurements versus METEOSAT images from seven locations in Tunisia. Sol Energy 1992;5:325–33.
[10] Mefti A, Adane A, Delorme C. Estimation of solar irradiance using Wefax and high resolution Meteosat images. World Renewable Energy congress VI; 2000.
[11] Stellbogen D. Use of PV circuit simulation for fault detection in PV array fields. In: Proceedings of the 23rd IEEE photovoltaic specialists conference. 1302-7; 1993.
[12] Drews A, De Keizer AC, Beyer HG, Lorenz E, Betcke J, van Sark WGJHM, et al. Monitoring and remote failure detection of grid-connected PV systems based on satellite observations. Sol Energy 2007;81:548–64.
[13] Firth SK, Lomas KJ, Rees SJ. A simple model of PV system performance and its use in fault detection. Sol Energy 2010;84:624–35.
[14] Chouder A, Silvestre S. Automatic supervision and fault detection of PV systems based on power losses analysis. Energy Convers Manage 2010;51:1929–37.
[15] Mukai T, Kawamoto S, Ueda Y, Saijo M, Abe N. Residential PV system users perception of profitability, reliability, and failure risk: an empirical survey in a local Japanese municipality. Energy Policy 2011;39:5440–8.
[16] Delorme C, Gallo A, Olivieri J. Quick use of Wefax images from Meteosat to determine daily solar radiation in France. Sol Energy 1992;3:191–7.
[17] Gokmen N, Karatepe E, Silvestre S, Celik B, P Ortega P. An efficient fault diagnosis method for PV systems based on operating voltage-window. Energy Convers Manage 2013;73:350–60.
[18] Solórzano J, Egido MA. Automatic fault diagnosis in PV systems with distributed MPPT. Energy Convers Manage 2013;76:925–34.
[19] W.M.O. Meteorological aspects of the utilization of solar radiation as an energy source. Technical note W.M.O. vol. 172; 1981. p. 57–85.

Simulation Modelling Practice and Theory 47 (2014) 236–247

Contents lists available at ScienceDirect

Simulation Modelling Practice and Theory

journal homepage: www.elsevier.com/locate/simpat

An innovative method based on satellite image analysis to check fault in a PV system lead–acid battery

Mohammed Tadj [a,1], Khalil Benmouiza [b], Ali Cheknane [a,*]

[a] Laboratoire des Semi-conducteurs et Matériaux Fonctionnels, Université Amar Telidji de Laghouat, BP 37G, Laghouat 03000, Algérie
[b] Department of Physics, Faculty of Science, Abou Bekr Belkaid University, Tlemcen BP 119, Tlemcen 13000, Algeria

ARTICLE INFO

Article history:
Received 3 March 2014
Received in revised form 20 June 2014
Accepted 21 June 2014
Available online 18 July 2014

Keywords:
Lead–acid battery
Estimation of solar radiation
GISTEL model
Faults checking
PV systems

ABSTRACT

Batteries are an important part in photovoltaic systems. They ensure reliability and good-operation of the overall PV system. In this paper, we proposed a method based on the estimation of the solar radiation to check the faults that occur in the lead–acid batteries. At first, the GISTEL (Gisement solaire par télédetection: Solar Radiation by Teledetection) model is chosen as a satellite image approach to estimate the hourly global solar radiation. Secondly, the estimated data are selected as input to check the faults of the lead–acid battery. A simple and effective method is developed to detect the internal resistance effect as well as the overcharging problem during the charging and discharging cycles. The experimental results show the easiness of the proposed method that possesses a good accuracy.

1. Introduction

The growing demand of energy in our life requires renewable solutions apart from the limited fossil energies. In addition, the negative effect of the traditional sources of energy that polluted the atmosphere leads us to search new environment-friendly solutions such as solar and wind energy. Solar energy is more and more used to generate electricity by converting solar radiation into useful DC power using PV panels. Nevertheless, the efficiency of panels is considered low due to financial and technical problems [16]. Hence, the optimal monitoring of PV systems is needed that depend strongly on the estimated solar radiation and checking the failures in the devices of PV systems such as panels, batteries and converters. In this view, we proceeded to study the effect of the losses in batteries to ensure the optimal operation of PV systems. For that, the estimation of solar radiation is considered to be an essential part in the PV system monitoring. Different methods were proposed in the literature to estimate the solar radiation data such as ground models [2,10,6] or the satellite images processing approaches [3,13,17]. Nevertheless, ground models are not effective because of the lack of the measured solar radiation. Hence, we have chosen in this paper the satellite methods due to their performances and accuracy. The GISTEL (Gisement solaire par télédetection) model is one of the most succeeded satellite methods to extract the solar radiation [18,15]. The first version of the GISTEL model was developed by Cano et al. [7]. The satellite images used in the GISTEL model provide an estimation of the solar radiation for any location around the world. The advantages of the GISTEL model are that it depends only on the satellite images and some parameters such as longitude, latitude and link turbidity. In addition, the

* Corresponding author. Tel./fax: +213 (0) 29 93 26 98, 29 93 21 17.
E-mail addresses: m.tadj@mail.lagh-univ.dz (M. Tadj), benkhalil3@gmail.com (K. Benmouiza), a.cheknane@mail.lagh-univ.dz, cheknanali@yahoo.com (A. Cheknane).
[1] Tel.: +213 553 00 90 11, + 213 (0) 29 93 21 17, fax: +213 (0) 29 93 26 98

http://dx.doi.org/10.1016/j.simpat.2014.06.010
1569-190X/

good operation of the batteries represents a very important task in the PV system monitoring [12,11,22]. Moreover, a periodical check of the state of the batteries, especially the lead–acid ones, can give information about the operation state of the PV systems. On the other hand, the results from the models to estimate the solar radiation are complex and require a lot of calculation time. Different methods were presented in literature to monitor the losses in PV system batteries. McKenna et al. [14] have studied the economic and environmental impact of the use of lead–acid batteries in grid-connected PV systems. Tsang and Chan [20] have explained the equivalent DC resistances of Lithium ion battery cells of several health conditions during charging mode under different temperatures and they have established the relationships between the equivalent DC resistance, health condition and operating temperature. However, those papers have studied the SOC of the battery without taking into consideration the solar radiation as an important input. Moreover, they presented complicated methods to detect faults in PV systems.

For these reasons, we propose, firstly, the GISTEL methodology improved by fuzzy logic technic as a satellite images approach to estimate the amount of the solar radiation. The GISTEL model is a physical approach that used real visible images to extract the solar radiation. These data have an important effect on the output of PV systems; a good estimation of the solar radiation data leads to an efficient PV system.

Secondly, the monitoring of the lead–acid solar battery requires to check it and to identify the failures in real-time. In this paper, we have chosen to test the effect of the battery internal resistance and the overcharging case in the floating diet. The variation of the internal resistance of the battery has negative impacts in the PV system efficiency as well as in the battery lifetime.

Hence, in this work, we intend to show the effects of an increase of the internal resistance and of the degradation of the storage unit capacity through the introduction of the battery internal resistance. Moreover, the second effect to be checked is the overcharging of the battery and its effects on the PV system performances as an overcharging cause a decrease of the water level in the lead–acid battery which results into degradation of the internal plates of the battery. In this study, the method is not developed to supervise PV plants, just small stand-alone applications where the cost of communications, as well as electronics for the measurements is not justified.

The follow up of this paper is organized as follows. Section 2 presents a background of the GISTEL model. In Section 3, we show the methodology used in this work to check the failures in PV system battery. In Section 4, we have simulated the results obtained from the GISTEL model and compared them to the measured solar radiation data. Moreover, the simulated results of the proposed approach in the case of the absence of failure in the PV system battery have been also carried out. The last section is devoted to the conclusion and discussion of future work.

2. Methodology

The identification of losses in PV systems presents a big task to achieve the desired output. For that, we are interested in detecting failures in the storage unit that causes a decrease in the efficiency of the PV system [9]. In this work, a proposed simulation method based on the Matlab/Simulink environment has been used to detect the faults in the batteries. The GISTEL method was first applied for the estimation of solar radiation data, based on the extracted satellite images. Secondly, these data were introduced into the PV array to produce the output power. After that, this energy was stored in batteries to ensure the autonomy of the PV system. The third stage consists in studying the behavior of the storage unit under different situations. The proposed structure presented in Fig. 1.

2.1. GISTEL model

In the previous paper by the authors of this study [18] the GISTEL model is defined as a satellite methodology based on a simple physical model. It is used to estimate global solar irradiance from METEOSAT data. The adopted methodology has several steps that we have summarized in the diagram of Fig. 2.

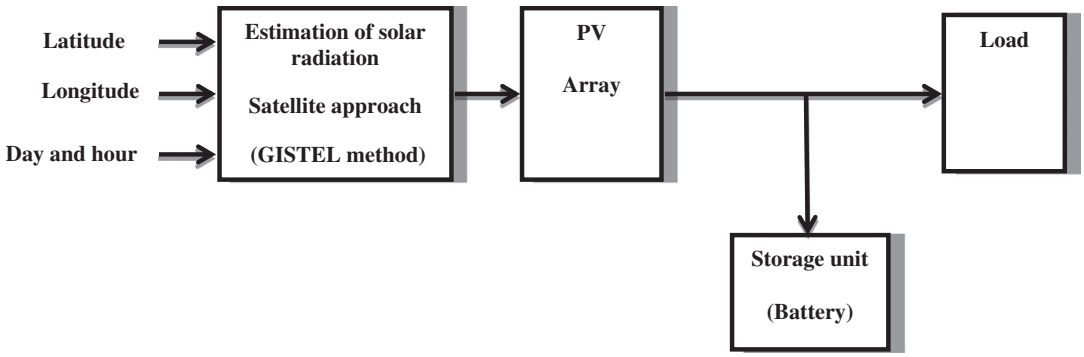

Fig. 1. Flowchart of the proposed methodology.

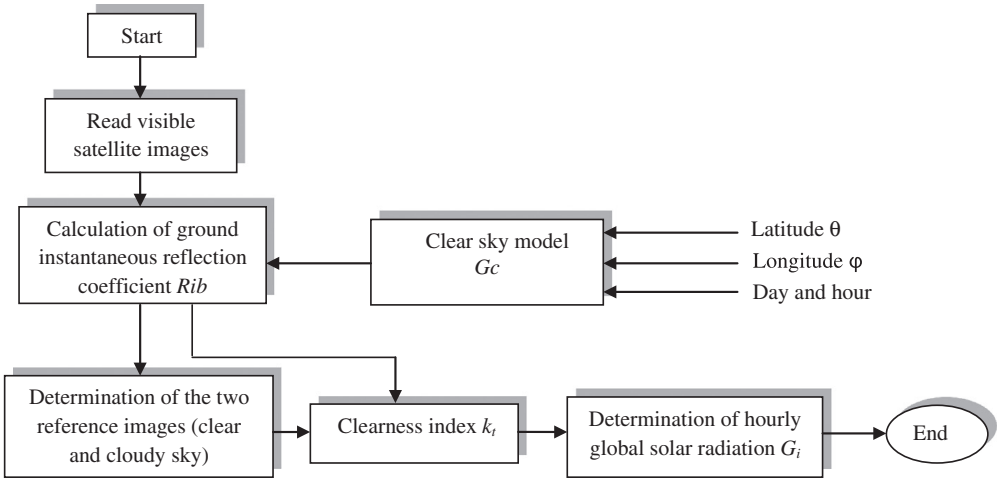

Fig. 2. The different steps of the GISTEL model.

1. To estimate the global solar radiation (Gc) under a clear sky, the world organization of meteorology (W.M.O.) [21] model given by Eq. (1) is used; this model depends on the solar height (h_s) and the linked turbidity factor (TL) used to quantify the effect of atmospheric components of solar radiation, the TL values generally vary from 2 (very pure and dry sky) to 6 (polluted and humid sky).

$$Gc = cor[1300 - 57T_L](\sin(h_s))^{(36+T_L)/33} \tag{1}$$

where cor is the correction factor of the earth–sun distance given by Eq. (2) and nj is the number of the days of the year.

$$cor = 1 + 0.034\cos(0.986(nj - 3)) \tag{2}$$

2. The ground instantaneous reflection coefficients $Rib(x, y, d, h)$ for each pixel (x, y) of the visible MSG image of the day d and the hour h are given by Eq. (3). Those coefficients represent the reflection of solar radiation on the surface.

$$Rib(x, y, d, h) = \frac{Bi(x, y, d, h) - Bia(x, y, d, h)}{K \cdot Gc(x, y, d, h) \cdot Ti(x, y, d, h)} \tag{3}$$

where $Bi(x, y, d, h)$ represents the brightness of the (x, y) pixel, $Bia(x, y, d, h)$ the atmospheric brightness recorded by the satellite above the sea by a clear sky. This brightness was considered constant, and it is equal to 12 [4]; K is the factor calibration of the visible channel sensor equal to 0.514. $Ti(x, y, d, h)$ is the transmission coefficient of the direct irradiation from the ground to the satellite. It is given by Eq. (4),

$$Ti = \frac{(1390 - 31T_L)}{1367} \exp\left[-\frac{T_L}{12.6\sin(h_v + 2)}\right] \tag{4}$$

where h_v is the height angle of the satellite, given by Eq. (5).

$$h_v = \arcsin\left(\frac{1.862\cos(\varphi)\cos(\theta) - 0.274}{\sqrt{3.41 - \cos(\varphi)\cos(\theta)}}\right) \tag{5}$$

θ and φ are respectively the latitude and the longitude.

3. To determine the two clear and cloudy reference images, a sequence of images was taken over a long period at 12 h UTC. Taking the minimum values of the reflection coefficients obtained from those sequence images, the clear sky reference image can be obtained. On the other hand, the cloudy sky reference image is constructed by using the greatest values of the reflection coefficient obtained using the same sequence of images.
4. The clearness index k_t is calculated for each image by comparing pixel by pixel and hour by hour the instantaneous reflection coefficients Rib with the two clear sky R_c and the cloudy sky R_n reflection coefficients. According to this comparison three types of skies can be observed namely clear sky, partially covered sky and completely covered sky [4], as expressed in Eq. (6).

$$\begin{aligned} &\bullet \text{ Clear sky :} && Rib \leqslant Rc : k_t = 1 \\ &\bullet \text{ Partially covered sky :} && Rc < Rib < Rn : k_t = 1 - (1 - K_0)\tfrac{(Rib - Rc)}{(Rn - Rc)} \\ &\bullet \text{ Completely covered sky :} && Rib \geqslant Rn : k_t = K_0 \end{aligned} \tag{6}$$

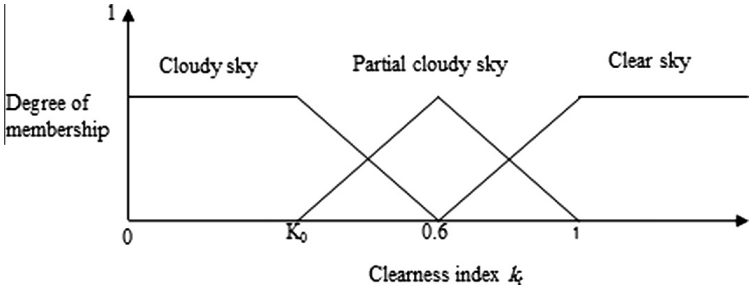

Fig. 3. Fuzzy logic membership functions.

where K_0 is the index by a cloudy sky equals to 0.2. However, for obtaining more precise results a fuzzy logic approach is proposed in this paper. Fuzzy logic methodology has the ability to translate human qualitative knowledge into formal algorithms; it deals with reasoning that is approximate rather than fixed. It consists of using expert rules that can sometimes produce a simple set of control for a dynamical system with less effort. Hence, three rules are introduced in this work to obtain logical values of the clearness index k_t as expressed in Fig. 3.

5. Finally the instantaneous global solar radiation $Gi(x, y, d, h)$ for each pixel is obtained by multiplying the clearness index k_t by the global solar radiation obtained under clear sky $Gc(x, y, d, h)$. As expressed in Eq. (7) as

$$Gi(x, y, d, h) = k_t \times Gc(x, y, d, h) \tag{7}$$

3. PV system modeling

3.1. Modeling of PV array

To obtain the DC output powers, the output current and voltage of the PV array has been calculated using a double diode PV model as expressed in Eq. (8) [1,8].

$$I = I_{ph} - I_{01}\left(\exp\left(\frac{V + R_s I}{n_1 V_t} - 1\right)\right) - I_{02}\left(\exp\left(\frac{V + R_s I}{n_2 V_t} - 1\right)\right) - \frac{V + R_s I}{R_{sh}} \tag{8}$$

where I_{ph} is the current generated by the incident light. I_{01}, I_{02} are the reverse saturation currents of the diodes D1 and D2 respectively. V_t is the thermal voltage. n_1, n_2 are the ideality factors of diodes D1 and D2. R_s and R_{sh} are the series and shunt resistance respectively. V and I are the output PV module voltage and current respectively.

3.2. Storage unit model

The battery used in this work is a lead acid battery with 12 V of voltage and 104 A h of capacity; it is expressed by the following equation [19]:

Charge model ($i^* < 0$):

$$f(it, i^*, i, Exp) = E_0 - K\frac{Q}{it - 0.1Q}i^* - K\frac{Q}{Q - it}it + Laplace^{-1}\left(\frac{Exp(s)}{Sel(s)} \cdot \frac{1}{s}\right) \tag{9}$$

Discharge model ($i^* > 0$):

$$f(it, i^*, i, Exp) = E_0 - K\frac{Q}{Q - it}i^* - K\frac{Q}{Q - it}it + Laplace^{-1}\left(\frac{Exp(s)}{Sel(s)} \cdot 0\right) \tag{10}$$

where E_0 is the constant voltage (V); $Exp(s)$ is the exponential zone dynamics (V); $Sel(s)$ represents the battery mode. $Sel(s) = 1$ during battery charging, $Sel(s) = 0$ during battery discharge; K is the polarization resistance (Ohm); i^* is the low frequency current dynamic (A); i is the battery current (A); it is the extracted capacity (A h); Q is the maximum battery capacity (A h).

4. Simulation results and discussion

The objective of this work is the identification of faults in the PV system battery. For that, we used in the simulation a PV system with four panels (two panels in series with two branches) that represent a 300 Wp as total output power. The characteristics of the PV panels are given in Table 1. The objective is the extraction of the solar radiation data via satellite images using GISTEL model and use this data for the identification of failure in the battery that allowed minimizing the losses in the PV system.

Table 1
The solar panel parameters.

Parameters	Values
Maximum power (Pmax)	75 W
Maximum power voltage (Vmpp)	21.68 V
Maximum power current (Impp)	3.33 A
Open circuit voltage (Voc)	21.40 V
Short circuit current (Isc)	3.69 A
Max system voltage	1000 V

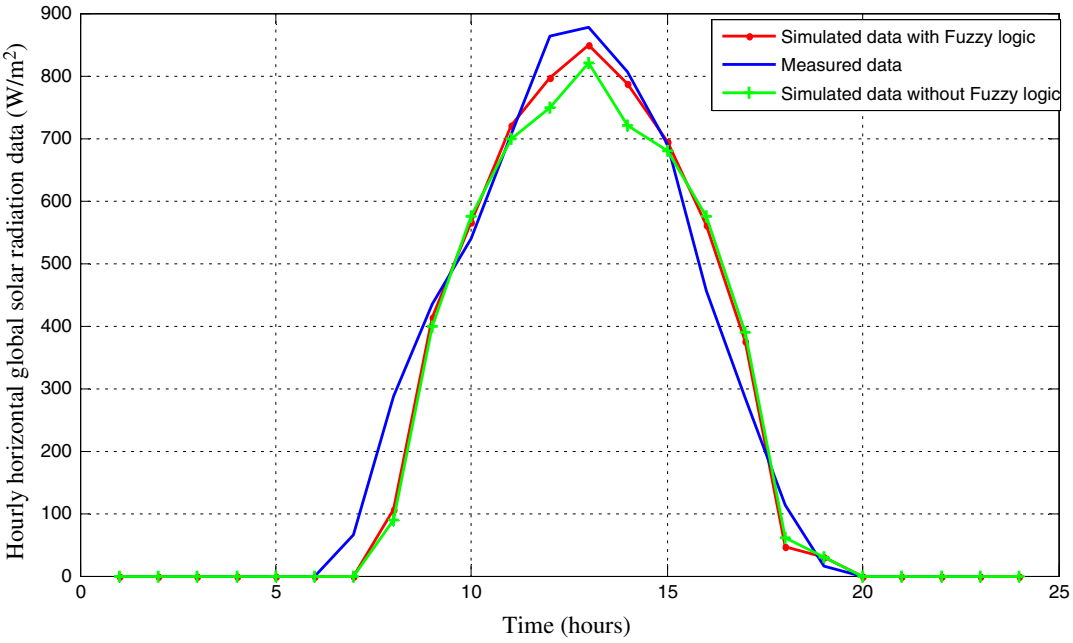

Fig. 4. Measured and simulated of the hourly global horizontal solar radiation with FL and without FL method for the day of 3rd March 2013 for the site of Bouzerah, Algeria.

In the first step, the satellite approach (GISTEL model) was improved using the fuzzy logic method. The obtained data from GISTEL model using FL and without FL were compared with the measured data. For the validation purpose, we have chosen three locations. First, in Algeria (Bouzareah 36.78°N, 3°E) for the days of 3rd of February 2013 and the 26th of February 2013 and (Ghardaia 32.48°N, 3.66°E) for the days of 22nd November 2012 and the 7th of December 2012; the data were collected from the National Meteorological Office (ONM) of Algeria. The third location is Almeria in Spain (36.84°N, 2.4°W) the data were collected from the GeoModel Solar S.R.O., M. Marecka 3, Bratislava, Slovakia for the days of 15th February 2011 and the 20th February 2011. Moreover, the satellite images for each hour were obtained from the Meteo Company B.V website: (http://www.sat24.com) for all locations of Bouzereah and Ghardaia in Algeria and Almeria in Spain.

The simulation results are shown in Figs. 4–9 that represents the hourly global horizontal solar radiation time series for the three locations; the blue[3] line represents the measured data, the red dot line indicate the simulation data improved by FL (fuzzy logic) technic and the green dot one presents the simulated data without FL method. The RMSE and NRMSE were used to give a value for our validation. Eqs. (11) and (12) represent the RMSE and NRMSE respectively [5]:

$$RMSE = \left[\frac{1}{n}\sum_{i=1}^{n}\left(I_{i,predicted} - I_{i,measured}\right)^2\right]^{\frac{1}{2}} \tag{11}$$

$$NRMSE = \left(\frac{\left[\frac{1}{n}\sum_{i=1}^{n}\left(I_{i,predicted} - I_{i,measured}\right)^2\right]^{\frac{1}{2}}}{\frac{1}{n}\sum_{i=1}^{n}\left(I_{i,measured}\right)}\right) \tag{12}$$

[3] For interpretation of color in Figs. 4–9 and 12–15, the reader is referred to the web version of this article.

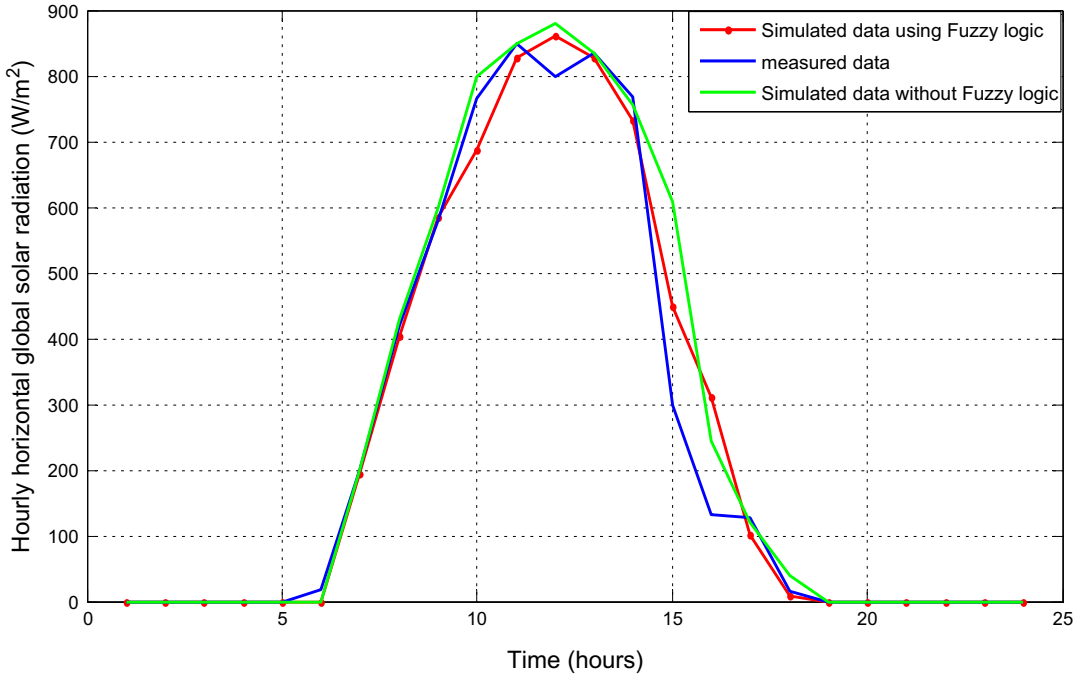

Fig. 5. Measured and simulated of the hourly global horizontal solar radiation with FL and without FL method for the day of 26th March 2013 for the site of Bouzerah, Algeria.

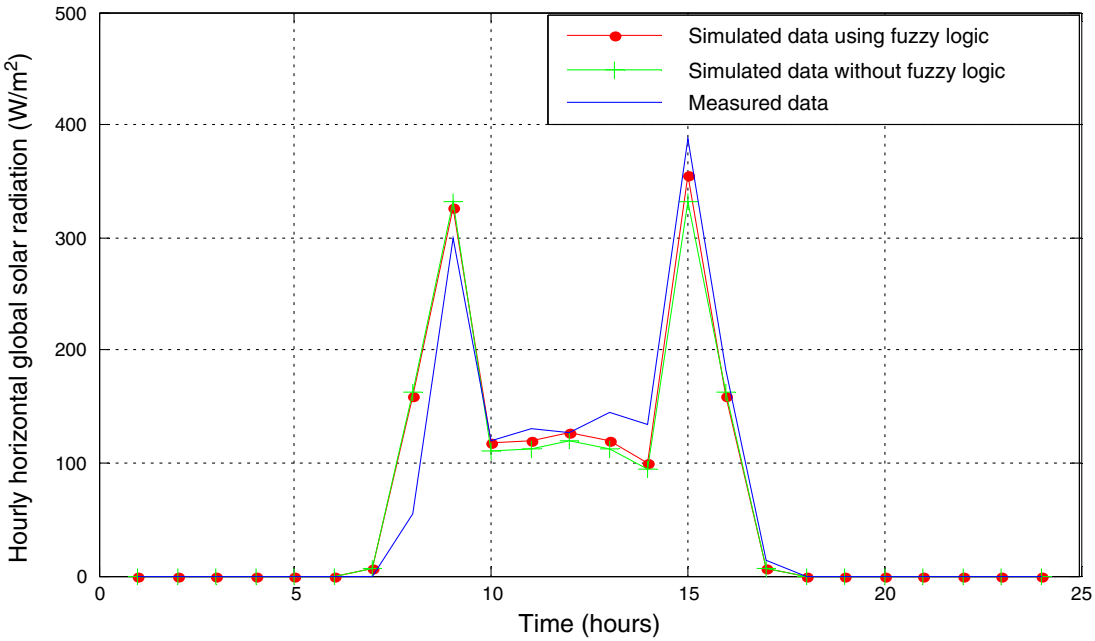

Fig. 6. Measured and simulated of the hourly global horizontal solar radiation with FL and without FL method for the day of 22nd November 2012 for the site of Ghardaia, Algeria.

In Figs. 4–9, we observed that the simulation solar radiation data are changed from low values in sunrise and sunset to high ones at noon. The simulation of hourly solar radiation using FL is almost the same as the measured data. Moreover; the occurrence of fluctuations indicates the passage of clouds.

Table 1 represents the RMSE and the NRMSE error of simulation results with and without FL technic for the three locations.

From Table 2, the simulation results of GISTEL model with FL represent good values of an NRMSE error between 0.2 and 0.28 comparing with the measured solar radiation data and the estimation without FL for all locations. For that, the GISTEL model with fuzzy logic method represents a good improvement for the estimation of hourly horizontal global solar radiation by satellite images.

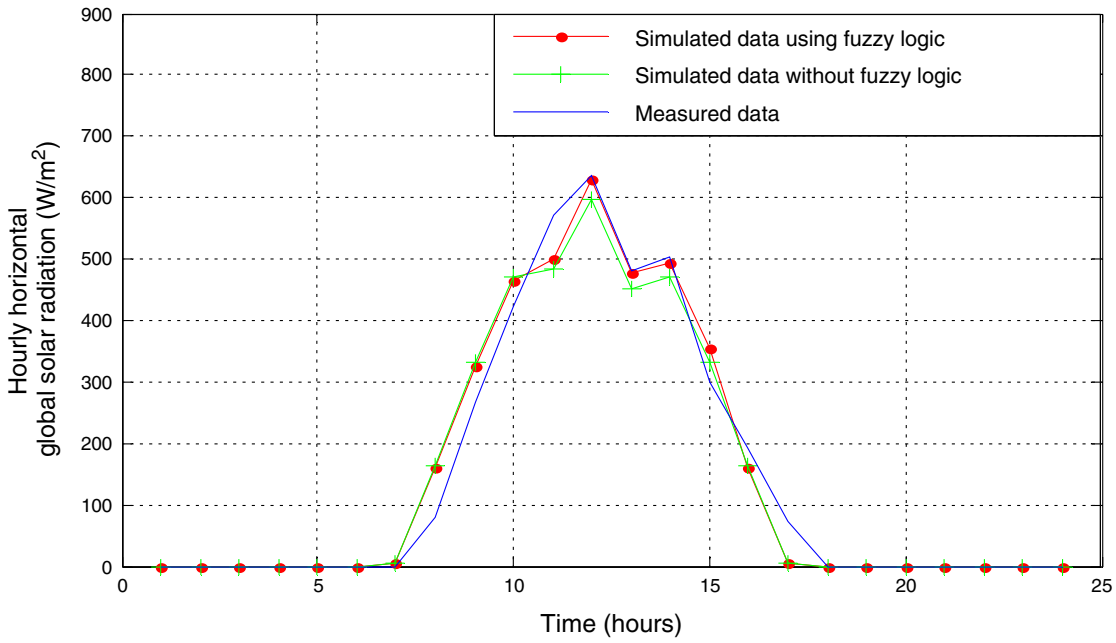

Fig. 7. Measured and simulated of the hourly global horizontal solar radiation with FL and without FL method for the day of 7th December 2012 for the site of Ghardaia, Algeria.

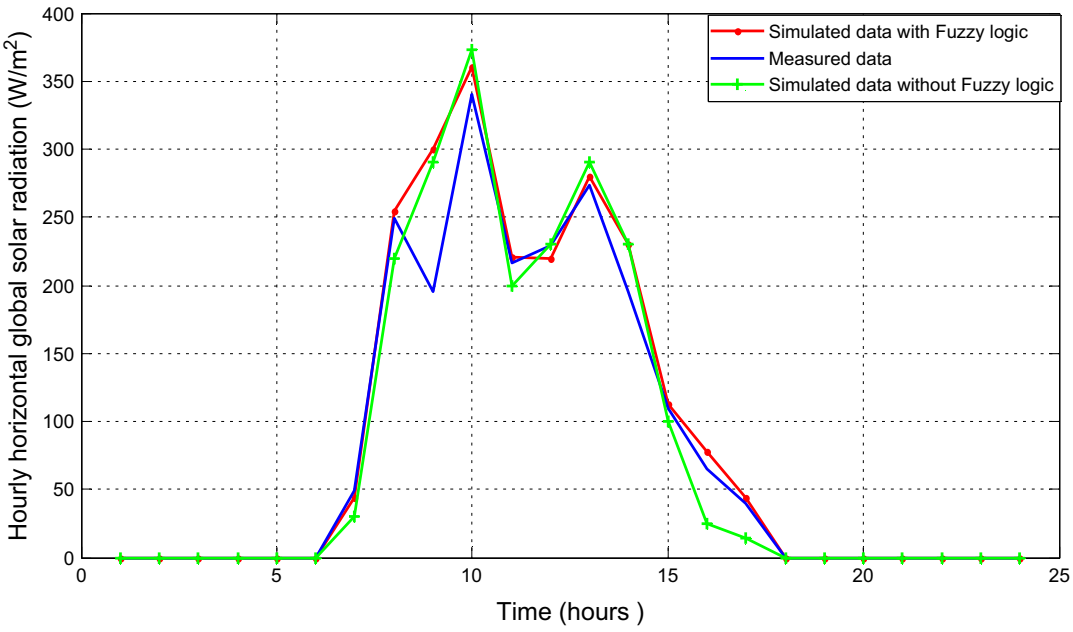

Fig. 8. Measured and simulated of the hourly global horizontal solar radiation with FL and without FL method for the day of 15th February 2011 for the site of Almeria, Spain.

The second step consists in identifying the failures in the storage unit (battery) as failures related to the internal resistance and the overcharging. We indicate that the lead–acid battery works in floating mode between 90% and 100% of state of charge (SOC).

4.1. PV system battery without faults

To check the failures in the PV system battery we used one sunny day for one location to realize our tests. For that, we have chosen the 5th June 2012 for the location of Ghardaia in Algeria. The GISTEL method supplies the PV array by the solar radiation requirements. The output of the PV array is connected to the storage unit and to the variable load. The storage part is used to feed the load at any time of the day. Hence, it is necessary to assure a good performance of the batteries. A good checking of battery means a long lifetime and little period of maintenance that leads to optimize the cost of PV systems. A PV system battery especially lead–acid type needs a special treatment and control of water level. In other hand, the simulation

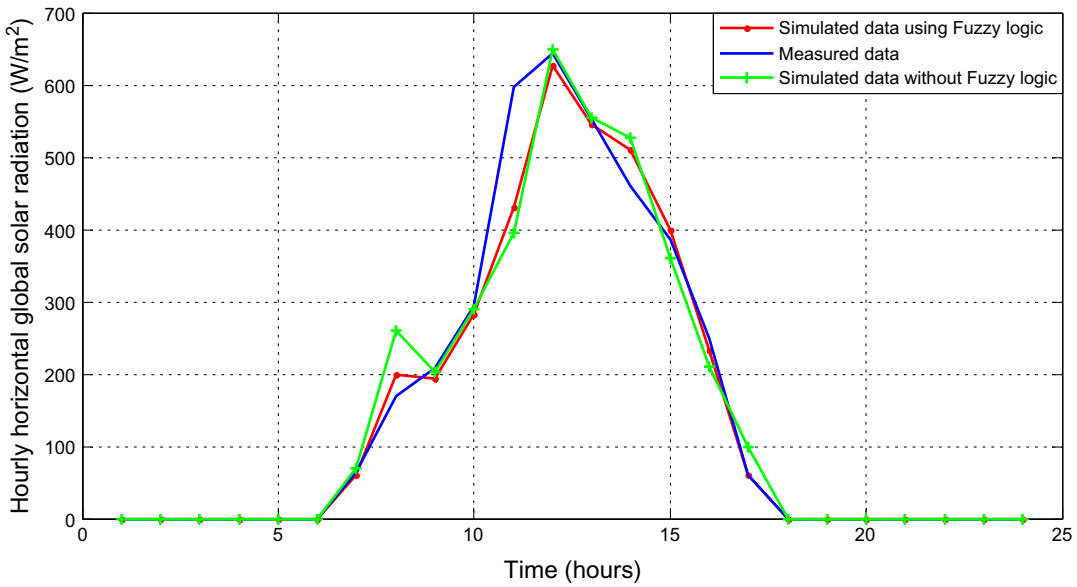

Fig. 9. Measured and simulated of the hourly global horizontal solar radiation with FL and without FL method for the day of 20th February 2011 for the site of Almeria, Spain.

Table 2
The RMSE and NRMSE between actual data and simulated data with and without fuzzy logic method (FL) method.

	Date	Error (RMSE)		Error (NRMSE)	
		With FL	Without FL	With FL	Without FL
Bouzereaha (Algeria)	26 March 2013	52.8788	69.8051	0.2185	0.2885
	03 April 2013	52.9886	63.6144	0.2072	0.2488
Ghardaia (Algeria)	22 November 2012	53.8455	69.9921	0.2285	0.2981
	07 December 2012	54.2156	64.3654	0.2181	0.2584
Almeria (Spain)	15 February 2011	23.3158	25.5123	0.2852	0.3121
	20 February 2011	36.9515	49.0828	0.2407	0.3197

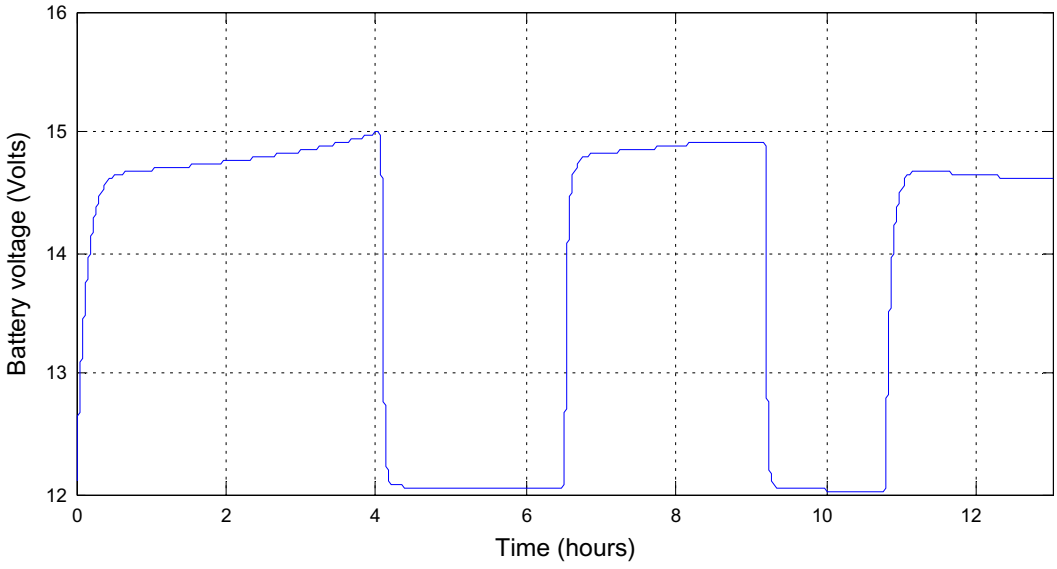

Fig. 10. Lead–acid battery voltage.

results of a PV system battery without faults are considered as a reference for the other simulation results. For that, Fig. 10 represents the battery voltage fixed at 15 V the maximum value and Fig. 11 represents the battery state of charge (SOC) without any faults.

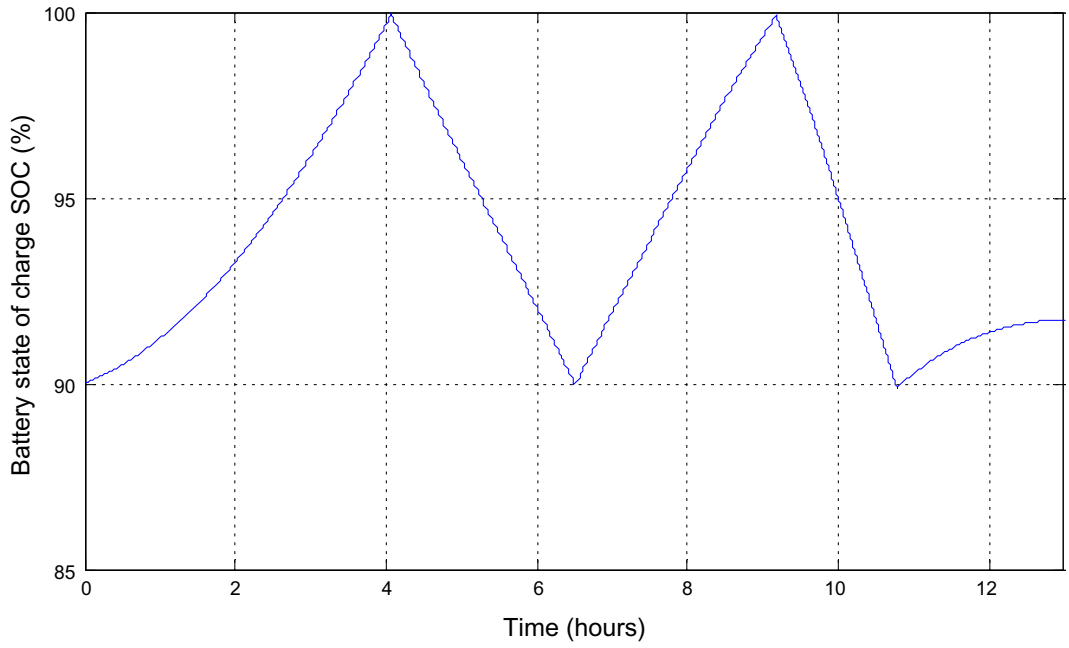

Fig. 11. Lead–acid battery state of charge (SOC).

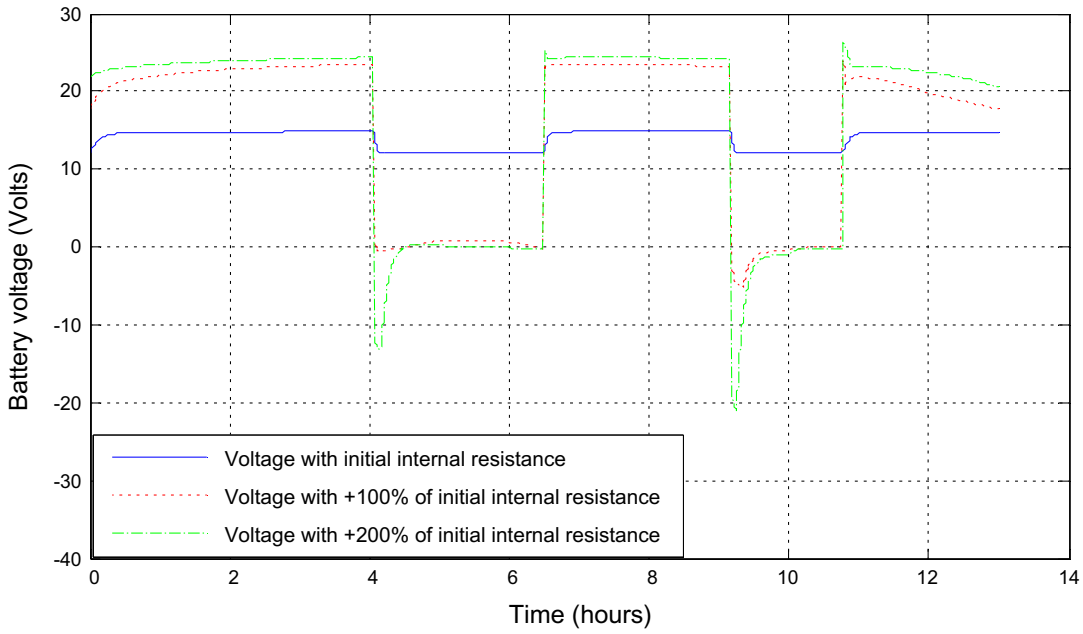

Fig. 12. Lead–acid battery voltage with different internal resistance values.

From Fig. 10 the battery voltage during charge mode does not exceed the fixed value 15 V for all tested cycles. But in the last cycle, the voltage was decreased depending on solar radiation at the sunset. We suppose it as an ideal curve or a reference result of a sunny typical day.

Fig. 11 explains the state of charge (SOC) of the PV system battery with two and half cycles that used for testing the battery performances. The first cycle was slowly charged due to the small values of solar radiation (case of the sunrise). The same effect was occurred at the sunset period (the battery in the charging mode was slowly increased).

4.2. The effect of the internal resistance in the PV system battery

In this stage, we have used two different values of the battery's internal resistance for checking the effect of the internal resistance in the behavior of the PV system battery. Hence, we have increased firstly the internal resistance of the PV system battery that equals to 1 Ohm by +100% of its initial value and secondly, by +200% of its ideal value.

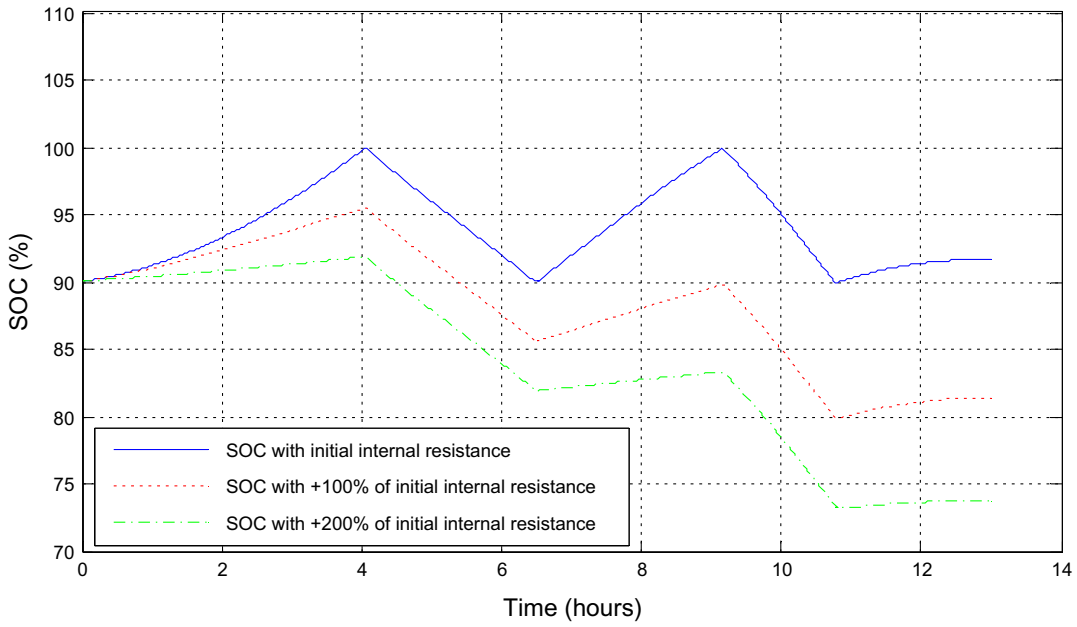

Fig. 13. Lead–acid battery state of charge (SOC) with different internal resistance values.

Fig. 12 represents the battery voltage under different values of the internal resistance, the blue line is the battery voltage at the initial internal resistance; the red line explains the voltage result under +100% of the initial value of the battery's internal resistance and the green line one represents the battery voltage output introduces +200% of the ideal internal resistance. We observed a big exceed in voltage at charge and discharge cases due to the increasing of the battery's internal resistance. An augmentation of the internal resistance with +100% gives high voltage than the initial voltage values. Moreover, the increasing of the internal resistances with +200% gives more voltage than the first case. Hence, and depending on Ohm's law, each increasing of the internal resistance of the battery lead us to an increase of the battery voltage.

Fig. 13 explains the SOC of the solar battery, when the blue curve is the SOC with the ordinary value of internal resistance, the red line represents the SOC cycles with +100% of initial worth of internal resistance and the green line is the SOC with +200% of ideal value of battery's internal resistance. The simulation results have the some input of the solar radiation (GISTEL the satellite method) but the effect of the battery's internal resistance prevented the curves to follow the references. The battery's internal resistance effect has a negative impact on the PV system efficiency. For that; it should be respect the maintenance period and well monitored the storage unit.

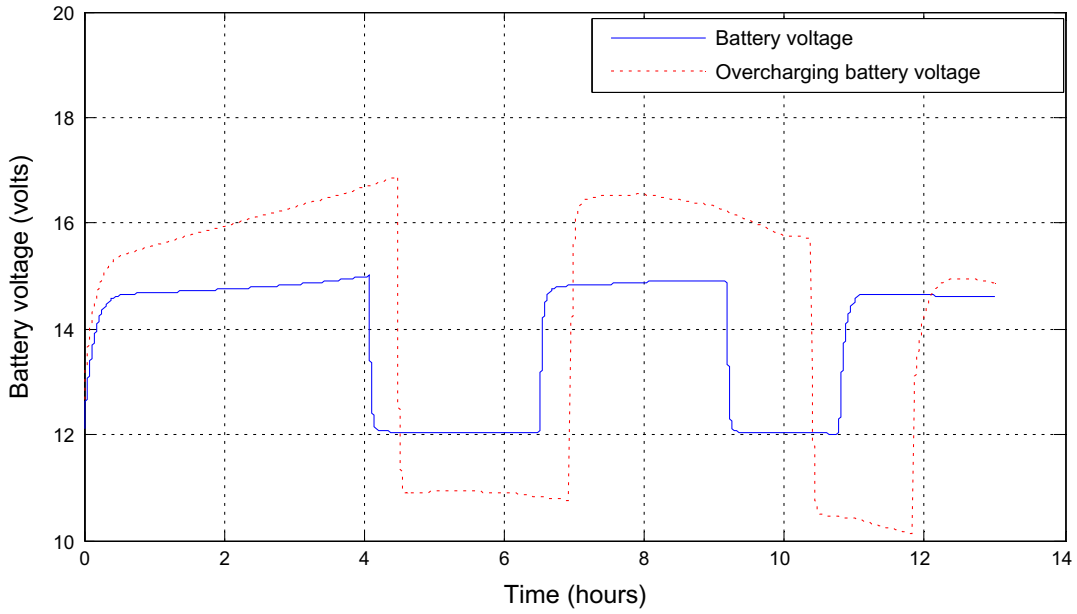

Fig. 14. Lead–acid battery voltage with under overcharging effect.

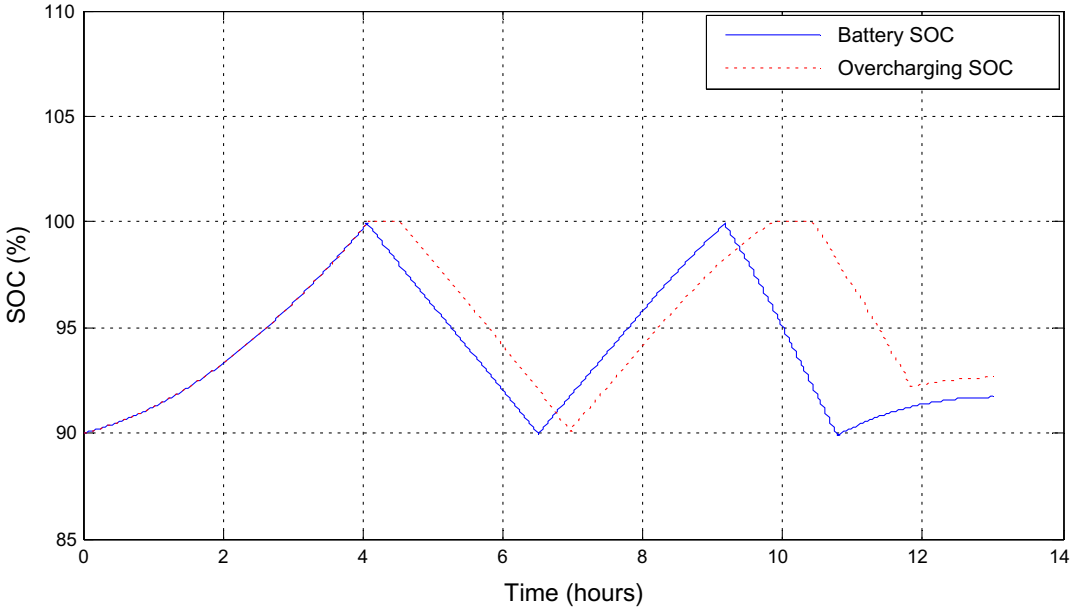

Fig. 15. Lead–acid battery state of charge (SOC) under overcharging effect.

4.3. The effect of the overcharging in the PV system battery

In order to show the negative impact of overcharging in the battery lifetime, we studied the behavior of battery after it is fully charged (arrived at the maximum point of SOC and voltage).

Fig. 14 represents the battery voltage under overcharging effect. The blue line is the battery voltage without any effect that means the reference curve, and the red line is the voltage under overcharging impact. The overcharging effect caused a gap in the allure of the voltage (red line) compared with the reference curve (blue line). These results show a very big degradation at the level of the battery construction that effects its life time.

In addition, Fig. 15 shows the curves of the SOC of the solar battery under the overcharging effect. The blue line is the ideal allure of SOC, and the red one represents the SOC curve under overcharging impact. From this figure, we note a gap between the reference curve and the curve under overcharge effect that causes a decreasing in the level of water in the PV system battery. Hence, the operator should be careful about the occurrence of this problem which results the degradation at the internal plates of the lead–acid battery. For that, the monitoring part is an important task to assure the PV system lifetime planned by the constructor.

5. Conclusion

In this paper, we proposed an approach for identifying the losses in the photovoltaic systems batteries, based on checking the lead–acid battery through the estimation of the solar radiation. The methodology used in this work consists, firstly on the estimation of the hourly global solar radiation data using an improved GISTEL model. The objective of this approach is to process the visible satellite images by calculating the transmission coefficients for each pixel of the image. A comparison between those coefficients and the ones obtained from the clear, partial and totally cloudy sky has been achieved; this allows determining the clearness index that is used for the estimation of the hourly global solar radiation. In addition, a combination of the base GISTEL model and a FL technic was used in this model in order to obtain more precise results. At the second stage, we have tested the battery to check the losses in the PV system. Hence, we review our work to study the internal resistances and the overcharging effects in the PV system battery. The detection of the battery faults guaranteed the PV system efficiency. Moreover, combining the estimation of the solar radiation by GISTEL model as the PV system input with the battery checking operation represents a good improvement in the case of a PV systems monitoring. The obtained experimental results showed the accuracy of this approach. In addition, the proposed method does not need a complicate calculation and is based on a few input parameters only.

Acknowledgements

The authors would like to thank the Amar Telidji University of Laghouat for the financial aspect of the present work and Professor Jean-Pierre Charles for his assistance that help improve the manuscript. The authors also like to thank the anonymous reviewers for their helpful comments.

References

[1] F. Attivissimo, F. Adamo, A. Carullo, A.M.L. Lanzolla, F. Spertino, A. Vallan, On the performance of the double-diode model in estimating the maximum power point for different photovoltaic technologies, Measurement 46 (2013) 3549–3559.
[2] V. Badescu, C. Gueymard, S. Cheval, C. Oprea, M. Baciu, A. Dumitrescu, F. Iacobescu, I. Milos, C. Rada, Accuracy analysis for fifty-four clear-sky solar radiation models using routine hourly global irradiance measurements in Romania, Renew. Energy 55 (2013) 85–103.
[3] B.N. Belcher, A.T. DeGaetano, A revised empirical model to estimate solar radiation using automated surface weather observations, Sol. Energy 81 (2007) 329–345.
[4] A. Ben Djemaa, C. Delorme, A comparison between one year of daily global irradiation from ground-based measurements versus METEOSAT images from seven locations in Tunisia, Sol. Energy 5 (1992) 325–333.
[5] K. Benmouiza, A. Cheknane, Forecasting hourly global solar radiation using hybrid k-means and nonlinear autoregressive neural network models, Energy Convers. Manage. 75 (2013) 561–569.
[6] J.S. Bojanowski, M. Donatelli, A.K. Skidmore, A. Vrieling, An auto-calibration procedure for empirical solar radiation models, Environ. Modell. Softw. 49 (2013) 118–128.
[7] D. Cano, J.M. Monget, M. Albuisson, H. Guillard, N. Regas, L. Wald, A method for the determination of the global solar radiation from meteorological satellite data, Sol. Energy 37 (1986) 31–39.
[8] J.P. Charles, I. Mekkaoui-Allaoui, G. Bordure, P. Mialhe, A critical study of the effectiveness of the single and double exponential models for I–V characterization of solar cells, Solid-State Electron. 28 (1985) 807–820.
[9] W. Chen, H. Shen, B. Shu, H. Qin, T. Deng, Evaluation of performance of MPPT devices in PV systems with storage batteries, Renew. Energy 32 (2007) 1611–1622.
[10] R. Enriquez, L. Zarzalejo, M.J. Jimenez, M.R. Heras, Ground reflectance estimation by means of horizontal and vertical radiation measurements, Sol. Energy 86 (2012) 3216–3226.
[11] T.A. Kattakayam, K. Srinivasan, Lead–acid batteries in solar refrigeration systems, Renew. Energy 29 (2004) 1243–1250.
[12] M. Kim, E. Hwang, Monitoring the battery status for photovoltaic systems, J. Power Sources 64 (1997) 193–196.
[13] A. Linares-Rodriguez, J.A. Ruiz-Arias, D. Pozo-Vazquez, An artificial neural network ensemble model for estimating global solar radiation from Meteosat satellite images, Energy 61 (2013) 636–645.
[14] E. McKenna, M. McManus, S. Cooper, M. Thomson, Economic and environmental impact of lead–acid batteries in grid-connected domestic PV systems, Appl. Energy 104 (2013) 239–249.
[15] F. Meziani, M. Boulifa, Z. Ameur, Determination of the global solar irradiation by MSG-SEVIRI images processing in Algeria, Energy Proc. 36 (2013) 525–534.
[16] R. Ranganathan, W. Mikhael, N. Kutkut, I. Batarseh, Adaptive sun tracking algorithm for incident energy maximization and efficiency improvement of PV panels, Renew. Energy 36 (2011) 2623–2626.
[17] R.A. Suarez, G. Abal, R. Siri, P. Muse, Brightness-dependent Tarpley model for global solar radiation estimation using GOES satellite images: application to Uruguay, Sol. Energy 86 (2012) 3205–3215.
[18] M. Tadj, K. Benmouiza, A. Cheknane, S. Silvestre, Improving the performance of PV system by faults detection using GISTEL approach, Energy Convers. Manage. 80 (2014) 298–304.
[19] O. Tremblay, L.A. Dessaint, Experimental validation of a battery dynamic model for EV applications, World Electr. Veh. J. 3 (2009) 2032–6653.
[20] K.M. Tsang, W.L. Chan, State of health detection for Lithium ion batteries in photovoltaic system, Energy Convers. Manage. 65 (2013) 7–12.
[21] W.M.O., Meteorological aspects of the utilization of solar radiation as an energy source, in: Technical note W.M.O., vol. 172, 1981, pp. 57–85.
[22] A. Widodo, M.C. Shim, W. Caesarendra, B.S. Yang, Intelligent prognostics for battery health monitoring based on sample entropy, Expert Syst. Appl. 38 (2011) 11763–117690.

Abstract

Algeria is an interesting country for the exploitation of solar energy; it has a considerable territory of solar energy, so it is a major interest for a country like ours to estimate this type of energy to identify possible and effective means that used in a policy context of energy of the country. The optimal sizing of photovoltaic systems is very important, especially in an economic point of view, it allows to design an efficient system, avoiding load losses while minimizing the cost of installation, this can be done by using data of solar radiation as well as insolation levels. Therefore, it is important to carry out the quantification of solar data on the Algerian territory. For that, and throughout this thesis, we will try to develop physical and empirical models for estimating and forecasting hourly, daily and monthly solar radiation data from multiple sources (insolation and radiation), these models will be applied and tested for different climatic regions of Algeria. At the end, a map of solar radiation zoning will be established. The application to the sizing of photovoltaic system will show that the results in an hourly scale are more precise than a daily scale especially for the performance of the photovoltaic system.

Keywords: Quantification, solar radiation, solar maps, stochastic models, neural networks, sizing.

Résumé

L'Algérie est un pays potentiellement intéressant pour l'exploitation de l'énergie solaire. En effet, son territoire dispose d'un gisement solaire considérable. Il est donc d'intérêt majeur, pour un pays comme le nôtre, de pouvoir estimer les potentialités offertes par ce type d'énergie afin d'identifier les moyens possibles et efficaces de s'en servir dans une perspective de politique énergétique du pays. Le dimensionnement optimal des systèmes photovoltaïques est très important surtout du point de vue économique. Il permet de concevoir un système performant, évitant les pertes de charge trop fréquentes tout en minimisant le coût de l'installation. Il s'effectue en utilisant les données de l'irradiation solaire globale du moins le moins ensoleillé. Par conséquent il est utile de procéder à la quantification des données solaires sur le territoire algérien. Tout au long de ce travail de thèse, nous essayerons de mettre au point des modèles semi empiriques et physiques pour estimer et prédire les données solaires à l'échelle horaire, journalière et mensuelle à partir de données multi sources (insolation et irradiation). Cette quantification du gisement solaire se fera pour différentes régions climatiques de l'Algérie. Enfin, une cartographie du gisement solaire algérien sera établie. En outre, nous présenterons une application portant sur un dimensionnement des systèmes photovoltaïques à l'échelle horaire. Le dimensionnement envisagé est qualifié plus précis que dans le cas où ce dernier est effectué à une échelle journalière.

Mots-clés: Quantification, rayonnement solaire, cartographie, modèles stochastiques, réseaux de neurones, dimensionnement.

ملخص

تعتبر الجزائر منطقة جد هامة لاستغلال الطاقة الشمسية وذلك لاحتوائها على مساحة كبيرة تحت الطاقة الشمسية. لذلك يعتبر استغلال هاته الطاقة مصلحة كبرى لبلد مثل بلدنا لتقدير هذا النوع من الطاقة وذلك لتحديد الوسائل الممكنة والفعالة التي تستخدم في سياق سياسة الطاقة في البلاد. الاختيار الامثل والمتكامل للأنظمة الضوئية مهم جدا خصوصا من الناحية الاقتصادية, حيث أنها تسمح بتصميم نظام فعال مع تجنب خسائر الحمل والتقليل من كلفة التركيب. يمكن القيام بهذا عن طريق استخدام بيانات الاشعاع الشمسي وساعات السطوع الشمسي. لذلك هنالك اهمية كبرى لدراسة الكمية لهاته البيانات في الجزائر. من أجل هذا و من خلال العمل المطروح سنحاول تطوير النماذج النظرية والفيزيائية لتقدير وتنبأ بيانات الاشعاع الشمسي على المستوى الساعي, اليومي و الشهري بدراسة عدة مصادر متنوعة (الاشعاع وساعات السطوع الشمسي) .سيتم تطبيق هاته النماذج واختبارها في عدة مناطق في الجزائر. في نهاية هذا العمل سيتم انشاء خريطة حرارية وذلك لتقسيم مناطق الاشعاع الشمسي في البلاد . النتائج المتحصل عليها في تصميم الانظمة الضوئية بينت أن الدراسة على المستوى الساعي تعتبر جد مهمة للنظام مقارنة مع المستوى اليومي.

الكلمات المفتاحية : تحديد الكمية ، الإشعاع الشمسي , الخرائط الشمسية، النماذج العشوائية، الشبكات العصبية، التحجيم.